Halogen bonding interlocked rotaxanes and transition metal-based host systems for charged guest recognition and sensing

Vihanga K. Munasinghe

Linacre College, University of Oxford



A thesis submitted for the degree of Doctor of Philosophy

Inorganic Chemistry Laboratory

University of Oxford

Trinity Term 2022

Halogen bonding interlocked rotaxanes and transition metal-based host systems for charged guest recognition and sensing

Vihanga K. Munasinghe, Linacre College, University of Oxford

Abstract of the thesis submitted for the degree of DPhil, Trinity term 2022

The main theme of this thesis is to incorporate multiple convergent halogen bonding (XB) donor motifs into anion binding sites of mechanically interlocked rotaxanes and transition metal-based host architectures and investigate their anion and ion-pair recognition capabilities.

Chapter 1 introduces the field of supramolecular host-guest chemistry with particular emphasis on XB interactions, anion and ion-pair recognition, followed by a review of the synthesis and applications of mechanically interlocked molecules (MIMs).

Chapter 2 presents the first examples of a series of novel XB heteroditopic [2]rotaxanes capable of selectively recognising lithium halide ion-pair species. A co-bound lithium cation was observed to switch-on halide anion binding, and the binding affinity increased with the number of halogen bond donors. This initial work is extended to develop a dynamic two-station [2]rotaxane to investigate the unprecedented use of an ion-pair as an external stimulus to control the translational motion of the macrocycle along the axle component.

Chapter 3 details the preparation, dicarboxylate anion recognition, and sensing properties of a novel iridium(III) complexed XB [3]rotaxane. The higher order mechanically bonded [3]rotaxane architecture exhibited higher luminescence quantum yields and superior anion recognition and sensing properties compared to analogous [2]rotaxane and acyclic hosts.

Chapter 4 explores the design, synthesis, and anion binding properties of bimetallic rhenium(I) complexed molecular tweezer host systems containing a tetradentate XB binding cavity. Comprehensive anion binding studies revealed the significant contribution of both Re(I) complexation and tweezer design to the enhanced anion recognition properties observed by the tweezer hosts.

Chapter 5 summarises the main conclusions of the thesis.

Chapter 6 details the experimental procedures employed in this work, including synthetic protocols and the characterisation of novel compounds.

Acknowledgements

Oxford is the first place I have lived away from home, Sri Lanka. I have had some of the most wonderful experiences in my life during my DPhil at Oxford, largely due to the many incredible people I have had the opportunity to meet and interact with.

First and foremost, I am immensely grateful to my supervisor, Professor Paul Beer, for giving me the opportunity to work at the Beer group. He is by far one of the nicest people I have met and looking back I could not have chosen a better supervisor for my DPhil. Thank you so much Paul for your guidance and unwavering support until the very end.

Having come from a research background in Metal-Organic Frameworks, with little experience in synthetic chemistry, I have had a steep learning curve at the Beer group. This would not have been possible if not for the support from past and present Beer group members. In particular, I would like to thank Jess, George, and Andrew for their help in my first year, and Richard and Rob for always being willing to discuss my research projects and for providing me with invaluable ideas. I was fortunate to guide a first-year DPhil student Hui, one of the cleverest students I have met, who later contributed to the results presented in the ion-pair project in Chapter 2. More than colleagues, we were friends, and I am thankful to her for reintroducing me to badminton, a long-forgotten hobby of mine. I want to extend my gratitude to the Beer and Langton group members I have worked with; TJ (for being a great lab mate and a housemate, and for all the unforgettable memories at house parties) Luiza (for always being there to help), Arya and Toby (for being such nice friends), Zongyao and Heike (for their expertise in crystallography), Jamie (for helping solve everyone's IT/tech issues) Laura, Krzysztof and Andrew T. (for the nice company). I am also very grateful to Richard, Luiza, Jess, and Krzysztof for proofreading my thesis within days.

Aside from research, Oxford played a pivotal role to help me grow as a person. I will always remember the amazing friends I made, the memories I have of organising events at OxfordHub as the kid's officer, at the Oxford University Sri Lanka society as the vice president, and at Linacre College as the race and ethnic minority representative and as a peer supporter. I am also grateful to the OU careers unit for allowing me to explore different career paths by providing an opportunity to work as a business consultant, and to the Young Entrepreneurship Competition (YES20) for the opportunity to walk in the shoes of an entrepreneur. I learned a lot from these experiences, and I was able to take a step toward discovering what I truly enjoy.

Away from CRL, I was lucky to be part of Linacre College, where I have some of my fondest memories of Oxford. Linacre provided me with accommodation for all four years (with a three-minute walk to my lab!), an amazing set of friends whom I now consider family, and the E.P.A Cephalosporin scholarship for my DPhil. Linacre's legendary BOPs, SSF, household parties, and celebrations in the CR were just the cherry on top. I especially want to thank Ani, Varnika, and Zuzana for being my constant support system. I will always remember Ani's fake B'day celebrations, girls' day-outs with Varnika and Yi, Zuzana whose home was always open for me when needed, and Sol for all the nice memories we had as a household. I am looking forward to seeing you all in Cambridge soon.

I am thankful for the free education system in Sri Lanka, and I am in debt to all the taxpayers who have funded my education in Sri Lanka. During this unprecedented economic crisis, I want to let you all know that I am there with you, even though I am miles apart physically.

To my loving family in Sri Lanka, thank you amma and thaththa for your unconditional love and constant care. You are the reason for who I am today. I hope I have made you proud. I cannot forget my aiya, Jayani akka, Dilhan's amma and thaththa, and Dilhara nangi for the unconditional support all the way from Sri Lanka. Finally, my niece and nephew, Esath and Liyara, my favourite little munchkins on earth, who never fail to make me happy!

Last but definitely not least, my caring and loving husband, Dilhan. To you, I would like to say: I would have never made it this far without you. You have always stood by me through my best and worst and made sure that I succeeded at all challenges I faced. Thank you for giving me the best time of my life during the past 4+ years of our marriage. I will forever cherish our memories in Oxford, but more so, I look forward to the many wonderful adventures we will embark on in future years to come.

This thesis is dedicated to Dilhan, who is a loving husband, collaborator (for DFT calculations), proof-reader of this thesis, my biggest motivator, and above all, the person who inspired me to see the beauty of science.

Vihanga Munasinghe

OCT Library, 30th July 2022

Publications

The work presented in this thesis forms the basis of the following publications:

Chapter 2:

- *"Mechanical Bond Enhanced Lithium Halide Ion-Pair Binding by Halogen Bonding Heteroditopic Rotaxanes"*
  V. K. Munasinghe, J. Pancholi, D. Manawadu, Z. Zhang, P. D. Beer, Chem. Eur. J. **2022**, 28, e202201209.

- *"Lithium halide ion-pair recognition mediated molecular shuttling in heteroditopic [2]rotaxanes"*
  V. K. Munasinghe, Hui Min Tay, Dilhan Manawadu, Jessica Pancholi, Zongyao Zhang, Paul D. Beer *(Manuscript in preparation)*

Chapter 3:

- *"Ir(III) complexed halogen bonding [3]rotaxane for optical sensing of dicarboxylate anions"*
  V. K Munasinghe, P. D. Beer *(Manuscript in preparation)*

Chapter 4:

- *"Re(I)-complexed halogen bonding molecular tweezers for enhanced anion recognition"*
  V. K Munasinghe, X. Li, Z. Zhang, P. D. Beer. *(Manuscript in preparation)*

Glossary of Abbreviations

δ	chemical shift
λ	wavelength
v	frequency
Å	Ångstrom
A^-	anion
AMT	Active metal template
Ar	aromatic
ATP	adenosine triphosphate
a.u.	arbitrary units
bipy	2,2'-bipyridine
Boc	*tert*-butyloxycarbonyl
CuAAC	copper(I)-catalysed azide–alkyne cycloaddition
DIPEA	*N*,*N*-di-*iso*-propylethylamine
DMF	*N*,*N*-dimethylformamide
eq., equiv.	equivalent
ESI	electrospray ionisation
HB	hydrogen bonding
HOMO	highest occupied molecular orbital
Hz	hertz
J	Joule
J	coupling constant
k	kilo
K	Kelvin
K_a	association constant
L	litre
Li-Rotaxane	Lithium cation precomplexed rotaxane
LUMO	lowest unoccupied molecular orbital
M	molar
m-	*meta*

m/z	mass-to-charge ratio
MIM	mechanically interlocked molecule
MLCT	metal-to-ligand charge transfer
mol	mole
MS	mass spectrometry
NMR	nuclear magnetic resonance
OAc	acetate
p-	*para*
PET	photoinduced electron transfer
pH	$-\log_{10}[H^+]$
ppm	parts per million
ROESY	rotating-frame Overhauser effect spectroscopy
rt	room temperature
s	singlet
St	stopper
t	triplet
t-, tert	tertiary
TBA	tetrabutyl ammonium
TBTA	tris[(1-benzyl-1*H*-1,2,3-triazol-4-yl)methyl]amine
TLC	thin layer chromatography
UV	ultra-violet
V	Volt
X	halogen atom
XB	halogen bonding

Table of Contents

Chapter 1: Introduction 3

1.1. Supramolecular chemistry 3

1.2. Design principles used in supramolecular chemistry 6

1.2.1. Chelate, macrocyclic, and cryptate effects 6

1.3. Non-covalent interactions 7

1.3.1. Electrostatic interactions 8

1.3.2. Hydrogen Bonding (HB) 8

1.3.3. Halogen bonding (XB) 9

1.3.4. π- π interactions 10

1.3.5. Ion-π interactions 11

1.3.6. Hydrophobic and solvophobic effects 12

1.4. Anion supramolecular chemistry 13

1.4.1. Importance of anion recognition 13

1.4.2. Challenges of anion recognition 14

1.4.3. Synthetic anion receptors 15

1.5. Ion-pair recognition 27

1.5.1. Ion-Pair binding modes 29

1.5.2. Applications of ion-pair receptors 31

1.6. Mechanically interlocked molecules 34

1.6.1. Synthesis of mechanically interlocked molecules 35

1.6.2. Template directed Synthesis 37

1.6.3. Applications of Mechanically Interlocked Molecules 42

1.7. Project outline 48

Chapter 2: Heteroditopic [2]rotaxanes for lithium halide ion-pair recognition 53

2.1. Introduction 53

2.1.1. Heteroditopic rotaxanes for ion-pair recognition 53

2.1.2. Lithium halide ion-pair recognition 55

2.2. Chapter aims 56

2.3. Part I: XB/HB heteroditopic [2]rotaxanes with an amide macrocycle 57

2.3.1. Synthesis of HB amide heteroditopic macrocycle and HB/XB [2]rotaxanes 57

2.3.2. Anion, cation, and ion-pair recognition studies 63

2.3.3. Solid-state structure analysis 72

2.3.4. DFT calculations 74

2.3.5. Preliminary Solid-liquid extraction (SLE) studies 78

2.4. Ion-pair mediated macrocycle translocation 80

2.4.1. Design, synthesis and characterisation of the two station rotaxane and analogous one station rotaxane 80

2.4.2. ^{1}H NMR spectroscopic studies of ion-pair induced macrocycle shuttling 86

2.4.3. Reversibility studies of macrocycle translocation 91

2.4.4. Conclusions and future work 91

2.5. Part II: Heteroditopic [2]rotaxanes with a XB/HB triazole macrocycle 94

2.5.1. Introduction 94

2.5.2. Design and synthesis of bidentate and tridentate halogen bonding heteroditopic [2]rotaxanes 96

2.5.3. Solid state structure analysis 101

2.5.4. Anion, cation, and ion-pair binding properties of heteroditopic [2]rotaxanes 102

2.5.5. Ion-pair binding studies of XB and HB macrocycles 106

2.5.6. DFT calculations 107

2.5.7. Conclusions 109

2.5.8. Future work 110

Chapter 3: Transition metal-based halogen bonding rotaxane hosts for anion recognition and sensing 114

3.1. Introduction 114

3.1.1. Iridium(III) based hosts for anion recognition and sensing 115

3.1. Chapter aims 118

3.2. Ir(III) based receptors for anion recognition and sensing 118

3.2.1. Design and synthesis of Ir(III) complexed XB acyclic receptor 118

3.2.2. Design and synthesis of Ir(III) complexed XB rotaxane receptors 120

3.2.3. Photophysical properties of Ir(III) complexed receptors 125

3.2.4. Electrochemical properties of Ir(III) complexed receptors 127

3.2.5. Anion binding studies of the Ir(III) based acyclic, [3]rotaxane, and [2]rotaxane receptors 130

3.3. Conclusions and Future work 139

Chapter 4: Halogen bonding rhenium(I) complexed tweezer type receptors for anion recognition 144

4.1. Introduction 144

4.1.1. Tweezer receptors 144

4.2. Chapter aims 146

4.3. Anion binding studies 151

4.3.1. Solid state structure analysis of anion-bound receptors. 151

4.3.2. Solution state ^{1}H NMR anion binding studies 153

4.4. Conclusions and Future work 162

Chapter 5: Conclusions 168

Chapter 6: Experimental section 174

6.1. General Remarks 174

6.1.1. Chemicals and solvents 174

6.1.2. Instrumentation 174

6.1.3. ^{1}H NMR titration protocol 175

6.1.4. Optical measurements 175

6.1.5. Electrochemical experiments 176

6.2. Synthetic procedures and characterisation of compounds 178

Appendices 207

Appendix A: Titration data of heteroditopic [2]rotaxanes 207

Appendix B: Crystallographic Data 213

Appendix C: DFT optimised structures 220

Appendix D: Titration data of dicationic Re(I) receptors. 226

Appendix E: Chemical structures of all receptors 227

References 229

Chapter 1

Introduction

Chapter 1: Introduction

1.1. Supramolecular chemistry

There are many hierarchical and intelligent systems in nature capable of performing complex functions in a highly accurate and precise manner.[1] This includes intricate packaging and replication of DNA which is the basis of life, enzyme-substrate interactions, and selective transport of molecules within the body.[2] The core concept that brings about these functions is the process of molecular recognition of chemical species, which is achieved via a combination of reversible non-covalent interactions. The most commonly employed non-covalent interactions utilised are electrostatic interactions, hydrogen bonding (HB), π- π stacking interactions and van der Waals forces. Taking inspiration from nature, the broad, interdisciplinary field of supramolecular chemistry is based on non-covalent interactions and their applications in host-guest chemistry and self-assembly.[3]

Supramolecular host-guest chemistry has its origins in the 'lock-and-key' concept, first proposed by Emil Fischer in 1884, to explain the selective molecular recognition process of enzymes in biological systems.[4] The complementary shape, size, and chemical functionality between a host (lock) and guest (key) species results in high selectivity .

Developing synthetic receptors that mimic the selectivity displayed by enzymes and proteins continues to stimulate the supramolecular host-guest chemistry chemist. One of the first pioneers in the field was Pedersen who in 1967 demonstrated how simple cyclic crown ethers can be used for selective binding of Group I metal cations (Figure 1.1a).[5] Selective cation recognition was developed further by Lehn's cryptands[6] with a three-dimensional binding cavity (Figure 1.1b) and Cram's design of rigid spherands (Figure 1.1c).[7] This seminal work led to Pedersen, Lehn, and Cram being awarded the 1987 Nobel Prize in Chemistry for

their contributions to the "development and use of molecules with structure-specific interactions of high-selectivity." [8–10]

Almost three decades later in 2016, the second Nobel Prize in Chemistry for supramolecular chemistry was awarded to Sauvage, Stoddart, and Feringa for the design and synthesis of molecular machines.[11–13] Sauvage's team used a copper(I) ion as a template to successfully link two molecular rings to form a 'catenane' (Figure 1.1d).[14] Stoddart and co-workers constructed a 'rotaxane' exploiting aromatic donor-acceptor interactions between an electron-deficient positively charged ring and an electron-rich 'axle' (Figure 1.1e).[15] Unlike the conventional covalent bond, both catenanes and rotaxanes possess *mechanical bonds*, that facilitate the ability of their constituent parts to move relative to each other, which is the basic requirement for the function of a molecular machine. Independently, Feringa developed the first molecular rotor blade capable of continuously rotating in the same direction (Figure 1.1f).[16] The work of all three Nobel Laureates has contributed to the development of a molecular lift,[17] a molecular muscle,[18] a nano car[19], and recently chemical engines[20] and pulse fuelled molecular ratchets.[21,22] Indeed, molecular motors are currently at the same stage as electric motors were in the 1830s, when no one imagined they would lead to everyday necessities such as washing machines, fans, and food processors.[23] There are thus no limits to the potential future nanotechnological applications of supramolecular chemistry.

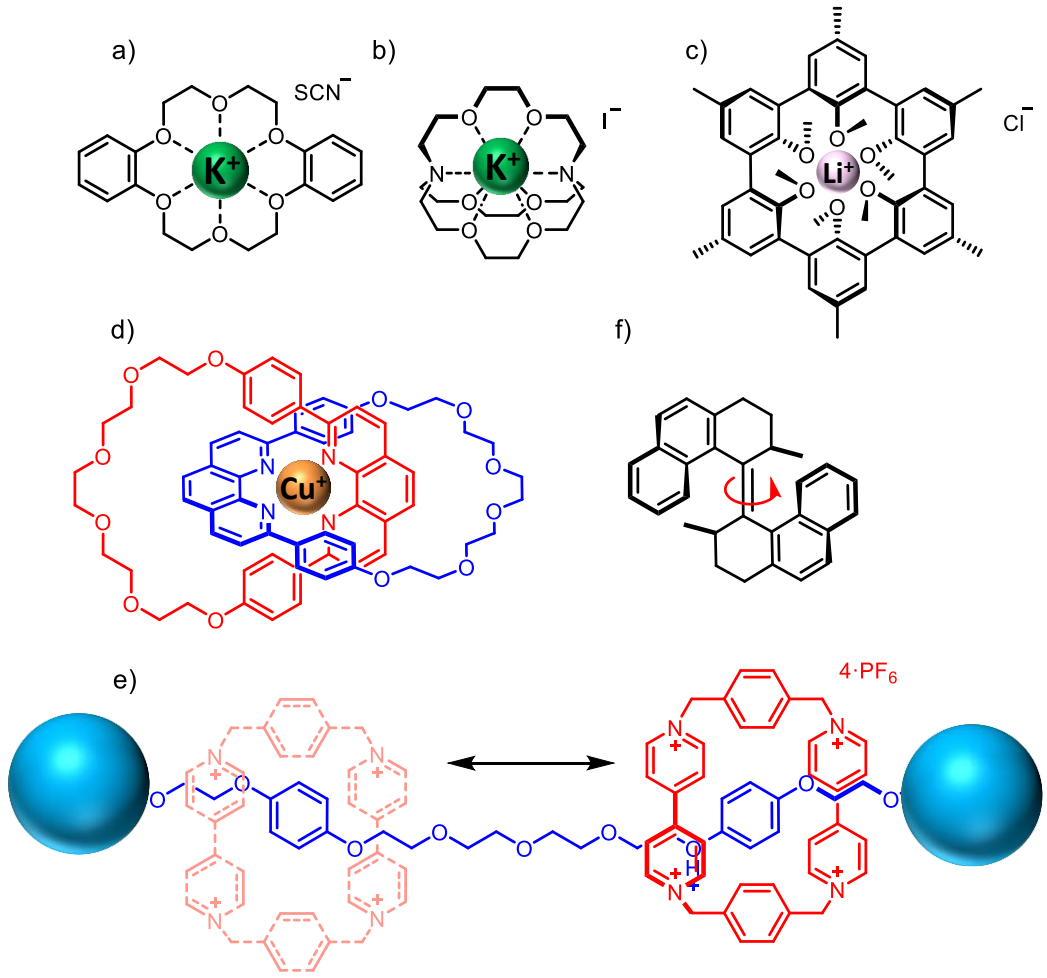

Figure 1.1: Structures of a) Pedersen's dibenzo[18]crown-6 K^+ complex,[5] b)Lehn's [2.2.2]Cryptand K^+ complex,[5] c) Cram's spherand Li^+ complex,[7] d) Sauvage's [2]catenane with the Cu(I) template,[14] e) Stoddart's [2]rotaxane molecular shuttle[15] and f) Feringa's molecular rotor.[16]

The theme of this thesis is based on supramolecular host-guest chemistry, with particular emphasis on the recognition of anion and ion pair guest species. This introductory chapter begins with an overview of supramolecular chemistry design principles and non-covalent interactions used for host-guest recognition, followed by a review of key examples of anion and ion-pair receptors. A discussion of the synthesis of mechanically interlocked receptors and their applications in host-guest chemistry concludes this chapter.

1.2. Design principles used in supramolecular chemistry

Taking inspiration from biological systems, supramolecular chemistry has established a set of design principles to ensure strong interactions between supramolecular synthons and/or supramolecular host and guest molecules.

1.2.1. Chelate, macrocyclic, and cryptate effects

Originating from metal coordination chemistry, the 'chelate effect' is the enhanced stabilisation of guest species by multidentate chelating ligands with respect to their monodentate ligand analogues.[24–26] The effect is attributed to both favourable enthalpy (by having guest binding groups proximally linked to each other which overcomes inter-ligand repulsions) and also entropic contributions (due to the release of solvent molecules upon complexation).

Compared to acyclic chelating receptors as podands shown in Figure 1.2, macrocyclic analogues with the same number and arrangement of binding motifs further stabilise host-guest complexation via the macrocyclic effect.[27,28] Macrocycles are often rigid and lose fewer degrees of freedom upon guest complexation, making the binding process more entropically favoured. Additionally, macrocycles are generally less solvated and hence complexation is more enthalpically favoured as a consequence of the cyclic ligand's lower desolvation energy.

The inherent three-dimensional binding cavities of cryptands stabilise host-guest complexation even further by complete encapsulation of the guest. This extra stabilisation offered by the cryptand three-dimensional cavity in comparison to a macrocyclic ligand is known as the 'cryptate effect'.[26,28,29]

These effects are illustrated in Figure 1.2 where the magnitude of Gibbs free energy (ΔG°) for potassium cation complexation increases from the acyclic podand (-25 kJ/mol) to the

macrocyclic crown-ether (-58 kJ/mol), which is surpassed by the cryptand receptor (-75 kJ/mol).[7]

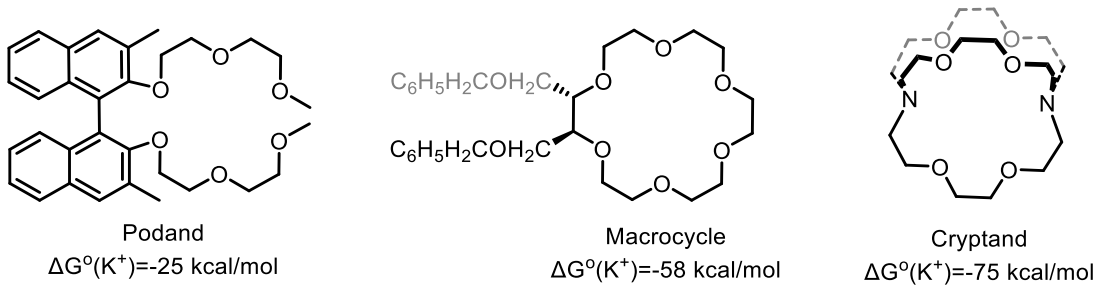

Figure 1.2: Structures of receptors depicting increased potassium cation binding from podand to macrocycle to cryptand. Thermodynamic parameters measured at 25 °C, in $CDCl_3$ saturated with D_2O. K^+ added as the picrate salt.

1.3. Non-covalent interactions

For the effective design of supramolecular host structures, an appreciation of the variety and relative strengths of non-covalent interactions is crucial. These attractive intermolecular forces vary in strength from weak van der Waals interactions (≈ 1 kJ mol^{-1}) to strong $F^-\cdots$H-F hydrogen bonds (≈ 160 kJ mol^{-1}) as depicted in Figure 1.3.[30] While these reversible individual supramolecular interactions tend to be relatively weak compared to irreversible covalent bond formation, when utilised in a concerted manner they can elicit powerful and selective host-guest binding.

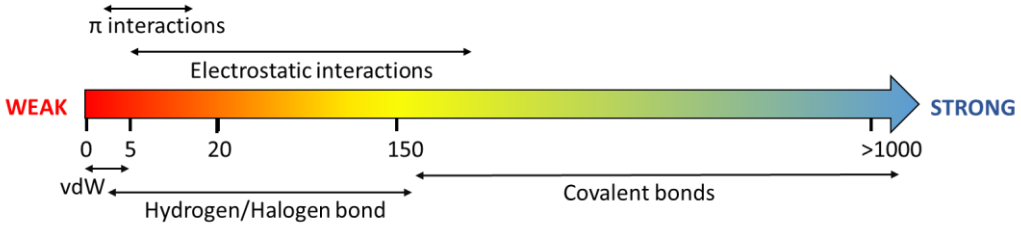

Figure 1.3: Relative strength of covalent and non-covalent bonds. Bond energy is given in kJ/mol.

1.3.1. Electrostatic interactions

Electrostatic interactions are Coulombic attractions that can be classified into ion-ion, ion-dipole, and dipole-dipole interactions. Ion-ion interactions are the strongest with stabilisation energies up to 250 kJ mol^{-1},[30] and distance dependence (r) ($E_{ion\text{-}ion} \propto r^{-1}$). However, they are non-directional. Ion-dipole (E=50-200 kJ mol^{-1}), and dipole-dipole ($E_{ion\text{-}dip}$=5-50 kJ mol^{-1}) interactions, which include hydrogen bonding (HB) are weaker, diminish more rapidly with distance ($E_{ion\text{-}dip} \propto r^{-2}$, $E_{dip\text{-}dip} \propto r^{-3}$) but importantly for host-guest chemistry, are directional.[30]

Strong electrostatic interactions have proven to be an efficient strategy for anion recognition in competitive protic solvents like water. A seminal example is Schmidtchen and co-worker's cationic quaternary ammonium tetrahedral cage which was capable of selectively binding Br^- and I^- over Cl^- in D_2O through favourable electrostatic interactions Figure 1.4.[31]

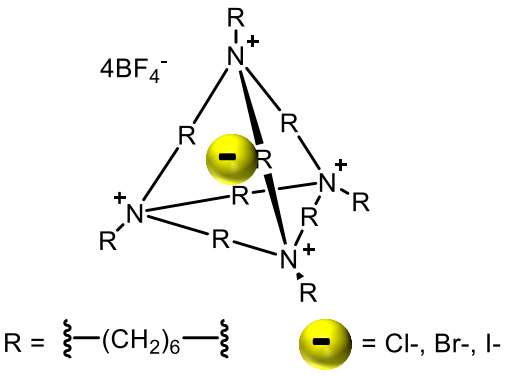

Figure 1.4: Schmidtchen's cationic quaternary ammonium cage

1.3.2. Hydrogen Bonding (HB)

When a hydrogen atom is covalently bound to a more electronegative atom (D) (e.g. N, O, F), the positively polarised hydrogen can form attractive interactions with Lewis bases (B) such as anions. This attractive non-covalent force, known as hydrogen bonding (HB), is

generally denoted as D-H···B.[32] The D-H···B angle is usually close to being linear for strong HB interactions, while deviations from linearity are observed for weaker HB interactions.[33] The strength of HB varies considerably depending on the electron-withdrawing nature of the covalently linked substituent. For example, hydrogen bonds in CH_4···F-CH_3 are weak, with bond energies of 1 kJ mol^{-1} while with F^-···HF (HF_2^-) strong HB interactions with bond energies of 162 kJ mol^{-1} are observed.[34,35] The tunability of hydrogen bond strength, combined with directionality and the wide synthetic accessibility of HB donor motifs such as amides, urea, triazoles, and imidazoles has resulted in this non-covalent interaction being the most commonly used in biotic and abiotic anion receptors in particular.[36]

1.3.3. Halogen bonding (XB)

Halogen bonding (XB) is usually denoted as R-X···B where X is a halogen atom covalently attached to an electron-withdrawing group (R) and B is a Lewis base (Figure 1.5a). The covalently linked electron-withdrawing group R imparts an anisotropic distribution of the electron density around the halogen nucleus, forming an electron-rich (blue) equatorial ring and an electron-deficient (red) region at the terminus of the C-X bond. This creates a small region of localised, partial positive charge at the pole of the halogen atom, termed a sigma (σ-) hole, which is responsible for attractive interactions with Lewis bases. Consequently, in comparison to HB interactions, XB is highly directional with the R-X···B bond angles close to 180^0.[37] The strength of XB interactions is comparable to HB (10-200 kJ mol^{-1}) and can be easily fine-tuned by varying the halogen atom and/or the electron-withdrawing group R. In general, the strength of XB increases with decreasing electronegativity and increasing polarizability of the halogen atom (I > Br > Cl >> F) (Figure 1.5b), as well as increasing electron-withdrawing ability of R.[38] Additionally, compared to HB, XB donors are more hydrophobic, a trait widely utilised in drug design as transportation and absorption of drugs often depend on lipophilicity.[39] Due to their unique hydrophobic properties, high directionality, and tunable

bond strength, in recent years XB interactions have gained popularity in many applications including molecular recognition,[40,41] catalysis,[42,43] and crystal engineering.[44]

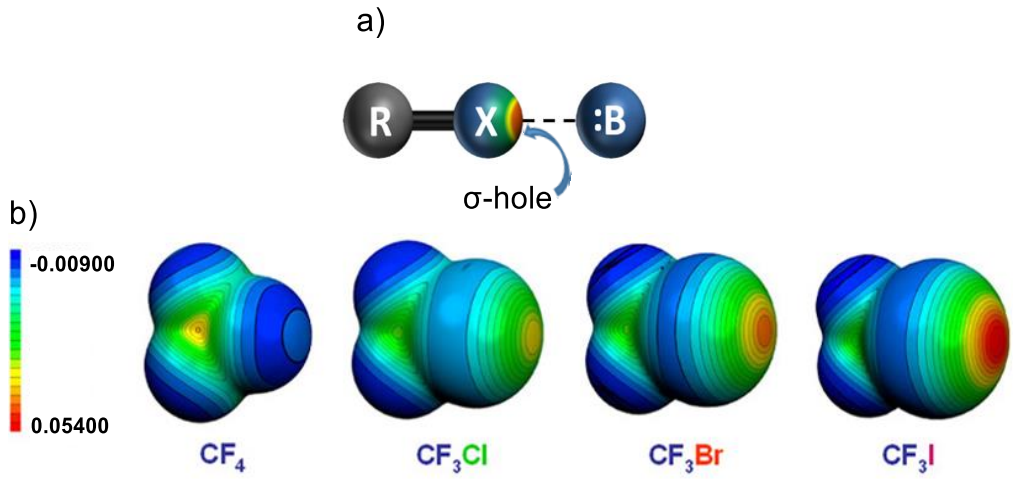

Figure 1.5: Halogen bonding (XB) interactions; a) Representation of a XB interaction with a Lewis base (R= electron withdrawing groups, X=Cl, Br, I; B=Lewis base); b) Electrostatic surface potentials, in Hartrees, at 0.001 electrons $Bohr^{-3}$ isodensity surfaces of halotrifluoromethanes. Reproduced from reference [45]

1.3.4. π- π interactions

π-π interactions can be classified to two main types based on the orientation of the interacting aromatic groups, face-to-face and edge-to-face (Figure 1.6a). The former, seen in graphite (Figure 1.6c), is responsible for the material's lubricating properties.[46] On the other hand, edge-to-face π-π interactions are crucial for stabilisation of the solid-state herringbone structure of benzene (Figure 1.6d).[47]

Sanders and Hunter rationalised the π-π orientation geometries using a simple electrostatic model, via a positively charged π framework sandwiched between two negatively charged π electron clouds (Figure 1.6b).[48] The attractive electrostatic interactions between oppositely charged frameworks determined the geometry of π-π stacking. The charge of the frameworks is reversed by attaching electron-withdrawing groups to the aromatic systems. For example, in perfluorobenzene, the charge of the framework inverts making it possible to

form face-to-face π-π interactions with electron-rich aromatic systems. This simple model successfully explains most of the experimentally observed geometries with π- π interactions. However, there is still a lot of debate over the nature of π-π effects, particularly on the contribution of London dispersion forces for aromatic interactions.[49]

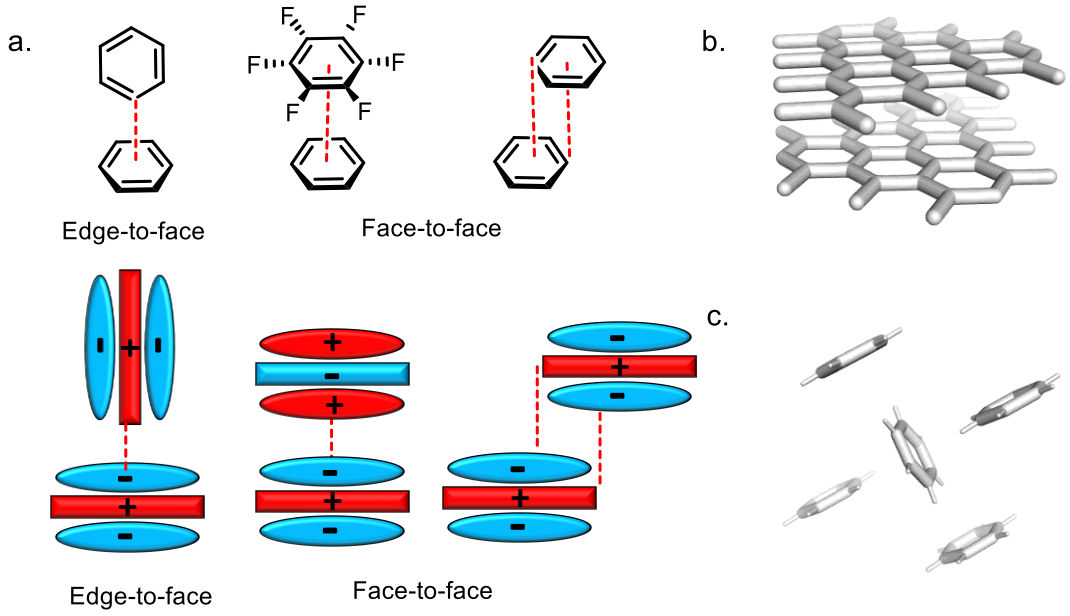

Figure 1.6: π- π interactions: a) orientation of π- π interactions as explained by Hunter and Sander's model, c) X-ray crystal structure of graphite in face-to-face orientation,[46] d) X-ray crystal structure of benzene depicting herringbone structure in edge-to-face orientation.[47]

1.3.5. Ion-π interactions

Cations and anions are known to form attractive interactions with electron-rich and electron-deficient aromatic systems respectively. Cation-π interactions are among the strongest supramolecular interactions reported in the literature. For example, the gas-phase association enthalpy between K^+ and benzene (Figure 1.7a) is more favourable than that between K^+ and water ($\Delta H_{(K\text{-ben})}$ = -19 kJ mol^{-1}, $\Delta H_{(K\text{-water})}$ = -18 kJ mol^{-1}).[50]

Compared to cation-π interactions, anion-π interactions are weaker and underexploited. However, it is possible to achieve appreciable binding affinities when multiple anion-π

interactions are used in a concerted manner. This is evident from anion receptors that function via anion-π interactions, as demonstrated by Wang and co-workers (Figure 1.7b). The electron-deficient cavities with alternating triazene and perfluoroarene groups bind F^- and N_3^- strongly (K_a>1000 M^{-1}) and selectively in d_3-acetonitrile.[51]

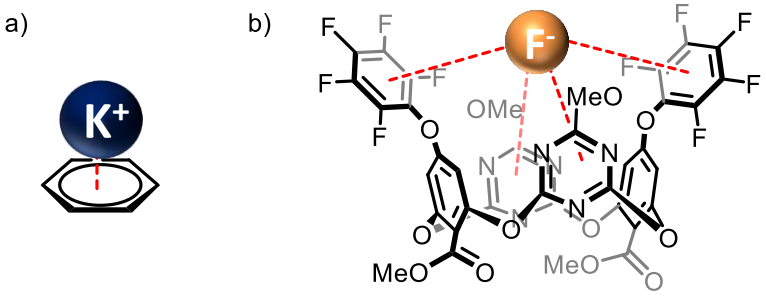

Figure 1.7: Ion- π interactions: a) K^+ - π interactions,[50] b) F^- - π interactions.[51]

1.3.6. Hydrophobic and solvophobic effects

The solvophobic effect is the association of non-polar solutes in a polar solvent to minimise the energetically unfavourable polar and non-polar intermolecular interactions. In water this is termed the hydrophobic effect. The 'classical' hydrophobic effect is driven by entropic contributions due to the release of highly organised water molecules from the hydration shell of the host and the guest during their association. The 'non-classical hydrophobic' effect is driven by favourable enthalpic effects arising from the released 'high energy' water molecules that form strong HB interactions with the bulk water solution.

The hydrophobic effect has been successfully utilised for anion recognition in water, as illustrated by Gibb's water-soluble cavitand. The cavitand (Figure 1.8a) preferentially binds the hydrophobic anion $Cl_3CCO_2^-$ (K_a=6227 M^{-1}).[52] Interestingly, the authors observed the binding of hydrophobic anions to increase in the presence of excess hydrophilic salts such as NaCl and NaF. This is attributed to enhanced hydrophobic host-guest interactions due to the increase in ionic strength of the bulk solvent, which in turn drives the strong and selective

hydrophobic anion encapsulation. Other types of deep cavity receptors capable of binding hydrophobic anions include bambusurils and cyclodextrins.[53] An example of the latter is γ-cyclodextrin (Figure 1.8b) which forms a strong association with dodecahaloborate clusters ($B_{12}Br_{12}^{2-}$) (K_a=2600 M^{-1}) in water.[54]

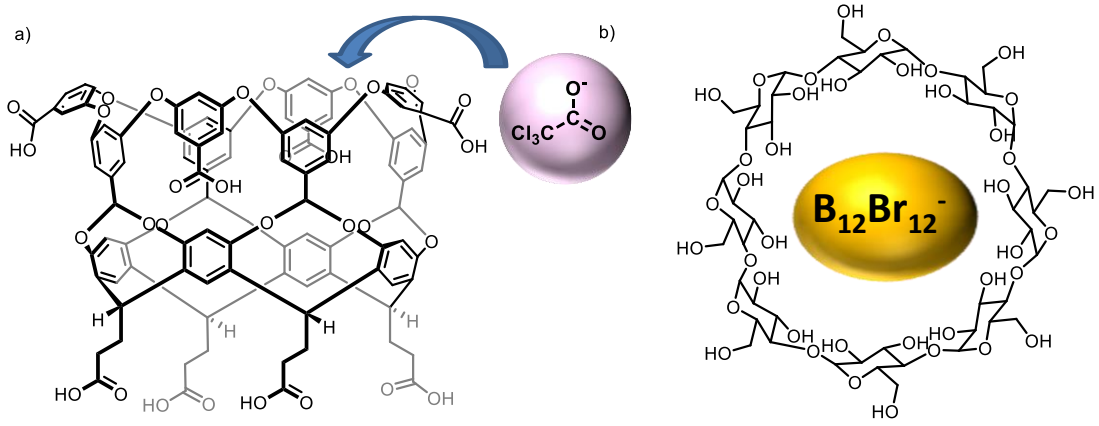

Figure 1.8: a) Gibb's water-soluble cavitand,[52] b) Hydrophobic cavity of cyclodextrin binding $B_{12}Br_{12}^{2-}$ in water.[54]

1.4. Anion supramolecular chemistry

1.4.1. Importance of anion recognition

Anions are omnipresent in the biosphere and are crucial in many biological, environmental, and industrial processes. Many important biomolecules such as DNA, RNA, several enzyme cofactors, and ATP are large polyanions.[55] Smaller inorganic anions play important roles in human biochemistry. With regard to halides, chloride misregulation causes several diseases such as cystic fibrosis, Best disease and Dent disease.[56] Iodide is essential for the synthesis of thyroid hormones responsible for the regulation of metabolism.[57] Fluoride helps protect teeth from decay.[58] In the environment, phosphates and nitrates resulting from the overuse of fertilisers for intensive arable farming and industrial waste water cause eutrophication, severely disrupting the ecosystem.[59] Overexposure to NO_3^- has been proven to have detrimental implications to human health. Examples include blue baby syndrome in infants

and in vivo formation of carcinogenic nitrosamines.[60] Industrial pollutants such as N_3^- and CN^- have lethal effects on the human respiratory system.[61,62] Hence, anion recognition has become an intensely investigated research avenue in supramolecular chemistry, with increasing attention towards the design and development of anion selective receptors,[63,64] sensors[65,66] and extracting agents.[67,68] The following sections discuss the challenges of anion recognition, followed by a review of seminal examples of synthetic anion receptors.

1.4.2. Challenges of anion recognition

The inherent properties of anions have made their recognition a challenging task, particularly in aqueous media.[53] Firstly, anions are larger than their isoelectronic cations, and thus possess a lower charge-to-radius ratio, resulting in weaker electrostatic interactions with neutral and positively charged electron-deficient binding sites of potential anion receptors.[69] Secondly, anions exhibit a wider range of geometries in comparison to cations as shown in Figure 1.9. This poses a synthetic design problem to construct receptors containing cavities of complementary size and shape for targeted anions.

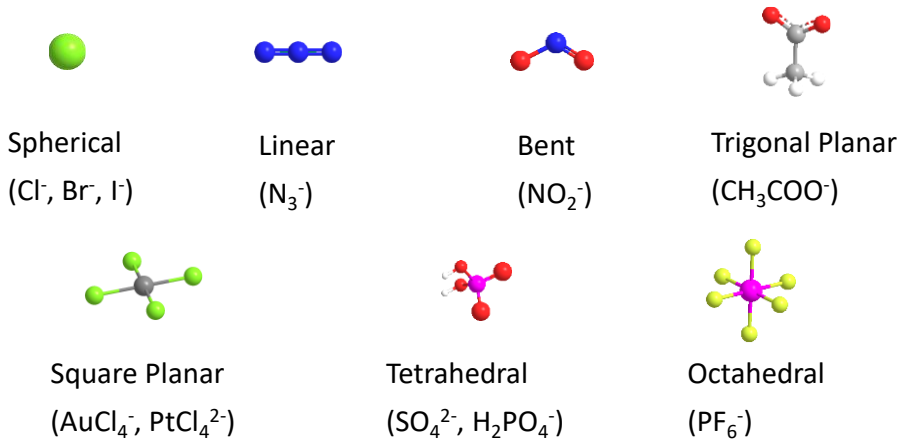

Figure 1.9: Anion geometries

Many anions such as carboxylates and phosphates are pH-sensitive, where the latter in particular can be in multiple equilibria between PO_4^{3-}, HPO_4^{2-} and $H_2PO_4^-$ species dependent

upon the pH of the solvent system.[70] In addition, pH dependent anion receptors such as those containing polyammonium motifs, are only capable of functioning in a limited pH window where both the target anion remains negatively charged and the receptor remains protonated (Figure 1.10).[71]

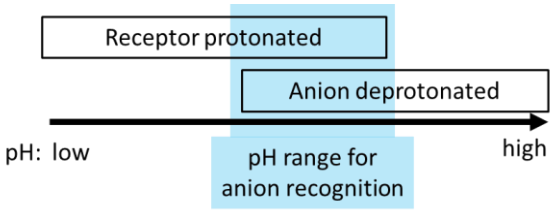

Figure 1.10: Schematic illustration showing the optimal pH range for anion recognition in pH dependant receptors

Finally, higher solvation energies of anions (compared to isoelectronic cations) is another problem to overcome when recognising anions in competitive polar solvents. For example, the standard free energy of hydration ($\Delta G_{hyd}°$) of F^- (-465 kJ mol^{-1}) is higher than Na^+ (-365 kJ mol^{-1}). Hence a larger thermodynamic desolvation penalty for the anion has to be paid prior to host recognition in aqueous media.[70]

In the past three decades or so, the judicious incorporation of ubiquitous HB and in more recent years XB donors into a wide variety of receptor structural frameworks has become a popular strategy for overcoming the anion recognition challenge. In the following sections, seminal examples of HB, XB and transition-metal based anion receptors capable of strong and selective binding of anions are discussed.

1.4.3. Synthetic anion receptors

This section provides an overview of synthetic anion receptors based on the type of non-covalent interactions they employ for host-anion guest binding.

1.4.3.1. *Hydrogen bonding receptors*

Hydrogen bonding interactions are the most widely utilised non-covalent interaction in supramolecular anion recognition. There is an enormous variety of HB receptors reported in the literature with either N-H and/or C-H donors. This section will summarise the development of HB anion receptors, highlighting key examples of cationic and neutral anion receptors reported to date.

Cationic hydrogen bonding receptors

Cationic hosts have the advantage of forming strong electrostatic interactions with anions. However, the non-directional nature of Coulombic interactions make it difficult for cationic receptors to achieve high degrees of selectivity.

In 1968 Parks and Simmons reported the first synthetic anion receptor, a macrobicyclic cryptand shown in Figure 1.11a.[72] This receptor exhibited moderate Cl^- binding (K_a = 4 M^{-1}) in acidic aqueous media, through a combination of electrostatic interactions via the protonated bridgehead ammonium groups and N-H hydrogen bonding interactions. Building on this work, Lehn developed a series of macrocyclic and macrobicyclic polyammonium receptors and fine-tuned their inner binding cavities for selective recognition of anions in aqueous media. For example, the hexaprotonated macrobicyclic receptor shown in Figure 1.11b exhibited selective binding for linear shaped azide (N_3^-) while the smaller binding cavity containing receptor in Figure 1.11c displayed selective binding for F^- in water.[73–76]

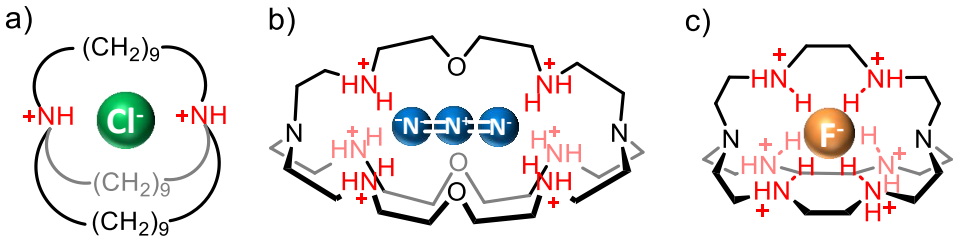

Figure 1.11: Early cationic NH bonding anion receptors; a) Parks and Simmon's cryptand [72] b) Lehn's N_3^- selective receptor[73,75] c) Lehn's F^- selective receptor.[74,76]

In contrast to the pH-dependent polyammonium receptors, pH-independent imidazolium and triazolium integrated receptors exploit charge assisted C-H donors to recognise anions in aqueous and competitive protic media. In one example, You and co-workers synthesised a tetrakis-imidazolium macrocycle capable of strong and selective recognition of SO_4^{2-} anions (K_a= 8 x 10^9 M^{-1}) in water (Figure 1.12a).[77] ^{1}H NMR and solid state evidence revealed the formation of a 2:1 host-guest complex as shown in Figure 1.12b.

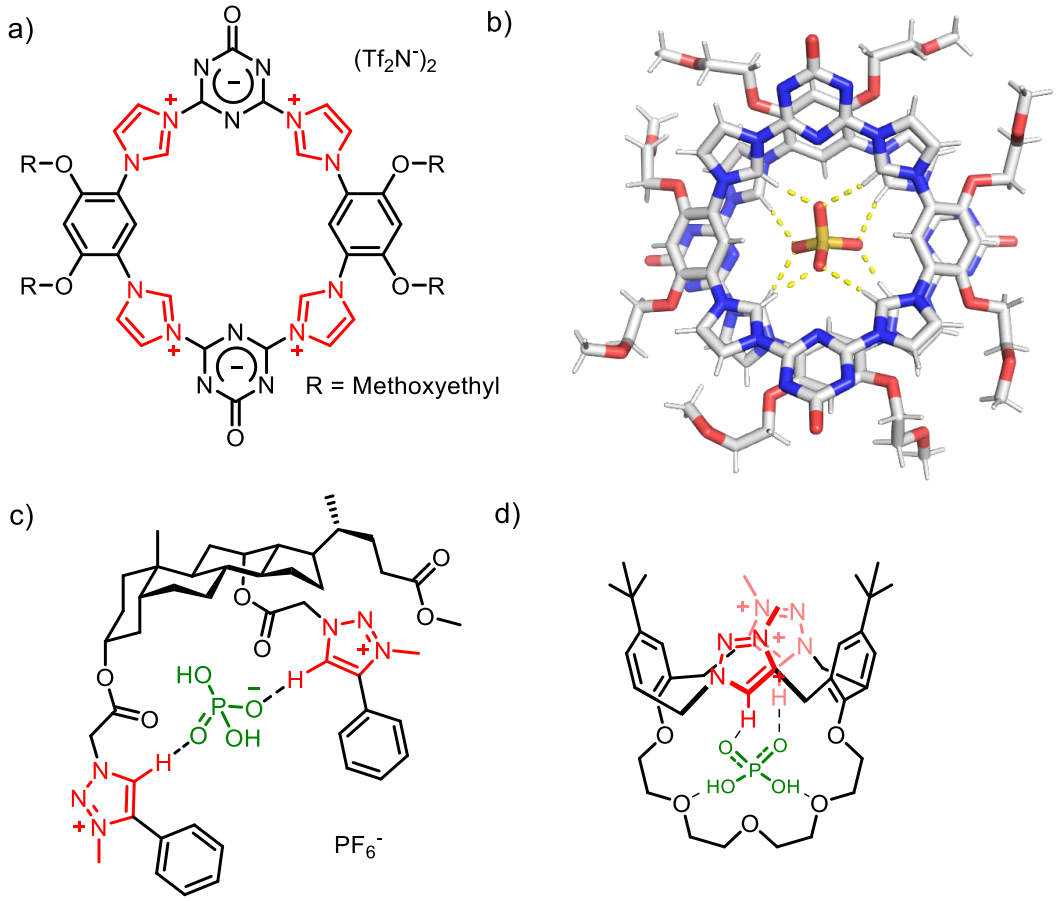

Figure 1.12:Examples of cationic anion receptors: a) You's cationic imidazolium macrocycle,[77] b) Crystal structure of the imidazolium macrocycle forming a 2:1 host-anion guest complex with SO_4^{2-}, c) Pandey's triazolium receptor,[78] d) crown ether-appended calix[2]triazolium[2]arene receptor.[79]

Due to the ease of synthesis of 1,2,3-triazole heterocycles via 'click chemistry', triazolium C-H donors have been widely employed in cationic anion receptors in recent years.[80,81] The first example of a triazolium based anion receptor was reported by Pandey and co-workers in

2007 (Figure 1.12c).[78] This receptor was capable of selectively binding tetrahedral $H_2PO_4^-$ over halide anions in $CDCl_3$ (K_a = 1920 M^{-1}). More recently, Hong, Kim and co-workers designed and synthesised a crown ether-appended calix[2]triazolium[2]arene, which selectively binds $H_2PO_4^-$ anions in CD_3CN.[79] According to ^1H NMR titration experiments, X-ray crystal structure analysis, and DFT calculations, the high selectivity for $H_2PO_4^-$ stems from the stabilisation of the oxoanion by triazolium C-H HB donors and crown ether HB acceptors (Figure 1.12d).

Neutral hydrogen bonding receptors

Whereas highly charged cationic receptors are primarily designed to recognise anions in competitive protic aqueous media, neutral anion receptors are commonly used for binding anions in aprotic organic solvents. However, through concerted interactions of multiple directional HB donors, neutral hosts can achieve high degrees of selectivity and anion binding strength.

The first example of a neutral amide based anion receptor was reported by Pascal and co-workers in 1986 (Figure 1.13a), which was capable of binding fluoride.[82] About a decade later Crabtree reported an isophthalamide based acyclic receptor capable of strong Cl^- binding in CD_2Cl_2 with an association constant of 6 x 10^4 M^{-1} (Figure 1.13b).[83,84] Due to the ease of synthesis and strong interactions with anions, amide motifs have since been incorporated into a variety of host architectures.[85,86] Kubik and co-workers synthesised a macrocyclic cyclopeptide (Figure 1.13c) capable of strongly binding SO_4^- and I^- anions with $K_a > 10^5$ M^{-1} in competitive 8:2 D_2O/CD_3OD solvent mixtures.[87,88] Based on crystallographic evidence, anions bind to the receptor forming a 2:1 host-guest complex via amide-HB interactions from both macrocycles (Figure 1.13d). In a recent study, the same group covalently attached two

macrocycles via one linker[89,90] and three linkers[91] in order to preorganise the anion binding site even more, resulting in enhanced anion binding strength.

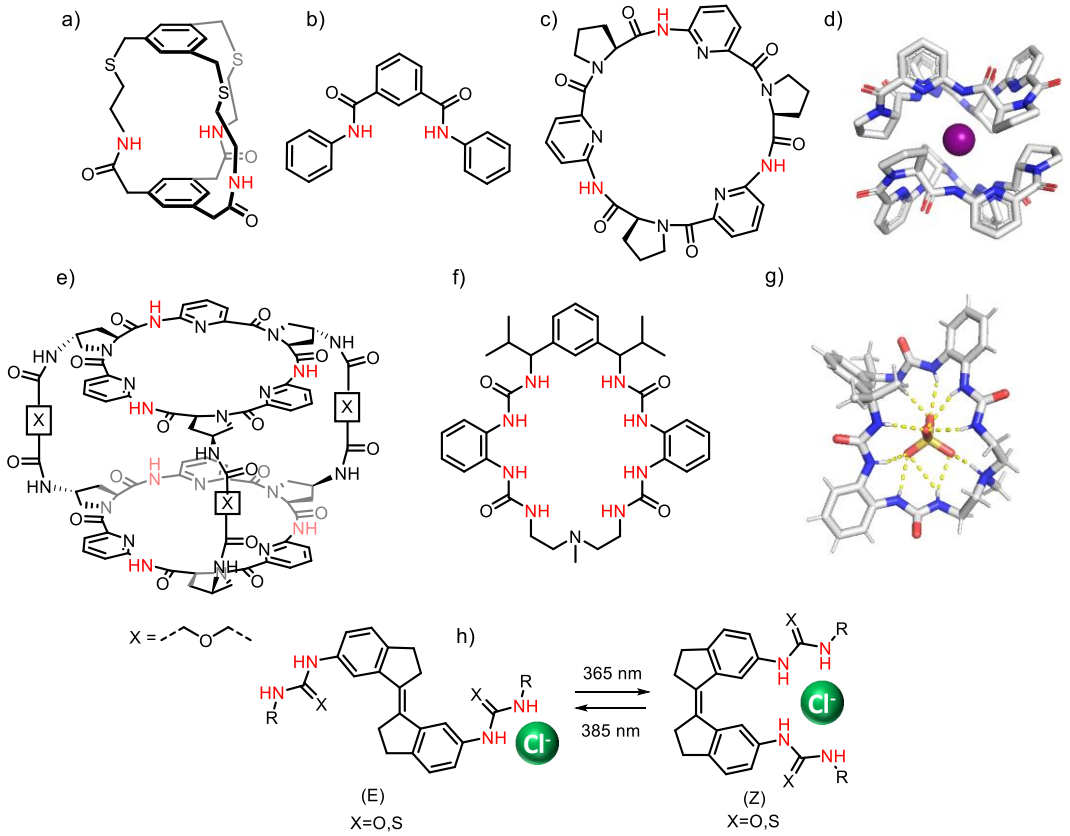

Figure 1.13: Neutral HB anion receptors: a) Pascal's amide based receptor,[82] b) Crabtree's isophthalamide receptor,[83,84] c) Kubik's macrocycle,[87] d) crystal structure of the iodide bound Kubik's macrocycle in 2:1 host: guest stoichiometry,[87] e) two Kubik's macrocycles covalently attached,[91] f) Bowman-James HB macrocycle,[92] g) crystal structure of SO_4^{2-} bound macrocycle (yellow lines indicate HB interactions),[92] h) Gale's photo switchable transmembrane transporter.[93]

Urea and thiourea are also powerful HB donors with facile synthetic accessibility, and have been incorporated into a variety of anion receptor frameworks.[94,95] Recently, Bowman-James and co-workers synthesised a tetraurea based macrocycle (Figure 1.13f) capable of strong and selective recognition of SO_4^{2-} (K_a = 9 x 10^4 M^{-1}) over Cl^-, OAc^-, NO_3^- and $H_2PO_4^-$, in 0.5% D_2O:DMSO-d_6 mixtures.[92] Crystallographic evidence revealed the oxoanion is stabilised by multiple HB interactions, complementing the tetrahedral geometry of the SO_4^{2-} anion (Figure 1.13g).

Gale and co-workers developed a bis-thiourea based, photoswitchable transmembrane transporter shown in Figure 1.13h.[93] Upon irradiation, the receptor's stilbene motif undergoes E to Z photoisomerization where the Z-isomer was shown by ^{1}H NMR and UV-vis titrations to display stronger Cl^- binding compared to the E-isomer. This was exploited to modulate membrane transportation of Cl^- anions through irradiation.

1.4.3.2. *Halogen bonding anion receptors*

Compared to ubiquitous HB interactions, XB interactions have only relatively recently emerged as a powerful addition to the supramolecular chemistry toolbox to utilise in anion receptor design. Like HB interactions, both neutral and cationic XB motifs (Figure 1.14) have been incorporated into various acyclic and macrocyclic structural frameworks.

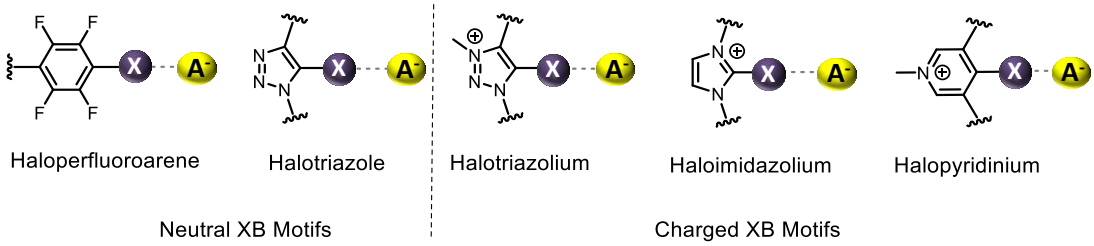

Figure 1.14: Commonly studied halogen bond motifs

Neutral halogen bonding receptors

One of the first anion receptors to exploit XB interactions was reported by Metrangolo, Resnati, and co-workers in 2005.[96] This tripodal iodoperfluoroarene polyether host was capable of binding a spatially separated NaI ion-pair as depicted in Figure 1.15a. However, according to crystallographic evidence, the three bulky para-substituted iodine atoms are unable to form concerted XB interactions with the halide anion due to spatial constraints. Five years later, Taylor and co-workers circumvented this issue through a tripodal system with ortho-substituted XB donors that allowed coordination of anions in a tridentate manner

within the receptor cavity (Figure 1.15b).[97] The receptor showed selectivity for halides over oxoanions (Cl^->Br^->I^->>TsO^-, HSO_4^-, NO_3^-) in acetone, which was postulated to arise due to the inherent preference of XB donors towards 'soft' anions.

Since then, the use of XB in anion recognition has made dramatic advances, due to its stringent directionality and hydrophobic nature. XB anion receptors often display superior anion binding affinities and contrasting selectivity compared to their HB receptor analogues. For example, Kubik's tris-iodotriazole containing peptide macrocycle binds halide anions via three convergent XB interactions (Figure 1.15c). The XB receptor exhibited strong binding for Cl^- (K_a = 1x10^3 M^{-1}) in a competitive solvent mixture of 2.5% D_2O in d_6-DMSO (v/v) while the analogous HB receptor integrated with tris-prototriazole motifs, showed no appreciable halide binding in the same solvent.[98] Notably, a neutral water soluble tetra-iodotriazole foldamer receptor (Figure 1.15d-e) synthesised by Beer and co-workers has achieved unprecedented iodide binding strength, exceeding that of the natural Na^+/I^- symporter protein receptor by several orders of magnitude. This was attributed to the hydrophobic nature of the XB donors which facilitated a dimeric 2:1 host-guest stoichiometric encapsulation of iodide, stabilised by eight convergent XB donors (Figure 1.15e).[99]

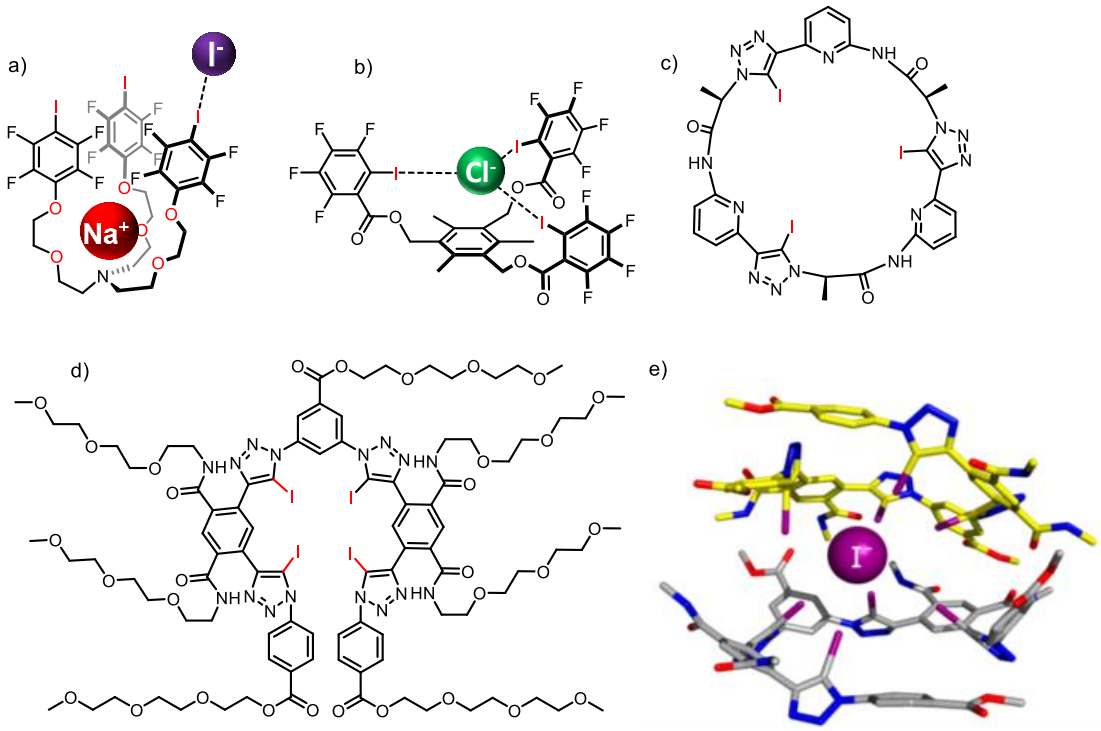

Figure 1.15: XB anion receptors; a) Metrangolo and Rasnati's perfluoroaryl receptor,[96] b) Taylor's tripodal XB anion receptor,[97] c) Kubik's XB pseudopeptide macrocycle,[98] d) monomer of Beer's XB receptor,[99] e) DFT optimised dimeric form of Beer's receptor in the presence of I^- anion, structure reproduced from reference [99].

Cationic halogen bonding receptors

Charge assisted cationic XB anion receptors predictably exhibit higher anion binding affinities than neutral XB congeners due to additional favourable electrostatic interactions and the positively charge-polarised XB donor atom.

In one example, Berryman and co-workers synthesised a bis-iodo-pyridinium containing acyclic receptor (Figure 1.16a) capable of forming strong XB interactions with ReO_4^- anions in $CDCl_3$-acetone-d_6 solvent mixtures (K_a = 8990 M^{-1}).[100] Subsequently, the same group prepared a tricationic foldamer receptor analogue (Figure 1.16b-c)[101] which upon iodide addition formed a triple helicate structure encapsulating two iodide anions via multiple XB interactions.

Triazole N-methylation has been exploited as an efficient method to increase the potency of XB interactions in halotriazoles. Schubert and co-workers synthesised a series of bidentate dicationic halo triazolium hosts with phenyl and thiophene spacer groups (Figure 1.16d).[102] The bis-iodotriazolium receptor with the phenyl spacer group exhibited the highest anion affinities with preferential binding for SO_4^{2-} (K_a = 3400 M^{-1}, DMSO-d_6) over halides. Selectivity for SO_4^{2-} was rationalised on the basis of size complementarity to the XB binding site and di-anion charge density.

Haloimidazoliums are another class of cationic XB receptors that display comparable anion binding affinities to halotriazoliums.[41] In one example, Jungbauer and Huber exploited the potent XB interactions of iodo-imidazolium for organocatalysis applications with the XB receptor shown in Figure 1.16e.[103] The central CF_3 substituent prevents the rotation of the haloimidazolium groups, fixing the XB donors in either a syn- or anti-conformation. ITC titration experiments in CH_3CN revealed that the syn isomer binds Br^- much more strongly than its anti isomer by 2 orders of magnitude (K_{syn} = 3.5 x 10^6 M^{-1}, K_{anti} = 4.4 x 10^4 M^{-1}). The syn isomer also catalysed a halide abstraction reaction of 1-chloroisochroman with silyl enol ether with unprecedentedly low catalyst loadings of 0.5%, resulting in 70% product yield.

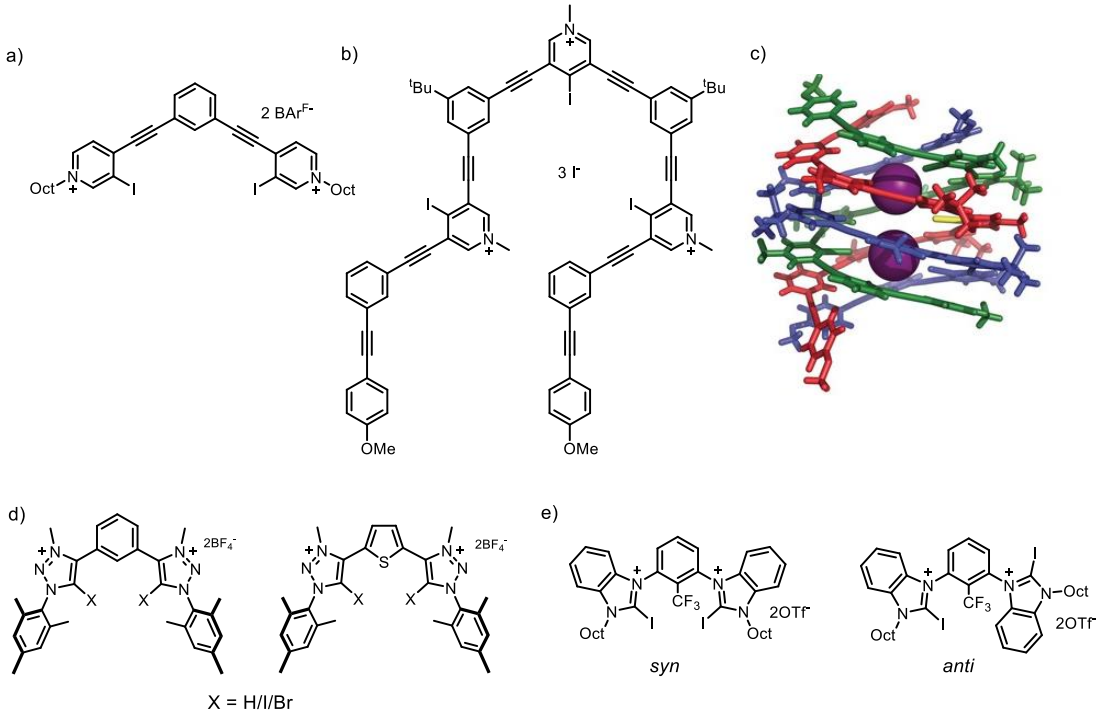

Figure 1.16: Cationic XB anion receptors: a) Berryman's iodopyridinium acyclic receptor,[100] b) Berryman's tricationic receptor,[101] c) crystal structure of I^- bound Berryman's tricationic receptor, reproduced from reference [101] d) Schubert's halo triazolium hosts,[102] e) syn and anti isomers of Jungbauer and Huber's iodo-imidazolium organocatalyst.[103]

1.4.3.3. *Transition metal-based anion receptors*

The incorporation of transition metal centres into anion receptor design offers many advantages to improve anion binding.[104,105] Firstly, Lewis acidic transition metals form strong interactions with anions through coordination bonds, enabling efficient binding of anions in competitive solvent media such as water.[53] Secondly, a positively charged metal proximal to the anion recognition site of a receptor enhances binding affinity through electrostatic interactions and by polarising adjacent HB/XB donors. Thirdly, redox/photoactive metals complexed near the anion binding site have the potential to act as optical/electrochemical reporter groups.[65,106] Finally, transition metal complexes possess defined geometries which can be utilised to synthesise receptors with preorganised binding sites. The collective effect of these advantages has led to the design of a variety of highly selective metal-based anion receptors with a range of applications including sensors,[65,107,108] disease diagnosis,[109] membrane transport[110] and catalysis.[111]

Since the early example of Lehn's copper(II) cryptate (Figure 1.17a), a wide range of transition metal-based receptors have been developed.[112] Most efficient transition metal-based anion receptors utilise electrostatic interactions to enhance anion binding, and a combination of non-covalent interactions to increase anion selectivity. For example, the dipicolylamine γ-cyclodextrin-Cu^{2+} receptor (Figure 1.17b) reported by Hayashita and co-workers displayed high selectivity for ATP over other phosphate species such as AMP and ADP, in a 99% water media at pH 7.4 (K_a = 6.64 x 10^3 M^{-1}).[113] The authors attribute the strong and selective recognition of ATP to the combined effects of hydrophobic interactions due to encapsulation of adenosine in the γ-cyclodextrin cavity and Lewis acidic interactions of phosphate groups with the Cu(II) coordination site.

An example of a transition metal-based membrane anion transporter was recently reported by Plajer, Wright and co-workers (Figure 1.17c).[114] Complexation of Rh and Mo metals to the receptor significantly improved anion binding properties by i) preorganising the receptor in the desired exo-exo formation for anion binding; ii) polarising the N-H hydrogen bond donors, and iii) stabilising the P_2N_2 ring from hydrolysis and oxidation under biologically relevant conditions. As a result, the bimetallic complexed receptors showed a significant enhancement in Cl^- transport through phospholipid bilayers compared to known phosphazene and thiourea transporters.

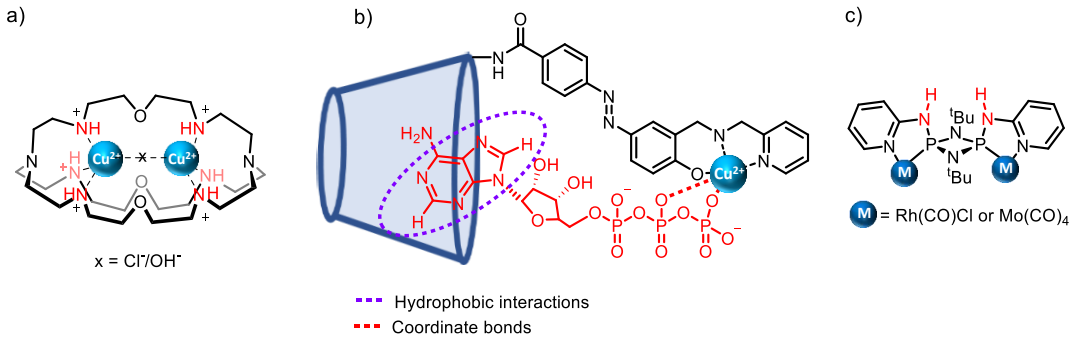

Figure 1.17: Transition metal complexed HB anion receptors: a) Lehn's copper(II) cryptate,[115] b) ATP selective copper(II) receptor,[113] c) transition metal based anion membrane transporter.[114]

Compared to the many transition metal-based HB anion receptors reported in the literature, there are far fewer numbers of transition metal-based XB receptor analogues. A charged metal coordinated close to a XB donor can further polarise the XB donor atom, increasing the size and the potency of the σ-hole and thereby strengthening interactions with Lewis basic anions. However, extensive polarisation leads to the risk of dehalogenation. Hence, developing transition metal based XB receptors is synthetically challenging.

Figure 1.18 depicts examples of transition metal-based XB receptors. Ghosh and co-workers synthesised a Ru(II) complexed XB receptor (Figure 1.18a) capable of selective binding and luminescence sensing of phosphate anions ($H_2PO_4^-$, $HP_2O_7^{3-}$) in aqueous acetonitrile solutions.[116] Beer and co-workers reported a bimetallic Re(I) bis-iodotriazole pyrimidine XB receptor that exhibits selective recognition of iodide over a variety of monocharged oxoanions in 1:1 (v/v) CD_3Cl/CD_3OD (Figure 1.18b). Complexation of the two Re(I) centres preorganises the binding site by orienting both XB donors so that they interact with an anion in a convergent manner.[117] Importantly, in both instances, receptor complexation with transition metals increased anion binding strength significantly compared to the analogous metal-free hosts. Furthermore, as noted previously with metal-free XB receptor systems, the transition metal-based XB receptors in general demonstrated superior anion binding affinities over their HB host analogues.

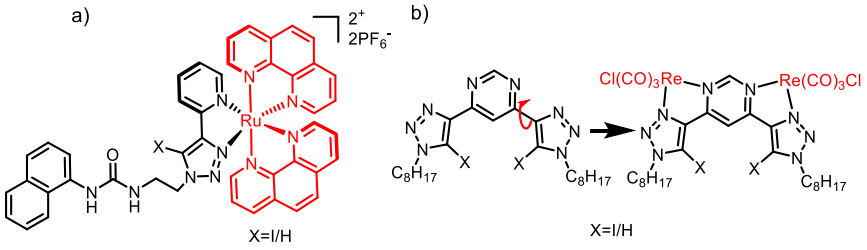

Figure 1.18: Transition metal-based XB receptors: a) Ghosh's Ru(II) chemosensor,[116] b) Beer's preorganised bimetallic Re(I) anion receptor.[117]

1.5. Ion-pair recognition

The recognition of a charged species by a monotopic receptor is critically influenced by the presence of its counter-ion, which through ion-pair association can compete with the receptor to bind the target ion of interest.[118] This problem is effectively circumvented in organic solvent media by the use of non-coordinating counter-ions such as tetrakis[3,5-bis(trifluoromethyl)phenyl]borate [$BAr^{F}_{4}^{-}$] or hexafluorophosphate [PF_6^-] anions for cation binding and tetrabutyl ammonium cation for anion recognition investigation. Nevertheless, in real-world applications, the competing counter-ion can greatly diminish host-ion interactions.[119,120] This has inspired the design of heteroditopic ion-pair receptors with binding sites for *both* the cation and anion. Ion-pair receptors have numerous applications, including salt solubilisation and extraction,[121–125] and membrane transportation.[126–128]

Ion-pair binding by heteroditopic receptors demonstrate multiple complex equilibria as shown in Figure 1.19. An individual anion (A^-) or a cation (C^+) can bind to a heteroditopic receptor (L) alone (respective binding constants denoted as K_A and K_C), or both ions can bind to the receptor simultaneously (K_{AC}). The anion and the cation could also form an ion-paired species external to the receptor (K_{EX}). External ion-pairing is reduced by using solvents with high dielectric constants which solubilises the salt, although it also weakens interactions between the receptor and the charged species.

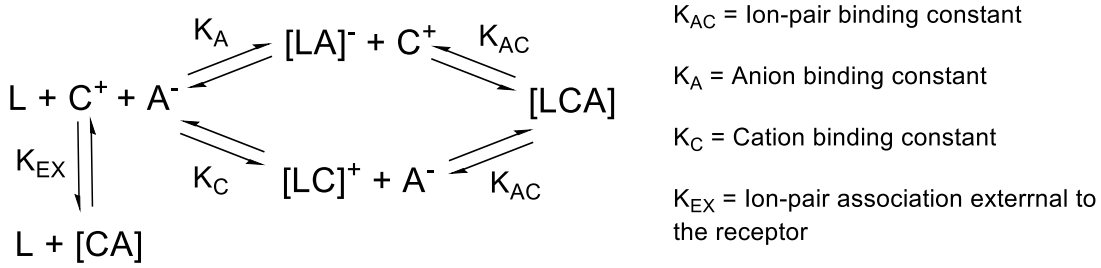

Figure 1.19: Illustration of various equilibria in ion-pair binding systems

The term *cooperativity factor* gives an estimation of how a co-bound cation or anion influences the binding affinity of the counter-ion. This is defined as the ratio of K_{AC}/K_A or K_{AC}/K_C for the anion and the cation respectively. Based on the way binding of the first ion influences the binding affinity of its counter-ion, cooperativity can be classified into three categories:

i. **Positive cooperativity** : The binding of one ion enhances the binding of the counter-ion. i.e. K_{AC}/K_A or $K_{AC}/K_C > 1$

ii. **Negative cooperativity:** The binding of one ion inhibits the binding of the counter-ion. i.e. K_{AC}/K_A or $K_{AC}/K_C < 1$

iii. **Non-cooperativity**: Each ion binds independently of the other. i.e. K_{AC}/K_A or $K_{AC}/K_C = 1$

Heteroditopic receptors are primarily designed to exhibit positive cooperativity whereby the binding of either charged species of an ion-pair enhances the subsequent binding strength of the counter-ion. This is generally attributed to favourable proximal electrostatic interactions between the co-bound ions and/or conformational allosteric effects. In one example, Flood and co-workers used ^{1}H NMR, X-ray crystallographic data and computational methods to determine the electrostatic and allosteric contributions for cooperative NaX ion-pair binding using a series of triazole-polyether macrocycles (Figure 1.20a).[129] The study revealed that when sodium salts bind to the macrocycle in 4:1 $CDCl_3/CD_3CN$, the observed positive cooperativity effects was dictated by favourable Coulombic electrostatic contributions; sodium salts with smaller more charge dense counter-anions displayed stronger positive cooperativity (NaI > $NaClO_4$).

Positive allosteric effects can be observed in heteroditopic receptors when the binding of the first guest ion preorganises the receptor in a more favourable conformation for the counter-ion to bind. In an elegant example, Beer and co-workers synthesised a calix[4]arene-based

crown ether heteroditopic receptor to exploit the size dependent bis-benzo[15]crown-5 coordination geometries of potassium and sodium alkali metal cations.[130] As shown in Figure 1.20b, the larger K^+ binds to the receptor forming a 1:1 host-guest stoichiometric complex, preorganising the crown ether linked amide groups to facilitate Cl^- anion binding in 1:1 CD_3CN/d_6-DMSO. In contrast, the smaller Na^+ cation binds in each of the receptor's benzo[15]crown-5 motifs, which inhibited the favourable conformation for anion binding due to electrostatic repulsion between the bound sodium ions.

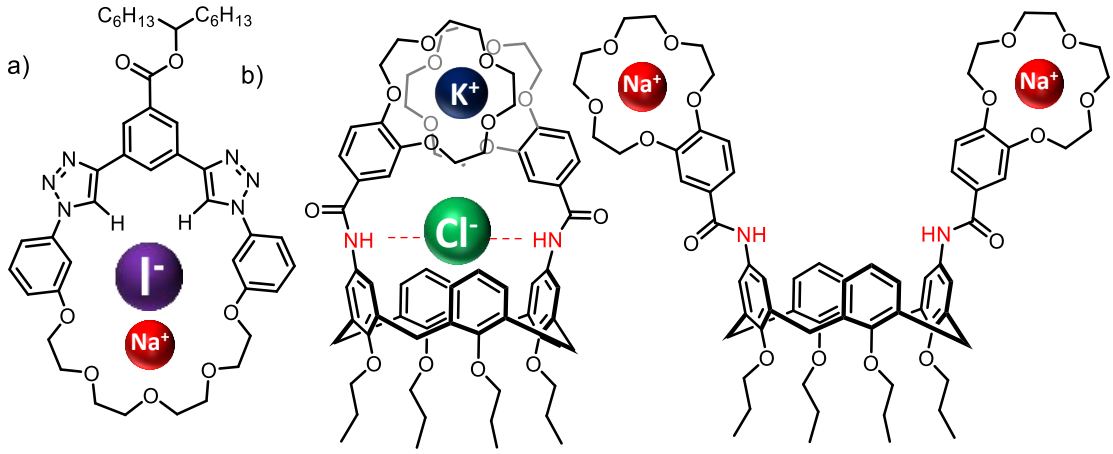

Figure 1.20: Ion pair receptors reported in the literature: a) Flood's triazole-polyether based macrocycle,[129] b) Beer's calix[4]arene heteroditopic receptor.[130]

1.5.1. Ion-Pair binding modes

Heteroditopic receptor ion-pair recognition design can be categorised according to the mode of ion-pair binding, as shown in Figure 1.21. Contact ion-pair binding results when respective cation and anion recognition sites are close to one another (Figure 1.21a), and there is evidence of direct contact between the oppositely charged ions as demonstrated by Flood's triazole polyether macrocycle binding NaI (Figure 1.20a). Having the co-bound ions in contact eliminates the enthalpic penalty required to separate the ion-pair. An example of a contact KCl ion-pair bound receptor synthesised by Smith and co-workers is depicted in Figure 1.22a.[131,132] Chloride anion binding strength in DMSO was demonstrated to increase

significantly in the presence of co-bound Na^+ and K^+ cations, primarily due to favourable electrostatic effects. X-ray crystallographic data provided conclusive evidence for contact ion-pair complexation between the aza-crown ether complexed alkali metal cation and isophthalamide bound Cl^- anion (Figure 1.22a).

'Separated' ion-pair binding modes are observed when the cation and anion binding sites are further apart from each other as depicted in Figure 1.21b or in Figure 1.21c where a solvent molecule is bound in between the ion-pair. The heteroditopic receptor exhibited in Figure 1.22b, synthesised by Saha and co-workers, is an elegant example of a separated ion-pair binding mode in Figure 1.21b.[133] The receptor consists of two electron deficient NDI motifs capable of forming anion-π interactions and a tridentate bis-imine-pyridine motif to bind a transition metal cation. The addition of Zn^{2+} or Cd^{2+} perchlorate salts resulted in forming a U-shaped 2:1 host-$M(ClO_4)_2$ ion-pair guest complex, as shown in Figure 1.22b. The authors demonstrated the reversibility of the 2:1 host-guest formation by adding competitive macrocyclic ligands such as cyclam that can extract the respective transition metal ion.

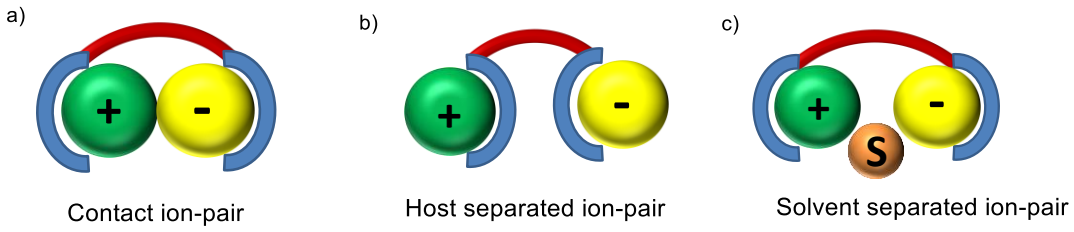

Figure 1.21: Cartoon representation of Ion-pair binding modes.

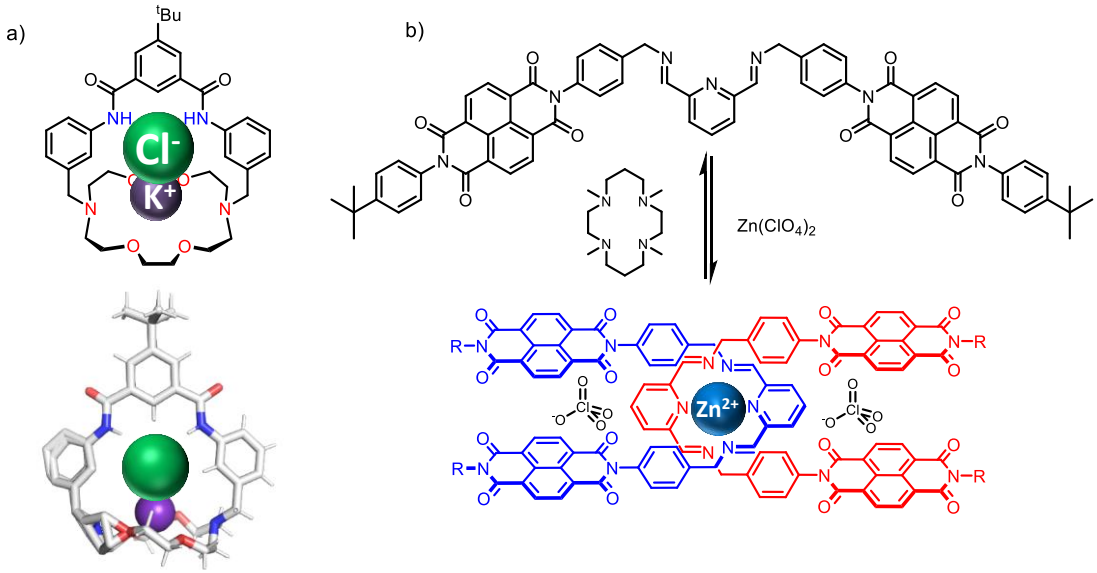

Figure 1.22: Examples of ion-pair binding receptors: a) chemical structure and crystal structure of a contact ion-pair,[131,132] b) example of a separated ion-pair.[133]

1.5.2. Applications of ion-pair receptors

Cooperative heteroditopic receptor ion-pair recognition and complex neutrality have led ion-pair receptors to be used in salt extraction, membrane transportation, and sensors, examples of which are discussed in the following sections.

1.5.2.1. *Salt Extraction*

The extraction of metal salts by ion-pair receptors has gained increasing attention in the past decade due to their applications in industrial and environmental remediation processes.[134] Tasker and co-workers synthesised a salen based ditopic receptor (Figure 1.23a) capable of cooperatively extracting $CuSO_4$ into chloroform solvent media from acidic aqueous solutions in nearly quantitative yields. Years later, the same group developed a urea functionalised cyclen based ion-pair receptor (Figure 1.23b),[135] which exhibited high selectivity for Cu(II) salts over Ni(II), Co(II), Zn(II) salt congeners.

Carboxylate anions are of significant environmental concern due to their widespread use in the food and pharmaceutical industries.[136,137] Piatek and co-workers recently reported a simple valine based heteroditopic receptor which cooperatively binds K^+ and acetate (OAc^-) anions in aqueous CH_3CN solutions (Figure 1.23c).[138] The ion-pair receptor can also extract KOAc from water into chloroform solutions. Notably, the ion-pair receptor is nearly ten times more effective than the combined use of the analogous monotopic cation/anion receptors.

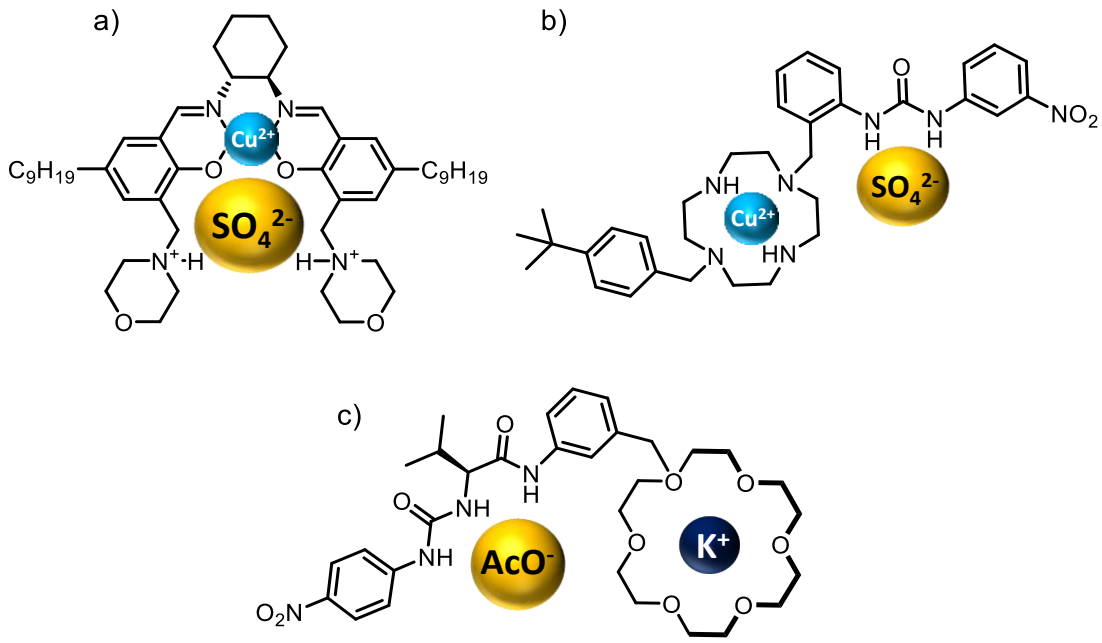

Figure 1.23: Examples of ion-pair receptors used for salt extraction.[135,138,139]

1.5.2.2. *Membrane transporting agents*

Ion-pair receptors have been used in membrane transportation due to their strong and selective guest binding properties. For example, Jeong and co-workers synthesised a heteroditopic receptor that selectively transports NaCl or KCl over other alkali metal chlorides through a lipid bilayer (Figure 1.24a).[126] The ditopic carrier with aza-15-crown-5 showed selectivity for NaCl, while the aza-18-crown-6 analogue displayed selectivity for KCl. Notably, the presence of a co-bound alkali metal cation doubled the Cl^- anion binding affinity

in 10% CD_3OH/CD_3CN, highlighting the importance of positive cooperativity to achieve strong halide binding.

Grauwels *et al.* recently synthesised a calix[6]arene based heteroditopic receptor to co-transport propylammonium chloride ($PrNH_3Cl$) ion-pair species across lipid bilayers (Figure 1.24b).[140] The ditopic receptor binds Cl^- via HB interactions with the thiourea groups and complexes the $PrNH_3^+$ cation within the calix[6]arene cavity. When the $PrNH_3^+$ cation is replaced with Na^+, Cl^- transport is reduced significantly, which is attributed to the smaller Na^+ cations not being co-transported by the calix[6]arene receptor.

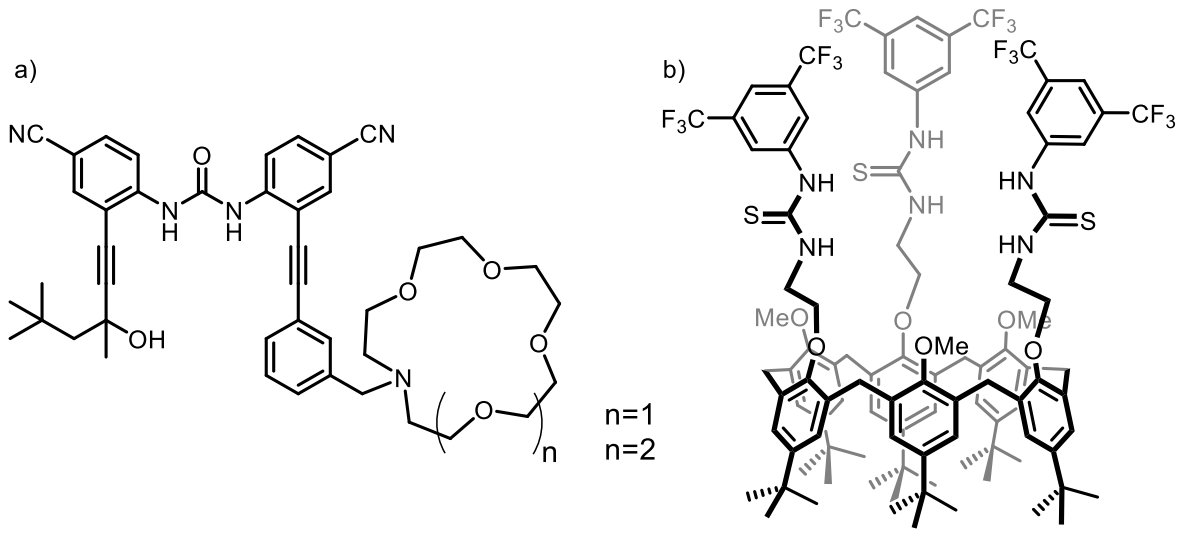

Figure 1.24: Example of ion-pair receptors used for membrane transportation.[126,140]

1.5.2.3. *Sensors*

Ion-pair sensing can be achieved by incorporating either a photo- or redox-active reporter group proximal to the ion-pair binding site. Costero, Rurack, and co-workers reported a heteroditopic receptor containing an aza-18-crown-6 moiety for cation binding and a calix[4]pyrrole for anion binding covalently linked via a boron-dipyrromethane (BODIPY) motif (Figure 1.25a).[141] The ditopic receptor optically sensed alkali metal halides and

zwitterionic amino acids such as γ-aminobutyric acid (GABA) in CH_3CN by monitoring the receptor's BODIPY UV-visible absorption and fluorescence emission properties.

In another example, Molina, Tarraga, Oton, and co-workers reported a series of heteroditopic receptors capable of optical and electrochemical sensing of ion pairs.[142] The receptor shown in Figure 1.25b is capable of the dual sensing of Pd^{2+} and $HP_2O_7^{3-}$ ion-pairs through perturbations of the redox potential of the ferrocene unit and the optical properties of the anthracene motif in 90:8:2 $CH_3CN/CH_2Cl_2/H_2O$ solvent systems.[143]

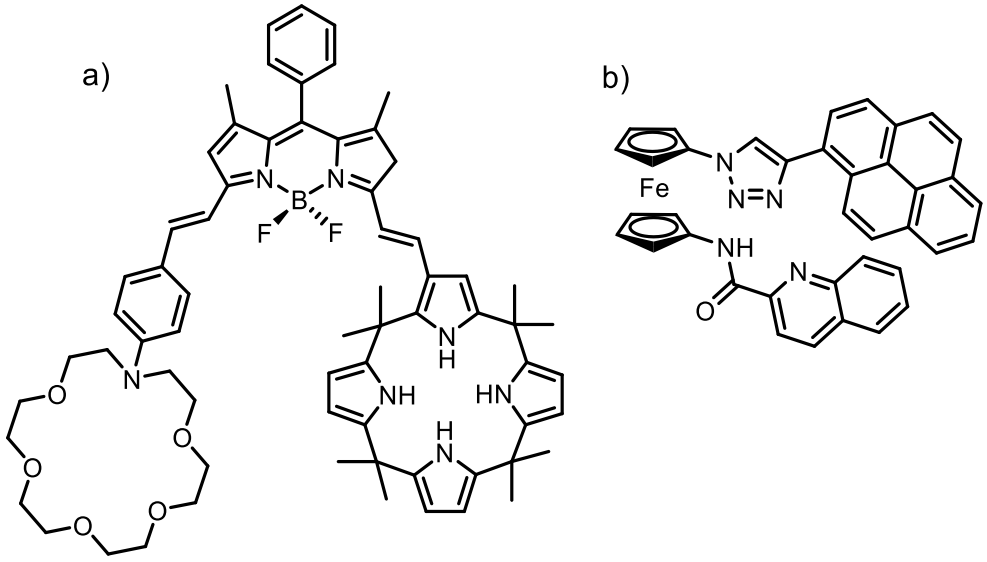

Figure 1.25: Receptors capable of optical and electrochemical sensing of ion-pairs.[141,143]

1.6. Mechanically interlocked molecules

Mechanically interlocked molecules (MIMs) consist of molecular subcomponents that are not linked covalently but entangled with each other in space so that they cannot be separated without breaking a covalent bond.[144] The most prevalent classes of MIMs are [n]catenanes and [n]rotaxanes, where n indicates the number of interlocked components. The term 'catenane' is derived from the Latin word *catena* (chain) and consists of two or more mechanically interlocked rings (Figure 1.26a). The word 'rotaxane' is derived from the Latin words *rota* (wheel) and *axis* (axle) and consists of a macrocyclic component threaded

through a dumbbell-shaped axle (Figure 1.26b). In addition to rotaxanes and catenanes, a variety of MIMs have been reported in the past few decades, including Solomon knots,[145] suitanes,[146] daisy chains[147], and Borromean rings.[148]

This section will discuss the methods used for the synthesis of MIMs, followed by applications of MIMs with particular emphasis on molecular recognition.

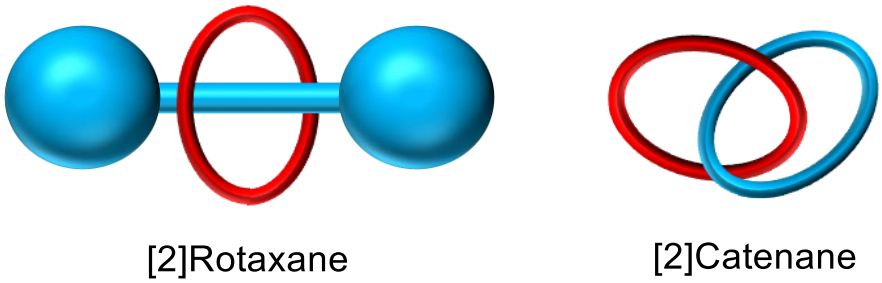

Figure 1.26: Schematic representation of a [2]rotaxane and a [2]catenane

1.6.1. Synthesis of mechanically interlocked molecules

Rotaxanes and catenanes can be constructed through a variety of synthetic routes, which in general require template methodology to assemble a pseudorotaxane intermediate. Numerous methods to synthesise rotaxanes include the initial formation of a pseudorotaxane followed by appending bulky stopper groups (stoppering, Figure 1.27a)[149] and swelling of the stopper groups (Figure 1.27b),[150,151] or slippage of a large macrocycle through an axle by applying external energy (i.e. heat/pressure) to form a kinetically stable rotaxane as shown in Figure 1.27c.[152] Additionally, the ring closure of a macrocycle around a dumbbell-shaped axle is often used for [2]rotaxane construction (clipping, Figure 1.27d).[153] Unlike rotaxanes, catenanes are restricted to being synthesised via single and double cyclisation methods shown in Figure 1.28. [154]

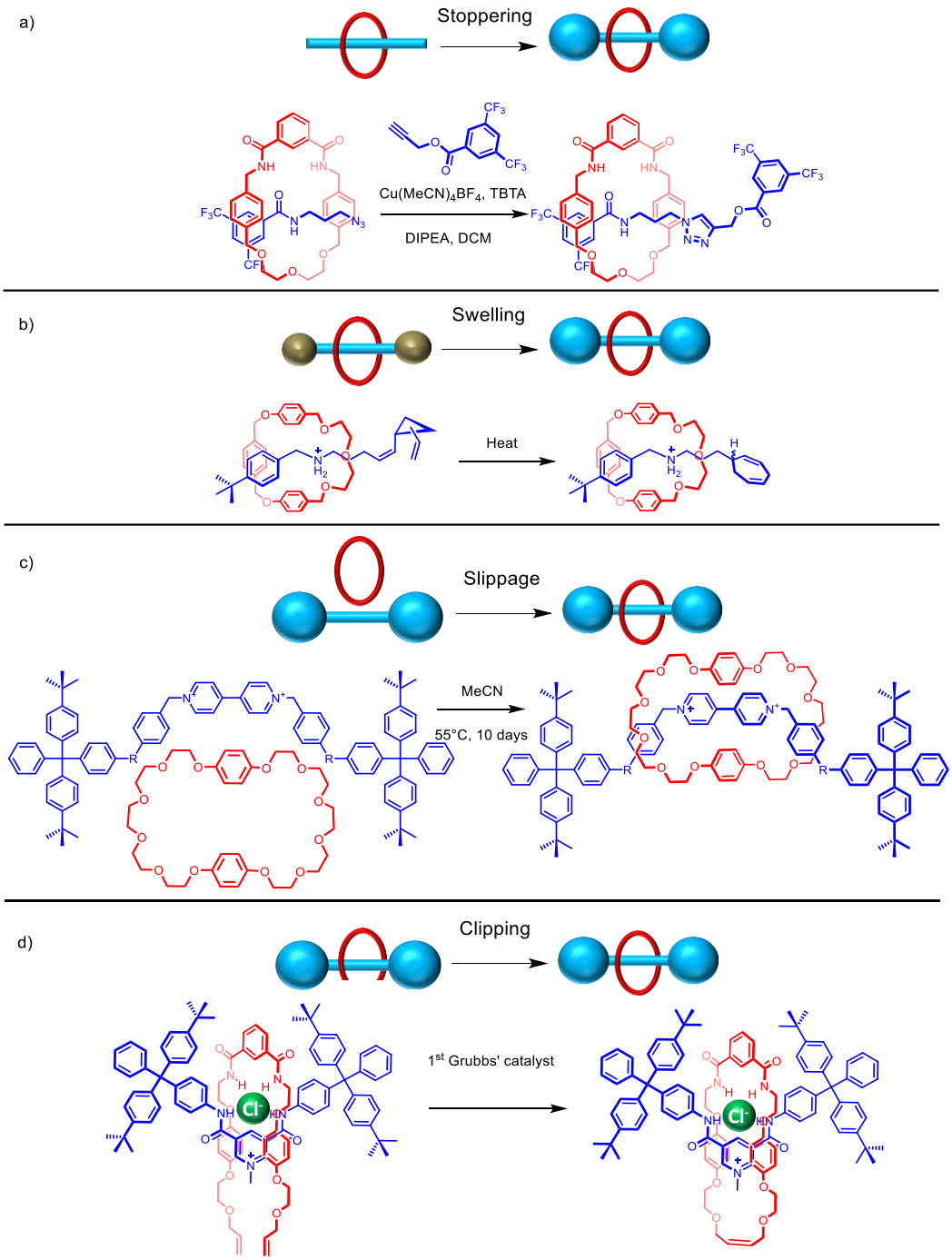

Figure 1.27: Examples of rotaxane synthesis via different routes; a) Stoppering,[155] b) Swelling,[150] c) Slippage,[156] d) Clipping[157]

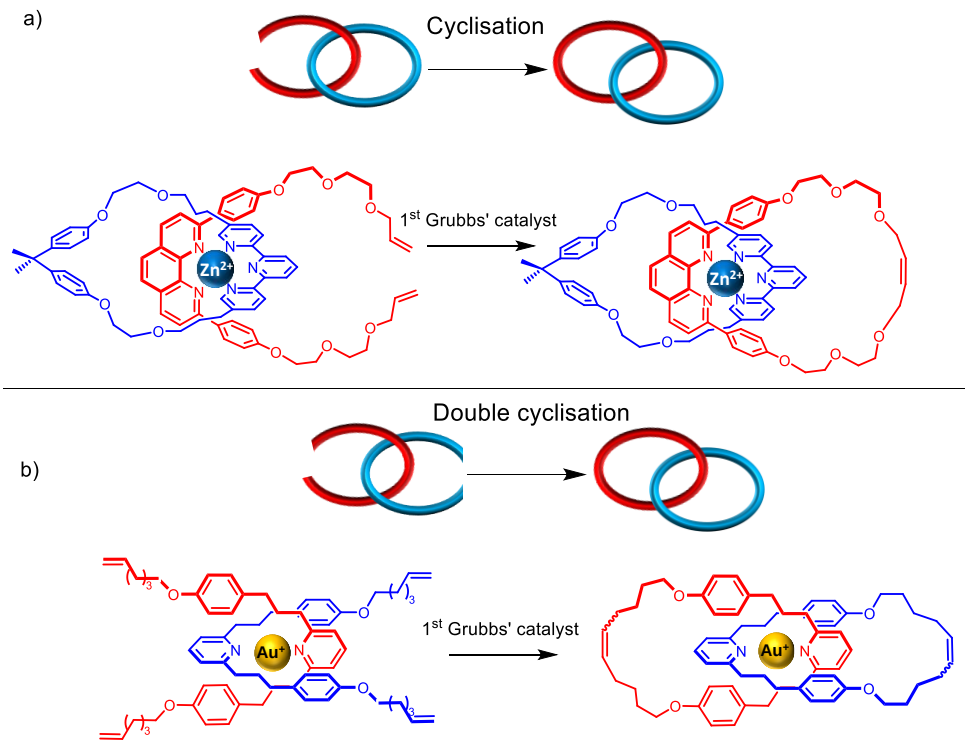

Figure 1.28: Examples of catenane synthesis via different routes; a) Cyclisation,[158] b) Double cyclisation.[159]

1.6.2. Template directed Synthesis

Early attempts to synthesise MIMs primarily relied on statistical methods. For example, Wasserman synthesised the first catenane in 1960, by cyclising an excess of bis-ester macrocycle precursor through a 34-membered deuterated cycloalkane (Figure 1.29). The formation of the MIM relied purely on the statistically random interpenetration of the bis-ester alkyl chain through the macrocycle, resulting in extremely poor yields (0.0001%).[160] A few years later Schill and co-workers developed another method to construct MIMs known as 'directed synthesis'. However, this method relied on laborious, multi-step synthetic routes, reducing the overall efficiency in product formation.[161] Almost two decades later, a pioneering metal cation template-directed approach was introduced by Sauvage, which enabled sufficient quantities of MIMs to be prepared for investigating the unique properties of the mechanical bond. [14]

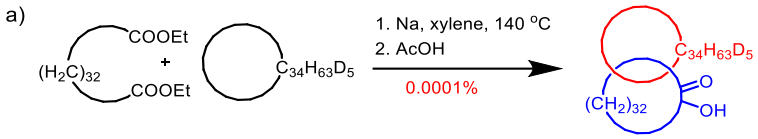

Figure 1.29: Wasserman's [2]catenane synthesis.[160]

1.6.2.1. *Cation templation*

Certain transition metal cations possess well-defined coordination geometries capable of controlling the spatial arrangement of surrounding ligands. This was first exploited for the synthesis of MIMs by Sauvage in 1983, to synthesise a [2]catenane.[14] Sauvage utilised a copper(I) metal template to initially form a homoleptic Cu(I) bis-phenanthroline complex in an orthogonal arrangement. A subsequent Williamson ether double cyclisation reaction resulted in the formation of a [2]catenane in 27% yield (Scheme 1.1-Route A). The yield increased to 42% when the [2]catenane was synthesised by a single cyclisation reaction of a Cu(I) template assembled pseudorotaxane intermediate (Scheme 1.1-Route B). The metal template was removed via treatment with excess KCN to obtain the metal-free [2]catenane. Following Sauvage's seminal work, a range of transition metal templates with different coordination geometries have been exploited to synthesise MIMs. This includes the linear geometry of Au(I),[159] square planar Pd(II)/Pt(II),[162,163] trigonal bipyramidal Zn(II),[158] and octahedral geometry of Ru(II).[164]

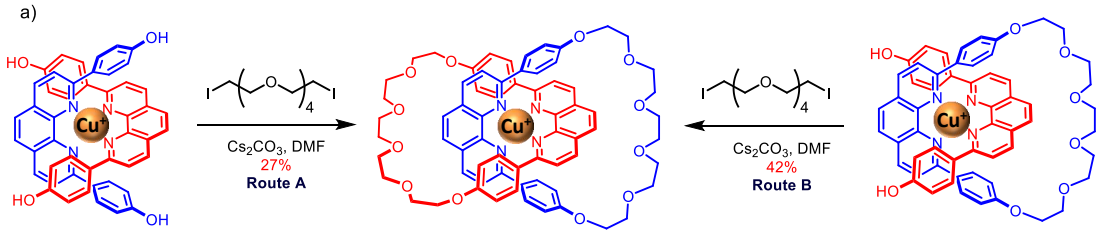

Scheme 1.1: Sauvage's Cu(I) templated synthesis of [2]catenane.[14]

In all the above examples, the metal acts as a '*passive template'* as its sole purpose is to assemble and preorganise precursor components in the appropriate orientation to form MIMs. In 2006, Leigh and co-workers introduced an '*active metal template (AMT)'* approach, where the transition metal simultaneously preorganises precursor components and catalyses the chemical reaction leading to formation of the mechanical bond. The first example of AMT MIM synthesis employed the Cu(I) azide-alkyne cycloaddition reaction (CuAAC).[165] As shown in Figure 1.30a, Cu(I) endotopically binds to the macrocycle pyridyl motif and catalyses the CuAAC reaction between alkyne and azide functionalised stopper precursors to form the interlocked [2]rotaxane in high yields of up to 94%. The yields of AMT reactions depend on various factors, including the nature and arrangement of Cu(I) binding donor atoms, the rigidity of the macrocycle, and the macrocyclic ring size.[166]

While the CuAAC reaction is the most commonly utilised AMT reaction, a range of other transition metal catalysed reactions have been exploited in AMT synthesis. For example, Anderson and co-workers synthesised a [2]rotaxane via a Cu(I) catalysed Cadiot-Chodiewicz alkyne cross-coupling reaction (Figure 1.30b).[167] Megiatto and co-workers used a Co(II) complexed porphyrinate macrocycle to form a [2]rotaxane by olefin cyclopropanation through radical carbene transfer reactions[168] (Figure 1.30c). Goldup and Leigh exploited Pd(II) to catalyse a Michael addition reaction to synthesise the [2]rotaxane shown in Figure 1.30d.[169] In addition to transition metals, alkali metals (e.g. Li^+, Na^+),[170,171] alkali earth metals (e.g. Ca^{2+}, Ba^{2+}),[172,173] lanthanide cations,[174,175] and organic cations (e.g. secondary ammonium cations, bipyridinium cations)[176–178] have also all been employed as templates for MIM synthesis.

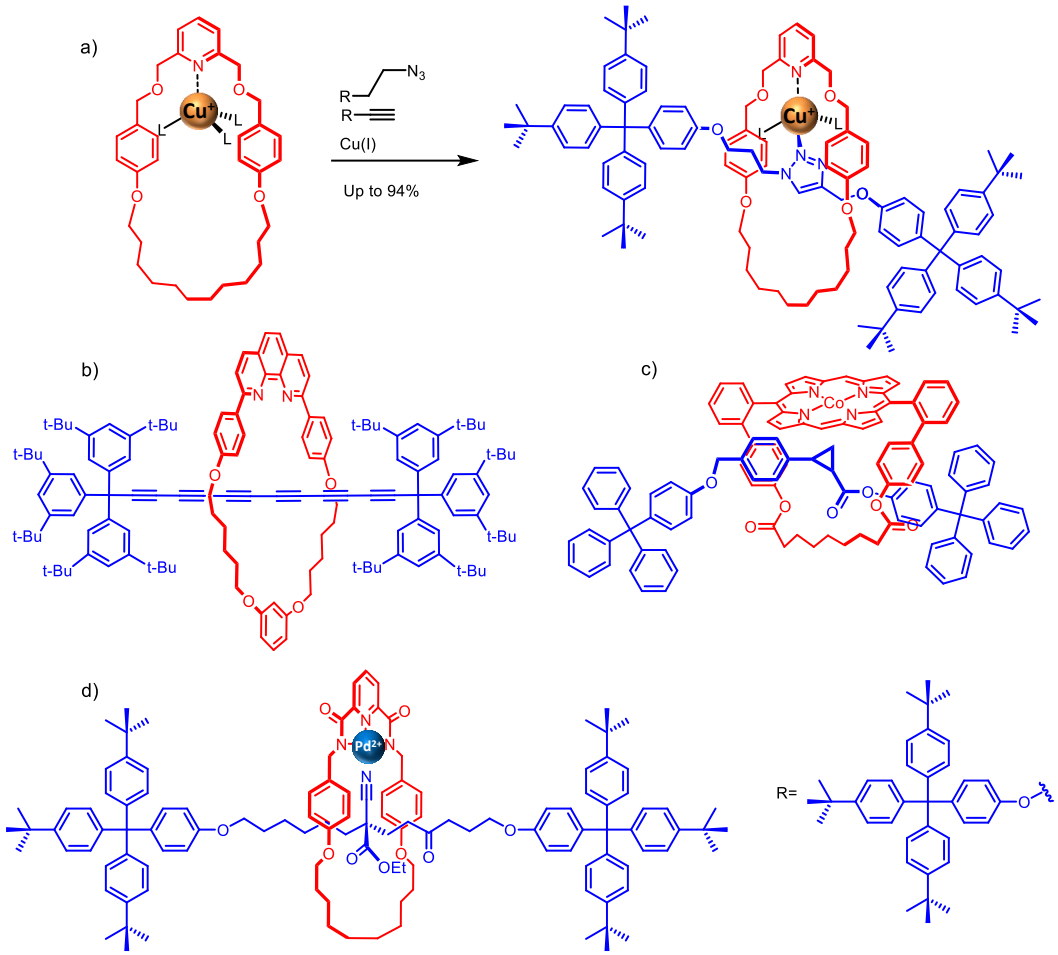

Figure 1.30: Rotaxanes synthesised via active metal template method: a) Leigh's pioneering [2]rotaxane synthesised via AMT method,[165] b) [2]rotaxane synthesis via Cu(I) catalysed Cadiot-Chodiewicz alkyne cross-coupling reaction,[167] c) [2]rotaxane synthesis via olefin cyclopropanation through radical carbene transfer reactions,[168] d) [2]rotaxane synthesis via Pd(II) to catalyse Michael addition reaction.[169]

1.6.2.2. *Anion templation*

MIMs have been successfully prepared using anion templation by either incorporating potent anionic motifs into precursor components or by using inorganic anions.

Vögtle synthesised the first anion templated MIM by exploiting the strong NH-donor HB interactions between the amide groups of tetralactam macrocycles and anionic nucleophiles.[179] As shown in Scheme 1.2a, the anionic phenolate stopper forms strong HB interactions within the tetralactam macrocycle cavity, which then reacts with the

bromobenzylic functional group of the tetraphenyl stopper to afford a [2]rotaxane in 95% yield. Recently, Flood and co-workers exploited the convergent C-H, HB interactions between a bis-alkyne functionalised phosphate anion template and a cyanostar macrocycle to form a [3]pseudorotaxane (Scheme 1.2b). The [3]rotaxane was synthesised by subsequently reacting the bis alkyne with stopper azide groups via a CuAAC click reaction.[180]

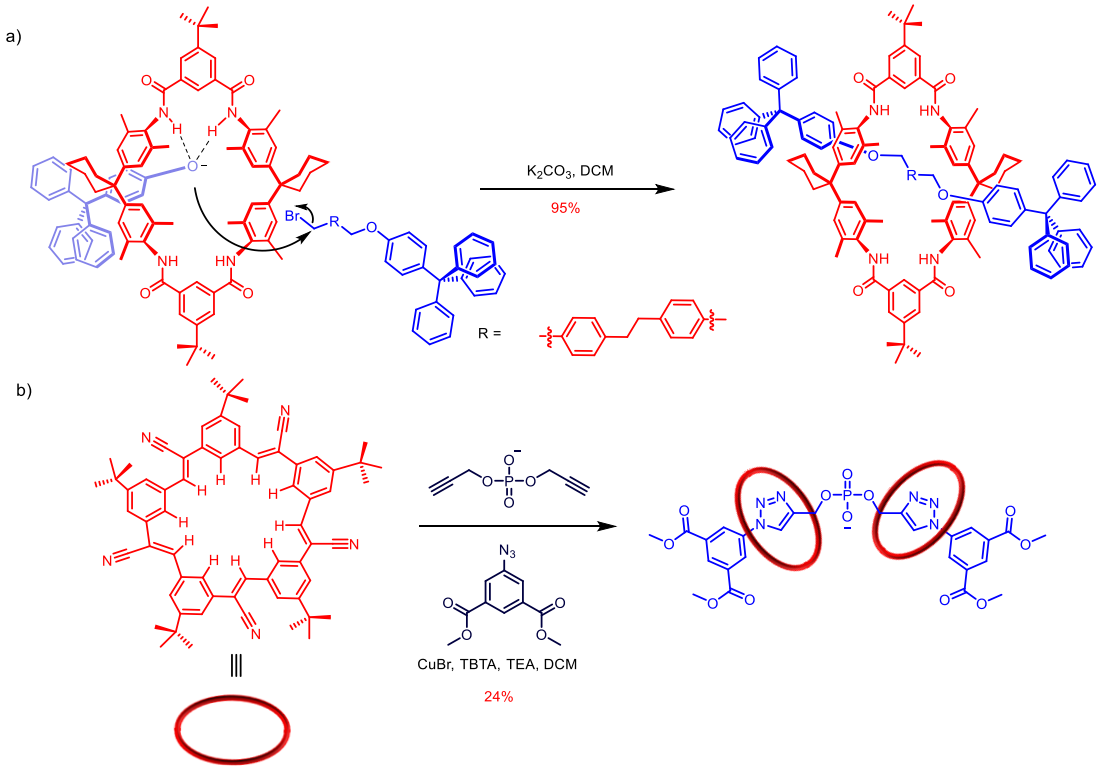

Scheme 1.2: Examples of MIMs synthesised by anion templation: a) [2]rotaxane synthesised via a reaction between phenolate stopper and bromobenzyl stopper,[179] b) [3]rotaxane synthesised via dialkyne phosphate template.[180]

Inspired by Sauvage's copper (I) metal template strategy, Beer and co-workers introduced a novel anion templating method where a discrete inorganic anion, including Cl^-, SO_4^{2-}, NO_3^- is used as a template to synthesise a range of MIMs.[157,181] Exploiting potent XB-anion interactions, the group recently synthesised a [2]rotaxane in 91% yield, using a Cl^- anion template strategy (Scheme 1.3).[182]

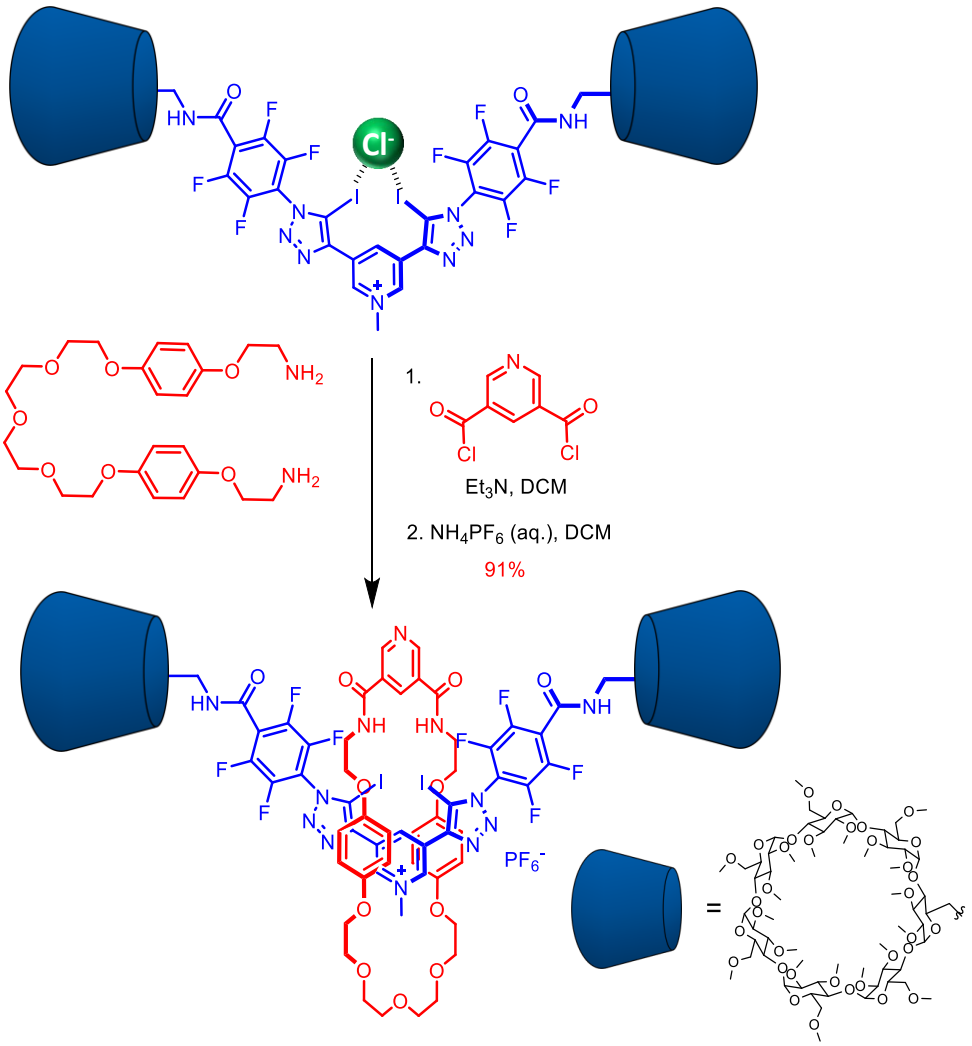

Scheme 1.3: Beer's Cl^- templated synthesis of [2]rotaxane.[182]

1.6.3. Applications of Mechanically Interlocked Molecules

The development of efficient synthetic templation strategies have enabled a wide variety of MIMs to be designed and prepared in sufficient quantities to be used in a range of applications that include molecular recognition and sensing, catalysis and molecular machines.

1.6.3.1. *MIMs for charged guest recognition and sensing*

MIMs possess unique three-dimensional cavities between interlocked components that can be decorated with complementary donor/acceptor groups for selective recognition of charged guest species. For example, Goldup and Rossler synthesised a family of [2]rotaxanes with an increasing number of nitrogen donor atoms in the rotaxane cavity and investigated their transition metal cation binding properties with Co^{2+}, Zn^{2+}, Cu^{2+} and Ni^{2+} ions in CH_3CN solvent media.[183] The mechanical bond coordination environment stabilised Ni^{2+} and Co^{2+} cations in unprecedented penta-coordinate geometries (Figure 1.31a). The unique 3D cavities in MIMs have also provided an attractive platform for enantioselective anion recognition. Niemeyer and co-workers synthesised a (S,S)-[2]catenane with chiral BINOL-phosphate groups shown in Figure 1.31b.[172] This chiral [2]catenane was capable of binding dicationic ammonium guest molecules such as lysine- and arginine- methyl esters (Lys-OMe/Arg-OMe) and 1,2-diammoniumcyclohexane (DACH), through the two chiral phosphate groups, in DMSO. Importantly, the chiral [2]catenane showed superior stereo discrimination, favouring the binding of D-Lys-OMe, D-Arg-OMe and (S,S)-DACH, compared to the non-interlocked macrocycle component.

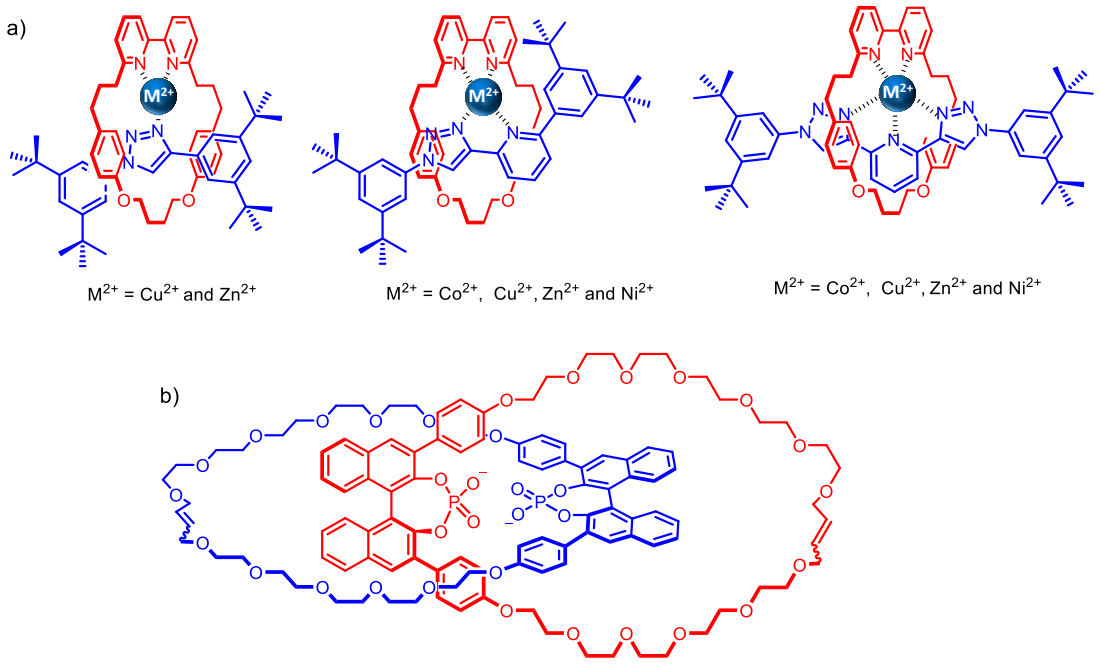

Figure 1.31: Examples of MIMs capable of cation recognition; a) Goldup's tri-, tetra-, and pentadentate [2]rotaxanes,[172] b) Niemeyer's chiral [2]catenane[172]

Mechanically interlocked hosts have also been designed and synthesised via anion templation methods to exhibit strong and selective anion binding properties. One such example is shown in Figure 1.32a, where a [2]catenane was prepared using a NO_3^- anion template methodology.[184] The recognition of nitrate is challenging due to the oxoanion's trigonal planar geometry and delocalised charge density. Nevertheless, the removal of the NO_3^- templating anion resulted in a [2]catenane receptor capable of selectively binding NO_3^- over a range of more basic oxoanions in 45:45:10 $CDCl_3/CD_3OD/D_2O$ solvent systems. This impressive NO_3^- selectivity was attributed to the trigonal multidentate binding cavity of the catenane which is complementary to the oxoanion's shape.

In another example, Smith and co-workers synthesised a fluorescent responsive [2]rotaxane capable of sensing Cl^-. The [2]rotaxane shown in Figure 1.32b comprises a squaraine dye axle component within a bis-anthracene containing tetralactam macrocycle. Exploiting the inherent dynamic properties of rotaxane MIMs, the binding of a Cl^- anion in $CHCl_3$/acetone

solvent mixtures resulted in a lateral displacement of the tetralactam macrocycle amide hydrogen bonded squaraine axle motif causing a red shift in fluorescence, detectable by the naked eye.[185]

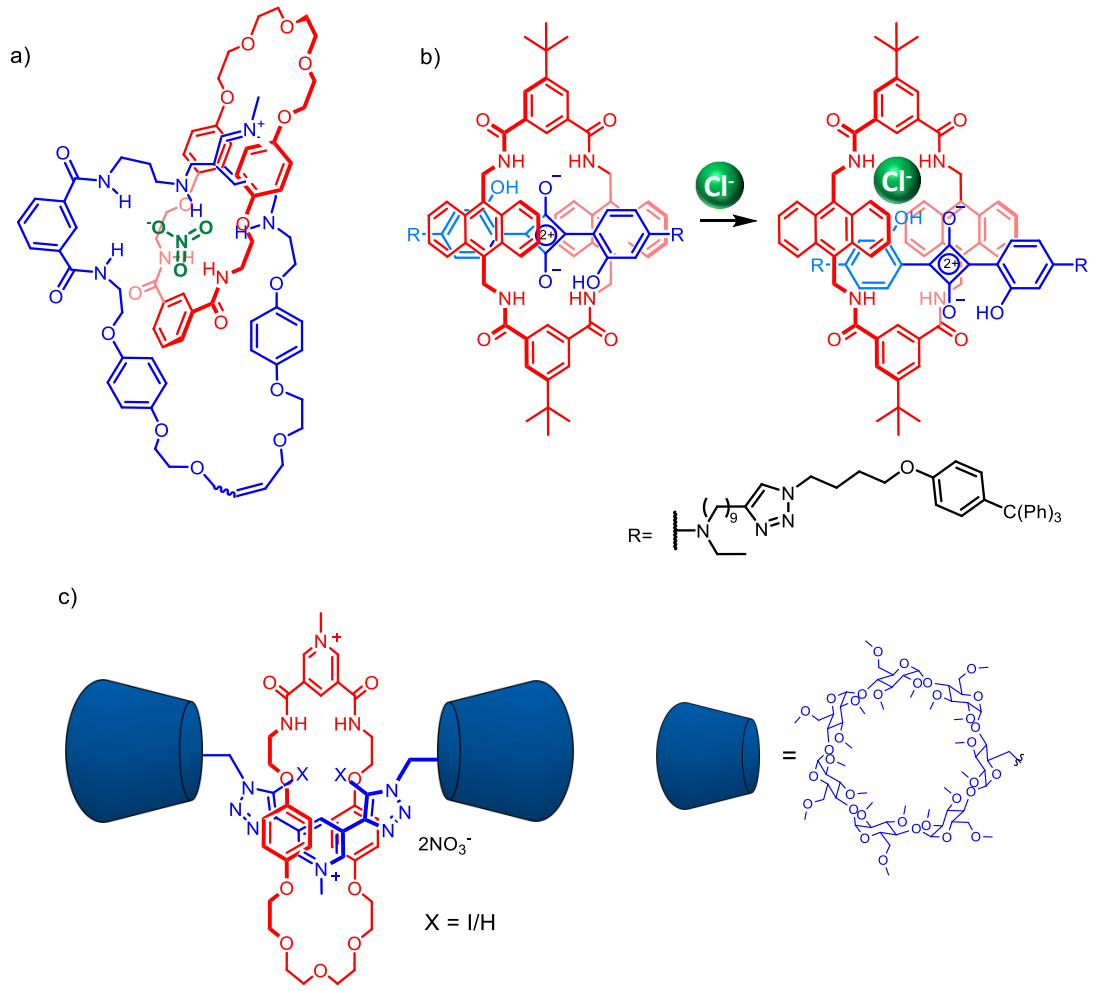

Figure 1.32: Examples of mechanically interlocked anion receptors; a) Beer's NO_3^- templated [2]catenane,[184] b) Smith's optically active [2]rotaxane,[185] c) Beer's water soluble XB/HB [2]rotaxane.[186]

In recent years, the incorporation of XB donors into MIMs has gained increasing attention due to acyclic and macrocyclic XB receptors often outperforming HB anion receptor analogues, particularly for softer halide anions.[41,187] An elegant example is the water soluble XB [2]rotaxane system shown in Figure 1.32c.[186] The XB rotaxane displayed superior halide anion binding, particularly for I^- in comparison to the analogous HB rotaxane in water (K_a (I^-

) = 2200 M^{-1} vs 20 M^{-1}). Van't Hoff analysis of variable temperature ^{1}H NMR titration data revealed the strong I^- binding displayed by the XB rotaxane is driven exclusively by favourable enthalpic contributions due to anion-XB interactions, while in stark contrast the weaker I^- binding by the HB rotaxane is entropically driven.

1.6.3.2. *Artificial molecular machines*

Molecular machines are systems that use molecular motion, such as rotation/translation, to perform tasks on a nanoscale.[188,189] The inherent dynamic properties of catenanes and rotaxanes make them ideal candidates for molecular machines due to the nature of the mechanical bond which facilitates the molecular motion of interlocked components. For example in rotaxanes, the mechanical bond allows the translational and rotary motion of the macrocycle (Figure 1.33a). Catenanes can exhibit rotational movements of the macrocycles (Figure 1.33b).

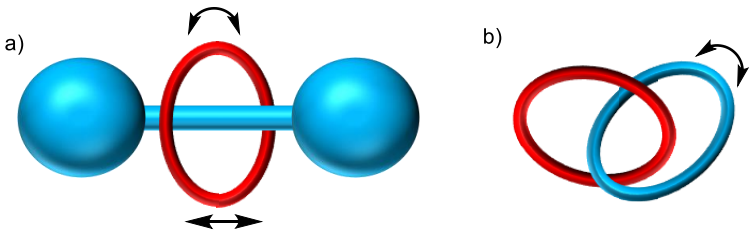

Figure 1.33: Molecular motion of interlocked structures: a) Rotational/translational motion of the macrocycle in a [2]rotaxane, b) Rotational motion of a macrocycle in a [2]catenane

Molecular machines can be divided into two sub-categories as molecular switches and molecular motors. Molecular switches have the capability to switch between two or more well defined co-conformations. An example of a molecular switch is the simple two station [2]rotaxane shown in Scheme 1.4.[189,190] In the absence of lithium cations, the macrocycle resides at the NDI station due to favourable aromatic donor-acceptor interactions between

the electron rich macrocycle and the electron deficient NDI axle motif. However, upon addition of Li^+, the macrocycle shuttles to the preferential pyromellitic diimide Li^+ coordination site station. The shuttling motion of the macrocycle could be reversed by adding 18-crown-6 to sequester Li^+. More complex rotaxane based switches have also been synthesised, including those that mimic the behaviour of elevators, muscles, and cable cars.[191–193]

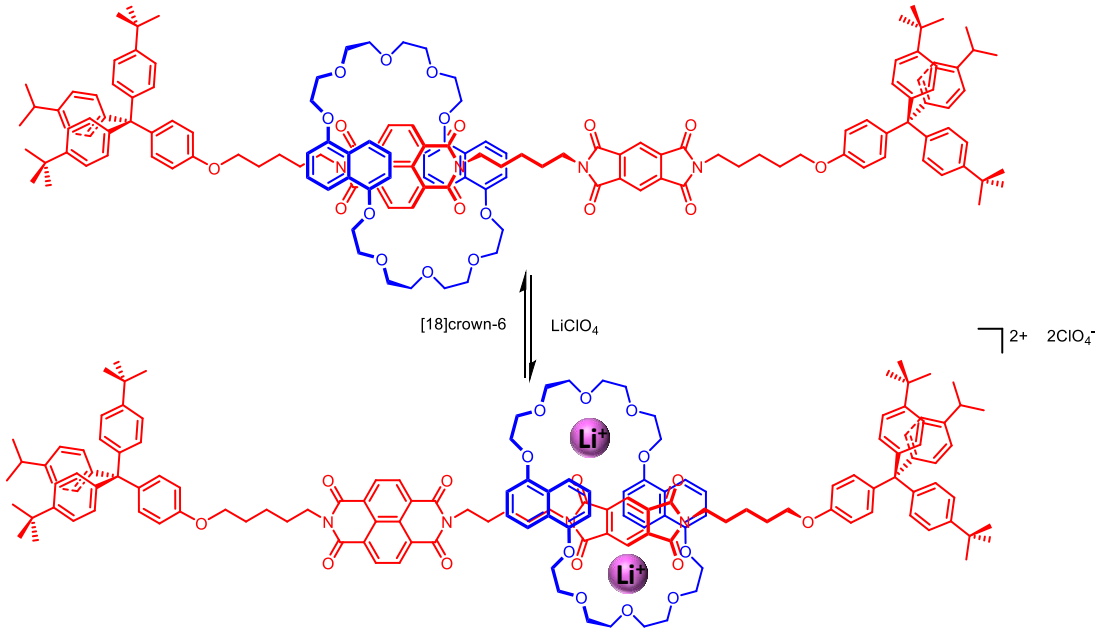

Scheme 1.4: Example of a molecular switch.[189,190]

In contrast to switchable molecular shuttles, molecular motors are capable of performing useful work. An example that demonstrates this concept is Leigh's [2]rotaxane ratchet (Scheme 1.5).[194] In the initial co-conformation, the macrocycle resides at the fumaramide axle station (State A). Photoisomerization results in the succinimide axle motif being the more thermodynamically preferred station for the macrocycle (State B). However, the translocation of the macrocycle to the succinimide station is restricted due to the presence of bulky silyl ether groups. Cleavage of the silyl motif allows the macrocycle to shuttle to the more favourable succinimide station as shown in state C. The system can be reset by re-

attachment of the bulky silyl group and isomerisation back to fumaramide (State D). However, the macrocycle is restricted to the thermodynamically less favoured succinimide station until the silyl groups are removed. Importantly, in state B and D the macrocycle is kinetically trapped in a thermodynamically less favoured state. This is known as a ratcheting mechanism which enables directional and repeatable translation of the macrocycle to perform useful work. Examples of more complex molecular motors include a sequence specific peptide synthesiser,[195] artificial molecular pumps,[196,197] and a molecular robotic arm that can transport peptides from site-to-site.[198]

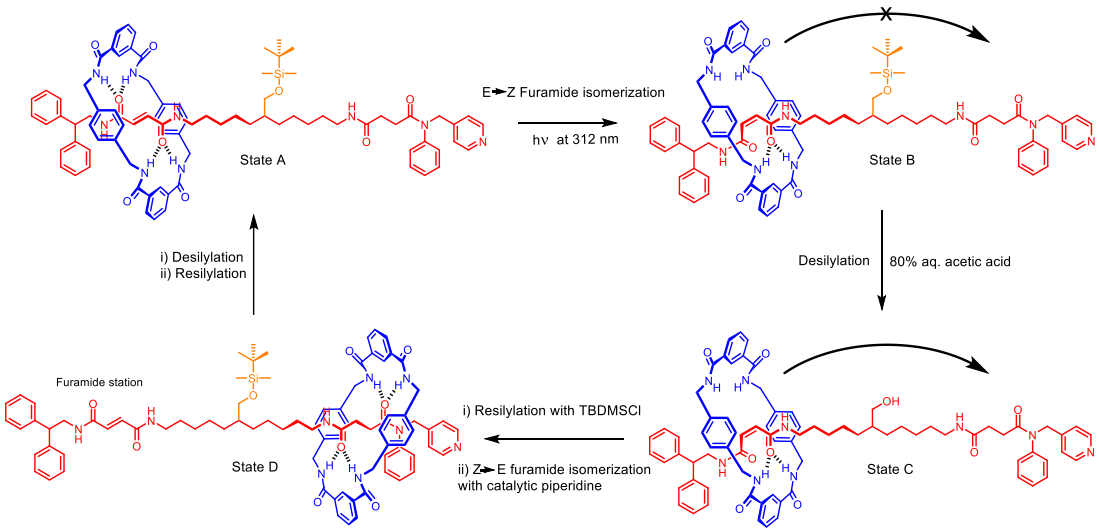

Scheme 1.5: Leigh's [2]rotaxane molecular ratchet

1.7. Project outline

As discussed in Section 1.4.3.2 and 1.6.3.1, the exploitation of XB interactions in the construction of host structural frameworks for anion and in particular ion-pair recognition applications is underdeveloped in comparison to ubiquitous HB interactions. This is somewhat surprising given the relatively few XB receptors reported to date have generally shown superior anion binding properties compared to HB analogues. Indeed, at the time of writing this thesis only one XB-heteroditopic interlocked receptor is known.[199] With this in

mind, the broad theme of this project is to design and synthesise novel interlocked and acyclic receptors containing multiple XB donor motifs for anion and ion-pair recognition investigation.

Chapter 2 discusses the synthesis and ion-pair binding properties of a series of novel heteroditopic [2]rotaxanes. The first part of this chapter examines their lithium halide binding properties and compares binding affinities with the corresponding non-interlocked macrocycle. This initial work is extended to include the preparation of a dynamic two-station [2]rotaxane, followed by an investigation of the unprecedented use of ion-pair binding as a stimulus to control the translational motion of the rotaxane's macrocycle component. The second part of this chapter focuses on investigating the influence of multiple XB interactions on lithium halide ion-pair recognition strength. To this end, a series of novel XB/HB triazole based heteroditopic rotaxanes are synthesised and their ion-pair binding properties are determined.

Chapter 3 details the design and synthesis of iridium(III) complexed cyclometalated bipyridine containing XB acyclic and rotaxane receptors capable of optically sensing anions. A novel Ir(III) complexed [3]rotaxane host system is prepared together with a [2]rotaxane and acyclic receptor analogues. Extensive ^{1}H NMR and fluorescence spectroscopy studies were used to elucidate their anion recognition and sensing properties.

Chapter 4 concerns the synthesis and anion binding properties of a series of acyclic rhenium(I) complexed XB and HB molecular tweezers. The influence of Re(I) complexation is investigated by comparing the anion binding properties of the metal complexed receptors with analogous metal-free receptors.

Chapter 2

Heteroditopic [2]rotaxanes for lithium halide ion-pair recognition

Chapter 2: Heteroditopic [2]rotaxanes for lithium halide ion-pair recognition

2.1. Introduction

2.1.1. Heteroditopic rotaxanes for ion-pair recognition

As detailed in Chapter 1, Section 1.5 heteroditopic receptors containing proximal separate binding sites for a cation and an anion commonly exhibit augmented guest ion affinity and selectivity relative to their monotopic receptor analogues.[128,134] To date, the majority of reported heteroditopic receptors are either of acyclic or macrocyclic receptor design.[128,134,200]

In the past decade or so mechanically interlocked molecules (MIMs) have become increasingly popular as selective host systems for charged guest species due to their unique topologies and multidentate three-dimensional binding cavities. In particular, the interlocked preorganised binding sites can provide shape and size complementarity for a wide range of cation[201–204] and anion[205–208] substrates. Importantly, MIM receptors display markedly stronger and enhanced selective guest binding properties compared to analogous non-interlocked acyclic axle and macrocycle counterparts.[209] Despite this advantageous MIM host mechanical bond recognition effect, surprisingly examples of heteroditopic MIMs for ion-pair recognition are extremely rare.[199,210–212]

The first heteroditopic [2]rotaxane capable of ion-pair binding was synthesised by Beer and co-workers in 2014 (Figure 2.1a).[210] This [2]rotaxane selectively binds sodium halide salts over other alkali metal halides in 4:1 CD_3Cl/CD_3OD solvent media. Since then, only a handful of heteroditopic rotaxanes have been reported. The same group subsequently developed a [2]rotaxane for recognising zinc halide and nitrate salts in $CD_3CN/CDCl_3$ solvent mixtures (Figure 2.1b).[199] More recently, Ballester and co-workers synthesised a heteroditopic [2]rotaxane for binding tetraalkylammonium salts with a range of anions including Cl^-, OCN^-,

and NO_3^- (Figure 2.1c).[212] The heteroditopic [2]rotaxane, synthesised by Goldup and co-workers demonstrated strong ion pair binding for H^+ and a range of anions (i.e. Cl^-, Br^-, HSO_4^-, TsO^-, AcO^-, MsO^-) in 1:1 $CDCl_3/CD_3CN$ solvent media (Figure 2.1d).[211] In 2021, Beer and Knighton reported the first heteroditopic catenane host structure including a X-ray crystal structure of a Na^+ and Cl^- bound catenane (Figure 2.1e).[213] However, to the best of our knowledge there are no heteroditopic MIM hosts capable of selectively binding lithium ion-pair species, despite the increasing importance of lithium salt recognition and extraction (*vide infra*).

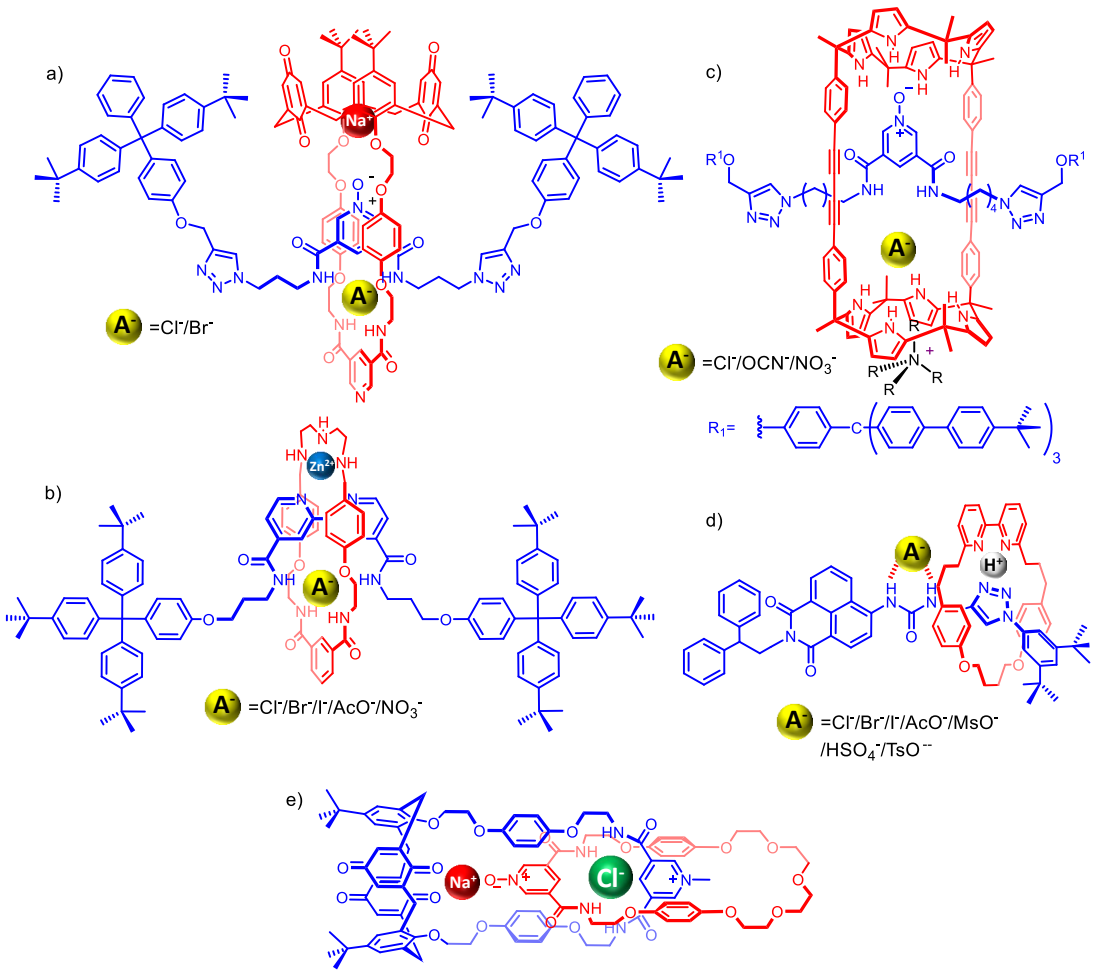

Figure 2.1: Hetroditopic [2]rotaxanes: a) Beer's sodium halide selective [2]rotaxane,[210] b) Beer's Zn^{2+} ion-pair species binding [2]rotaxane,[199] c) Ballester's [2]rotaxane binding tetraalkylammonium salts,[212] d) Goldup's acid triggered anion binding [2]rotaxane,[211] e) Beer and Knighton's NaCl bound heteroditopic catenane.[213]

2.1.2. Lithium halide ion-pair recognition

During the past two decades the worldwide demand for lithium has increased substantially due to its many applications in lithium ion-batteries, pharmaceuticals, ceramics, glass, lubricants, and polymer production.[214] Lithium is currently extracted predominantly from brine (62%), followed by hard rock (29%), and clay (7%).[215] Experts predict that it will be difficult to meet the rising lithium demand by conventional extraction methods within the next few decades.[216] Thus, there is an urgent need to look for alternative sources of lithium and improve efficiency in current lithium extraction techniques.

A major obstacle in the current extraction processes of lithium is the presence of interfering ions. For example, cations such as sodium, potassium, calcium, magnesium, and anions like chloride have greatly reduced the efficiency and increased the cost of lithium extraction from salt lake brine.[217,218] Therefore developing efficient and selective lithium extraction methods is of great importance.

Additionally, lithium salts can cause severe toxic effects due to their impact on the central nervous system. This includes irreversible neurological impacts such as dementia, Parkinson's disease, cerebellar impairment and peripheral neuropathies.[219,220] Recent reports show an alarming increase in lithium concentration in streams and tap water which corelates with the population density of the area.[221] Hence, to minimise adverse environmental and biological effects, it is important to develop receptors that can selectively recognise lithium salts.

Despite the importance, heteroditopic receptors designed to selectively recognise and extract lithium ion-pair species are scarce and have been mainly restricted to acyclic and macrocyclic systems.[222–225] In one example, Sessler and co-workers synthesised a series of hemispherand strapped calix[4]pyrroles for the recognition and extraction of lithium ion-pair species (Figure 2.2). Varying the number of nitrogen and oxygen donors in the cation

binding cavity of the three receptors were reported to significantly affect lithium salt extraction efficiency and selectivity. The receptor shown in Figure 2.2a demonstrated selective solid-liquid and liquid-liquid extraction of $LiNO_2$ in the presence of $NaNO_2$ and KNO_2. However, the receptor could not perform liquid-liquid extraction of LiCl. Interestingly, by reducing the cavity size, the receptors shown in Figure 2.2b/c were able to extract LiCl under both solid-liquid and liquid-liquid conditions.

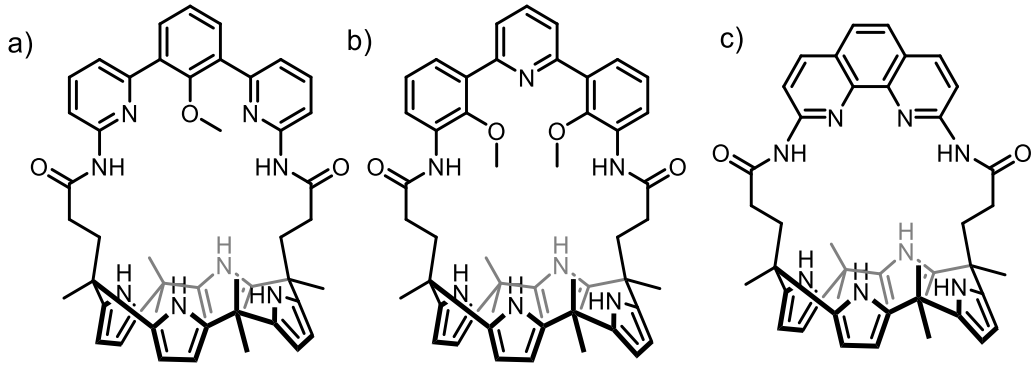

Figure 2.2: Sessler's hemispherand calix[4]pyrrole based ion-pair receptors for extraction of lithium salts

2.2. Chapter aims

Taking into account the few reported examples of heteroditopic mechanically interlocked hosts, and the absence of MIMs for lithium ion-pair species recognition, this chapter's project aims focus on synthesising novel heteroditopic [2]rotaxane host systems for strong and selective recognition of lithium halide salts. The chapter is divided into two sections:

Part I: The first part of this chapter aims to develop novel heteroditopic [2]rotaxanes consisting of a ditopic methoxy pyridyl-isophthalamide macrocycle component and axle integrated XB/HB triazole donors. Anion, cation, and ion-pair binding properties of the heteroditopic [2]rotaxanes are investigated by extensive ^{1}H NMR titration experiments, X-ray crystallography, and DFT calculations.

This initial work is extended to include the design and synthesis of a dynamic [2]rotaxane for the unprecedented investigation of exploiting ion-pair binding as a stimulus to control the relative translational motion of the macrocycle along the rotaxane's two-station axle component.

Part II: In order to further investigate the effect of XB interactions for ion-pair binding, the second part of this chapter is concerned with replacing the amide groups of the macrocycle component with iodotriazole XB donor groups to produce a series of novel heteroditopic [2]rotaxanes for lithium halide recognition.*

2.3. Part I: XB/HB heteroditopic [2]rotaxanes with an amide macrocycle

2.3.1. Synthesis of HB amide heteroditopic macrocycle and HB/XB [2]rotaxanes

As shown in Figure 2.3, the target heteroditopic rotaxane design consists of an axle separated cation and an anion binding site. It was envisaged that the macrocycle's Lewis basic methoxy pyridyl oxygen and nitrogen donor atoms in combination with the axle triazole nitrogen donor would facilitate lithium cation complexation. This cation binding induced preorganisation generates an optimal binding cavity for subsequent halide anion recognition via the macrocycle's HB amides and axle HB/XB donors.

* This project was done in collaboration with Dr. Jessica Pancholi

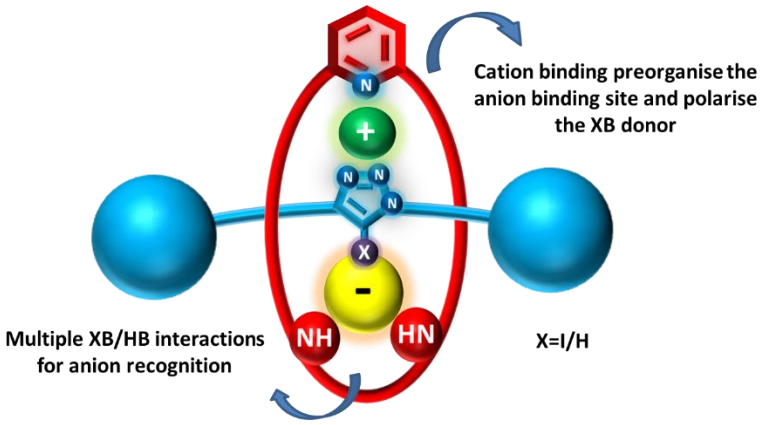

Figure 2.3: Schematic representation of the designed heteroditopic [2]rotaxane

The multistep synthetic procedure employed for the preparation of the ditopic macrocycle **2.6** is outlined in Scheme 2.1. The initial preparation of the azide functionalised phenyl hydroxyl methylene precursor **2.1** followed a literature procedure.[226] The reaction of 2,6-bis-bromomethyl pyridine **2.2** with two equivalents of **2.1** in the presence of NaH in dry THF gave the bis-azide derivative **2.3** in 70% yield. Reduction using hydrazine monohydrate in the presence of Pd/C in methanol afforded the bis-amine **2.4** in 90% yield. A condensation reaction between the bis-amine **2.4** and bis-acid chloride **2.5** under high dilution conditions in dry DCM and triethylamine produced the target macrocycle **2.6** in 34% isolated yield after column chromatographic purification.

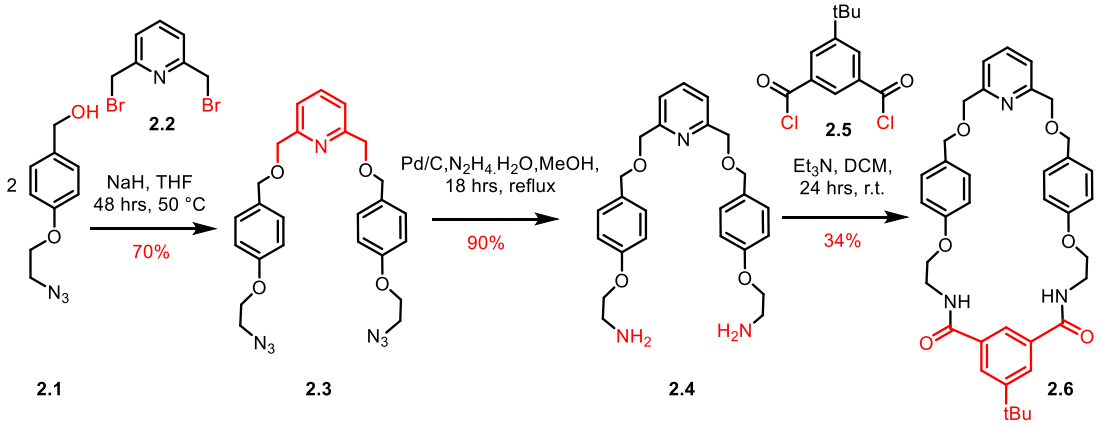

Scheme 2.1: Synthesis of macrocycle **2.6**

The target XB and HB heteroditopic [2]rotaxanes were synthesised using the CuAAC-AMT approach as depicted in Scheme 2.2. Macrocycle **2.6** was precomplexed with 0.96 equivalents of $[Cu(MeCN)_4]PF_6$ and was subsequently reacted with five equivalents of stopper azide **2.7**[165] and stopper proto- and iodo-alkynes **2.8a** and **2.8b**[165,227] in DCM for two days. The target HB and XB [2]rotaxanes **2.9** and **2.10** were isolated in excellent yields of 77% and 74% respectively, by preparative TLC. This high yield of rotaxanation may be attributed to the combined effects of the relative small size of the HB macrocycle, and the ability of the methoxy pyridine motif to form strong interactions with the Cu(I) AMT catalyst.[165,166]

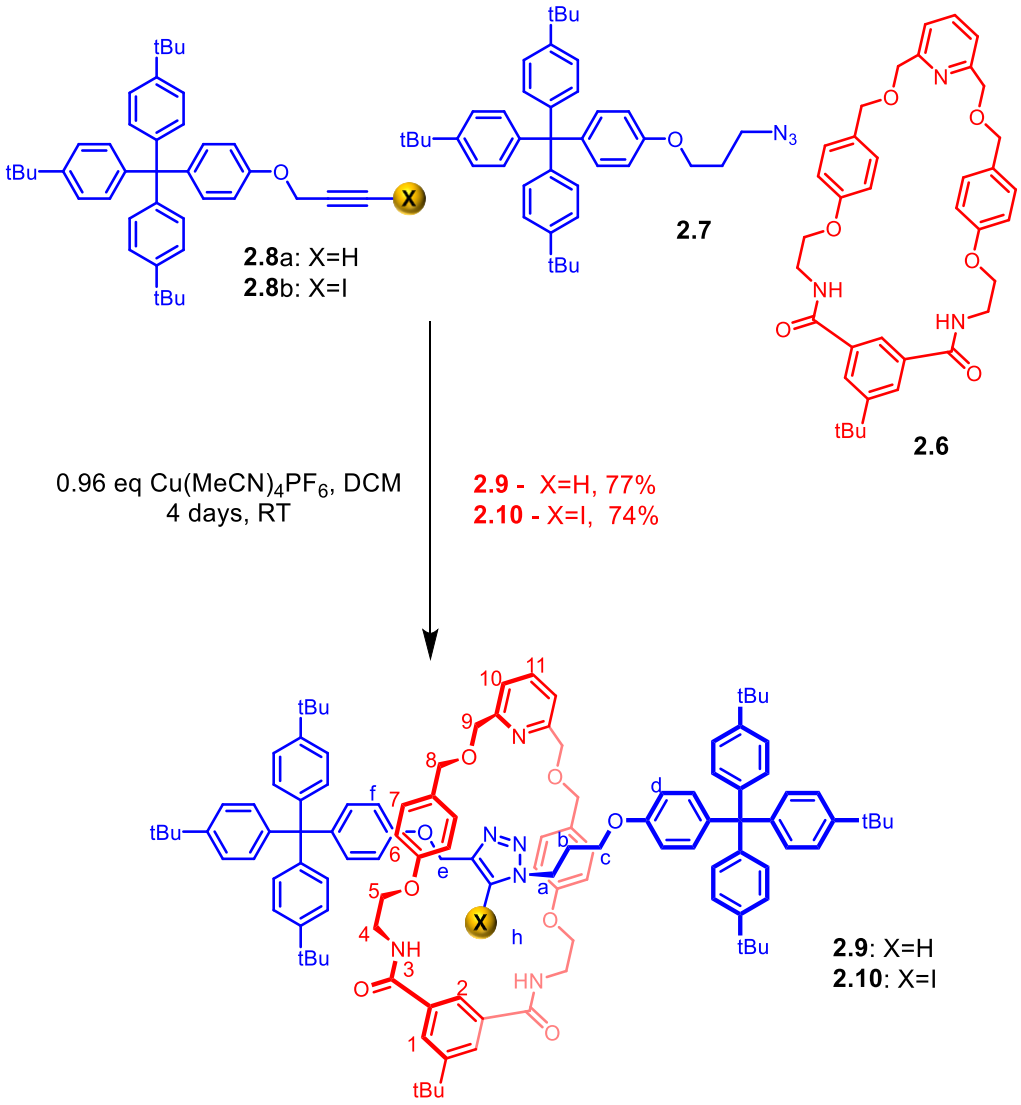

Scheme 2.2: Synthesis of heteroditopic [2]rotaxanes **2.9** and **2.10**

2.3.1.1. *Characterisation of rotaxane structures*

Both rotaxanes were characterised by ^{1}H NMR and ^{13}C NMR and high-resolution electrospray ionisation (ESI) mass spectrometry. A comparison of the ^{1}H NMR spectra of rotaxanes **2.9** and **2.10** with macrocycle **2.6** in $CDCl_3$, revealed proton perturbations indicative of the formation of an interlocked structure (Figure 2.4). Internal isophthalamide proton $\mathbf{H_2}$ and amide proton $\mathbf{H_3}$ of the macrocycle displayed notable downfield shifts in the respective rotaxane's ^{1}H NMR spectrum, presumably due to HB interactions with the basic nitrogen atoms of the triazole axle. In addition, diagnostic upfield shifts were observed for the macrocycle aryl protons $\mathbf{H_6}$ and $\mathbf{H_7}$, indicative of aromatic donor-acceptor interactions between the electron-rich macrocycle aryl groups and the relatively electron-deficient axle triazole unit. Interestingly, the signal for methylene protons $\mathbf{H_8}$, which appeared as a singlet in the macrocycle, splits into a multiplet in the rotaxane spectrum. This could be due to the loss of symmetry of the methylene protons upon formation of the interlocked structure. Conclusive evidence of the interlocked nature of the [2]rotaxanes was obtained by ^{1}H-^{1}H ROESY spectroscopy experiments, which showed cross-peaks arising from through-space interactions between the interlocked axle and the macrocycle components (Figure 2.5).

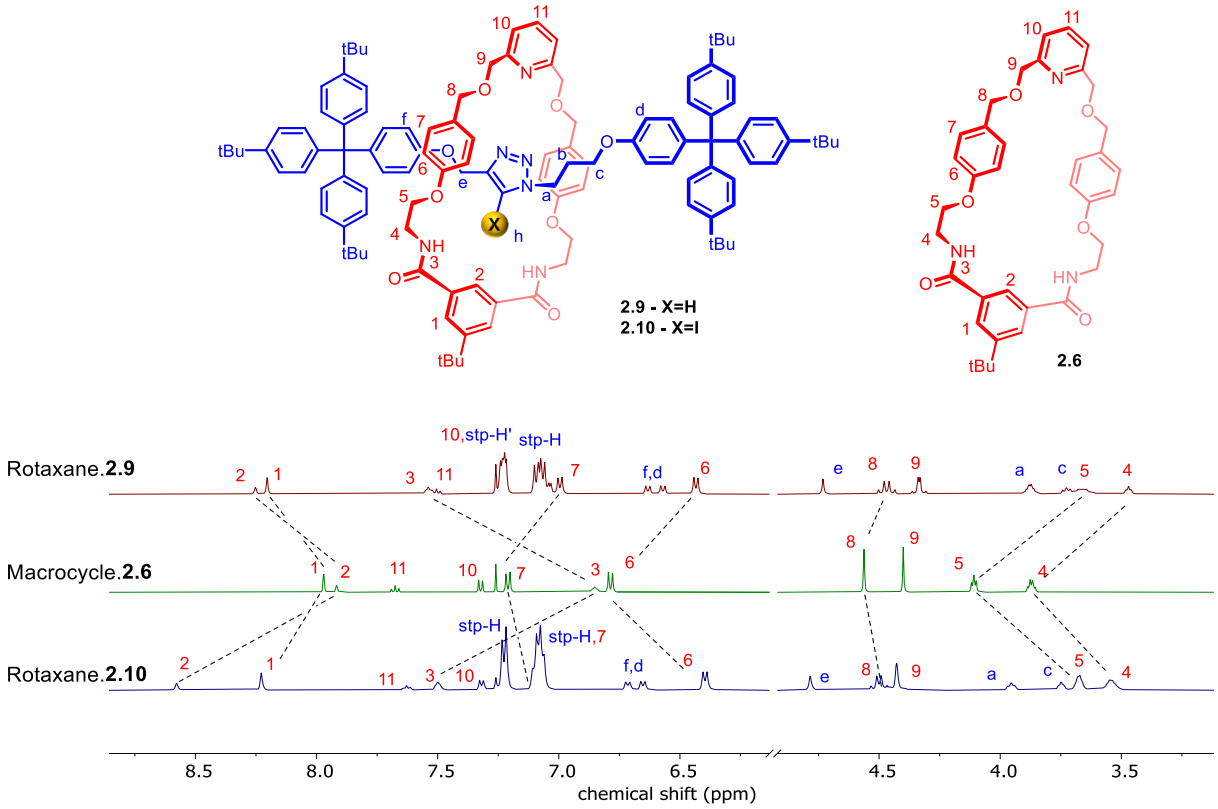

Figure 2.4: Comparison of ^{1}H NMR spectra of macrocycle **2.6** with rotaxane **2.9** and **2.10** in $CDCl_3$, 298 K, 500 MHz. Stropper protons are denoted as stp-H.

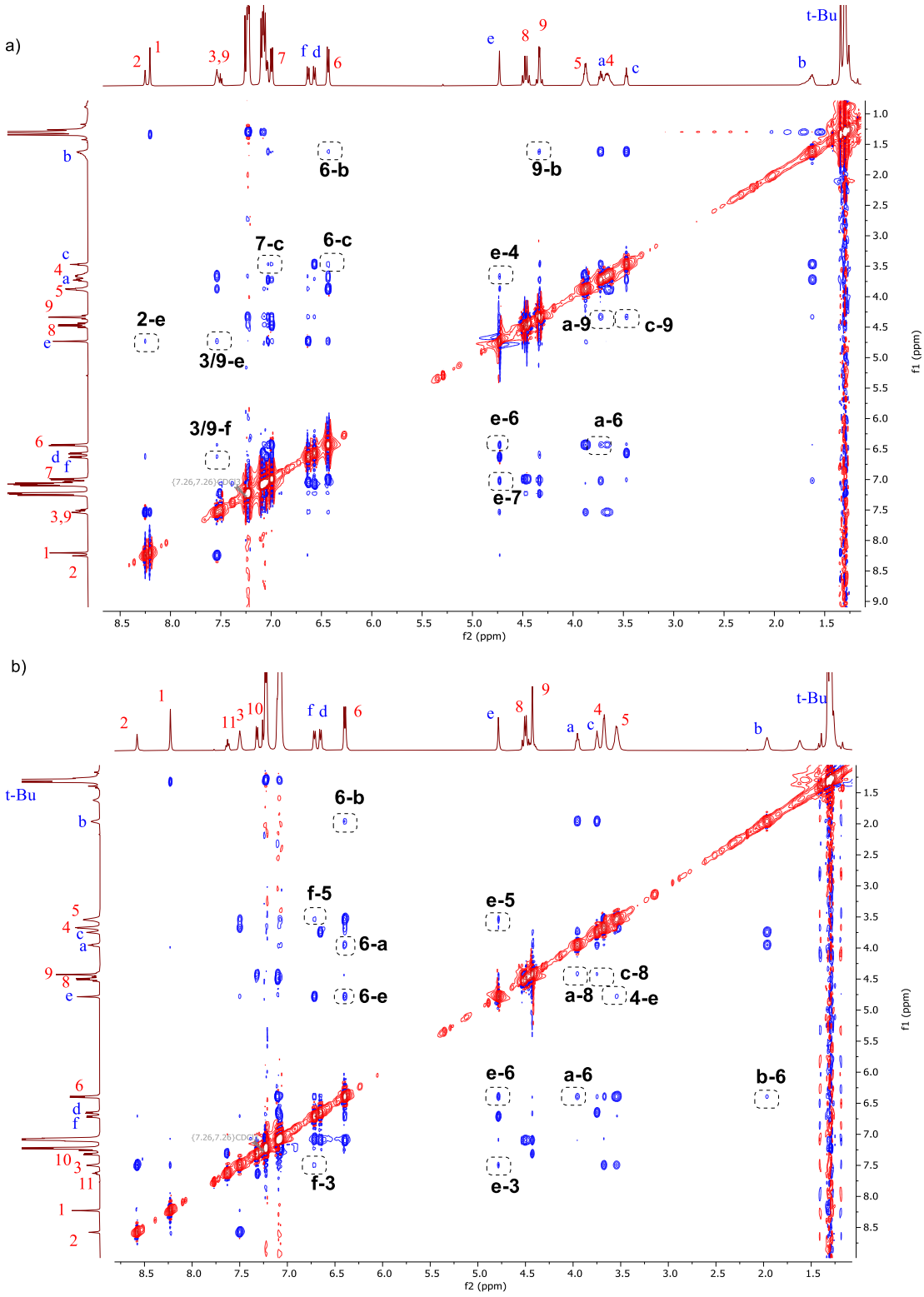

Figure 2.5: ^{1}H-^{1}H ROESY NMR spectra of: a) rotaxane **2.9**, b) rotaxane **2.10**, in $CDCl_3$, 298 K, 500 MHz

2.3.2. Anion, cation, and ion-pair recognition studies

2.3.2.1. *Anion, Cation and Ion-pair binding studies of Heteroditopic [2]rotaxanes and macrocycle*

Following the successful synthesis of the XB and HB [2]rotaxanes attention was turned towards investigating their guest binding properties. The anion binding properties of both rotaxanes **2.9** and **2.10** were initially investigated by qualitative ^{1}H NMR titration experiments in 3:7 $CD_3CN/CDCl_3$ (v/v) solvent mixtures. This particular solvent system was chosen based on the solubility of both host systems, tetrabutylammonium (TBA) anion and alkali metal cation salts. In a typical titration experiment, increasing equivalents of TBA halide salts were added to a rotaxane solution and ^{1}H NMR spectra recorded. Notably, addition of the halide salts did not cause any significant rotaxane proton perturbations, suggesting that both interlocked receptors were incapable of binding halides in this mixed solvent system.

With the addition of one equivalent of $LiClO_4$ to rotaxanes **2.9** and **2.10**, notable perturbations were observed in macrocycle methylene proton H_9 and axle methylene proton H_e, indicative of cation complexation proximal to the macrocycle pyridyl motif and axle triazole motif (Figure 2.6). However, protons in the anion binding site H_4, H_5, H_2 showed only minor perturbations indicating that ClO_4^- serves as a non-coordinating anion. In stark contrast to the anion binding studies conducted in the absence of lithium cation, when TBA bromide was added to the rotaxane precomplexed with 1 equivalent of $LiClO_4$, protons in the anion binding site H_2, H_3, H_4, H_5 were perturbed significantly indicating halide complexation (Figure 2.6). This suggests the bromide anion binding affinity of both rotaxanes **2.9** and **2.10** is 'switched on' by pre-complexation to Li^+, attributed to a combination of favourable electrostatic interactions between the co-bound ions and preorganisation of the mechanically interlocked components upon Li^+ complexation. Similar ^{1}H NMR spectral perturbations were observed in analogous experiments with Li^+-**2.9** and Li^+-**2.10**, with TBACl

and TBAI. It is important to note that proton signals perturbed by Li^+ did not reverse to their original peak positions upon addition of the halide anions, indicating concomitant cation and anion ion pair complexation (Figure 2.6).

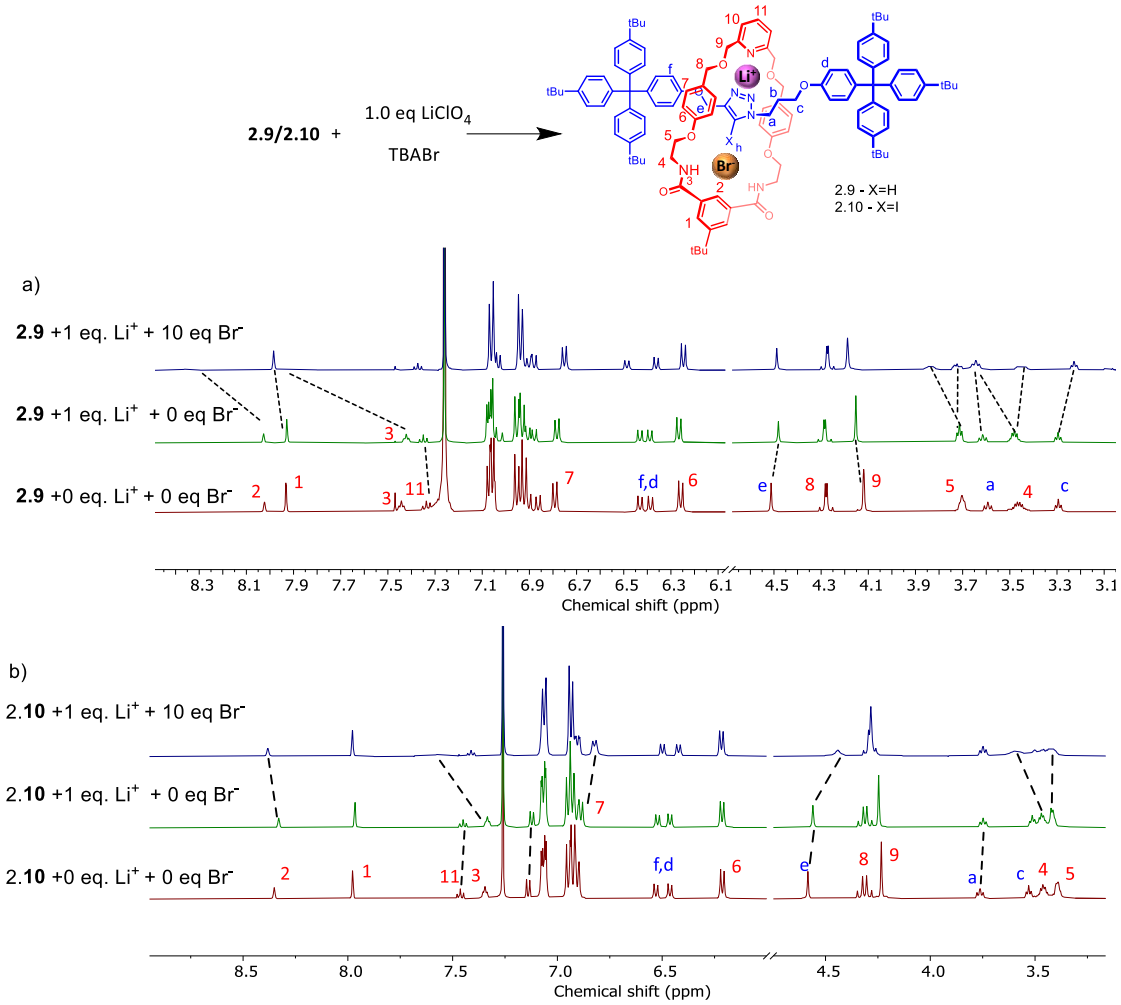

Figure 2.6: Superimposed ^{1}H NMR spectra in 3:7, CD_3CN-$CDCl_3$ (v/v), of a) (bottom to top) Rotaxane **2.9**, Rotaxane **2.9** in the presence of 1 eq. of $LiClO_4$, Rotaxane **2.9** with further addition of 10 eq. of TBABr, b) (bottom to top) Rotaxane **2.10**, Rotaxane **2.10** in the presence of 1 eq. of $LiClO_4$, Rotaxane **2.10** with further addition of 10 eq. of TBABr.

The halide anion association constants of **2.9** and **2.10** in the presence of 1 eq. $LiClO_4$ were determined by monitoring the perturbations of multiple non-overlapping ^{1}H NMR signals (H_1, H_3, H_f, H_e) with increasing halide concentration. Global fit analysis using Bindfit software[228,229] of the binding titration isotherms (Figure 2.7), determined 1:1 stoichiometric 'apparent'

host-guest association constants displayed in Table 2.1. It is important to note that under these experimental ^{1}H NMR anion titration conditions of one equivalent of $LiClO_4$ and rotaxane host, lithium cation binding is not quantitative; only a fraction of rotaxane host molecules in the solvent mixture are complexed with the metal cation and there remains at equilibrium a significant proportion of both free rotaxane and metal cation (See Section 2.3.2.2).

Both rotaxanes bind all lithium halide ion-pairs strongly in 3:7 $CD_3CN/CDCl_3$, including LiCl, which is impressive given the salt's high lattice energy of 834 kJ mol^{-1}.[70] Notably, the binding constant values for LiCl and LiBr in 3:7 $CD_3CN/CDCl_3$, are more than six times larger than for LiI. This maybe attributed to a combination of the lower basicity of iodide as well as size complementarity between the respective rotaxane's anion binding cavity for the smaller halide ions. As the binding constants of LiCl and LiBr were too high to be reliably determined by ^{1}H NMR spectroscopy (>10^4 M^{-1}) in 3:7 $CD_3CN/CDCl_3$, the binding studies were repeated in a more competitive solvent system comprising 4:6 $CD_3CN/CDCl_3$. In this mixed solvent, HB rotaxane **2.9** displayed a more than four-fold selectivity preference for LiCl over LiBr and an even greater degree of selectivity over LiI. The higher basicity and size complementarity of the Cl^- anion for the lithium precomplexed all HB rotaxane's three-dimensional anion binding cavity may account for the observed LiCl selectivity.

However, the lithium precomplexed XB iodotriazole axle containing rotaxane Li^+-**2.10** unexpectedly displayed lower halide binding constants than HB rotaxane Li^+-**2.9**. This result is further investigated through DFT calculations (Section 2.3.4), which revealed that the binding of Li^+ to the XB rotaxane **2.10** causes the axle XB donor to be sterically inaccessible to form linear XB···anion interactions.

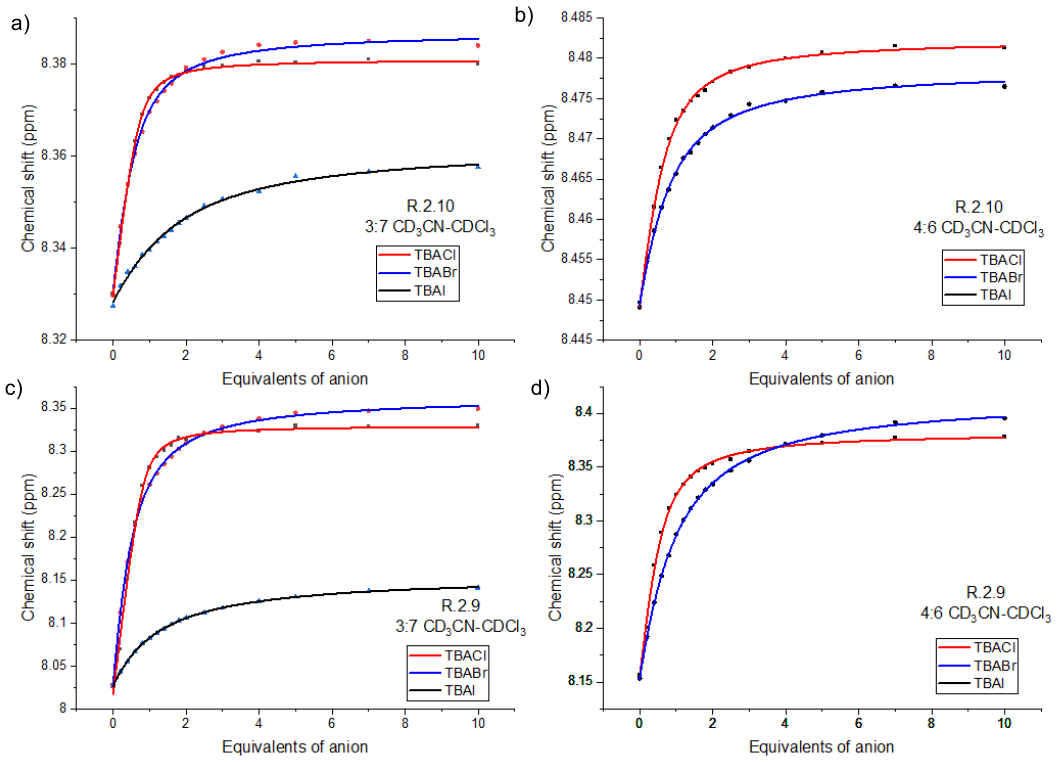

Figure 2.7: Binding isotherms showing changes in chemical shifts of internal benzene proton H_2 of Li^+ precomplexed heteroditoric rotaxanes; a) R.**2.10** in 3:7 CD_3CN-$CDCl_3$, b) R.**2.10** in 4:6 CD_3CN-$CDCl_3$, c) R.**2.9** in 3:7 CD_3CN-$CDCl_3$, d) R.**2.9** in 4:6 CD_3CN-$CDCl_3$ upon addition of the anions.

Table 2.1: Anion association constants (K_a/M^{-1}) for Rotaxanes **2.9** and **2.10** in the presence of 1 eq. of $LiClO_4$ in $CD_3CN/CDCl_3$ (v/v) solvent mixtures.[a]

Anion	Cation	**2.9**	**2.10**	**2.9**	**2.10**
		3:7 $CD_3CN/CDCl_3$		4:6 $CD_3CN/CDCl_3$	
Cl^-	Li^+	$>10^4$	$>10^4$	$>10^4$	5081(406)
Br^-	Li^+	9291(929)	7496(750)	2144(64)	2480(99)
I^-	Li^+	1408(42)	1117(33)	[b]	[b]

[a] K_a values were calculated using Bindfit software using 1:1 binding model.[228] Absolute errors are in brackets. All anions were added as their TBA salts. [Receptor]=1mM, T=298K. [b] ^1H NMR perturbations were too small (<0.05ppm) implying weak/no binding

Attention was then given to investigating the ion-pair binding properties of the non-interlocked heteroditopic macrocycle **2.6**. To this end, analogous ^{1}H NMR titration experiments were conducted by the initial addition of one equivalent of $LiClO_4$ to macrocycle **2.6**, in 4:6 $CD_3CN/CDCl_3$ solvent system. As shown in Figure 2.8, addition of $LiClO_4$ to the macrocycle resulted perturbations in protons H_9 and H_{10}, suggesting Li^+ coordination to the pyridyl motif. Subsequent addition of TBA halide salts caused significant downfield shifts in the internal benzene proton H_1 and amide protons H_3 indicating anion binding through amide HB donors.

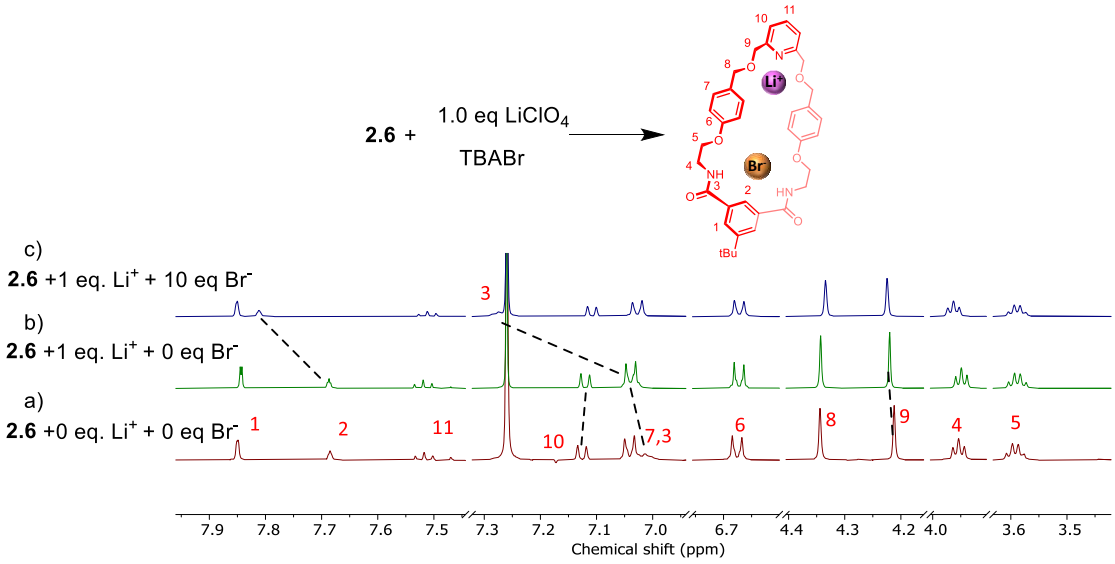

Figure 2.8: Superimposed ^{1}H NMR spectra in 4:6, CD_3CN-$CDCl_3$, of a) Macrocycle **2.6**, b) Macrocycle **2.6** in the presence of 1 eq. of $LiClO_4$, c) Macrocycle **2.6** with further addition of 10 eq. of TBABr.

Bindfit analysis of chemical shift perturbations of protons H_2 determined 1:1 host-guest association constants for halide anions (Table 2.2). Macrocycle **2.6** exhibited significantly lower binding constant values for lithium halides in comparison to rotaxanes **2.9** and **2.10** (for TBACl: $K_a(Li^+$-**2.9**$)$ / $K_a(Li^+$-**2.6**$)$ = 35, for TBABr: $K_a(Li^+$-**2.9**$)$ / $K_a(Li^+$-**2.6**$)$ = 5). This can be attributed to a combination of the respective rotaxane's additional triazole axle guest binding sites and preorganised three-dimensional binding cavity with limited conformational

freedom which aids the process of binding of guests with a reduced entropic penalty. Overall this emphasises the importance of the mechanical bond effect as an efficient strategy for enhanced ion-pair recognition.

Table 2.2: Anion association constants (K_a/M^{-1}) for macrocycles **2.6** in the presence of 1 eq. of $LiClO_4$ in 4:6 $CD_3CN/CDCl_3$ solvent mixtures.[a]

Anion	Cation	**2.6**
Cl^-	Li^+	289(20)
Br^-	Li^+	439(22)
I^-	Li^+	[b]

[a] K_a values were calculated using Bindfit software using 1:1 binding model.[228] Absolute errors are in brackets. All anions were added as their TBA salts. [Receptor]=1mM, T=298K. [b] ^1H NMR perturbations were too small (<0.05ppm) to accurately quantify K_a

2.3.2.2. *Alkali metal cation binding studies of the [2]rotaxane*

The alkali metal cation binding properties of rotaxane **2.9**, were investigated by ^1H NMR titration experiments in 3:7 $CD_3CN/CDCl_3$ solvent mixtures (Figure 2.9). $LiClO_4$ was used as the Li^+ cation source. However, due to the poor solubility of $NaClO_4$ at the required concentration of (50 mM) the sodium salt tetrakis[3,5-bis(trifluoromethyl)phenyl]borate (NaBArF) was used instead. As shown in Figure 2.9a, addition of NaBArF and $LiClO_4$ resulted in similar ^1H NMR perturbations, suggesting that the cations are bound to rotaxane **2.9** in a similar coordination mode. Importantly, the addition of NaBArF and, as noted above $LiClO_4$, led only to minor perturbations in the proton signals associated with the anion binding site (H_2, H_4, H_5), verifying that $BArF^-$ and ClO_4^- serve as non-coordinating counterions. The cation association constants were calculated by fitting the changes in the chemical shifts of H_e and H_9 protons to a 1:1 host-guest stoichiometric binding model using Bindfit.[228,229] Table 2.1 reveals Li^+ binding by **2.9** to be more than 4-fold higher than Na^+ binding, which is attributed

to the higher charge density of Li^+ as well as the size complementarity of Li^+ to the rotaxane's cation binding site.

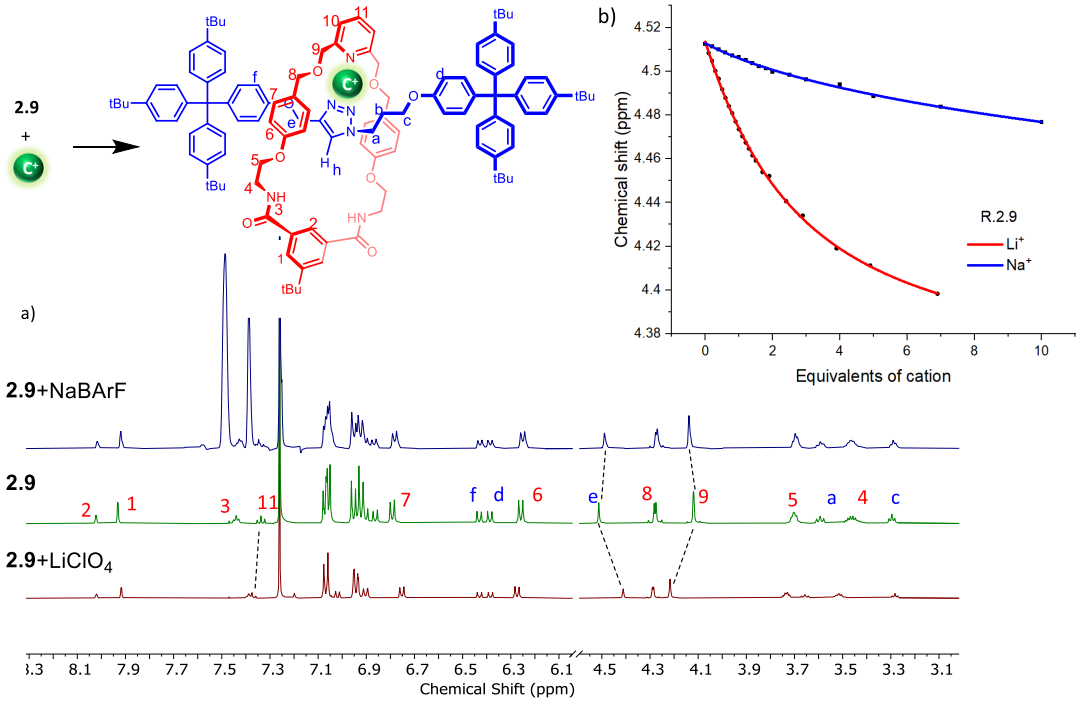

Figure 2.9: Cation binding studies with rotaxane **2.9**: a) Superimposed ^{1}H NMR spectra in 3:7, CD_3CN-$CDCl_3$: (bottom) Rotaxane **2.9** in the presence of 5 eq. of $LiClO_4$,* Rotaxane **2.9**, (top) Rotaxane **2.9** in the presence of 5 eq. of NaBArF , b) Binding isotherms showing changes in chemical shifts of proton H_e upon addition of the cation.* Spectra were recorded only until the addition of 7 eq. of $LiClO_4$ as rotaxane-Li^+ complex was observed to precipitate with subsequent addition of cation.

Table 2.3: Cation association constants (K_a/M^{-1}) for rotaxane **2.9** in 3 :7 $CD_3CN/CDCl_3$ (v/v) solvent mixtures.[a]

Cation	K_a (M^{-1})
Li^+	312 (3)
Na^+	69 (1)

[a] K_a values are calculated using Bindfit software, 1:1 host-guest binding model. Absolute errors are in brackets. Li^+ was added as the $LiClO_4$ salt and Na^+ as the NaBArF salt. All anions were added as their TBA salts. [Receptor]=1mM, T=298K.

The lithium cation binding association constant determined for rotaxane **2.9**, can be used to estimate the amount of Li^+ bound to the rotaxane in the presence of 1 eq. of $LiClO_4$. Details of the calculation are given the appendix A. According to calculations, when 1 eq. of $LiClO_4$ is added to a 3:7 CD_3CN-$CDCl_3$ solution of 1 mM **2.9**, ca.20% of the rotaxane is bound to Li^+. Hence the apparent halide anion binding constants reported in Table 2.2 clearly underestimate the strength of halide recognition that would result from the rotaxane quantitatively binding the lithium cation.

Attention then turned to investigate the alkali metal chloride ion-pair binding selectivity of rotaxane **2.9**. To this end, ^1H NMR titration studies were conducted by adding increasing amounts of TBACl to Na^+ and K^+ precomplexed **2.9** (Na^+-**2.9** / K^+-**2.9**) in 4:6 $CD_3CN/CDCl_3$. $NaClO_4$ and $KClO_4$ were soluble at the required concentrations (1 mM) and were used as Na^+ and K^+ salts respectively. Interestingly, ^1H NMR spectra showed no perturbations upon adding TBACl indicative of no binding of NaCl or KCl, suggesting that rotaxane **2.9** is highly selective for LiCl.

2.3.2.3. *Anion binding studies in the presence of HBF_4*

To our surprise, the lithium precomplexed XB rotaxane Li^+-**2.10** displayed lower halide binding constants compared to the HB rotaxane Li^+-**2.9**, even though monotopic XB anion receptors are known to exhibit more potent halide binding than HB receptor analogues.[41]

To further investigate these observations, ion-pair titrations were performed by precomplexing rotaxanes **2.9**/**2.10** with the smaller H^+ cation, using HBF_4 as the protic acid source. As shown in Figure 2.10 addition of 1 eq. of HBF_4 in 4:6 $CD_3CN/CDCl_3$ caused significant downfield shifts in the respective rotaxane's macrocyclic component protons (H_{11}, H_{10}, H_8, and H_9) indicative of the expected protonation of the pyridyl motif, while the subsequent addition of TBA halide salts led to shifts in macrocycle aryl and amide protons H_2 and H_3, as well as axle protons H_h, indicating the involvement of both the axle and the

macrocycle in halide binding. The anion binding constants of rotaxane **2.9** and **2.10** in the presence of 1 eq. of HBF_4 were calculated by monitoring the chemical shifts of protons H_2 and H_3 using Bindfit software (Table 2.4).[228,229]

Interestingly, the protonated XB iodotriazole axle containing rotaxane H^+-**2.10** exhibited significantly higher halide binding constant values than the protic triazole axle rotaxane analogue H^+-**2.9**, representing a reversal of the trend observed with lithium halides salts. These observations are explored in detail through a DFT analysis of the Li^+ and H^+ binding modes in the rotaxanes (See Section 2.3.4).

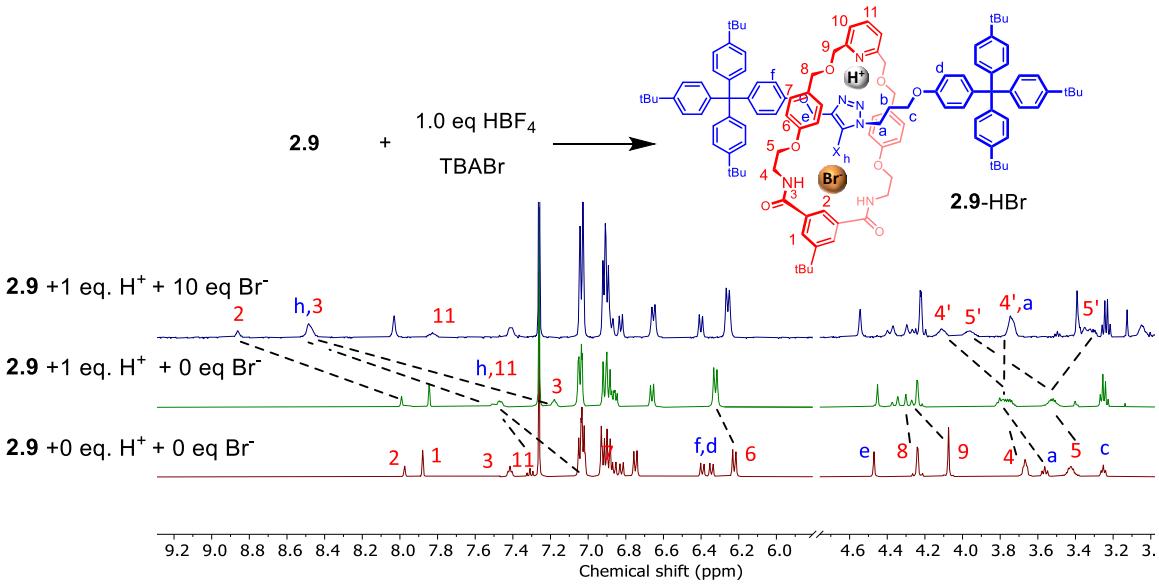

Figure 2.10: Superimposed ^1H NMR spectra in 4:6, CD_3CN-$CDCl_3$ (v/v), of (bottom to top) Rotaxane **2.9**, Rotaxane **2.9** in the presence of 1 eq. of HBF_4, Rotaxane **2.9** with further addition of 10 eq. of TBABr.

Table 2.4: Anion association constants (K_a/M^{-1}) for Rotaxanes **2.9** and **2.10** in the presence of 1 equivalent of HBF_4 in $CD_3CN/CDCl_3$ (v/v) solvent mixtures. [a]

Anion	Cation	R.**2.9**	R.**2.10**
		4:6 $CD_3CN/CDCl_3$	
Cl^-	H^+	8011(560)	$>10^4$
Br^-	H^+	3291(66)	$>10^4$
I^-	H^+	725(14)	3712(260)

[a] K_a values were calculated using Bindfit software using 1:1 binding model.[228] Absolute errors are in brackets. All anions were added as their TBA salts. [Receptor]=1mM, T=298K.

2.3.3. Solid-state structure analysis†

Further evidence for the axle-separated ion-pair binding mode in the rotaxanes was obtained via solid-state characterisation of rotaxane **2.10** co-crystallised with H^+ and Cl^-. Crystals suitable for single crystal X-ray diffraction structural analysis were obtained by slow evaporation of a $CH_3CN/CHCl_3$ solution containing rotaxane **2.10**, HBF_4, and TBACl. The structure (Figure 2.11a) revealed a 1:1:1 host-cation-anion complex. The macrocycle pyridinium H^+ cation forms interactions with the axle iodotriazole nitrogen atom, which is similar to lithium cation binding suggested by the ^1H NMR titrations (Section 2.3.2.2). As a result, the axle iodotriazole motif adopts a conformation in which the XB donor is directed towards the isophthalamide motif of the macrocycle. The Cl^- anion is located within this binding cavity, where it forms HB interactions with the two amide groups of the macrocycle and strong axle iodotriazole XB-anion interactions as evidenced from a C-I···Cl bond angle of 173° and the short I-Cl distance, which is 79% of the summation of ionic radii of chloride ion and iodine van der Waals radii.

† X-ray crystallography data was collected and the solid state structure determined by Zongyao Zhang

Single crystals of macrocycle **2.6** for suitable for XRD analysis were obtained by slow evaporation of a $CH_3CN/CHCl_3$ solution of the macrocycle in the presence of $LiClO_4$ (Figure 2.11b). Multiple attempts to crystalise the macrocycle with guest ions were unsuccessful, presumably due to poor guest binding properties of the macrocycle. The macrocycle ether oxygen atoms proximal to pyridine are directed away from the macrocycle cavity, in contrast to the configuration observed for H.Cl bound **2.10** where one of the ether oxygen atoms is directed at the cation binding cavity to interact with H^+ cation.

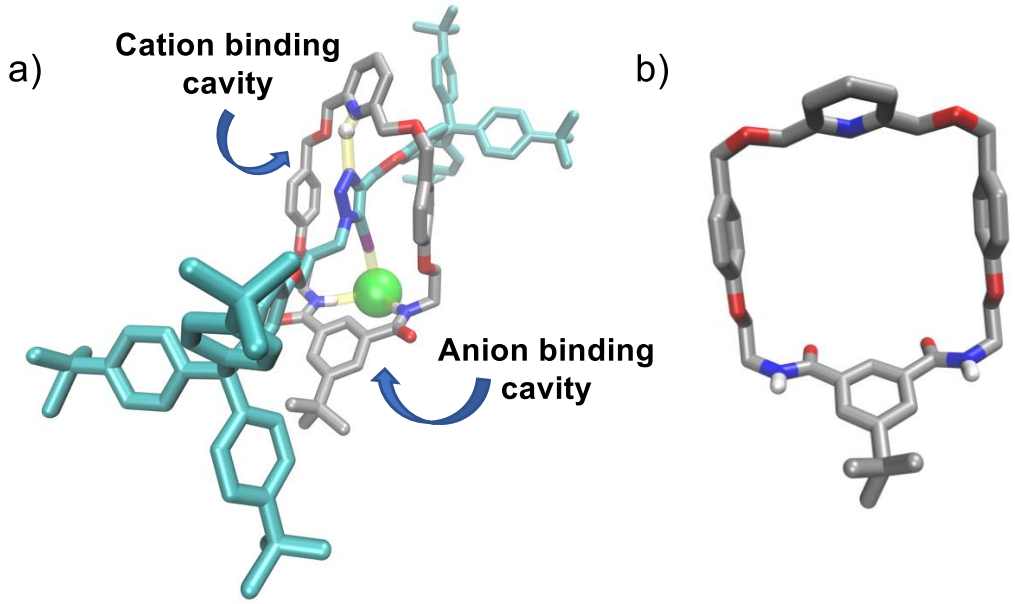

Figure 2.11: Crystal structures of a) axle separated H.Cl bound **R.2.10** b) **M.2.6**. Colour code of atoms: O-red, N-blue, I-purple, Cl-green, H-white, C(axle) - teal C(MC)-gray. Non-covalent host-guest interactions are shown in yellow

2.3.4. DFT calculations[‡]

Density Functional Theory (DFT) studies were performed in the gas phase using Gaussian 16[230] to further investigate the ion-pair binding properties of rotaxanes **2.9, 2.10**, and macrocycle **2.6**. Initial input structures based on the crystal structures of rotaxane **2.10** and macrocycle **2.6** were optimised at the B3LYP level of theory[231,232] using aug-cc-pVTZ basis set for chlorine atoms, aug-cc-pVTZ-PP basis set for larger halide atoms, and 6-31g* basis for the other atoms.[233–235] Computationally expensive terminal terphenyl stopper groups were replaced by methyl groups for ease of calculations. Counterpoise correction was invoked to correct for the basis set superposition error.[236,237]

Geometry optimised structures of ion-pair bound rotaxane **2.10** are shown in Figure 2.12a-c. Optimised structures show that both Li^+ and H^+ reside in the rotaxane's cation binding site. Li^+ interacts with the triazole nitrogen and oxygen in the axle, and pyridyl nitrogen and the adjacent oxygen on the macrocycle. H^+ only interacts with the axle triazole nitrogen and macrocycle pyridyl nitrogen, as evident by both crystallography data and DFT calculations (Figure 2.11-a and Figure 2.12-c). The binding of H^+ preorganises the axle triazole donor atom to enable the guest anion to interact with the rotaxane via both the amide HB donors of the macrocycle and the triazole XB donor of the axle. This is reflected in the DFT-optimised structure, which features a linear C-I$\cdots$$Cl^-$ interaction (178°) with an I$\cdots$$Cl^-$ distance equal to 69% of the sum of iodine van der Waals radius and Cl^- ionic radius (Figure 2.12-c). The DFT analysis is supported by the results of the ^{1}H NMR binding studies, wherein the halide binding constants of protonated rotaxane **2.10** are significantly higher than that of lithium-bound rotaxane **2.10**.

[‡] DFT calculations were performed in collaboration with Dilhan Manawadu

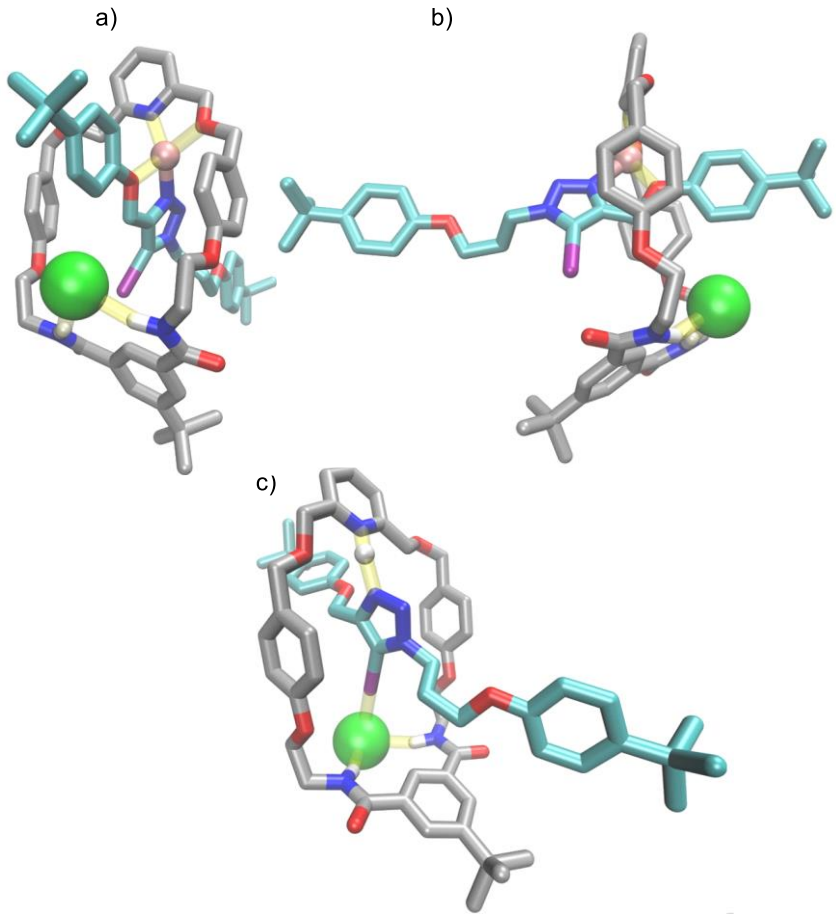

Figure 2.12: DFT optimised structures of ion-pair bound [2]rotaxanes **2.10**; a) Front view of LiCl bound rotaxane, b) Side view of LiCl bound rotaxane, c) H.Cl bound rotaxane, Colour code of atoms: O-red, N-blue, I-purple, Cl-green, Li-pink, C(axle) – teal, C(MC)- grey. Non-covalent host-guest interactions are shown by yellow

A corresponding analysis of rotaxane **2.9** (Figure 2.13a-c) shows that both Li^+ and H^+ bind to **2.9** in a similar manner to **2.10**. However, unlike in **2.10**, the HB donor atom of the axle in **2.9** is capable of participating in anion binding in the presence of both cations. This is evident from the combined analysis of DFT optimised lithium halide bound rotaxanes Figure 2.13a/b and the ^{1}H NMR halide anion binding studies of the Li^+ precomplexed rotaxane **2.9** (see Section 2.3.2.1) which showed superior anion binding properties compared to the XB analogue **2.10**. In addition, as depicted in Figure 2.14, addition of halide anions to Li^+-**2.9** caused a downfeild shift of proto triazole H_h, suggesting HB interactions with the anion. This contrasting behavior of the proto triazole of Li-**2.9** from Li-**2.10** is due in part to the sterically

less bulky HB donor atom, as well as the less stringent requirement for a linear donor-acceptor binding geometry of HB interactions relative to XB. This enables the HB donor in the axle of rotaxane **2.9** to participate in anion binding despite the sub-optimal non-linear geometry. Therefore, in contrast to rotaxane **2.10**, the triazole HB interaction is realised in both Li^+ and H^+ bound rotaxane **2.9**. This is reflected in the experimentally-determined HX and LiX (X = Cl, Br, I) association constants of **2.9**, which do not differ by as much as those of **2.10** (Table 2.1 and Table 2.4).

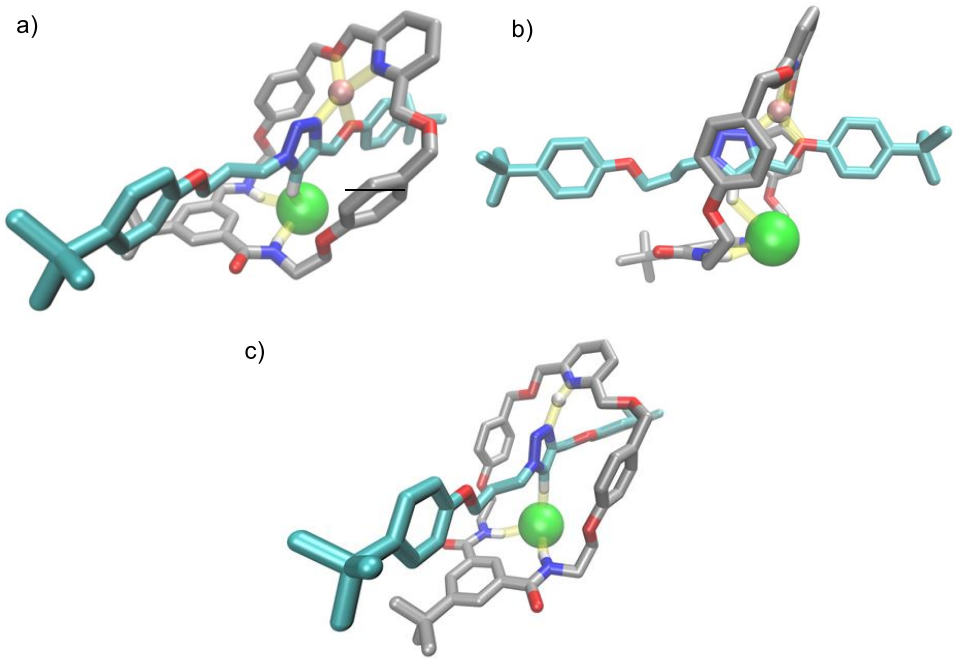

Figure 2.13: DFT optimised structures of ion-pair bound [2]rotaxane **2.9:** a) Front view of LiCl bound rotaxane **2.9**, b) side view of LiCl bound rotaxane **2.9**, c) HCl bound rotaxane **2.9**. Colour code of atoms: O-red, N-blue, I-purple, Cl-green, Li-pink, C(axle) – teal, C(MC)- gray. Non-covalent host-guest interactions are shown by yellow

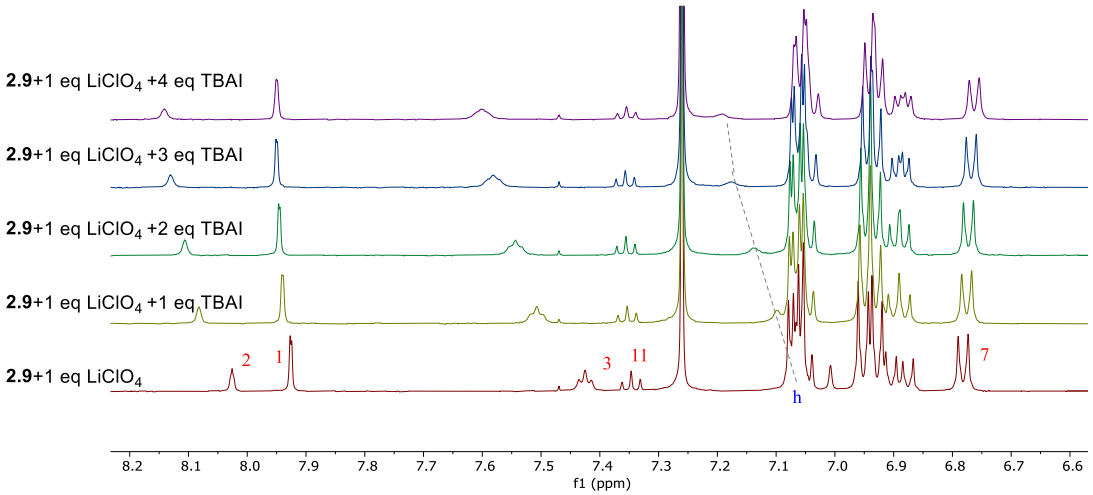

Figure 2.14: Superimposed ^{1}H NMR spectra of Li^{+}-**2.9** upon addition of increasing equivelents of TBAI in 3:7 $CD_3CN/CDCl_3$. Dotted lines indicate downfield shifts of triazole proton H_h suggesting HB interactions with the I^{-}.

Experimental data revealed cation binding to significantly increase the anion association constants of rotaxanes **2.9** and **2.10**. The electrostatic contribution to this cooperative binding is quantified via the calculation of electrostatic potential maps of neutral and cation-bound rotaxanes. The isoelectronic potential energy surfaces of rotaxanes **2.9** and **2.10** in both neutral and cationic forms are presented in Figure 2.15. The binding of Li^{+} and H^{+} increases the electrostatic potential of the axle HB donor of rotaxane **2.9** from 186 kcal/mol to 252 kcal/mol and 249 kcal/mol. A similar increase from 227 kcal/mol to 284 kcal/mol and 288 kcal/mol is observed for the axle XB donor of rotaxane **2.10**. For both rotaxanes, the binding of the cations causes a significant polarisation of the HB/XB interaction.

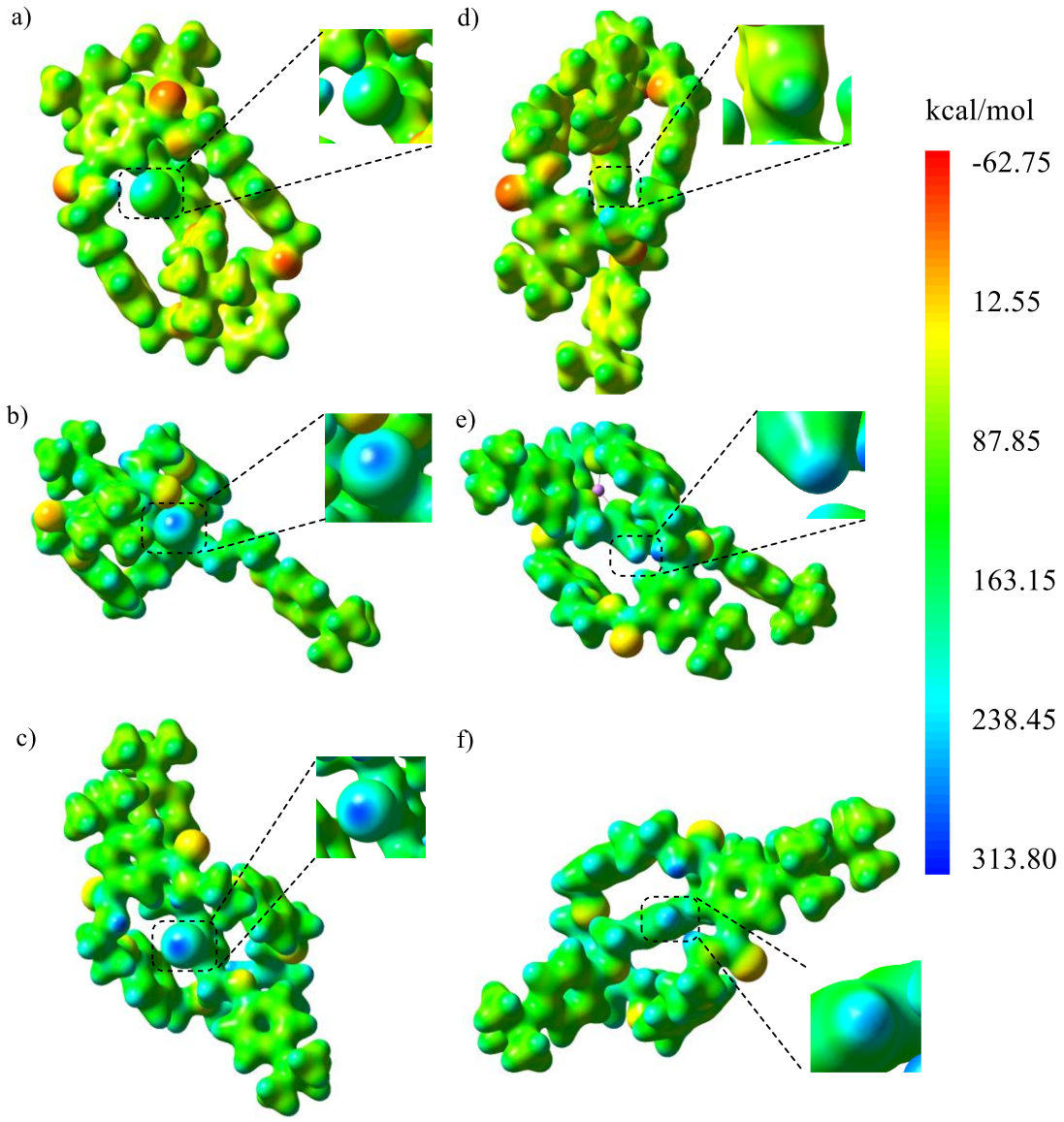

Figure 2.15: Electrostatic potential maps of a) rotaxane **2.10**, b) Li^+ complexed rotaxane **2.10,** c) H^+ rotaxane **2.10**, d) rotaxane **2.9**, e) Li^+ complexed rotaxane **2.9**, f) H^+ rotaxane **2.9**. Triazole XB/HB donors of rotaxane **2.9** and **2.10** are magnified for clarity. Colour coded isosurface values are given in kcal/mol.

2.3.5. Preliminary Solid-liquid extraction (SLE) studies

Encouraged by the strong cooperative ion-pair binding of heteroditopic [2]rotaxanes, preliminary solid-liquid extraction (SLE) studies were conducted to investigate the ability of **2.9** and **2.10** receptors to solubilise lithium halide salts in organic solvents. In a typical SLE experiment, an excess of solid lithium halide salt was added to a solution of the rotaxane in

$CDCl_3$, the mixture was sonicated for 30 minutes, and the ^1H NMR spectra were recorded. Pre- and post-extraction ^1H NMR spectra are depicted in Figure 2.16. No significant chemical shifts were observed upon the addition of LiCl to both rotaxanes, most likely due to the high lattice enthalpy of LiCl. In contrast, rotaxane **2.9** and **2.10** samples with LiBr and LiI resulted in significant proton shifts in both the respective rotaxane's cation (H_e, H_9, H_{11}) and anion (H_2, H_3, H_4, H_5) binding sites depicting the potential of neutral heteroditopic MIMs to act as solid-liquid extractants for lithium halide salts.

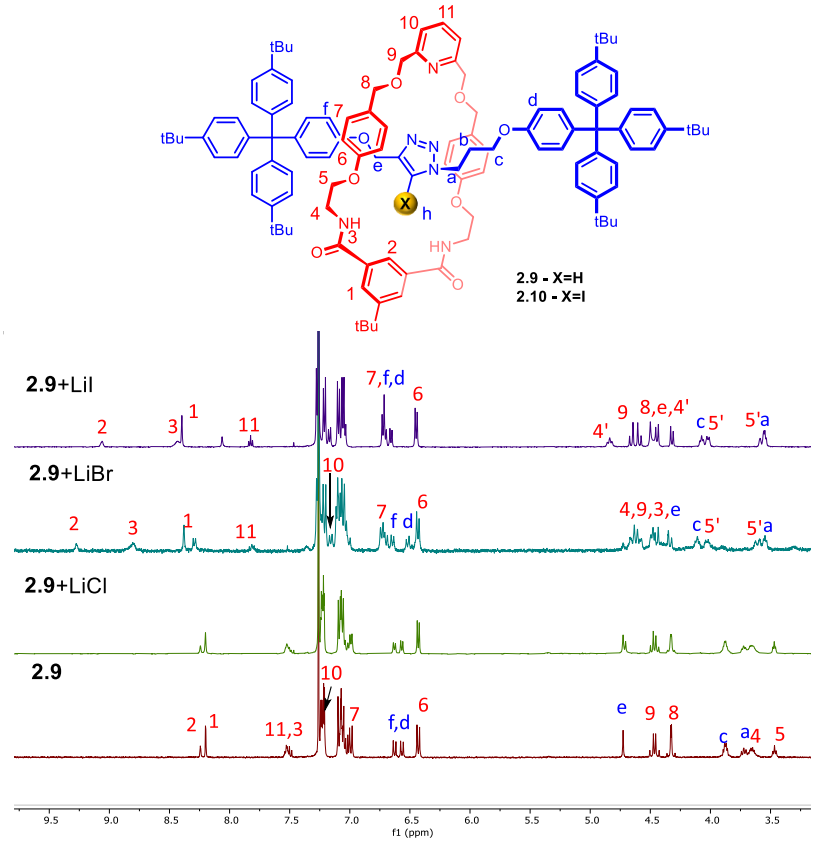

Figure 2.16: Comparative pre- and post- extraction ^1H NMR spectra of Rotaxane **2.9** with excess solid LiCl, LiBr and LiI (500 MHz, 298 K, 9:1 $CDCl_3$:CD_3CN).

2.4. Ion-pair mediated macrocycle translocation[§]

The potential binding properties in neutral heteroditopic rotaxane MIM receptors are particularly attractive to exploit for designing stimuli-responsive dynamic molecular shuttle systems, wherein intercomponent motion can be effectively controlled via cooperative ion-pair recognition. Conceivably, the reliance on ion-pair binding compared to single ion binding will improve the fidelity of molecular motion, as it provides an additional experimental variable to fine-tune dynamics. MIMs with controlled molecular motion have been employed in a range of applications, including sensing,[238–241] catalysis,[242–244] drug delivery[245–247], and advanced materials.[248–253] The dynamic properties of these MIMs are controlled mainly by light[254], redox-based stimuli[255–258] and chemical stimuli.[259,260] Most of the reported chemical stimuli are either based on anions[238,239,261] or cations.[262–264] However, to the best of our knowledge, the use of ion-pair binding to control the translational motion of a macrocycle along the axle of a rotaxane is unprecedented.

2.4.1. Design, synthesis and characterisation of the two station rotaxane and analogous one station rotaxane

The promising lithium halide binding properties of rotaxanes **2.9** and **2.10** prompted an investigation into the use of lithium halide salts to direct molecular shuttling in a two-station [2]rotaxane. For this purpose, a two-station rotaxane analogue of **2.9** rotaxane, with an axle comprising a naphthalene diimide (NDI) station in addition to the triazole station, was designed (Figure 2.17). It was anticipated that, in the free rotaxane, the macrocycle would preferentially reside at the NDI station due to the formation of stabilising aromatic donor-acceptor charge-transfer interactions between the electron-rich aromatic units on the macrocycle and the electron-deficient NDI system.[240] Upon addition of an ion-pair the

[§] The research results discussed in this section were undertaken in collaboration with fellow graduate student, Hui Min Tay

macrocycle was expected to translocate to the triazole station due to formation of concerted interactions by the axle and the macrocycle with guest ions, as previously demonstrated in rotaxane **2.9** (Figure 2.17). Preliminary studies, conducted with graduate student Hui Min Tay, suggested that macrocycle **2.6** preferentially resides at the triazole station instead of the NDI station of the two station rotaxane (See Appendix A). This could presumably be because of steric effects of the macrocycle and the inability of 4-(alkoxymethyl)phenol units in **2.6** to form strong aromatic charge-transfer interactions with the NDI unit. Therefore, an electron-rich hydroquinone-based macrocycle **2.12**, which possesses cation and anion binding sites analogous to **2.6**, was used instead.

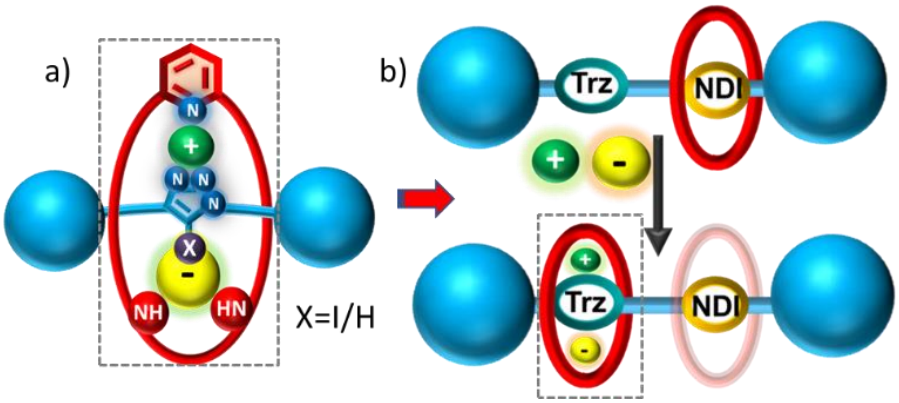

Figure 2.17: Schematic representation of the: a) Heteroditopic [2]rotaxane in **2.9** and **2.10**, b) ion-pair induced translational motion of the macrocycle in two station rotaxane. NDI-naphthalene diimide station, trz-triazole station, (-)-anion, (+)-cation.

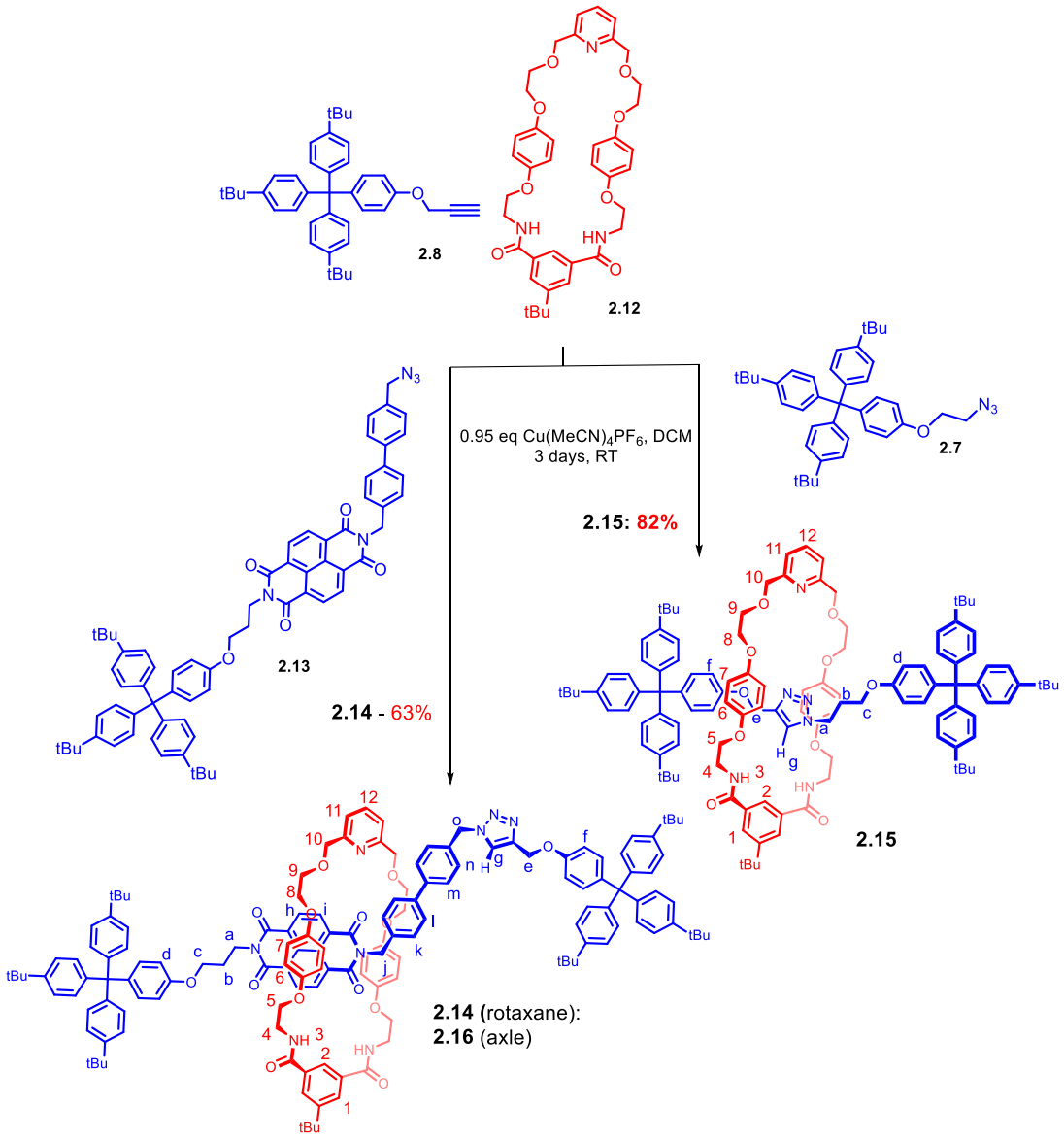

Scheme 2.3: Synthesis of two station [2]rotaxane **2.16** and the analogous one station [2]rotaxane **2.15**

The synthesis of the two station [2]rotaxane is summarised in Scheme 2.3. Following the general CuAAC-AMT method, macrocycle **2.12**[265] was initially precomplexed with 0.95 eq. of $[Cu(CH_3CN)_4]PF_6$ and subsequently reacted with five equivalents each of axle precursors **2.13**[240] and **2.8**[165] to afford the target two station [2]rotaxane **2.14** in 63% yield (relates to the equivalence of the macrocycle added) after preparative TLC purification. The two-station axle **2.16** was isolated as a by-product in 55% yield (relates to equivalence of axle precursor

added). Following the same CuAAC-AMT procedure, using the azide stopper precursor **2.7**,[165] the analogous one station [2]rotaxane **2.15** was synthesised in 82% yield. Both rotaxanes were characterised by ^{1}H NMR and ^{13}C NMR spectroscopy and high-resolution electrospray ionisation (ESI) mass spectrometry. Evidence for the interlocked nature of the [2]rotaxanes was provided by inspection of their ^{1}H NMR spectra relative to their non-interlocked macrocycle and axle components. As shown in Figure 2.18 and Figure 2.19, ^{1}H NMR spectra of both rotaxanes depict characteristic upfield perturbations of aryl proton peaks (H_6, H_7) relative to their free macrocycle, presumably due to aromatic donor-acceptor π-π stacking interactions between the macrocycle and the axle. Notable upfield shifts were also observed for the internal benzene proton H_2 and amide protons H_3 of both rotaxanes, likely resulting from HB interactions with the axle. Further evidence for the interlocked nature of both rotaxanes was provided by ^{1}H-^{1}H ROESY NMR spectroscopy experiments which showed numerous cross peaks arising from through space interactions between axle and macrocyclic components.

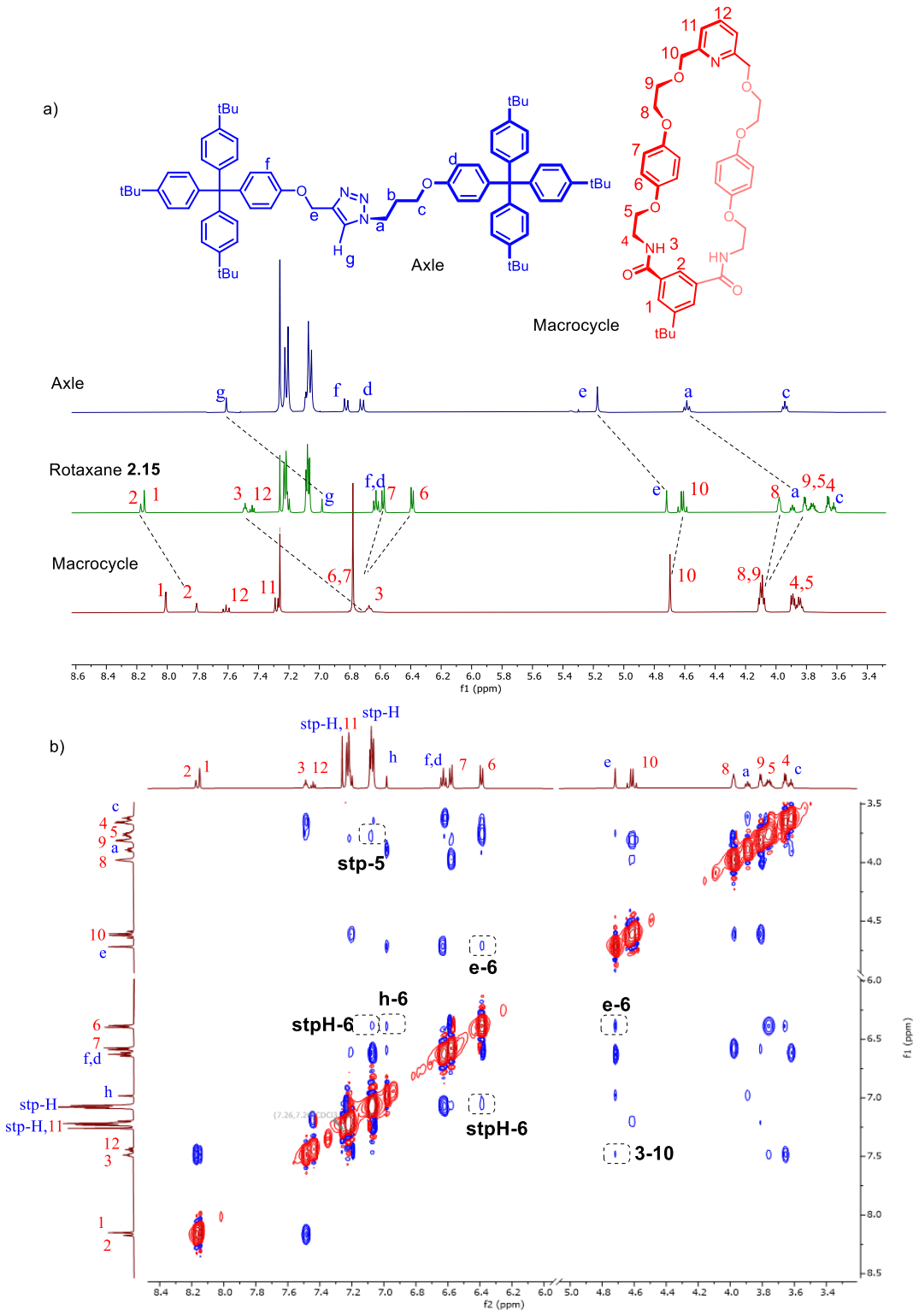

Figure 2.18: a) Comparison of ^{1}H NMR spectra of axle (top), rotaxane **2.15** (middle) and macrocycle (bottom) ($CDCl_3$, 500 MHz, 298 K), b) ^{1}H-^{1}H ROESY NMR spectrum of Rotaxane **2.15** ($CDCl_3$, 500 MHz, 298 K). Selected cross-peaks arising from through-space interactions of the interlocked macrocycle and axle components of the rotaxane are circled. Stopper sp^2 protons are denoted as 'stp-H'.

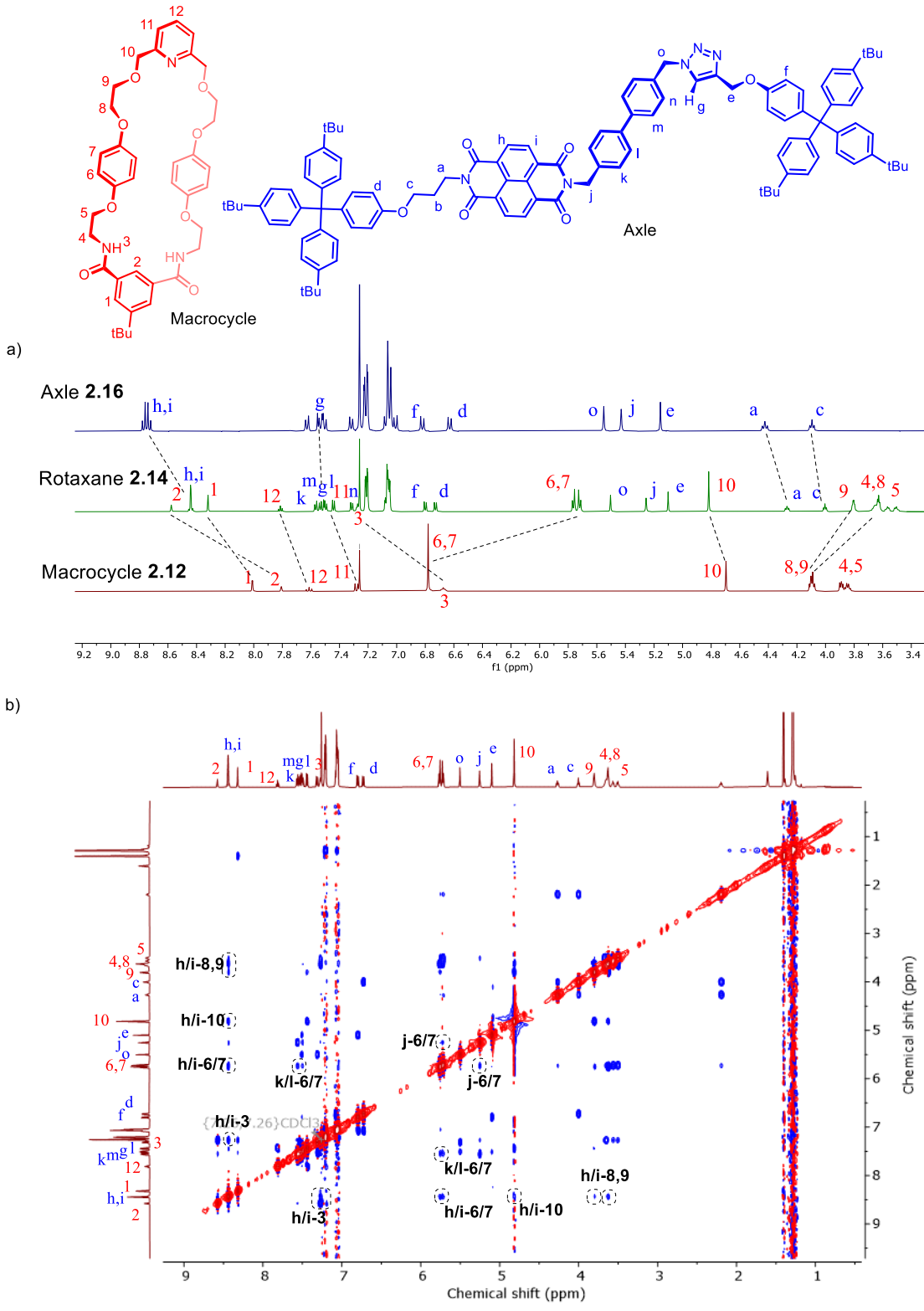

Figure 2.19: a) Comparison of ^{1}H NMR spectra of axle **2.16** (top), rotaxane **2.14** (middle) and macrocycle **2.12** (bottom) ($CDCl_3$, 500 MHz, 298 K), b) ^{1}H-^{1}H ROESY NMR spectrum of Rotaxane **2.14** ($CDCl_3$, 500 MHz, 298 K). Selected cross-peaks arising from through-space interactions of the interlocked macrocycle and axle components of the rotaxane are circled. Stopper sp^2 protons are denoted as 'stp-H'

2.4.2. ^{1}H NMR spectroscopic studies of ion-pair induced macrocycle shuttling

2.4.2.1. *^{1}H NMR spectroscopic studies of the two station rotaxane in the absence of guest ions*

Following the successful synthesis of the two station [2]rotaxane **2.14**, 1D and 2D ^{1}H NMR spectroscopy techniques were used to determine the percentage occupancies of the macrocycle at the respective axle NDI and the triazole stations. As shown in Figure 2.19, a qualitative comparison of the ^{1}H NMR spectra of **2.14** and axle **2.16** is consistent with the macrocycle residing at the NDI station of the two station [2]rotaxane **2.14**. The NDI protons $H_{i/h}$ in **2.14** have undergone significant upfield shifts relative to the analogous protons in axle **2.16**, indicating the formation of aromatic donor-acceptor interactions between the NDI and the macrocycle hydroquinone groups.[240] In contrast, only small upfield shifts were observed in protons H_g and H_e, suggesting that the chemical environment near the triazole station remains similar in the rotaxane and axle. Further evidence for this co-conformation was provided by ^{1}H-^{1}H ROESY NMR spectra (Figure 2.19-b), which contain prominent cross-peaks between NDI protons $H_{i/h}$ and several macrocycle protons including the hydroquinone protons $H_{6/7}$. In contrast, no cross-peaks were observed between the macrocycle protons and the axle protons near the triazole station (H_o, H_g, H_e).

Attempts were then directed to quantify the percentage occupancy of the macrocycle at the triazole station. For this purpose, comparative ^{1}H NMR studies of the two-station rotaxane **2.14** and analogous one-station rotaxane **2.15**, as well as two-station axle **2.16**, were undertaken in the mixed solvent system 3:7 $CD_3CN/CDCl_3$. It was assumed that rotaxane **2.15** represents the environment at the triazole station when it is fully occupied by the macrocycle, while **2.16** corresponds to the triazole station in the absence of the macrocycle. Hence, **2.15** and **2.16** were therefore treated as models for the two extremes of triazole station occupancy (100% for **2.15**; 0% for **2.16**). Assuming that the chemical shifts of the

protons near the triazole station in **2.14** scale linearly with station occupancy, comparing these peaks to the analogous signals in **2.15** and **2.16** provides an estimate of the triazole station occupancy. Further details of the calculations are described in the appendix A. By monitoring the chemical shifts of the proton, H_e the percentage occupancy of the triazole station was found to be only 7%, in the 3:7 CD_3CN:$CDCl_3$ solvent system. This indicates that the macrocycle primarily resides at the NDI station, presumably due to strong NDI-hydroquinone charge-transfer interactions.

2.4.2.2. *^{1}H NMR spectroscopic studies upon addition of cation, anion, and ion-pair to two station [2]rotaxane*

The effect of cation, anion and ion-pair binding on the co-conformation of the two station rotaxane **2.14** was investigated by a series of ^{1}H NMR binding studies. Cation binding studies were conducted by the sequential addition of $LiClO_4$ to a solution of **2.14** in 3:7 CD_3CN:$CDCl_3$. Upon addition of $LiClO_4$, proton signals near the pyridyl group of the macrocycle, H_{10} split, and H_{12} shifted progressively upfield, indicating that Li^+ binding occurs as expected, primarily via the pyridyl group of the macrocycle component **2.12** (Figure 2.20). Meanwhile, the two station axle **2.16** contains two potential sites capable of participating in lithium coordination: the triazole nitrogen atoms (established above in the one-station rotaxane **2.9**) as well as the diimide motif present in the NDI station.[266] Hence, due to the competition between the two Li^+ binding sites, Li^+ binding was not expected to significantly bias the macrocycle towards either station. This was also evident by ^{1}H NMR peak perturbations, where the addition of $LiClO_4$ caused protons $H_{h/i}$ of the NDI station to split and undergo small downfield shifts and triazole proton H_g to progressively shift downfield. Correspondingly, the percentage occupancy of the triazole station only marginally increased from 7% to 11% in the presence of 1 eq. of $LiClO_4$. The addition of excess $LiClO_4$ resulted in a minor further increase in triazole

occupancy, which plateaued at 19% after 10 eq. $LiClO_4$ had been added (see appendix A for calculations).

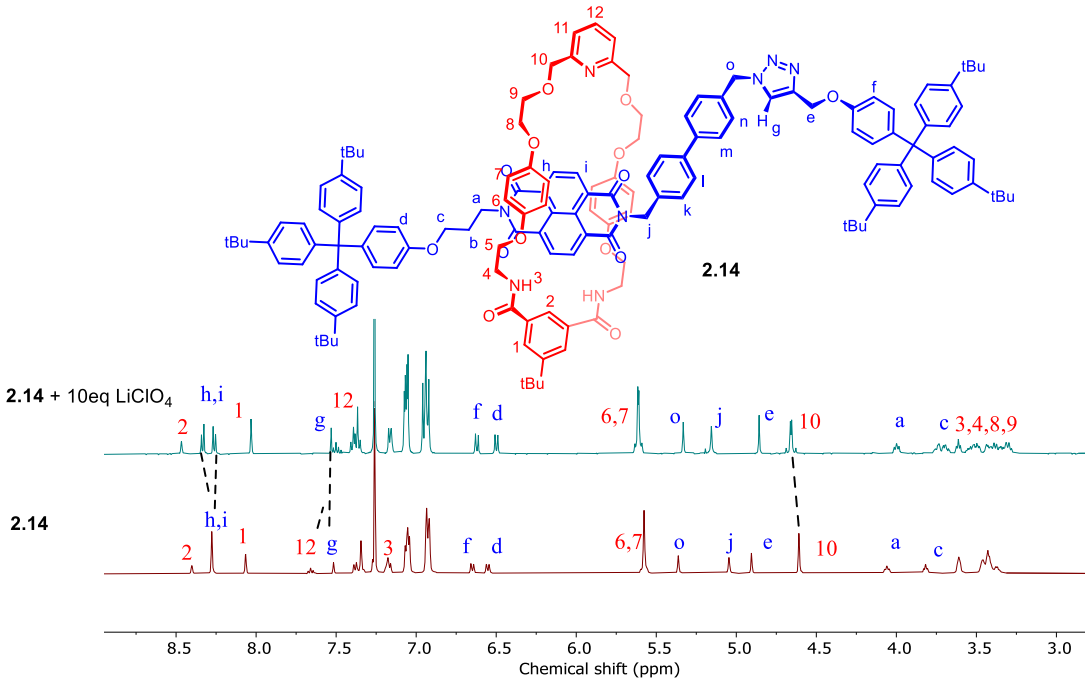

Figure 2.20: Superimposed spectra of two station rotaxane **2.14** and **2.14** in the presence of 10 eq. of $LiClO_4$, (500 MHz, 298 K, 3:7 $CDCl_3$:CD_3CN, [**2.14**] = 1.0 mM)

Attention then turned to investigate the effect of anion binding towards macrocycle translocation. To this end, TBABr was progressively added to rotaxane **2.14,** and the respective ^1H NMR spectra were recorded. Interestingly only negligible changes in the ^1H NMR spectra were observed upon the addition of TBABr, indicating that the neutral rotaxane is incapable of binding Br^- or undergoing macrocyclic shuttling towards the triazole station in the moderately competitive 3:7 $CD_3CN/CDCl_3$ solvent system. This is not surprising as a similar observation was noted with the addition of TBABr to the analogous one station triazole rotaxane **2.15**, indicating no binding of TBABr to rotaxane **2.15** in the same solvent system.

Ion-pair titrations were then conducted wherein **2.14** was first treated with 1.0 eq. of $LiClO_4$, followed by sequential addition of up to 10 eq. of TBABr (Figure 2.22). The addition of TBABr to the Li^+-**2.14** rotaxane resulted in progressive downfield shifts of the macrocycle internal benzene proton H_2 and the amide protons H_3, suggesting that anion binding via HB interactions at the isophthalamide group, as expected. In addition, downfield shifts and broadening of the triazole proton H_g indicate that the triazole participates in anion binding, through HB interactions between H_g and the anion which are enhanced by the presence of the co-bound Li^+ cation. These changes indicate that the anion is convergently bound by HB donors in both the macrocycle and the triazole station of the axle, which is expected to favour translocation of the macrocycle to the triazole station. The percentage occupancy of the triazole station was found to be 19% after addition of 1 eq. TBABr to Li-**2.14** (see appendix-A for detailed calculations), showing that 1 eq. of the ion-pair (LiBr) is capable of altering the macrocycle station preference to a similar degree as a large excess (10 eq.) of the cation alone. Further addition of TBABr led to a progressive increase in the triazole station occupancy, which reached approximately 27% in the presence of 10 eq. TBABr. This represents a three-fold increase of the triazole station occupancy compared to the free rotaxane, highlighting the importance of cooperative ion-pair binding in 'switching on' anion binding, which consequentially induces macrocycle shuttling in **2.14**. The shuttling behaviour of rotaxane **2.14** is therefore akin to the 'AND' logic gate, wherein shuttling from the NDI to the triazole station is augmented in the presence of both Li^+ AND Br^-, while either guest alone results in attenuated (Li^+) or no shuttling (Br^-).

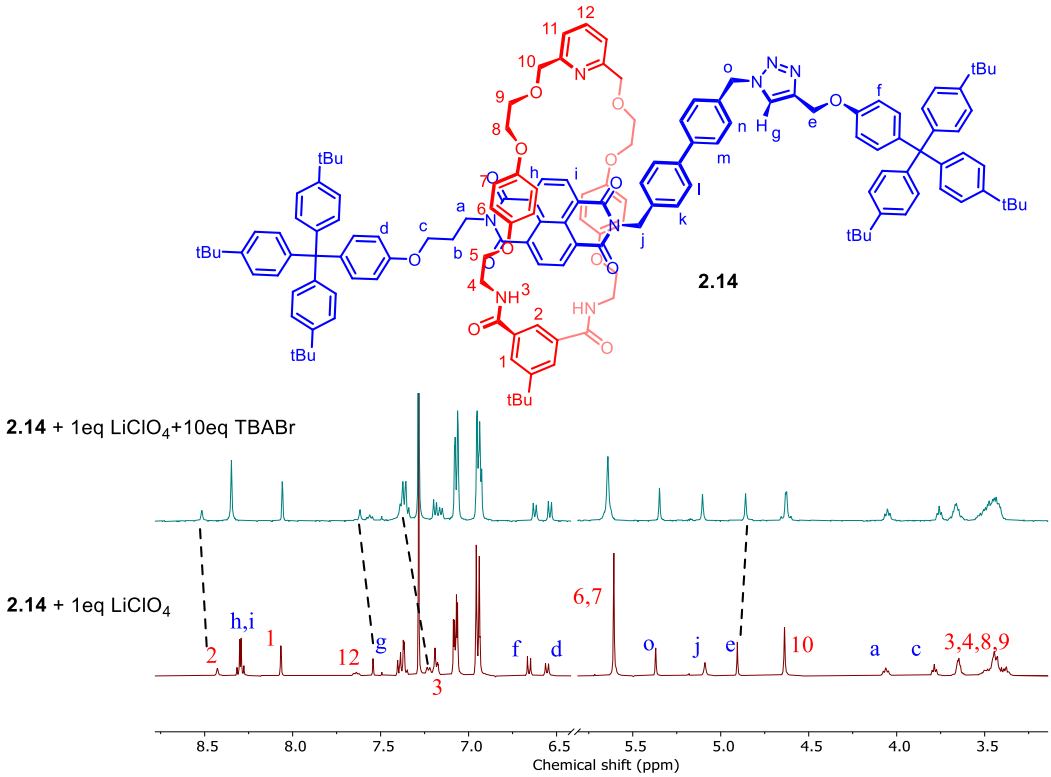

Figure 2.22: Comparison of ^{1}H NMR spectra of lithium precomplexed two station rotaxane **2.14** (Li^{+}-**2.14**) and Li^{+}-**2.14** in the presence of 10 eq. of TBABr (500 MHz, 298 K, 3:7 $CDCl_3$:CD_3CN, [**2.14**] = 1.0 mM).

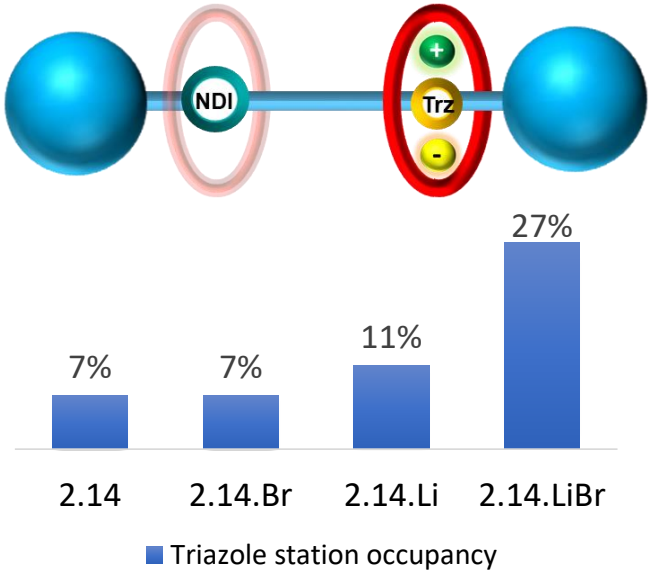

Figure 2.21: Estimated percentage occupancy of the triazole station of rotaxane **2.14** in 3:7 CD_3CN/$CDCl_3$. Columns correspond to **2.14** occupancy: in the absence of guest ions (left), in the presence of 10 eq. TBABr (second from left), in the presence of 1 eq. $LiClO_4$ (second from right), in the presence of 1 eq. $LiClO_4$ and 10 eq. TBABr (right).

2.4.3. Reversibility studies of macrocycle translocation

To investigate the reversibility of the translocation of the macrocycle, the Li^+ and Br^- bound rotaxane **2.14** was washed with D_2O to remove both Li^+ and Br^- guest ions. Importantly, the resulting ^1H NMR spectrum (Figure 2.23d) was identical to the spectrum of the free rotaxane (Figure 2.23a) indicating that the ion-pair induced macrocycle translocation is fully reversible.

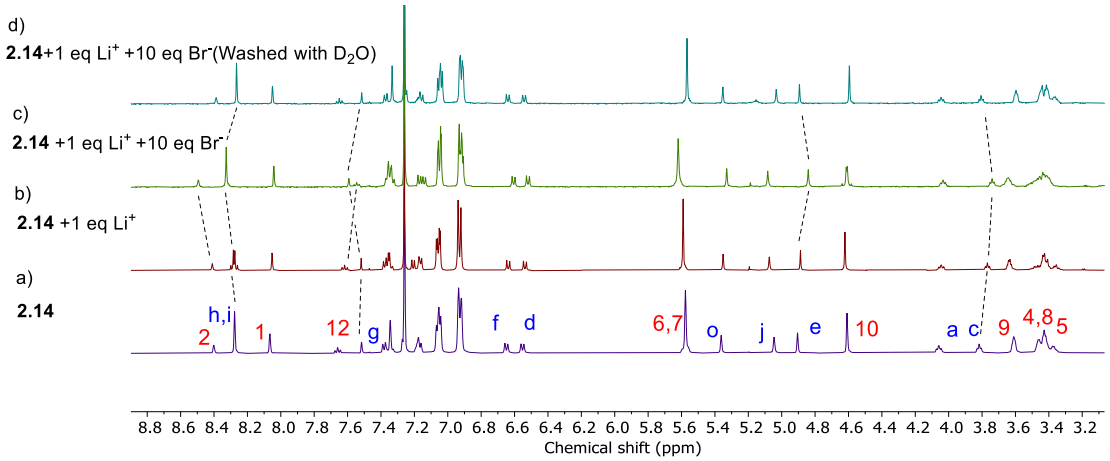

Figure 2.23: ^1H NMR spectra in 3:7 $CD_3CN/CDCl_3$ solvent media; a) rotaxane **2.14**, b) rotaxane **2.14** in the presence of 1 eq. of Li^+, c) Li^+ precomplexed rotaxane **2.14** in the presence of TBABr, d) Li^+ and Br^- bound rotaxane **2.14** after a D_2O wash.

2.4.4. Conclusions and future work

In conclusion, XB and HB heteroditopic rotaxanes **2.9** and **2.10** were synthesised in good yields of 74-77%, and their anion, cation and ion-pair binding properties were investigated using a combination of X-ray crystallography, ^1H NMR titrations, and theoretical modelling. Binding of Li^+ was found to 'switch on' the halide anion binding properties of both rotaxanes. Rotaxane **2.9,** in particular, showed notable selectivity for LiCl with respect to other lithium halides and group I metal chlorides. ^1H NMR titrations and DFT calculations showed the axle iodotriazole XB donor motif of Li^+-**2.10** was sterically inaccessible for anion binding, whereas H^+ protonated precomplexed rotaxanes facilitated XB/HB-anion interactions involving both

macrocycle and axle components. As a result, as evidenced by significantly larger association constant values, XB rotaxane H^+-**2.10** displayed superior halide anion affinities compared to the HB rotaxane H^+-**2.9**, demonstrating the use of sigma-hole interactions to achieve enhanced anion binding.

In a proof-of-concept study, ion-pair binding was exploited for the first time to control the macrocycle shuttling behaviour in a two station NDI-triazole axle containing rotaxane **2.14**. ^{1}H NMR titrations suggested that the addition of Li^+ to **2.14** induced a modest increase in the percentage occupancy of the triazole station by the macrocycle from 7% to 11%. The addition of TBABr to the Li^+-bound rotaxane induced a further translocation of the macrocycle to the triazole station, up to an estimated 27% station occupancy. Notably, the addition of TBABr to the neutral rotaxane did not change the triazole station occupancy, highlighting the 'switch on' cooperative effect associated with ion-pair binding. This behaviour is reminiscent of a molecular Boolean AND logic gate, in which the presence of both cation and anion stimuli is required to elicit a response. To the best of our knowledge, this is the first example of using ion-pair binding to control solution-phase molecular shuttling in an interlocked molecule. With the increasing focus on exploiting the dynamic nature of mechanically interlocked molecules in functional switches and machines, this study highlights the exciting possibility of exploiting ion-pair binding as a two-input stimulus to control the co-conformation of interlocked components.

Future work of this project will focus on improving the translational motion of the macrocycle by increasing interactions between the ion-pair and the axle. To this end, the triazole station could be replaced by motifs shown below, which contain multiple cation and anion binding donors, which could potentially form stronger interactions with an ion-pair (Figure 2.24).

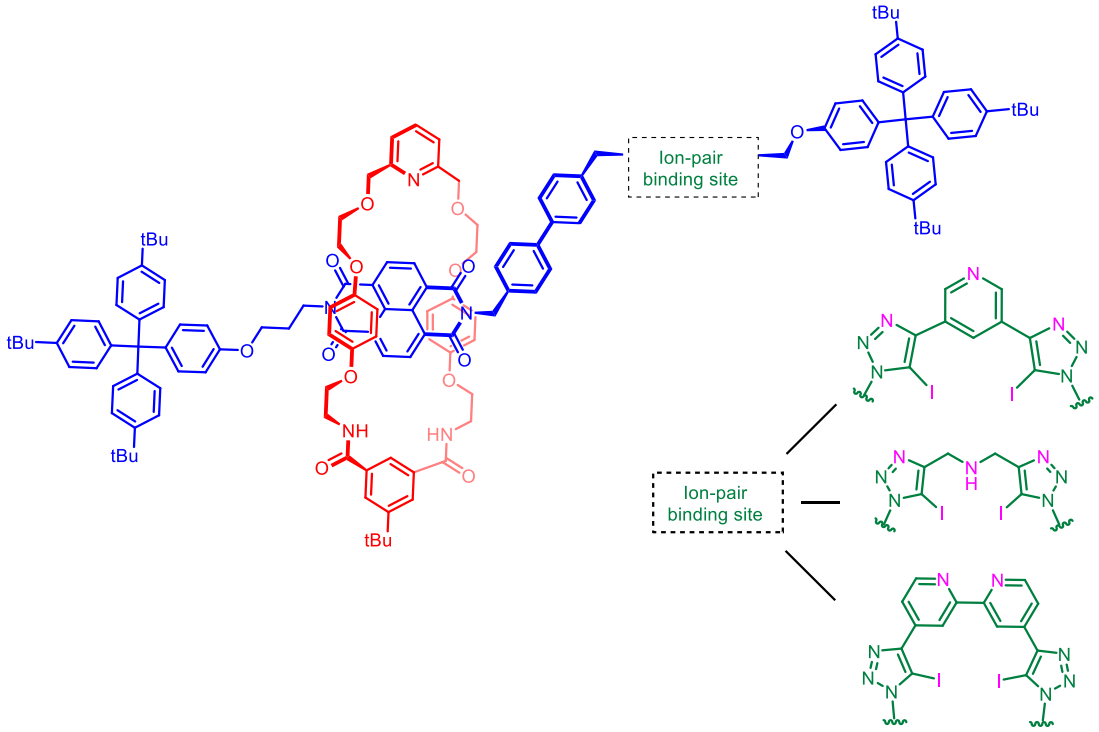

Figure 2.24: Proposed heteroditopic two station [2]rotaxanes to potentially improve translational motion of the macrocycle. Anion and cation binding donor atoms are designated in pink.

2.5. Part II: Heteroditopic [2]rotaxanes with a XB/HB triazole macrocycle**

2.5.1. Introduction

As discussed in Chapter 1 - Section 1.5, hydrogen bonding (HB) donors have been widely exploited for the anion recognition site in heteroditopic receptor design. However, in the past decade, sigma hole interactions such as halogen bonding (XB) have risen to prominence in the field of anion recognition due to their potent and contrasting binding selectivity.[41] Despite these advantages, ion-pair receptors employing XB interactions are rare.[134] Although the first example of a XB heteroditopic receptor was reported by Resnati and Metrangolo in 2005 (Figure 1.15),[96] it was more than a decade later for the second sigma hole-mediated heteroditopic receptor to appear.[267] In this study, Schubert and co-workers investigated the sodium halide ion-pair binding properties of an iodotriazole-based polyether macrocycle (Figure 2.25a). Crystallographic evidence of the NaI complexed ion-pair revealed a six-coordinated Na^+ cation binding to the macrocycle's polyether backbone and triazole cavity, with a XB bound iodide being bound in an exodentate fashion. Solution phase ^{1}H NMR titration experiments in 3:1 (v/v) CD_2Cl_2/CD_3CN determined a more than 25-fold increase in the iodide binding constant in the presence of co-bound Na^+ ion, which polarises the receptor's iodo-triazole XB donor to enhance halide recognition. Interestingly, the analogous HB receptor did not display any cooperative ion-pair binding due to the formation of intramolecular HB interactions, which prevented a potential Na^+ cation from being bound inside the cavity (Figure 2.25a). Recently, Beer and co-workers reported a series of phenanthroline containing heteroditopic HB, XB, and chalcogen bonding (ChB) macrocycles for lithium halide ion-pair binding investigation (Figure 2.25b).[224] The phenanthroline-Li^+ complexed XB macrocycle was the most potent ion-pair receptor with a two- to seven- fold

** This work was published as a full paper.
V. K. Munasinghe, J. Pancholi, D. Manawadu, Z. Zhang, P. D. Beer, *Chem. Eur. J.* **2022**, e202201209

increase in Br^- and I^- binding compared to analogous lithium cation complexed HB and ChB receptors. Importantly, the XB macrocycle, was the only macrocycle capable of simultaneously binding the LiCl ion-pair while analogous titrations with ChB and HB hosts resulted in LiCl salt precipitation. Superior LiCl binding properties of the XB macrocycle was attributed to strong XB···Cl interactions, preventing the recombination of Cl^- and Li^+ co-bound ions. This study highlights the exciting potential of using XB donors for ion-pair recognition.

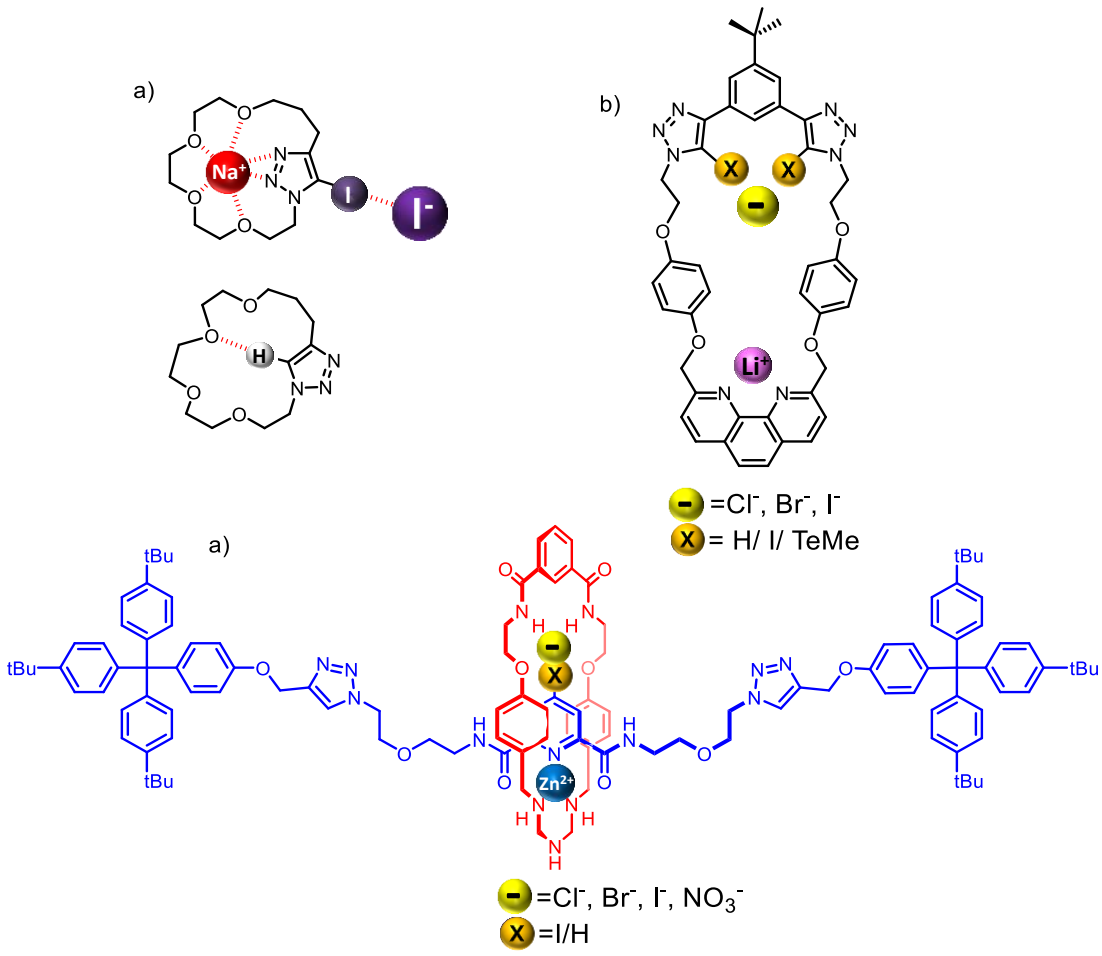

Figure 2.25: Examples of heteroditopic receptors: a) Schubert's XB/HB heteroditopic macrocycle, b) Beer's heteroditopic macrocycle, c) Beer's heteroditopic XB/HB rotaxane.

As described in Section 2.1.1, mechanically interlocked hosts display superior binding properties for guest ions compared to non-interlocked acyclic/macrocyclic receptor

analogues. However, prior to this work there is only one reported example of a heteroditopic XB mechanically interlocked receptor (Figure 2.25c).[199] The scarcity of reported heteroditopic XB MIMs capable of forming XB-anion interactions presents an avenue for further research.

2.5.2. Design and synthesis of bidentate and tridentate halogen bonding heteroditopic [2]rotaxanes

As discussed in Chapter 2- Part I, the single iodotriazole XB donor in the axle of Li^+-**2.10** rotaxane (Figure 2.26) was unable to form linear XB interactions with halide anions, due to the rotaxane's co-conformation resulting from the lithium cation's coordination mode. In an attempt to facilitate the formation of linear XB-anion interactions, the amide groups of the macrocycle were replaced with iodotriazole motifs as shown in Figure 2.26. It was envisaged that the larger iodine atoms of the two macrocycle iodotriazole groups, together with the single iodotriazole axle XB donor, could potentially enable XB interactions with halide anions in an exodentate fashion.

To this end, bidentate and tridentate XB [2]rotaxanes (**2.22**, and **2.23**) were synthesised to investigate the effect of XB interactions on the respective rotaxane's lithium halide ion-pair recognition properties.

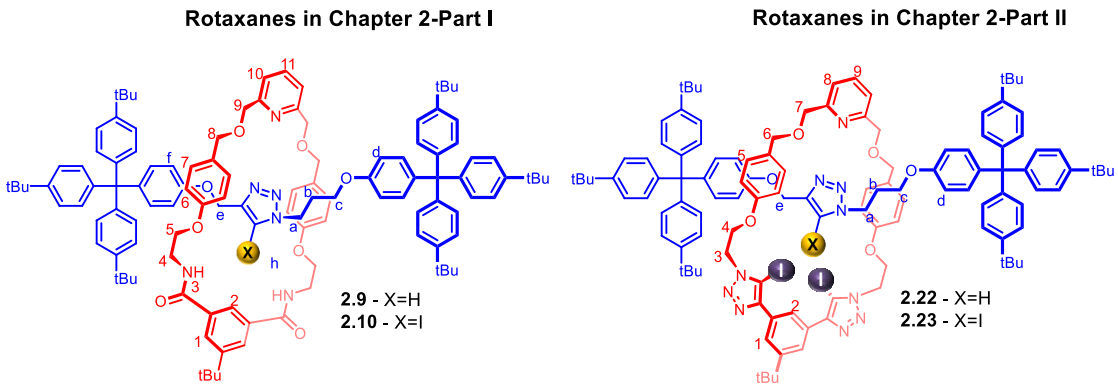

Figure 2.26: Rotaxane structures in part I and part II of Chapter 2.

2.5.2.1. *Synthesis of macrocycles and heteroditopic [2]rotaxanes*

The XB and HB macrocycles **2.29** and **2.30** were prepared in 27% and 29% yields respectively by a copper(I)-catalyzed azide-alkyne cycloaddition (CuAAC) 'click' reaction between the previously synthesised bis-azide **2.3** and the bis-alkyne **2.28** under high dilution conditions in anhydrous DCM (Scheme 2.4).

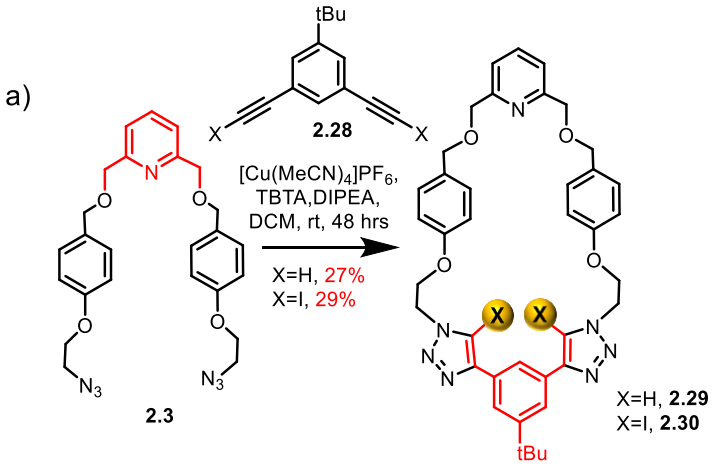

Scheme 2.4: Synthesis of macrocycles **2.29** and **2.30**

The preparation of the target heteroditopic [2]rotaxane host systems was achieved *via* CuAAC active metal template (AMT)[165] synthesis (Scheme 2.5).To this end, macrocycles **2.29** and **2.30** were pre-complexed with 0.95 equivalents of $[Cu(MeCN)_4]PF_6$ in CH_2Cl_2 and subsequently reacted with 5 equivalents of stopper precursors **2.8**[165,227] and **2.7**[165] in the presence of catalytic amounts of DIPEA at room temperature for 48 h to afford rotaxanes **2.21** and **2.22** in 34% and 35% isolated yields, respectively. The synthesis of the tridentate all-XB rotaxane **2.23** proved much more challenging, presumably due to steric hindrance from the XB donor atoms preventing the formation of the interlocked structure. However, by increasing the reaction time to 5 days, the temperature of the reaction to 30 °C and adding more $[Cu(MeCN)_4]PF_6$ catalyst to the reaction mixture, rotaxane **2.23** was successfully isolated following purification in a modest yield of 9%.

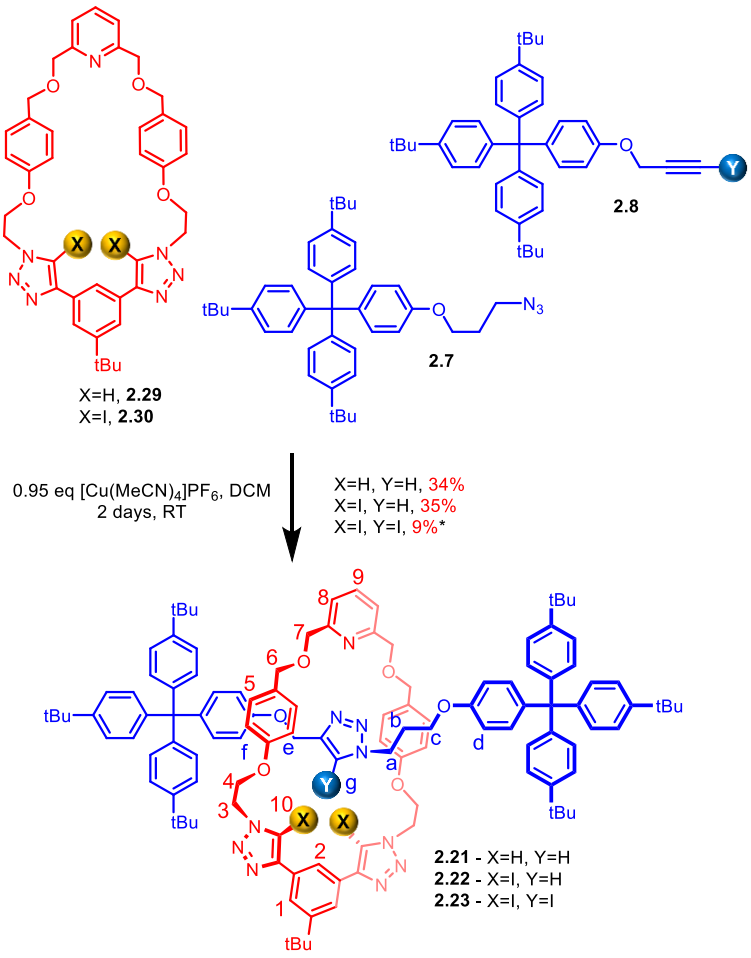

Scheme 2.5: Synthesis of target XB and HB heteroditopic [2]rotaxanes **2.21**, **2.22** and **2.23.** *3.8 eq. of $Cu(MeCN)_4PF_6$, at 30°C for 5 days.

All novel structures were characterized by ^{1}H NMR and ^{13}C NMR spectroscopy, and high-resolution electrospray ionisation (ESI) mass spectrometry. Evidence for the successful formation of the interlocked structures **2.21, 2.22,** and **2.23** is given by comparison of ^{1}H NMR spectra of the rotaxane products and those of the non-interlocked macrocycle and axle components. In particular, diagnostic upfield shifts of the macrocyclic hydroquinone protons H_5 in the interlocked product are indicative of aromatic donor-acceptor interactions between the electron rich macrocyclic hydroquinone groups and the electron deficient triazole axle (Figure 2.27). Further evidence for the interlocked nature of the synthesised compounds was provided by 2D ROESY NMR spectroscopy, which showed multiple cross peaks arising from through-space interactions between the axle and the macrocycle (Figure 2.28).

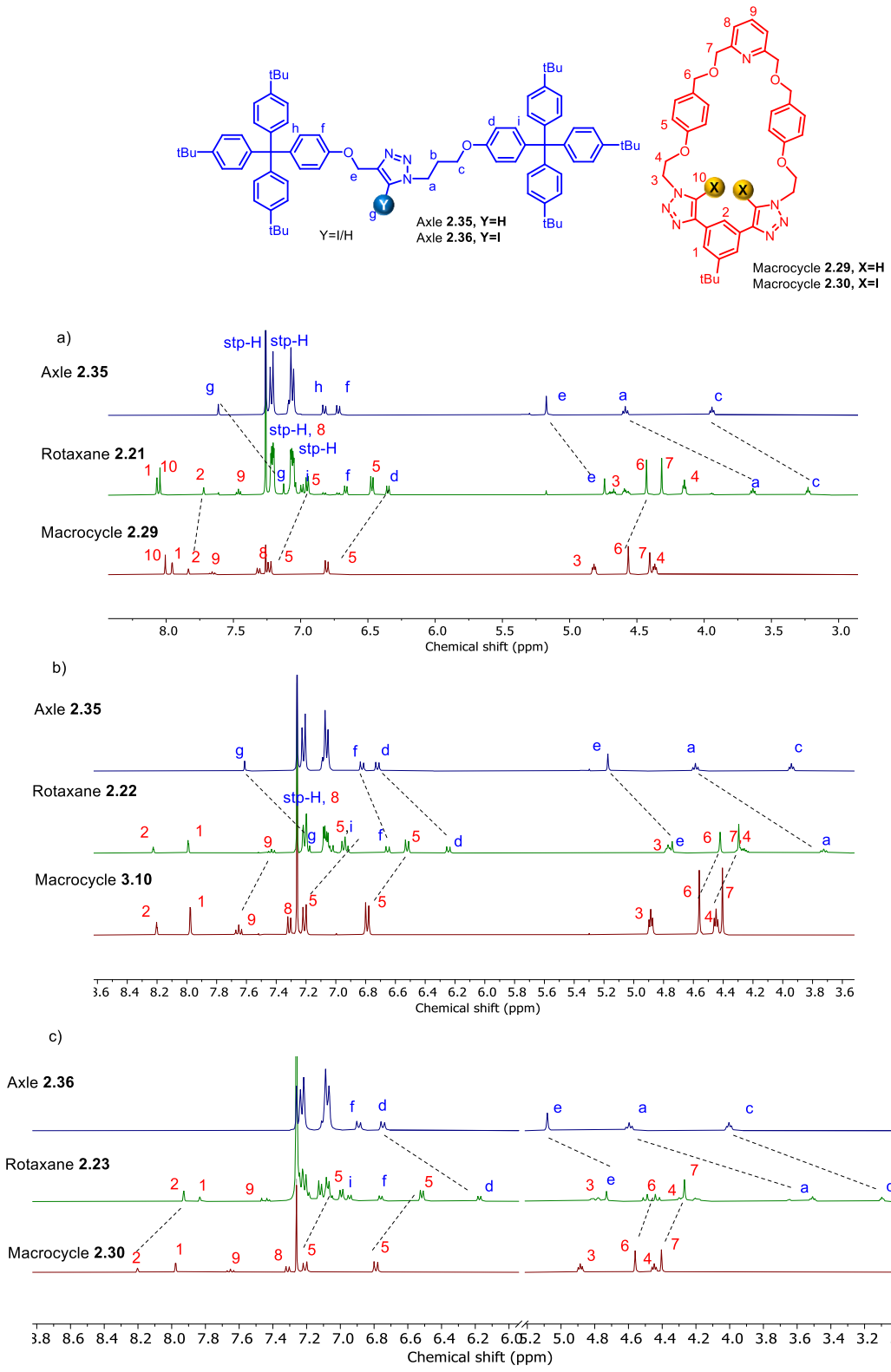

Figure 2.27: Comparison of ^{1}H NMR spectra of axle (top), rotaxane (middle) and macrocycle (bottom) in $CDCl_3$, 500 MHz, 298 K for a) rotaxane **2.21**,b) rotaxane **2.22**, c) rotaxane **2.23.** Stopper sp^2 protons are depicted as 'stp-H'.

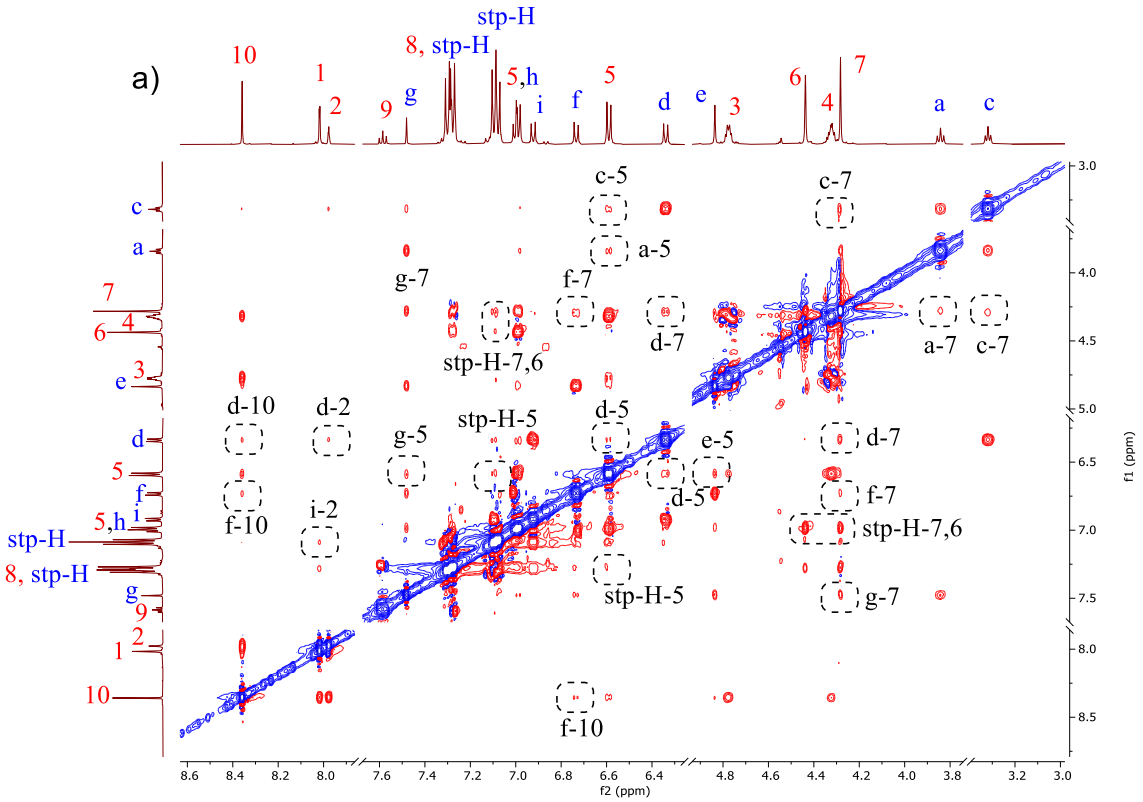
a)
stp-H
8, stp-H
10
1
2
9
g
5,h
i
f
5
d
e
3
6
4
7
a
c
c-5
c-7
a-5
g-7
f-7
d-7
stp-H-7,6
a-7
c-7
d-10
d-2
stp-H-5
d-5
g-5
e-5
d-7
f-10
i-2
d-5
f-7
stp-H-7,6
stp-H-5
g-7
f-10
f2 (ppm)
f1 (ppm)

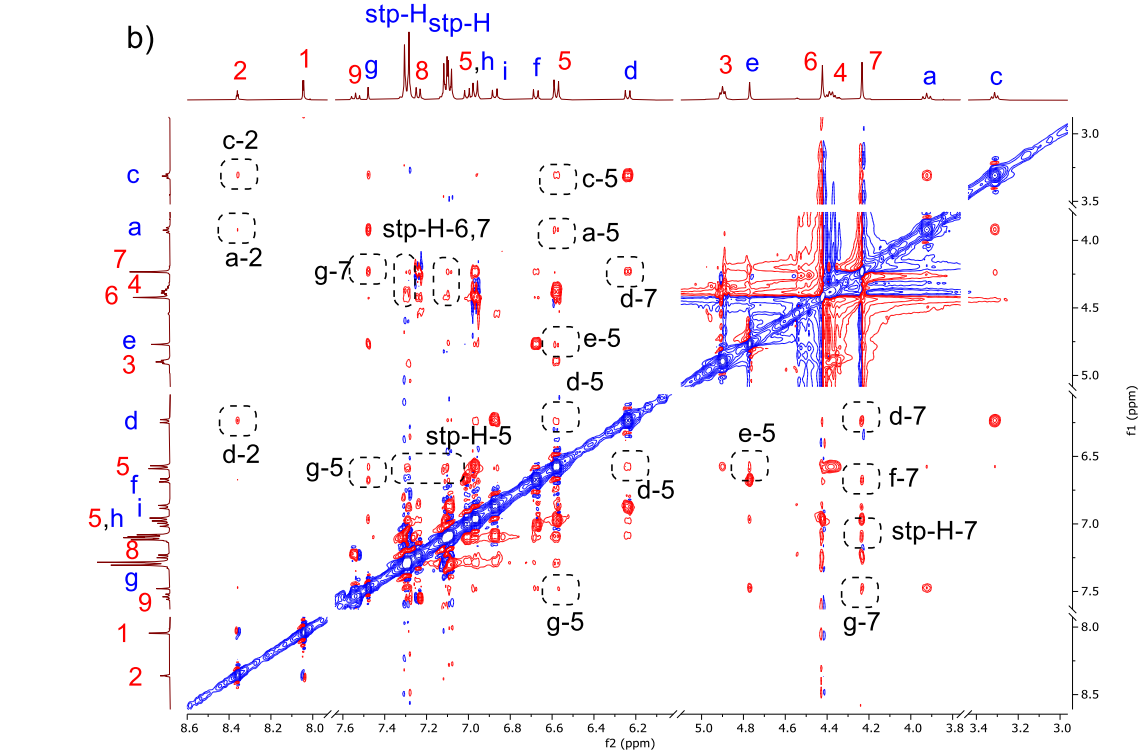
b)
stp-H
stp-H
2
1
9
g
8
5,h
i
f
5
d
3
e
6
4
7
a
c
c-2
c-5
a-5
stp-H-6,7
a-2
g-7
d-7
e-5
d-5
d-2
stp-H-5
e-5
d-7
g-5
d-5
f-7
stp-H-7
g-5
g-7
f2 (ppm)
f1 (ppm)

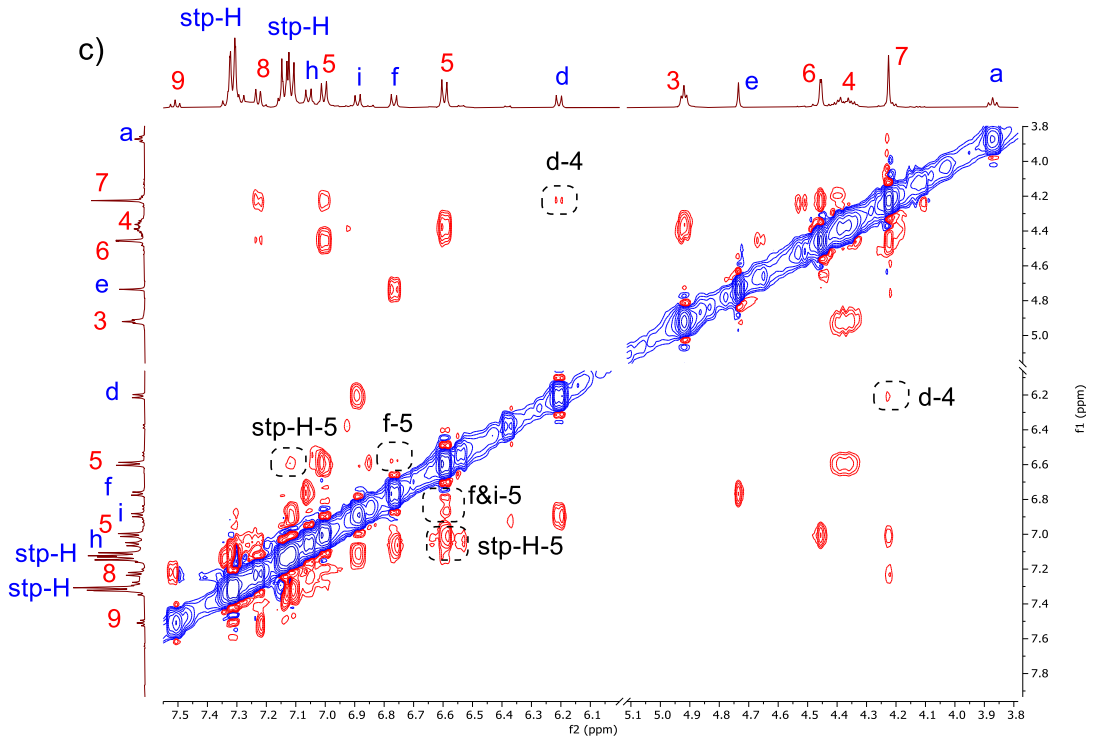

Figure 2.28: ^{1}H-^{1}H ROESY NMR spectra of Rotaxane a) **2.21**, b) **2.22**, c) **2.23** $(CD_3)_2CO$, 500 MHz, 298 K). Selected cross-peaks arising from through-space interactions of the interlocked macrocycle and axle components of the rotaxane are circled. Stopper sp^2 protons are depicted as 'stp-H'.

2.5.3. Solid state structure analysis[††]

Crystals of the XB macrocycle bound with the H^+ and Cl^- ion-pair (**2.30.HCl**), suitable for single crystal X-ray diffraction structural analysis were obtained by slow evaporation of a $CDCl_3$ solution of the macrocycle in the presence of excess of TBACl (Figure 2.29). The macrocycle's pyridyl motif was observed to be protonated, presumably due to trace acid residues in $CDCl_3$. The solid-state structure reveals the two iodo-triazole based XB donors to exhibit near linear (an average of 170°) XB interactions with the Cl^- anion in a concerted manner. A significantly shorter distance between the XB donors and Cl^- compared to their van der Waals radii (an

[††] X-ray crystallography data was collected and the solid state structure determined by Zongyao Zhang

average of 87%) is also observed. The structure thus highlights the respective cation and anion binding sites of the heteroditopic macrocycle.

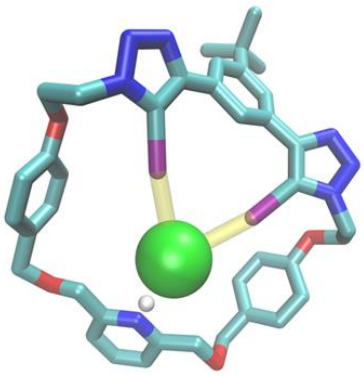

2.30.HCl

Figure 2.29: Crystal structure of XB macrocycle hydrochloride **2.30.HCl**. Colour code of atoms: O - red, N - blue, I - purple, H^+ - white, Cl^- - green, C - teal. Non-covalent host-guest interactions are shown in yellow.

2.5.4. Anion, cation, and ion-pair binding properties of heteroditopic [2]rotaxanes

In order to establish the lithium halide ion-pair binding mode of the heteroditopic [2]rotaxanes **2.21**, **2.22**, and **2.23,** ^{1}H NMR ion-pair complexation experiments were performed in CD_3CN:$CDCl_3$ solvent mixtures. Following a similar procedure as described in Section 2.3.2.1, ^{1}H NMR titrations were performed by sequential addition of TBA-halide salts to a lithium pre-complexed host solution. Truncated ^{1}H NMR spectra of rotaxane **2.22** before and after the addition of one equivalent of $LiClO_4$ and TBABr are shown in Figure 2.30. Upon addition of $LiClO_4$, significant perturbations of the rotaxane protons were observed in the axle methylene signal H_e and terphenyl stopper signal H_f, as well as the macrocyclic methylene signal H_7 adjacent to the pyridyl moiety, indicating Li^+ complexation in the rotaxane's designed cation binding cavity. As expected, alkyl proton H_3 and triazole proton H_g in the anion binding site did not show any perturbations indicating no coordination of the perchlorate counteranion. Subsequent titration of TBABr caused prominent perturbations to

proton signals H_2, H_3, H_f and H_a, which are local to the postulated anion binding site. Additionally, the peak signal corresponding to the triazole proton H_g broadens and progressively shifts downfield indicative HB interactions with the anion. All rotaxanes showed similar perturbations in the presence of $LiClO_4$ and TBABr/TBAI. Additionally, all-HB rotaxane **2.21** displayed significant downfield peak perturbations of triazole protons H_{10} and H_g upon the addition of anions, further indicating the direct involvement of both macrocycle and axle triazole C-H donors in the anion recognition process. While not observed upon titrations with TBABr and TBAI, the addition of TBACl to lithium cation precomplexed rotaxanes caused decomplexation of the cation in all cases, as evident by the observation of free rotaxane species in the ^1H NMR spectra. This may be attributed to the strong lattice enthalpy of LiCl driving salt recombination.[70]

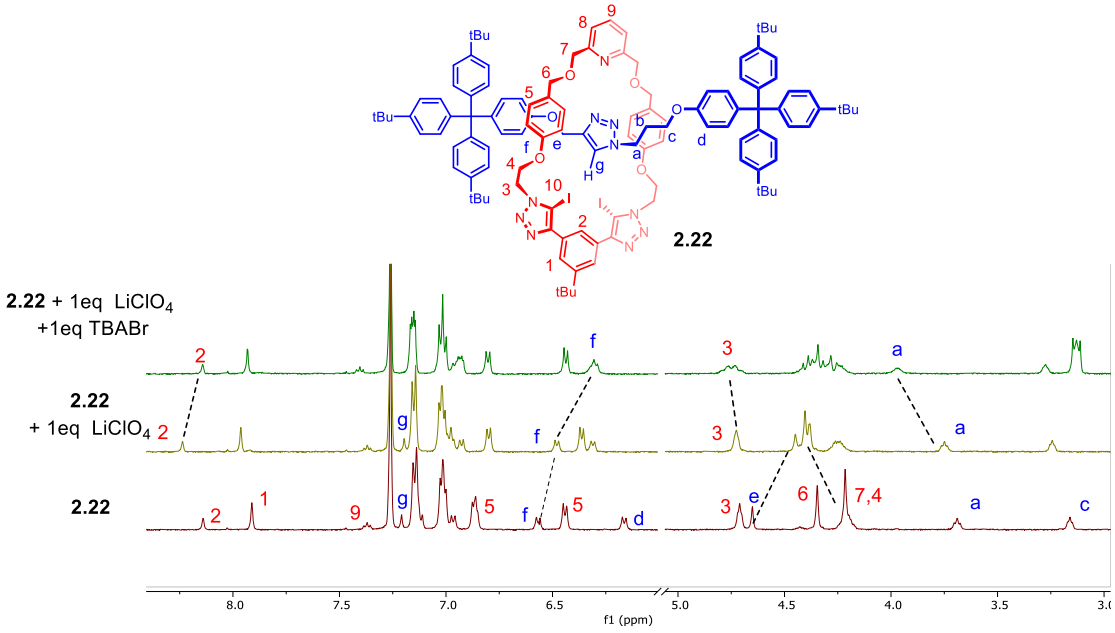

Figure 2.30: Superimposed ^1H NMR spectra in 1:9 $CD_3CN/CDCl_3$ (v/v), of a) Rotaxane **2.22;** b) Rotaxane **2.22** in the presence of 1 equivalent of $LiClO_4$; c) Rotaxane **2.22** in the presence of 1 equivalent of $LiClO_4$ and 1 equivalent of TBABr.

Quantitative ion-pair binding data was determined by monitoring non-overlapping ^{1}H NMR chemical shifts of rotaxane protons H_2, H_5, H_f, H_a, and H_{10} in the presence and absence of one equivalent of $LiClO_4$ as a function of halide anion concentration. With the lithium complexed rotaxanes, Bindfit[228] analysis determined the 1:1 stochiometric host-guest apparent association constants displayed in Table 2.5. All rotaxanes precomplexed with lithium were found to bind Br^- and I^- anions in CD_3CN:$CDCl_3$ solvent mixtures. However, no evidence of halide anion binding was observed in the absence of Li^+. Therefore, as observed with rotaxanes **2.9** and **2.10** in part I, the presence of the bound metal cation in the rotaxane host effectively 'switches ON' anion binding, due to favourable electrostatic interactions between the two co-bound ions and the preorganisation of the anion binding site *via* the mechanical bond (see section 2.5.6). It is important to note that, similar to the ion-pair titrations mentioned in part I, only 32% of rotaxane host molecules in the solvent mixture are complexed with Li^+ cation upon adding 1 eq. of $LiClO_4$ (See Appendix A). Therefore, the apparent halide anion binding constants reported in Table 2.5 underestimate the strength of halide recognition that would result from the rotaxane quantitatively binding the lithium cation.

Table 2.5: Anion association constants (K_a/M^{-1}) for rotaxanes **2.21**, **2.22**, and **2.23** in the presence of 1 equivalent of $LiClO_4$ in CD_3CN:$CDCl_3$ solvent mixtures.[a]

Anion	Cation	**2.21**	**2.22**	**2.22**	**2.23**
		1:9 CD_3CN:$CDCl_3$		3:7 CD_3CN:$CDCl_3$	
Cl^-	Li^+	[b]	[b]	-	[b]
Br^-	Li^+	6946 (625)	$>10^4$	5666 (397)	$>10^4$
I^-	Li^+	2369 (166)	$>10^4$	2890 (144)	3419 (239)

[a] K_a values were calculated using the global fit option in Bindfit software using a 1:1 binding model. Absolute errors are included in brackets. Li^+ is added as $LiClO_4$ and all anions as their TBA salts. [Receptor] = 1mM, T = 298K. [b] Salt recombination occurred.

As was hoped, Table 2.5 highlights halide anion binding strength is enhanced as the number of XB donors decorating the rotaxane cavity increases. In 1:9 CD_3CN:$CDCl_3$ (v/v) mixtures, a significant increase in the magnitudes of the association constants of LiBr and LiI is observed for the bidentate XB rotaxane **2.22** compared to the HB rotaxane analogue **2.21**. As the K_a values for **2.22** were $>10^4$ M^{-1}, a more competitive solvent mixture of 3:7 CD_3CN:$CDCl_3$ (v/v) was used to obtain numerical K_a values for rotaxanes **2.22** and **2.23**. Replacement of the axle's single triazole HB bond donor of **2.22** with an XB bond donor in **2.23** resulted in a large enhancement of halide anion binding strength, particularly with the smaller Br^- anion. All the rotaxane hosts showed two- to three-fold selectivity for the LiBr ion-pair over LiI. This may be attributed to the relative higher basicity of Br^- and the size complementarity of LiBr to the preorganised ion-pair binding cavities of the rotaxanes.

To further investigate the anion selectivity of rotaxane **2.22**, analogous ^{1}H NMR titrations were performed for the lithium precomplexed rotaxane (Li^+**-2.22**) with the sequential addition of AcO^-, NO_3^- and SCN^- anions as their TBA salts. In all instances, Li^+ decomplexation was observed upon addition of the respective anion, even though the lattice energies of $LiNO_3$ and LiSCN are lower than the lattice energy of LiBr.[‡‡70] Hence, the selectivity presumably stems from the preferential halide binding properties of rotaxane **2.22**, specifically the binding of the softer Br^- and I^- anions to XB donors[41] and size complementarity of halide anions to the rotaxane's anion binding site.

Attention then turned towards investigating the selectivity of rotaxane **2.22** for Group I metal cations. Due to poor solubility of the receptor in the presence of $NaClO_4$, NaBArF was used as the source of Na^+ cations. ^{1}H NMR titration experiments in 3:7 CD_3CN:$CDCl_3$ (v/v) determined that the association constant with Li^+ was more than three times higher than the

‡‡ U(LiBr)=788 kJmol^{-1}, U(LiI)=730 kJmol^{-1}, U(LiSCN)=764 kJmol^{-1}, U($LiNO_3$)=662 kJmol^{-1}.

association constant value with Na^+ (K_a (Li^+) =697(1) M^{-1} compared to only 181(1) M^{-1} for Na^+). This may be attributed to the size complementarity and higher charge density of the Li^+ cation.

2.5.5. Ion-pair binding studies of XB and HB macrocycles.

In contrast to the rotaxanes, HB macrocycle **2.29** and XB macrocycle **2.30** did not bind any lithium halide ion pairs in 1:9 CD_3CN:$CDCl_3$ (v/v). Upon addition of $LiClO_4$, the proton signals adjacent to the respective macrocycle's pyridyl moiety (H_6 and H_7) shifted downfield, whereas H_8 shifted upfield (Figure 2.31). This suggests complexation of Li^+ occurs in the proximity of the pyridyl cation binding site, as observed in the solid-state structure (Figure 2.29). Upon subsequent addition of TBABr or TBAI, these signals reverted back to their original metal cation-free chemical shift values, suggesting potential ion-pair formation outside of the respective macrocycle, preventing simultaneous binding of an ion-pair to the macrocycle.

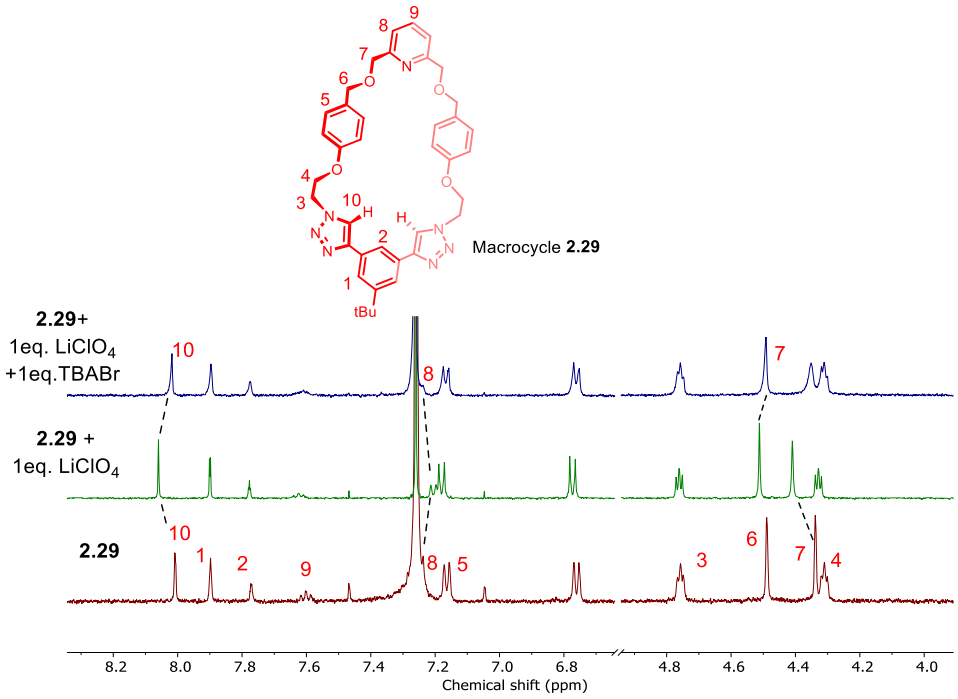

Figure 2.31: Superimposed ^1H NMR spectra of macrocycle **2.29:** a) free (not complexed); b) in the presence of $LiClO_4$; c) in the presence of both Li^+ and TBABr.

2.5.6. DFT calculations[§§]

DFT studies were performed to investigate the binding modes of lithium halides to rotaxanes **2.21**, **2.22,** and **2.23**. Simulations were performed in the gas phase following the method presented in Section 2.3.4. The initial input structures were generated from modifying solid state crystal structures of macrocycle **2.30** and of the HB triazole axle.[268] The terminal terphenyl stoppers of the axle were replaced by methyl groups for ease of simulation.

A geometry-optimised structure of LiBr-bound rotaxane **2.23** is shown in Figure 2.32. According to the optimised structure, Li^+ interacts with the pyridyl nitrogen and the adjacent oxygen of the macrocycle as well as the triazole nitrogen and the neighbouring oxygen of the axle, in a four-coordinated geometry. As postulated, the bromide anion interacts with all three triazole XB motifs present in the rotaxane in an exodentate fashion, forming characteristic near linear interactions (168^0 - 172^0). The average C-I···X^- bond length of bromide bound rotaxanes **2.22** and **2.23** is 82.5% of the sum of the bromide ion and the iodine van der Waals radii. The corresponding value for iodide bound rotaxanes **2.22** and **2.23** is 85%, which is in line with the experimental evidence for stronger halogen bonding in the case of bromide bound rotaxanes. The optimised structures agree with the corresponding ^{1}H NMR titration data where significant proton perturbations were observed in the postulated rotaxane anion (H_g, H_3 and H_a) and cation (H_e, H_f and H_7) binding sites (Figure 2.30).

[§§] DFT calculations were undertaken in collaboration with Dilhan Manawadu.

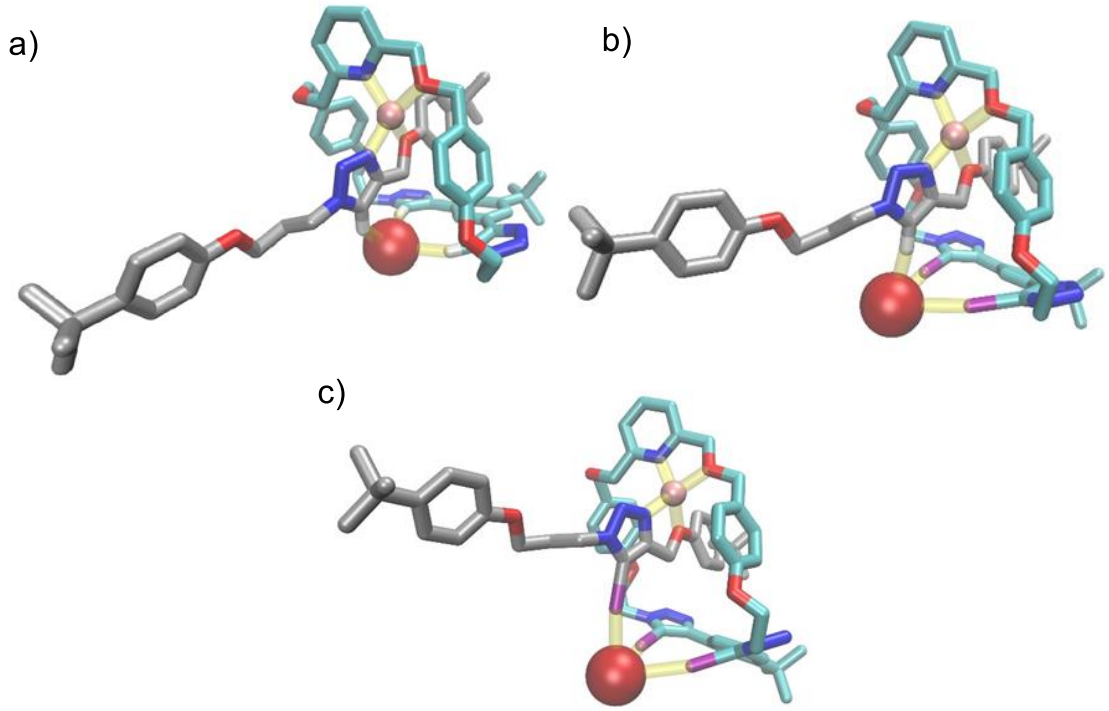

Figure 2.32: DFT optimised structure of LiBr bound rotaxanes: a) **2.21**, b) **2.22**, c) **2.22**. Hydrogen atoms are omitted for clarity. Colour code of atoms: O-red, N-blue, I-purple, Li-pink, Br- brown, C(axle) -gray C(MC)-teal. Non-covalent host-guest interactions are shown in yellow.

The second sphere electrostatic effect of Li^+ for cooperative binding of anions is reflected in the distribution of the electrostatic potential mapped onto the electron density surface. The isoelectronic maps for rotaxanes **2.22** and **2.23** are presented in Figure 2.33. Binding of Li^+ increases the potential energy of the proximal XB/HB donor atom of the axle leading to a significant polarisation of triazole XB/HB donors. This is evident from the increase of potential energy surrounding the axle iodine atom of rotaxane **2.23** from 245 kcal mol^{-1} to 301 kcal mol^{-1}, and that of the axle H atom of rotaxane **2.22** from 195 kcal mol^{-1} to 257 kcal mol^{-1} when Li^+ is bound.

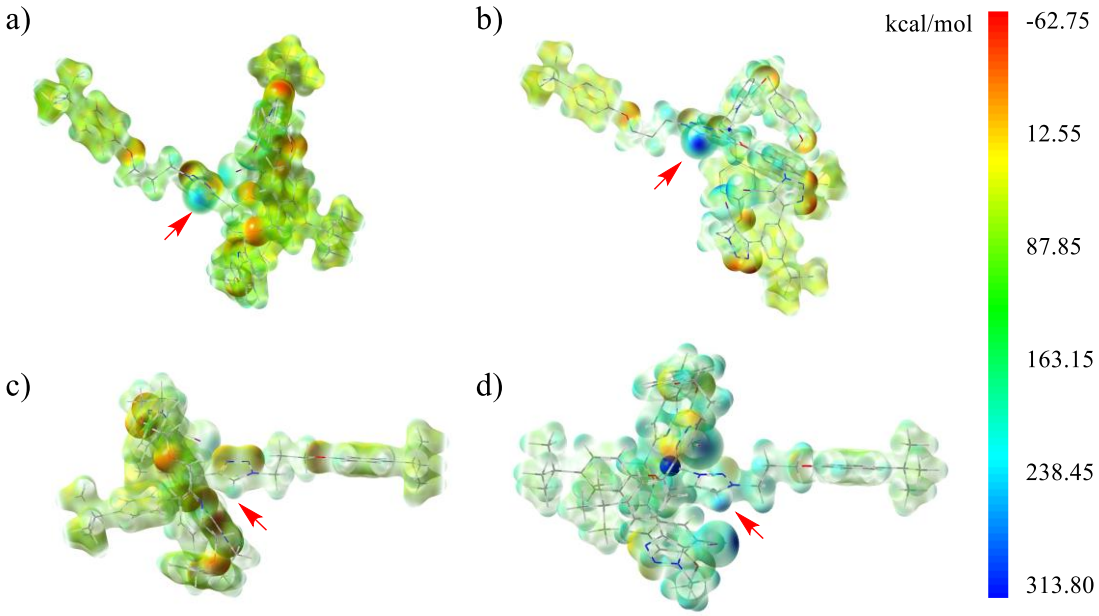

Figure 2.33: Electrostatic potential maps of a) free rotaxane **2.23**, b) Li^+ - complexed rotaxane **2.23,** c) free rotaxane **2.22**, d) Li^+ complexed rotaxane **2.22**. Arrows indicate the axle triazole XB/HB donor atoms of rotaxane **2.23** and **2.22,** respectively. Colour coded isosurface potential values are given in kcal mol^{-1}.

2.5.7. Conclusions

Novel heteroditopic [2]rotaxane hosts with bidentate and tridentate XB donors were synthesised and their anion, cation, and ion-pair binding properties were investigated. As observed in part I, binding of Li^+ was found to 'switch on' cooperative anion recognition of the rotaxanes by polarising the axle XB donor and preorganising the rotaxane anion binding site. Replacing the macrocyclic amide HB donors of rotaxanes in part I, with triazole-XB donors facilitated the Li^+-rotaxane to form concerted XB interactions with halide anions. Consequently, a progressive increase in lithium halide binding strength was observed when the triazole HB groups were replaced with XB donor motifs, making the all-XB **2.23** rotaxane the strongest ion-pair binding interlocked host of the family. The postulated exodentate concerted XB binding mode of halide anions to the Li^+-precomplexed rotaxanes was corroborated by computational DFT calculations. Quantitative ion-pair binding data revealed both bidentate and tridentate XB rotaxanes to exhibit strong cooperative ion-pair binding of

LiBr and LiI compared to non-interlocked macrocycle hosts and a notable selectivity towards LiBr over LiI.

2.5.8. Future work

Inspired by the strong anion binding properties of XB motifs,[224] and recent reports on enhanced anion binding of XB host molecules in water,[99] future work will focus on the synthesis of water-soluble ion-pair receptors to investigate their potential ion-pair binding properties in aqueous media. This would require the integration of water-solubilising monofunctionalised cyclodextrin motifs[182] or polyethylene glycol (PEG) groups into the stopper motifs of the axle (R_1) and PEG groups to the macrocycle (R_2) as shown in Figure 2.34. Additionally, electron withdrawing groups such as perfluorobenzene could be appended to the axle triazole motifs to further strengthen the anion···XB interactions.

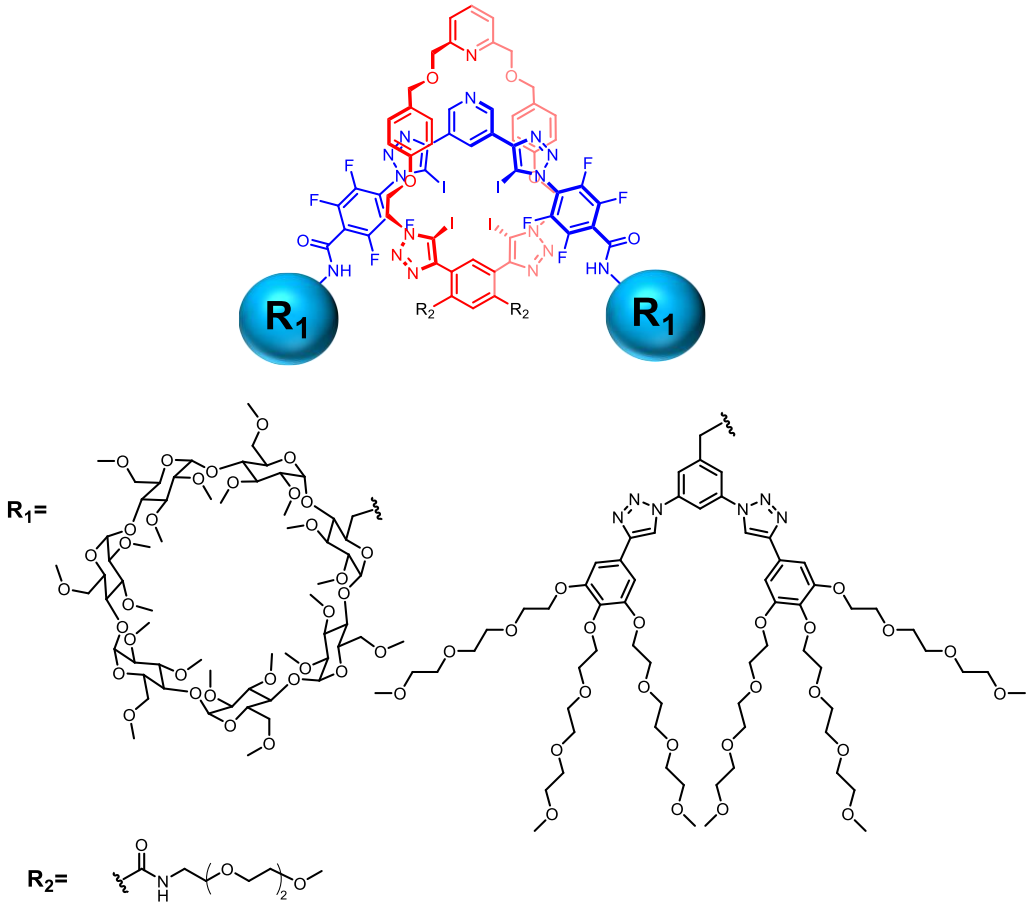

Figure 2.34: Proposed structures of potential water soluble heteroditopic [2]rotaxanes.

Chapter 3

Transition metal-based halogen bonding rotaxane hosts for anion recognition and sensing

Chapter 3: Transition metal-based halogen bonding rotaxane hosts for anion recognition and sensing

3.1. Introduction

As discussed in Section 1.4.3.3, the integration of transition metals proximal to XB donors enhances a receptor's anion binding strength and selectivity by neutral or charged-assisted transition metal coordinated XB donor polarisation and preorganisation. Additionally, incorporating redox- or photo-active transition metals produces potential chemosensing capability, where anion recognition elicits a detectable electrochemical or optical response. Mechanically interlocked receptors have demonstrated potent and selective anion binding and sensing properties (see Section 1.6.3.1 for examples). However, transition metal-based XB mechanically interlocked anion receptors are limited to only a few examples reported by Beer and co-workers. The XB rhenium (I) rotaxane anion receptor (Figure 3.1a)[269] displayed enhanced halide and AcO^- anion binding compared to the acyclic receptor (Figure 3.1b) in $CDCl_3$. Unfortunately, the Re(I) bis triazole motif displayed no luminescent sensing properties upon anion binding. Attempts to incorporate photoactive metals such as cyclometalated Ir(III), Ru(II) and Os(II) in place of Re(I) were unsuccessful due to the undesired dehalogenation of the receptor presumably due to extensive polarisation of the C-I bond. However, the Re(I) complexed bipyridyl rotaxane (Figure 3.1c)[270] is capable of selectively sensing halides over a range of oxoanions, in 1:1 H_2O/CH_3CN solvent mixtures via luminescence quenching of the interlocked receptor's MLCT emission band. Subsequently, the first example of a transition metal-based interlocked receptor capable of sensing anions in 100% water was realised (Figure 3.1d).[206] This rotaxane contains a luminescent Ru(II) complexed macrocycle and a XB axle component stoppered by water-solubilising permethylated β-cyclodextrin motifs. ^1H NMR titration studies revealed potent and selective

I^- binding (K_a=6300 M^{-1}) by the rotaxane in water with a modest increase in the Ru(II) MLCT emission intensity (6%) with the addition of 100 eq. of NaI.

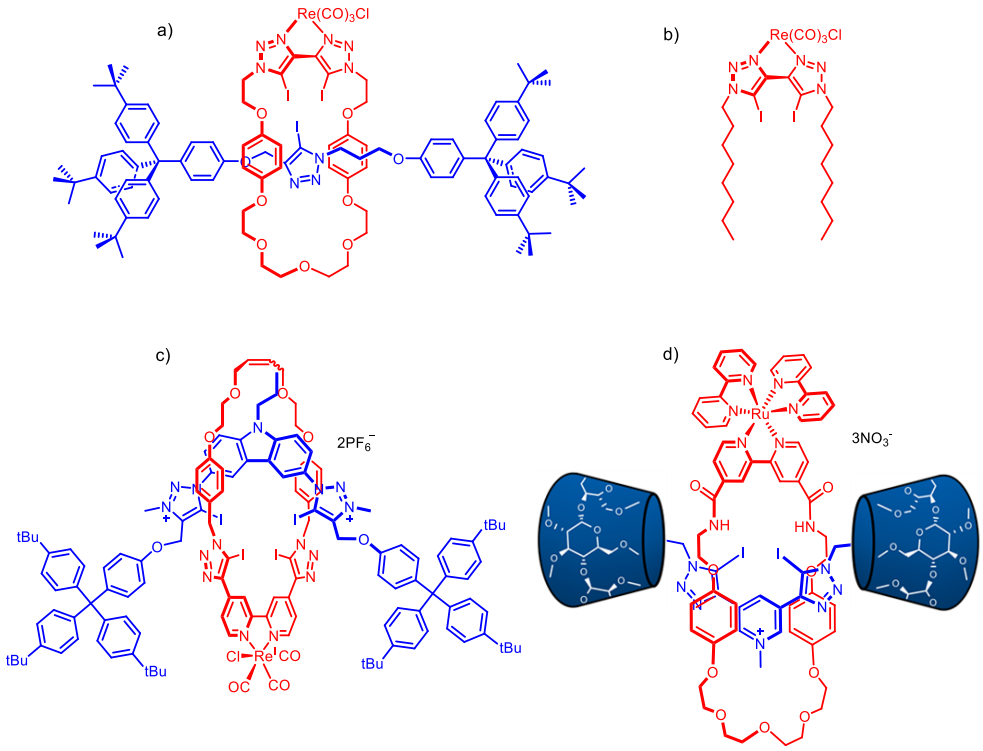

Figure 3.1: Transition metal based XB mechanically interlocked anion receptors: a) Re(I)-bis triazole complexed [2]rotaxane,[269] b) Analogous acyclic receptor of [2]rotaxane shown in 'a',[269] c) Luminescent Re(I) complexed bipyridine [2]rotaxane,[270] d) Luminescent Ru(II) complexed water soluble [2]rotaxane.[206]

3.1.1. Iridium(III) based hosts for anion recognition and sensing

Iridium(III) complexes are commonly employed as photoactive groups in many applications, including cell imaging,[271,272] organic-light emitting diodes (OLEDs)[273–275] and chemosensors.[276,277] This broad use of the photo-active Ir(III) metal centre is attributed to its exceptional optical properties, characterised by high luminescence quantum yields[278] and substituent tunable emission wavelengths.[279]

A molecular orbital diagram of a cyclometalated Ir(III) complex depicted in Figure 3.2[278,280] identifies three key electronic transitions: 1) metal-centred (MC, d-d); 2) metal to ligand

charge transfer (MLCT) and 3) ligand centred (LC, $\pi - \pi^*$). Luminescent emission from Ir(III) complexes arises through the triplet energy states of ^{3}MLCT and ^{3}LC (Figure 3.2-b).[280,281] Due to the heavy metal atom effect, Ir(III) complexes exhibit strong spin-orbit coupling (SOC). Therefore, even though electron transitions between triplet and singlet states are spin forbidden, SOC facilitates efficient intersystem crossing, affording high emission quantum efficiencies in Ir(III) complexes.[278,282]

Ir(III) complexes can be easily colour-tuned by varying the luminescence emission wavelength. As shown in Figure 3.2, the lowest unoccupied molecular orbital (LUMO) is a ligand-centred molecular orbital (π_L^*). Typically, the energy gap between the highest occupied molecular orbital (HOMO) and LUMO can be adjusted through ligand cyclometalated aryl substituent variation, resulting in complexes with a wide range of colours.[279]

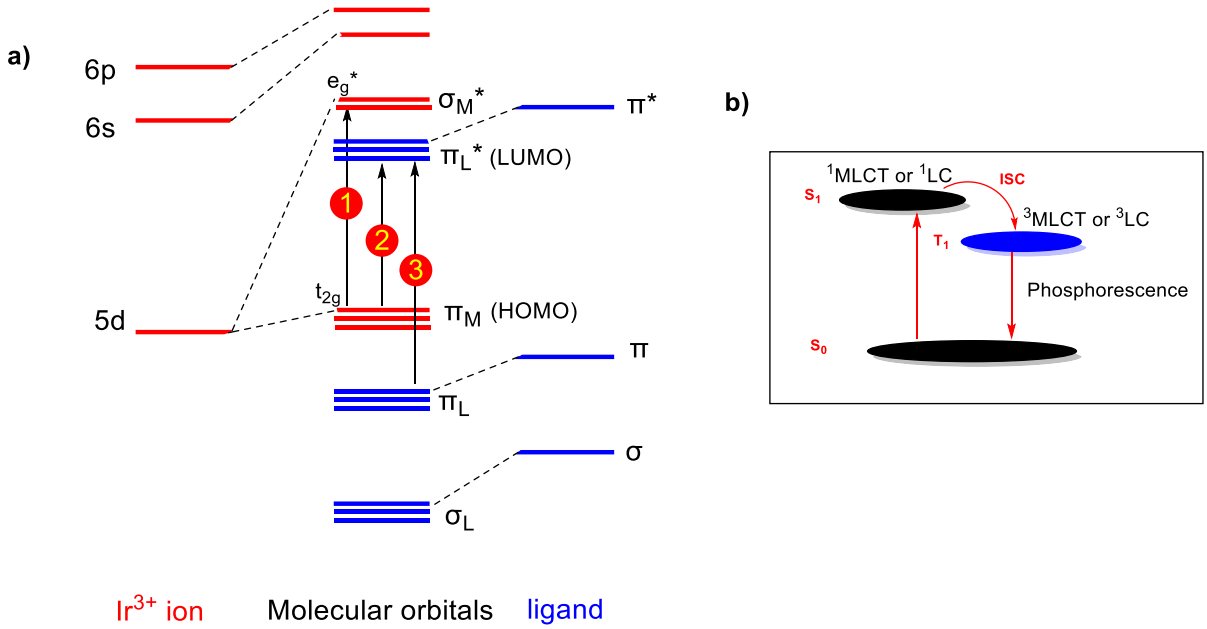

Figure 3.2: Simplified molecular orbital diagram of an Ir(III) octahedral complex a)Electron transitions: (1)MC (d–d),(2) MLCT, (3) LC (π–π*), b)Phosphorescence emission by Ir(III) complex.[279]

Despite their attractive luminescent properties, only a limited number of Ir(III) based anion receptors have been reported. In one example, Hyun and co-workers synthesised an Ir(III) based chemosensor containing a chiral 4,4'-bis-urea-naphthalene substituted bipyridyl Ir(III) coordinated ligand for chiral anion recognition (Figure 3.3a).[283] Upon addition of a series of Boc amino acid protected D/L carboxylate derivatives in acetonitrile, such as phenylglycine, valine, threonine and phenylalanine, the receptor exhibited a progressive increase in MLCT luminescence emission. The highest chiral selectivity was observed for phenylglycine (K_D/K_L=5).

Recently, Schubert and co-workers synthesised an acyclic bidentate XB-based receptor with a luminescent cyclometalated Ir(III) fragment for anion recognition and sensing. The receptor was able to bind and optically sense halide anions (Cl^-, Br^-) and acetate (AcO^-) in CD_3CN (Figure 3.3b).[284] Addition of these anions resulted in a diagnostic blue shift of the MLCT emission band and an enhancement in luminescence emission intensity. Importantly, the XB receptor displayed superior binding strength for all examined anions compared to the analogous HB host. To the best of our knowledge, there are no examples of Ir(III) complexed mechanically interlocked anion receptors. Hence, this chapter's primary focus is investigating the anion recognition and sensing properties of Ir(III) based XB rotaxane MIMs.

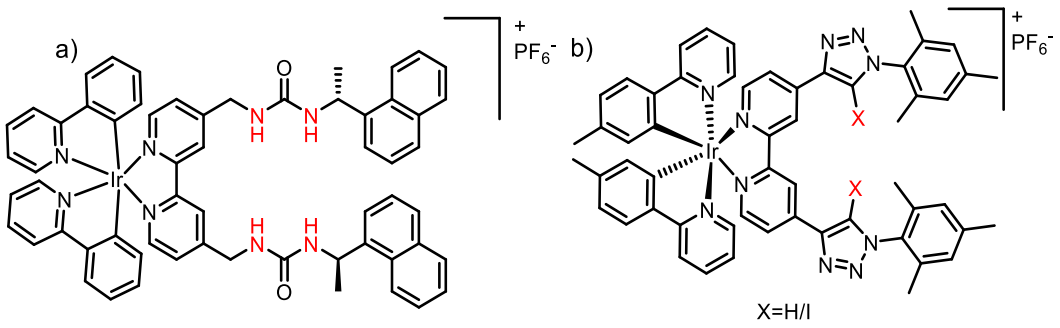

Figure 3.3: Ir(III) complexed anion receptors: a) Ir(III) complexed urea based receptor,[283] Ir(III) complexed XB/HB receptor.[284]

3.1. Chapter aims

Due to the attractive optical properties of cyclometalated Ir(III) complexes and the absence of Ir(III) complexed mechanically interlocked anion receptors, this project aims to investigate the synthesis, anion binding and sensing properties of novel Ir(III) complexed rotaxane MIMs. When recognising biologically and environmentally important dicarboxylate anions, higher order [3]rotaxane hosts offer an advantage over [2]rotaxanes, as the target dianion guest species are too large to be accommodated by the single binding pocket of the latter interlocked host system. In a recent report by Beer and co-workers, a (S)-1,1'-bi-2-naphthol (BINOL) axle incorporated chiral XB [3]rotaxane demonstrated selective stereo/geometric recognition and sensing of common biologically important dicarboxylate anions.[285] Specifically, this [3]rotaxane was able to bind (*S*)-N-Boc-gluterate with a remarkable enantioselectivity of 5.7 and fumarate over maleate with an impressive geometric selectivity of 4.4, by forming 1:1 stoichiometric host-guest complexes in ($CHCl_3$/CH_3OH/H_2O, 60:39:1). This is the only example of a higher order MIM capable of selective dicarboxylate recognition and sensing. To the best of our knowledge there are no examples of transition metal based higher order MIMs capable of recognising and sensing dicarboxylate anions. To this end, Ir(III) based bipyridyl [2]- and [3]rotaxanes are synthesised, and their dicarboxylate binding and sensing properties are investigated by ^{1}H NMR and fluorescence spectroscopic studies.

3.2. Ir(III) based receptors for anion recognition and sensing

3.2.1. Design and synthesis of Ir(III) complexed XB acyclic receptor

To begin with, a simple cyclometalated bipyridyl Ir(III) complexed XB acyclic receptor **3.4** was designed (Scheme 3.1). Complexing Ir(III) to a 4,4-bis-iodotriazole methylene bipyridine ligand preorganises the XB iodotriazole donors to facilitate concerted interactions with an anion. Previous work in our group had revealed the lability of the C-I bond in a 4,4-bis-iodotriazole bipyridine osmium(II) complex, where the triazole XB donor group is directly

linked to the metal complexed bipyridine ligand.[286] Hence it was anticipated that methylene CH_2 group spatial separation between the charged metal centre and XB donors would circumvent this problem.

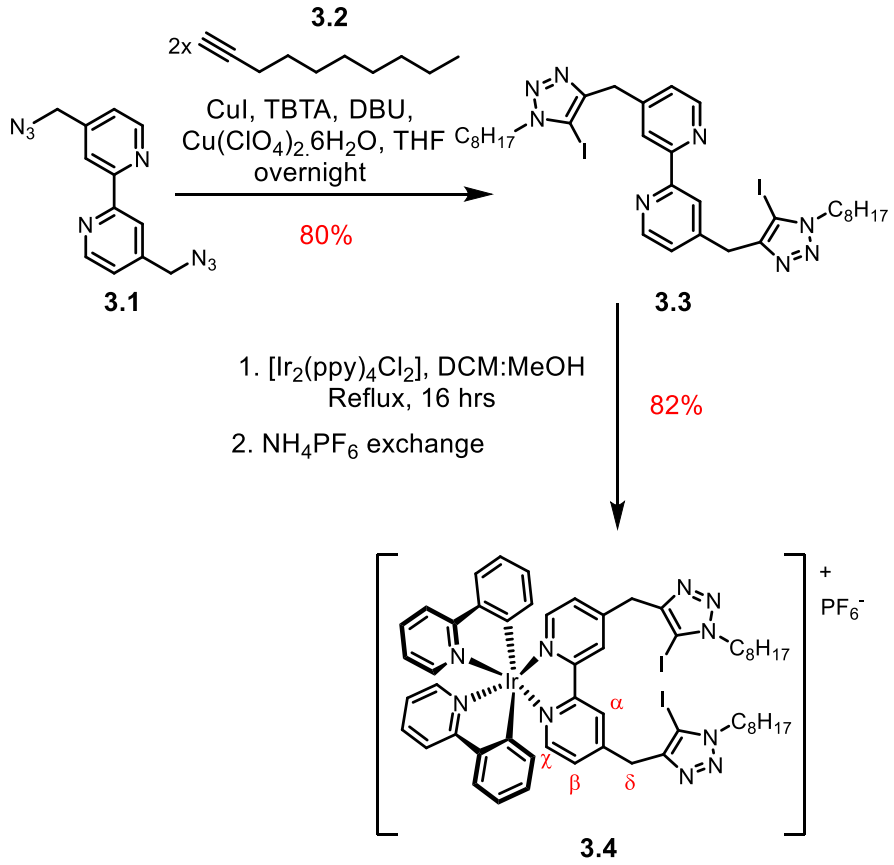

Scheme 3.1: Synthesis of the acyclic Ir(III) complexed bipyridine XB receptor, **3.4**

The synthetic procedure for the target Ir(III) acyclic receptor **3.4** is shown in Scheme 3.1. The bis-azide methylene bipyridine precursor **3.1**[287] was reacted with two equivalents of 1-decyne **3.2** under one-pot CuAAC click reaction conditions to afford the bis-iodotriazole-bipyridine motif **3.3** in 80% yield. The bipyridine precursor **3.3** was then heated with $Ir_2(ppy)_4Cl_2$ [288] for 16 hours, and anion exchanged with NH_4PF_6 to synthesise the acyclic receptor **3.4** in 82% yield after chromatographic purification.

3.2.2. Design and synthesis of Ir(III) complexed XB rotaxane receptors

Following the successful synthesis of the acyclic receptor **3.4**, the preparation of the target Ir(III) complexed rotaxane host systems was undertaken. To this end, a [3]rotaxane receptor **3.8** shown in Scheme 3.2 was designed. The [3]rotaxane consists of an axle with an anion binding site similar to the acyclic receptor **3.4**, and two amide-based macrocycles on either side of the central Ir(III) motif. It was anticipated that multiple concerted XB and HB interactions from the axle and both macrocycles would enhance the anion recognition properties of the [3]rotaxane **3.8** in comparison to the acyclic receptor **3.4**. Furthermore, numerous studies have investigated the effect of different substituent groups on the photophysical properties of cyclometalated Ir(III) complexes.[275,278,289] However, to the best of our knowledge, there are no reports investigating the influence of the mechanical bond on the optical properties of Ir(III) complexes.

The synthetic procedure employed for the synthesis of the Ir(III) complexed [3]rotaxane is summarised in Scheme 3.2. The bis-azide methylene bipyridine precursor **3.1** was refluxed with $[Ir_2(ppy)_4Cl_2]$[288] to afford the Ir(III) complexed bis-azide **3.5** in 71% yield. Following the general CuAAC-AMT procedure, macrocycle **2.6** was initially precomplexed with 0.95 equivalents of $Cu(MeCN)_4PF_6$ and subsequently reacted with the prepared Ir(III) bis-azide precursor **3.5** and stopper alkyne motif **2.8** in a 3:6:2, (**3.5**/**2.8**/Cu-**2.6**) mole equivalents ratio. The progress of the CuAAC-AMT click reaction was slow with no product formation in the first three days. This prolonged reaction time may be attributed to the electrostatic repulsion between the positively charged Ir(III) complexed azide precursor **3.5** and the cationic Cu(I) catalyst inhibiting the formation of the interlocked structure. After 9 days the formation of the [2]rotaxane was observed by TLC and mass spectrometry with no traces of the [3]rotaxane. Therefore, on the 9th day, an additional 1 eq. of Cu(I) precomplexed macrocycle and 1 eq. of stopper alkyne were added to the reaction mixture. After 14 days, preparative

TLC purification followed by anion exchange with NH_4PF_6 led to the successful isolation of the novel [3]rotaxane **3.8** in a modest isolated yield of 7% yield, together with the [2]rotaxane **3.9** by-product in 5% yield. However, by changing the reactant mole equivalents to 1:3:3 (**3.5**/**2.8**/Cu-**2.6**) the yield of the [3]rotaxane **3.8** increased significantly to 20% with only a trace amount of [2]rotaxane by-product detected. Both rotaxanes were characterised by ^{1}H NMR, ^{13}C NMR, and high-resolution electrospray ionisation (ESI) mass spectrometry (Figure 3.4a, Figure 3.5a, Figure 3.6).

Upon close inspection, differences between the ^{1}H NMR spectra of the [2]rotaxane and the [3]rotaxane were detected. As shown in Figure 3.4a and Figure 3.5a, axle methylene H_h proton is split to a AB quartet in the [3]rotaxane whereas in the [2]rotaxane the H_h proton is a multiplet, presumably due to the overlap of two AB quartets of the chemically non-equivalent H_h/$H_{h'}$ protons. Additionally, the unsymmetrical environment of the phenyl pyridyl (ppy) protons in the [2]rotaxane is evident by the presence of additional peaks in the ^{1}H NMR spectrum of the [2]rotaxane between 7.4 ppm – 8.0 ppm compared to the ^{1}H NMR spectrum of [3]rotaxane. Furthermore, the ^{1}H NMR peak integration ratio of macrocycle-protons/ axle-protons of [2]rotaxane and [3]rotaxane differ correctly. For example the integration of H_h/H_1 is 4:4 in the [3]rotaxane and 4:2 in the [2]rotaxane.

The interlocked nature of rotaxanes **3.8** and **3.9** was confirmed by diagnostic peak shifts of the macrocycle and by ^{1}H-^{1}H ROESY NMR spectra, which indicated through-space interactions between macrocycle and axle component protons H_7 and H_h respectively (Figure 3.4 and Figure 3.5).

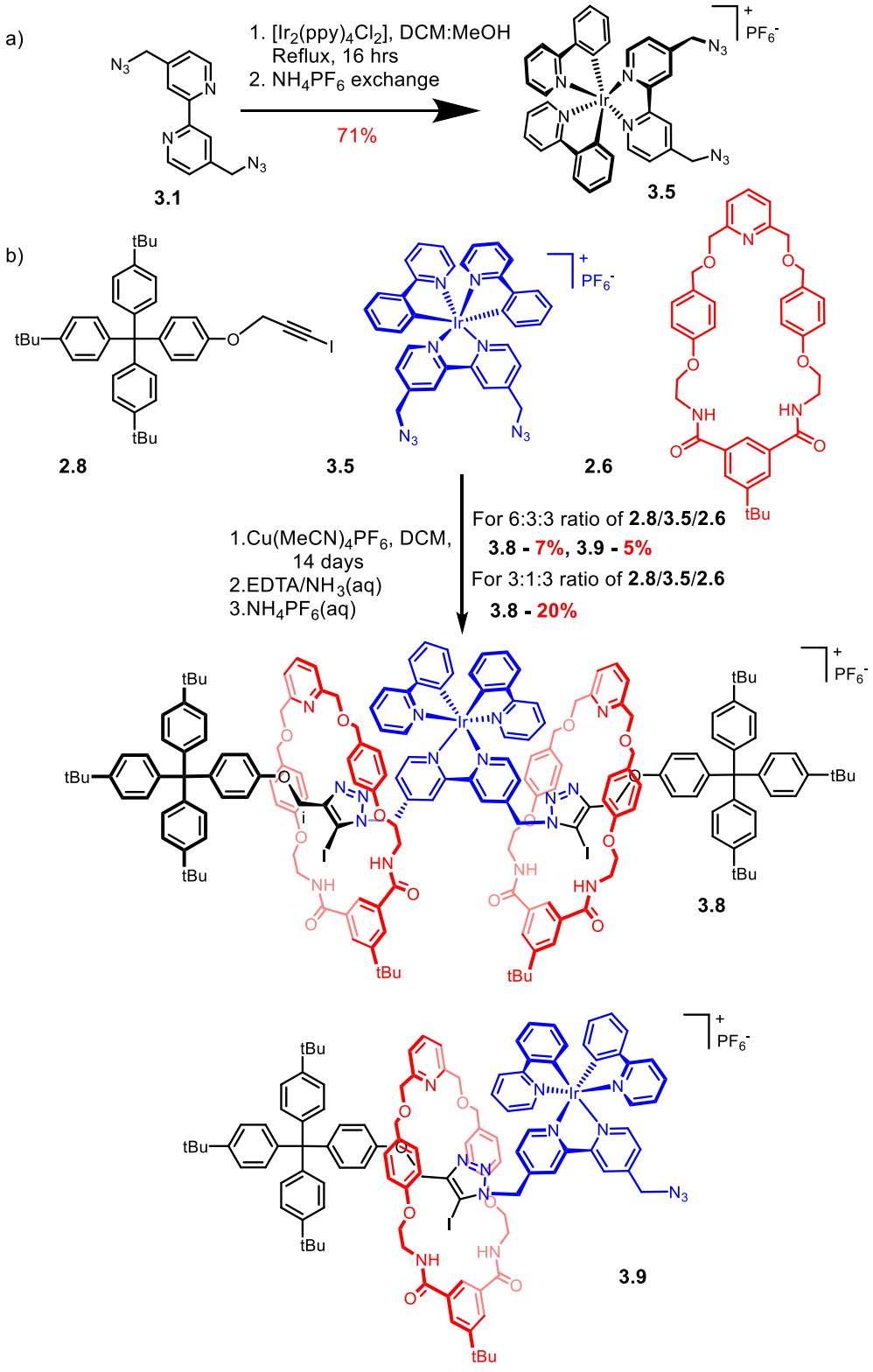

Scheme 3.2: Synthesis of Ir(III) complexed, a) Ir(III) bis azide precursor **3.5**, b) [3]rotaxane **3.8** and [2]rotaxane **3.9**

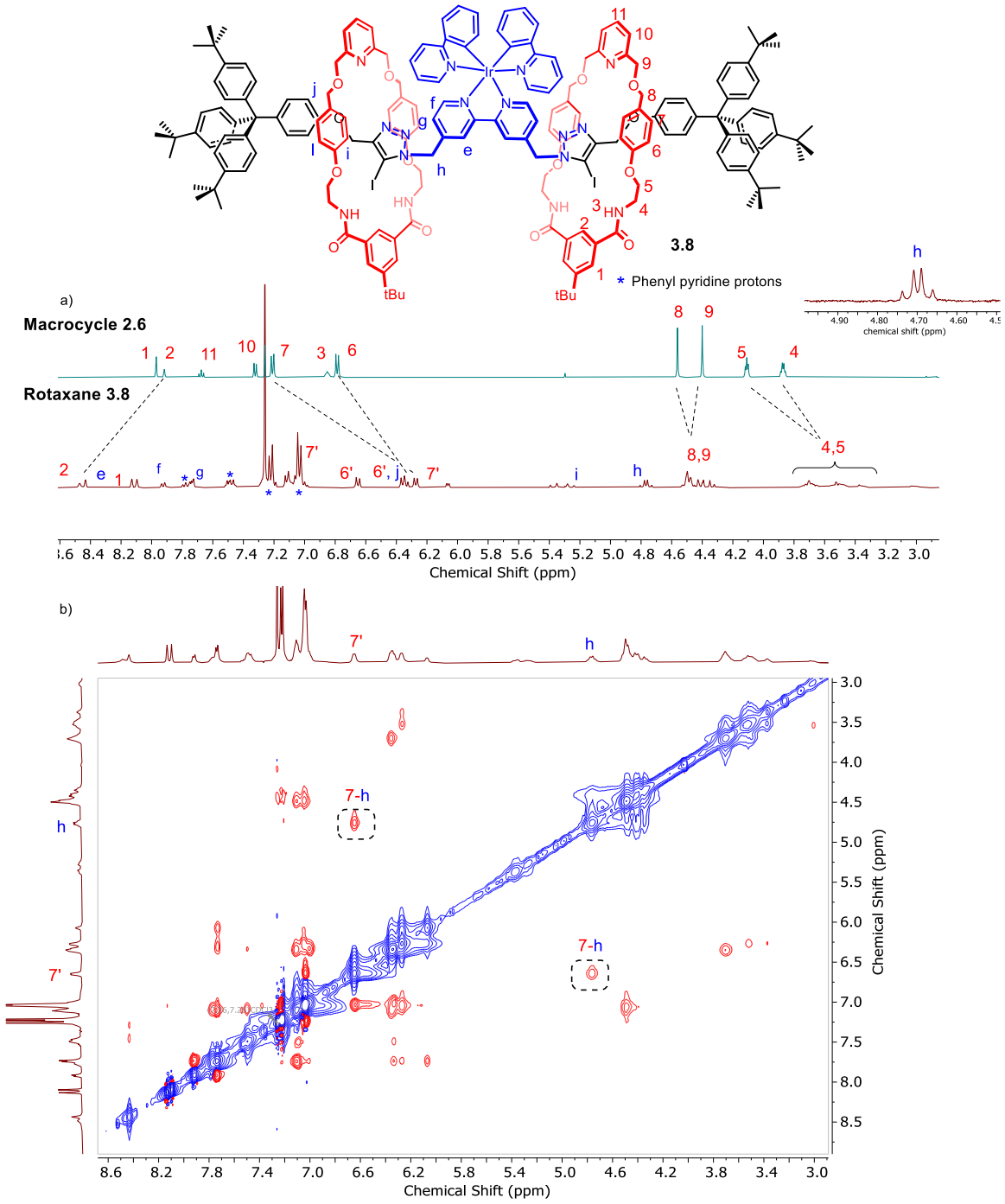

Figure 3.4: ^{1}H NMR characterisation of [3]rotaxane **3.8**; a) Superimposed ^{1}H NMR spectra of the macrocycle **2.6** and [3]rotaxane **3.8** and an expansion of the 4.5-4.9 ppm region of the [3]rotaxane ^{1}H NMR spectra, b) ^{1}H-^{1}H ROESY NMR spectra of [3]rotaxane **3.8**

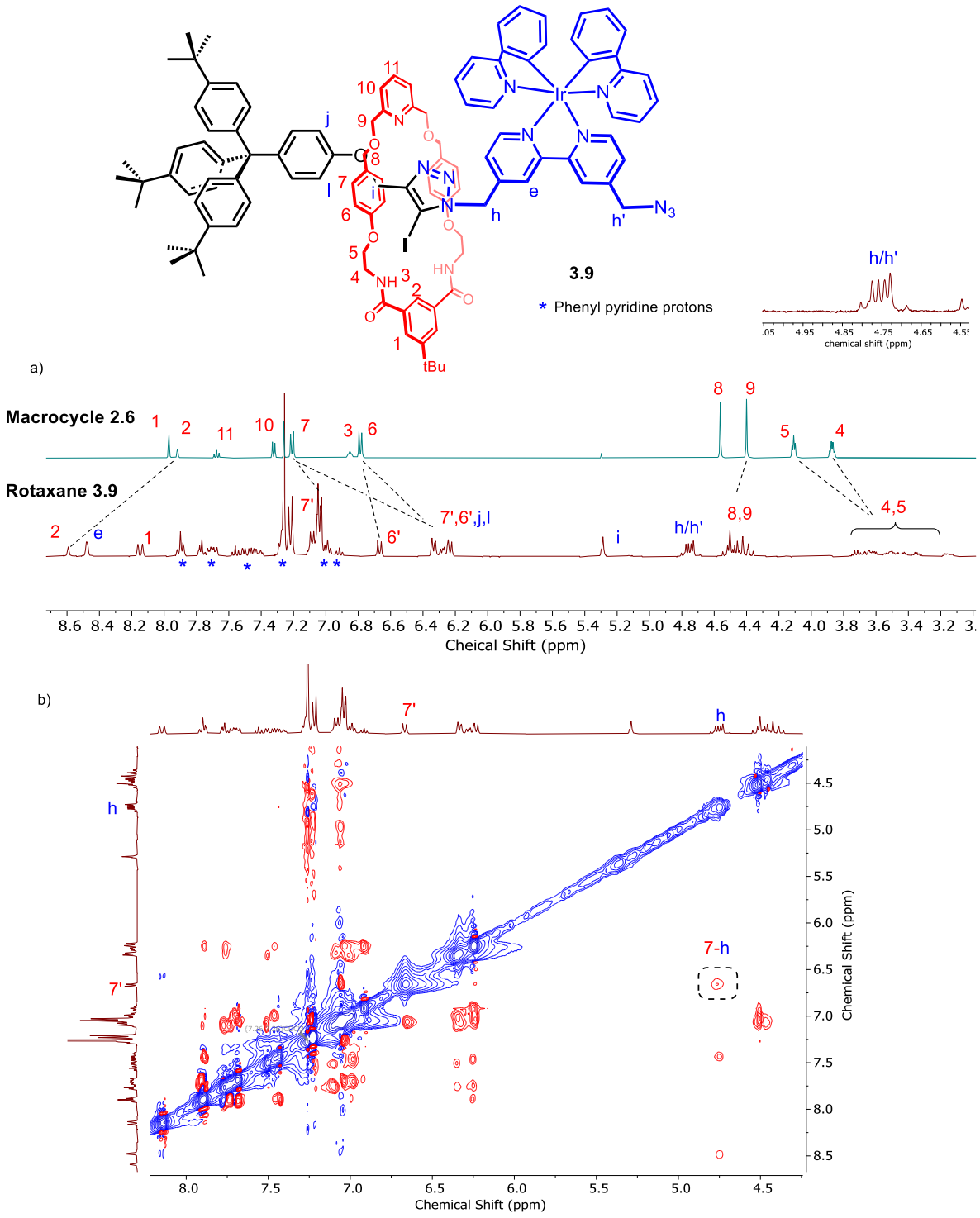

Figure 3.5: ^{1}H NMR characterisation of [2]rotaxane **3.9**; a) Superimposed ^{1}H NMR spectra of the macrocycle **2.6** and [2]rotaxane **3.9** and an expansion of the 4.6-5.0 ppm region of the [2]rotaxane ^{1}H NMR spectra, b) ^{1}H-^{1}H ROESY NMR spectra of [2]rotaxane **3.9**

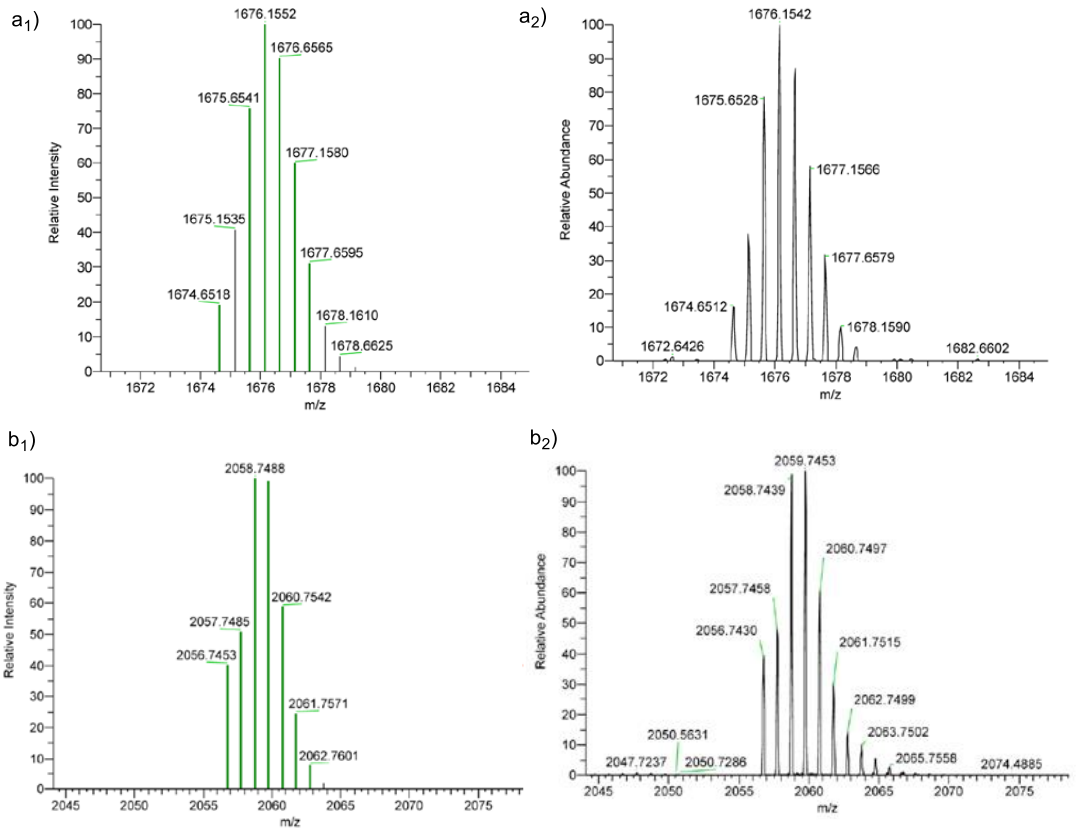

Figure 3.6: a_1) Theoretical and a_2) measured high resolution ESI mass spectra of [3]rotaxane **3.8** $[M+H]^{2+}$ fragment, b_1) Theoretical and b_2) measured high resolution ESI mass spectra of [2]rotaxane **3.8** $[M+H]^{+}$ fragment.

3.2.3. Photophysical properties of Ir(III) complexed receptors

The photophysical properties of the Ir(III) acyclic complexes **3.4**, **3.5**, and rotaxane hosts **3.8** and **3.9,** were investigated in aerated CH_3CN. UV-visible absorption spectra of all four Ir(III) complexes are depicted in Figure 3.7a. Based on reported photophysical data of similar compounds, intense absorption peaks below 280 nm were assigned to spin-allowed ligand centred (^{1}LC) π-π* transitions of cyclometallating phenylpyridine (ppy) and ancillary bipyridine (bpy) ligands. Low-intensity absorption peaks higher than 300 nm are generally assigned to charge transfer (CT) transitions.[288] Excitation of all four receptors at 400 nm

wavelength produced broad emission bands with emission maxima ranging from 627-639 nm (Figure 3.7b). This orange-red emission is generally assigned to mixed metal-to-ligand and ligand-to-ligand charge transfer transition (^{3}MLCT and ^{3}LLCT).[288]

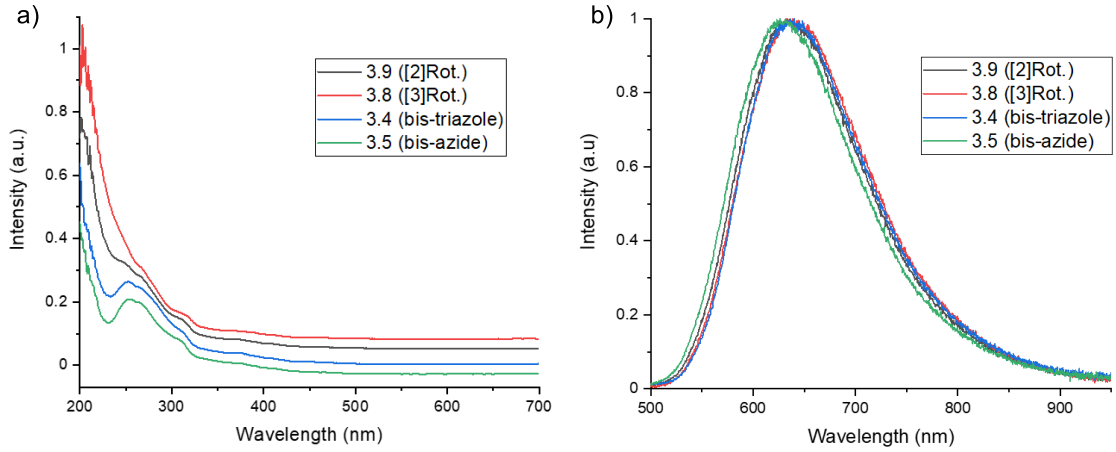

Figure 3.7: Optical spectra of Ir(III) complexed **3.4**, **3.5**, **3.8**, **3.9** in oxygen saturated CH_3CN, with [host]=10^{-5} M, at 298 K, a) absorption spectra (Spectra are vertically translated for clarity), b) normalised emission spectra for excitation at 400 nm. λ_{max} of: **3.4**=637 nm, **3.5**=627 nm, **3.8**=639 nm, **3.9**=634 nm.

Photoluminescence quantum yields (Φ_{PL}) of all four Ir(III) compounds were measured in O_2 saturated CH_3CN at 298 K using a reference standard $[Ru(bpy)_3]Cl_2$ (Φ_{PL}=1.80%, in aerated conditions),[290] under optically dilute conditions as described by Resch-Genger.[291] The calculated Φ_{PL} values are given in Table 3.1. The Φ_{PL} of both the acyclic Ir(III) bis-azide **3.5** and bis-iodotriazole **3.4** complexes are similar. Interestingly, both Ir(III) rotaxanes exhibit notably higher Φ_{PL} values compared to the acyclic Ir(III) receptors, with the [3]rotaxane displaying the highest Φ_{PL}. It is important to note even though the Φ_{PL} of the [3]rotaxane **3.8** is significantly higher than the acyclic receptor **3.4**, substituent groups on Ir(III) in both compounds are similar. Hence, the increase in Φ_{PL} of the [3]rotaxane **3.8** may be attributed to the two macrocycles shielding the metal centre from solvent molecules, which in turn

could reduce non-radiative emission. Importantly, these results suggest that the mechanical bond could be used as an efficient strategy to enhance the Φ_{PL} in Ir(III) compounds.

Table 3.1: Photochemical data of Ir(III) based compounds **3.4**, **3.5**, **3.8** and **3.9**.[a]

Compound	λ_{ems} (nm)	Φ_{PL} (%)
3.5 (bis azide)	627	1.6
3.4 (bis triazole)	637	1.6
3.8 ([3]Rot.)	639	2.7
3.9 ([2]Rot.)	634	2.3

[a] Measured in aerated CH_3CN, at 298 K at excitation wavelength 400 nm, using $[Ru(bpy)_3]Cl_2$ as the standard (Φ_{PL}=1.80%, in aerated conditions).

3.2.4. Electrochemical properties of Ir(III) complexed receptors***

The electrochemical properties of all four Ir(III) complexed receptors (**3.4**, **3.5**, **3.8**, **3.9**) were investigated in dry degassed CH_3CN with $TBAPF_6$ electrolyte. All potentials were measured with respect to ferrocene ($Fc|Fc^+$) redox couple as an internal reference. Figure 3.8 depicts a representative example of the electrochemical analysis of acyclic Ir(III) receptor **3.4**. Cyclic voltammetry (CV) and square wave voltammetry (SWV) experiments revealed a prominent sharp oxidative peak at ~ 0.9 V for all receptors, which was attributed to the Ir(III)/Ir(IV) redox couple (Figure 3.8a/b). The observed reductive peaks were ascribed to ligand-centred reduction, based on the data of similar compounds reported in the literature.[288,292,293] When the potential range was limited to the window expected for the Ir(III)/Ir(IV) couple, a well-defined, one electron redox wave was observed with quasi-reversibility in all cases (Figure 3.8c). A linear relationship was observed for plots of peak current (i_p) against the square root of the scan rates ($v^{0.5}$), showing that the redox transducer is under diffusive conditions in all

*** Electrochemical studies were performed by Dr. Robert Hein and Ms. Sophie Patrick

cases (Figure 3.8d). These electrochemical observations are in agreement with similar cyclometalated Ir(III) complexed structures.[288,292,294]

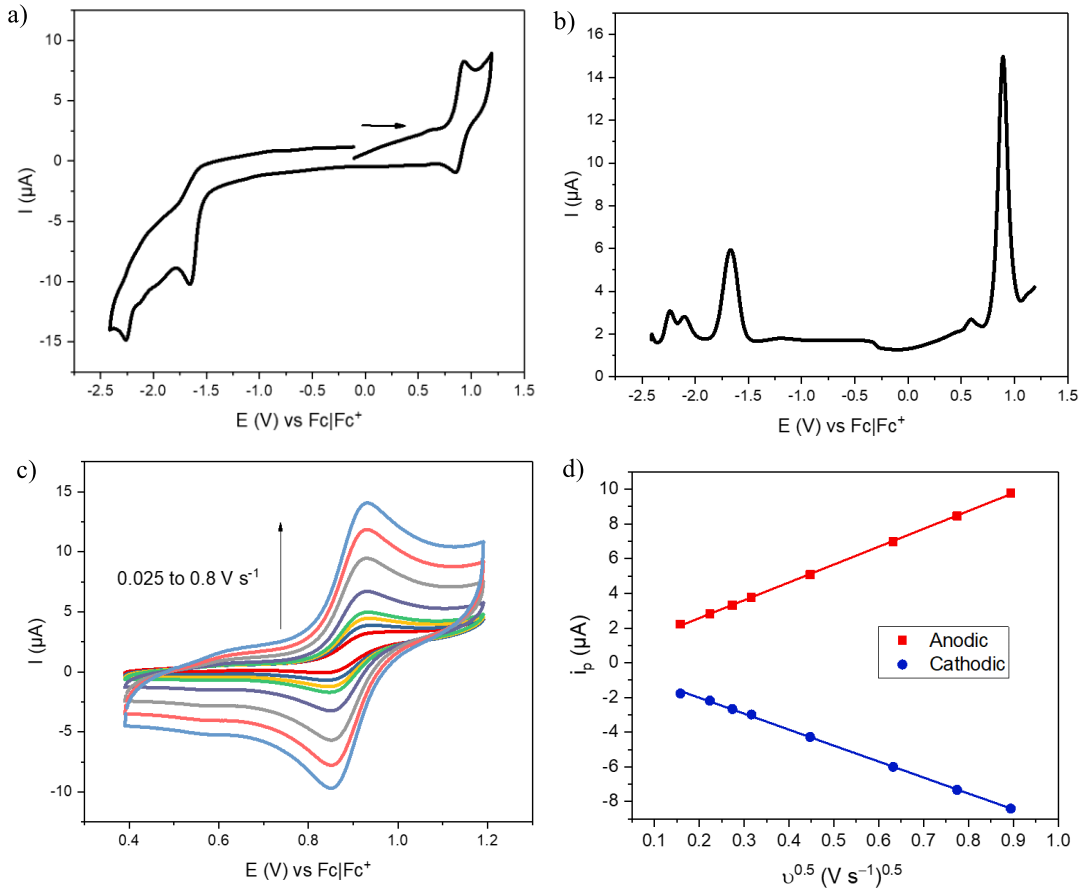

Figure 3.8: Electrochemical studies of bis iodo-triazole host **3.4** (0.25 mM) in dry, degassed CH_3CN (100 mM $TBAPF_6$): a) Cyclic voltammogram, arrow indicates the direction of scan, b) Square wave voltammogram, c) Cyclic voltammograms at varying scan rates (0.025-0.8 V/s), d) Plots of peak potential (i_p) vs the square-root of the scan rate ($v^{0.5}$) determined from cyclic voltammograms at varying scan rates shown in c.

The observed half-wave potentials ($E_{1/2}$) of all receptors are listed in Table 3.2. Reported work on similar cyclometallated Ir(III) complexes has demonstrated $E_{1/2}$ increases, becomes more anodic, with the addition of electron-withdrawing substituents to the bipyridine motif.[288,289,294] Accordingly, in comparison to the bis-azide Ir(III) precursor complex **3.5**, despite the insulating methylene spacer groups, the two electron-withdrawing iodo-triazole

motifs of **3.4** results in an increase of 22 mV (anodically, vs $Fc|Fc^+$ in CH_3CN) of the $E_{1/2}$ of this acyclic receptor, signifying a ~11 mV increase in $E_{1/2}$ per iodo-triazole unit. Notably, the acyclic receptor **3.4** and the [3]rotaxane **3.8** have two iodotriazole groups; hence, the through bond inductive effect caused by the complexed Ir(III) metal centre in both receptor systems should result in similar electrochemical properties. Nevertheless, a further increase of 21 mV in the $E_{1/2}$ value was observed for the [3]rotaxane **3.8** in comparison to the acyclic receptor **3.4.** As this is not a consequence of the through bond inductive effect, this increase in $E_{1/2}$ may be attributed to the mechanical bond of the interlocked [3]rotaxane. Therefore, the enhanced stabilisation of the Ir(III) oxidation state in the MIM **3.8** (i.e. the Ir(III)/Ir(IV) redox couple is more oxidising) is presumably due to the solvent exclusion from the Ir(III) metal centre caused by the two macrocycles on either side. The [2]rotaxane **3.9** has an Ir(III) complexed bipyridine with a CH_2-N_3 and a CH_2-iodotriazole substituent. Hence, based on through bond substituent effects alone, the $E_{1/2}$ of the [2]rotaxane **3.9** would be expected to have a value between that of **3.4** and **3.5**. However, $E_{1/2}$ (**3.9**) > $E_{1/2}$ (**3.4**) >$E_{1/2}$ (**3.5**) suggests an additional mechanical bond stabilisation of the Ir(III) metal centre due to the presence of the macrocycle in the [2]rotaxane structure of **3.9** resulting in the more anodic value of the Ir(III)/Ir(IV) redox couple.

Table 3.2: Electrochemical data of Ir(III) receptors.[a]

Compound	No. of Trz.	No. of MC	$E_{1/2}$ vs $Fc|Fc^+$ (mV)	ΔE per Trz. (mV)	ΔE per MC (mV)
3.5 (bis azide)	0	0	883	-	-
3.4 (bis triazole)	2	0	905	11	-
3.8 ([3]Rot.)	1	2	926	11	11
3.9 ([2]Rot.)	1	1	907	11	13

[a] Electrochemical studies were conducted in dry, degassed CH_3CN (100 mM $TBAPF_6$), [host] = 0.25 mM, Trz: Triazole motifs, MC: Macrocycle

3.2.5. Anion binding studies of the Ir(III) based acyclic, [3]rotaxane, and [2]rotaxane receptors

3.2.5.1. *Preliminary ^{1}H NMR titration experiments*

To initially investigate the anion binding behaviour of Ir(III) based acyclic **3.4** and [3]rotaxane **3.8**, receptors, qualitative ^{1}H NMR titration experiments were performed in CD_3CN. Due to the low solubility of TBA dicarboxylate anion salts in this solvent, preliminary ^{1}H NMR studies were carried out at 10^{-4} M host concentrations employing the 700 MHz, AV700 NMR spectrometer. The ^{1}H NMR spectra of [3]rotaxane **3.8** and acyclic receptor **3.4** upon addition of TBA-glutarate and TBACl are shown in Figure 3.9a/b. Glutarate binding to **3.8** caused the rotaxane's axle component proton signals H_e, H_h, and H_f, between the two iodotriazole donors to be perturbed significantly. Interestingly, H_h proton, which is initially split due to the asymmetric environment, becomes symmetric upon adding 2.0 eq. of glutarate. Also, the macrocycle component amide protons H_3 and internal benzene proton H_2 are deshielded, and H_4 and H_5 protons are perturbated, indicative of the dicarboxylate anion binding proximal to the amide groups of the macrocycle. However, when TBACl was added to **3.8** (Figure 3.10), H_h proton remained split as a quartet presumably due to different host-guest binding modes of monodentate and bidentate anions. Progressive perturbations of internal bipyridyl proton H_α and H_δ protons between the two XB donors were observed upon addition of glutarate to acyclic receptor **3.4** (Figure 3.9c), suggesting anion binding proximal to the iodo-triazole binding cavity.

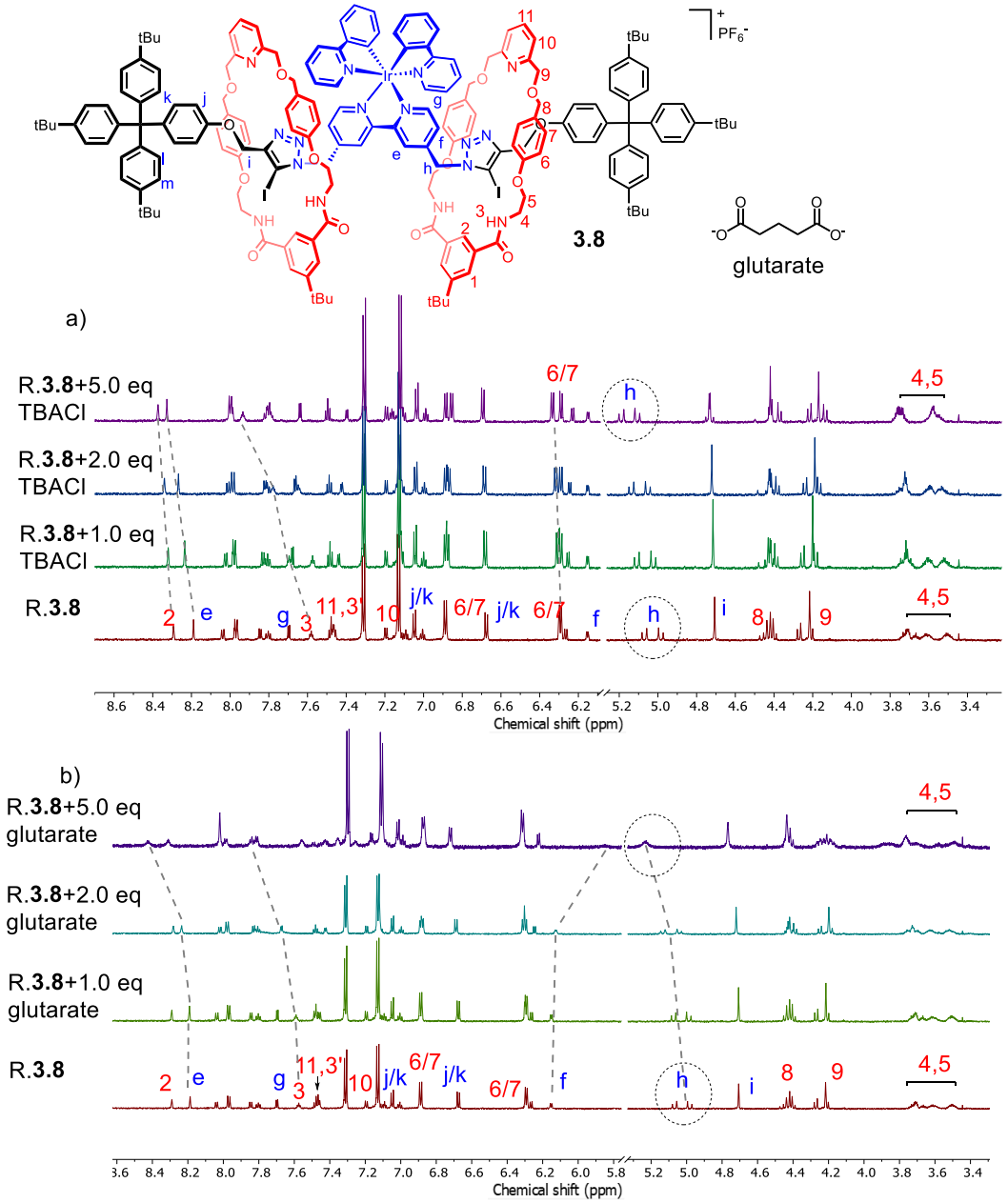

Figure 3.9: ^{1}H NMR titration spectra of a) [3]rotaxane **3.8** upon addition of TBACl, b) [3]rotaxane **3.8** upon addition of glutarate.

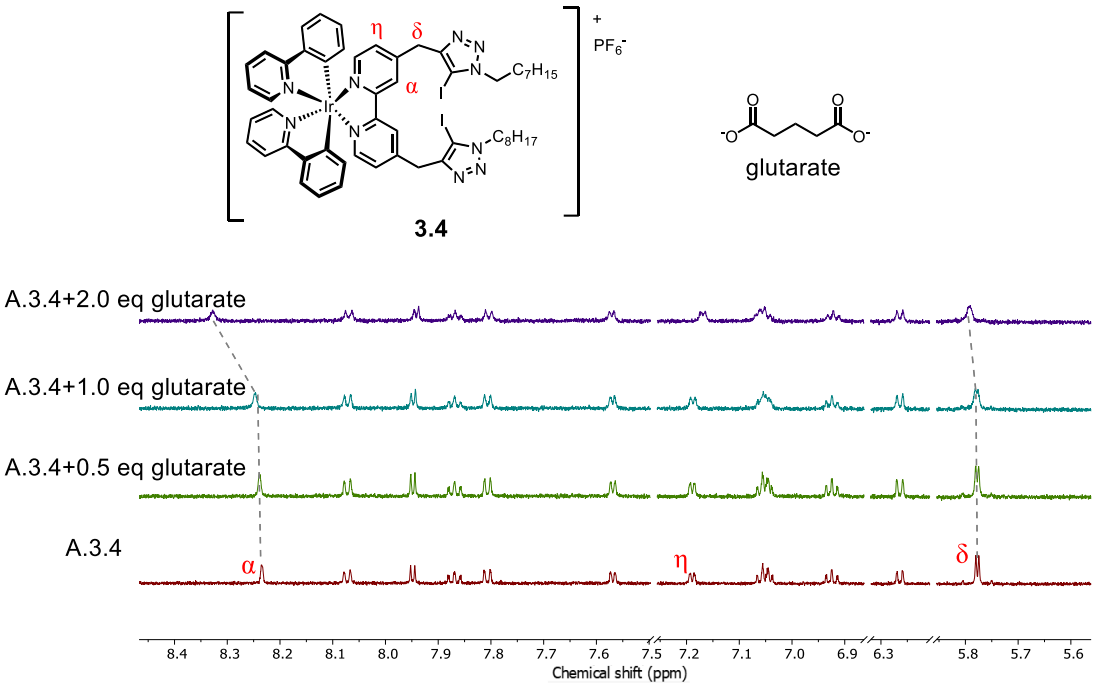

Figure 3.10: ^{1}H NMR titration spectra of acyclic receptor **3.4** upon addition of glutarate. All spectra were recorded in CD_3CN (700 MHz, 298 K)

3.2.5.2. *Luminescence spectroscopic anion titrations*

The [3]rotaxane **3.8** was designed to have the luminescent Ir(III) group between the two mechanically bonded interlocked XB/HB donor anion binding sites. Dicarboxylate dianions were expected to bind in a 1:1 stoichiometric host-guest fashion, rigidifying the interlocked components proximal to the photo-active Ir(III) centre, thereby inducing a luminescent sensory response. Luminescence spectroscopic titration experiments were conducted in dry degassed CH_3CN to investigate the anion sensing properties of the Ir(III) complexed rotaxanes **3.8** and **3.9,** and acyclic receptor **3.4**. Preliminary qualitative luminescence anion sensing studies were performed by adding up to 500 eq. of TBA-dicarboxylate anions to 10^{-6} M CH_3CN solution of Ir(III) hosts. Representative titration spectra of receptors upon addition of isophthalate are depicted in Figure 3.11. With all three receptors, an increase in the emission intensity of the respective MLCT band was observed, concomitant with a hypsochromic shift in λ_{max}. This blue shift can be attributed to the increase in π^*_{bpy} energy

level upon anion binding, which increases the HOMO-LUMO energy gap.[292] The enhancement in emission intensity can be explained by the *rigidity effect*; the formation of the anion-receptor complex increases the rigidity of the receptor, thereby disfavouring non-radiative decay processes.[295]

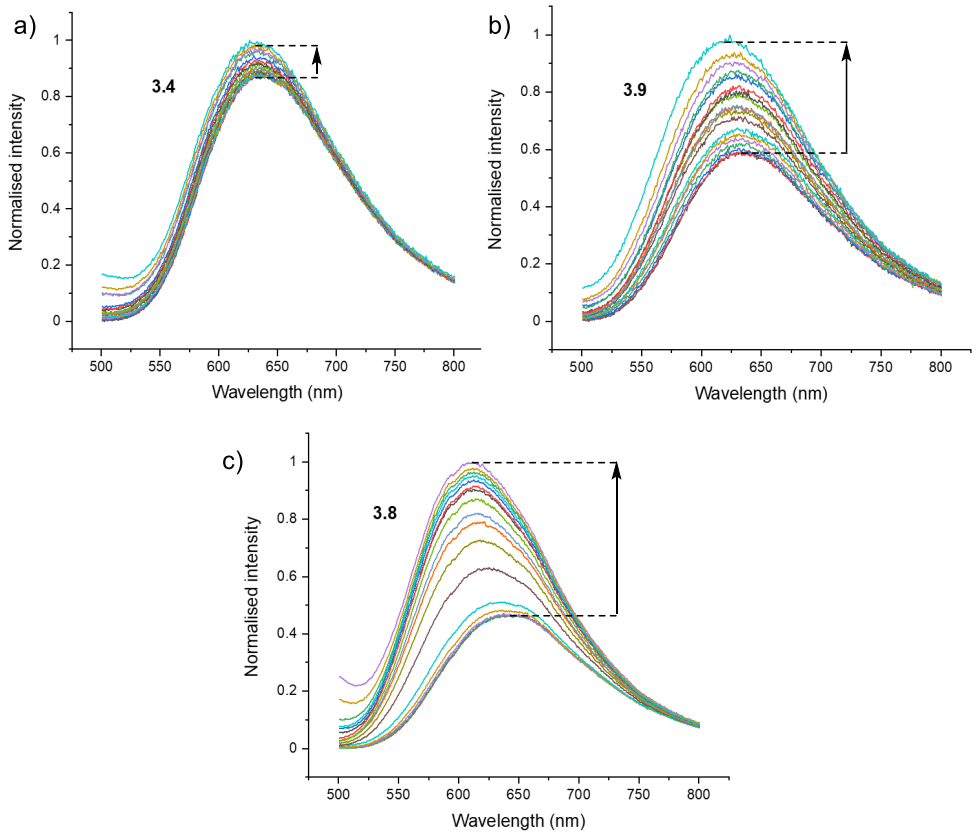

Figure 3.11: Luminescence titration spectra of acyclic receptor **3.4**, [2]rotaxane **3.9** and [3]rotaxane **3.8** upon sequential addition of up to 500 eq. of TBA-isophthalate. Titrations were performed in CH_3CN, [host]=10^{-6} M.

Quantitative luminescence titration experiments were conducted by sequential addition of TBA-dicarboxylate anion salts to a 10^{-6} M solution of Ir(III) hosts in CH_3CN as described in the Experimental Section. A global fit analysis of luminescence titration data using Bindfit software,[228,229] determined 1:1 stoichiometric host-dicarboxylate guest association constants displayed in Table 3.3. The binding constants are depicted pictorially in Figure 3.12 for greater ease of comparison. As expected, the [3]rotaxane **3.8** forms the strongest

dicarboxylate complexes, utilising its two anion binding sites capable of forming multiple cooperative XB and HB interactions.

The acyclic receptor **3.4** exhibits a selective optical response for phthalate over its geometric isomers isophthalate and terephthalate. This could be due to the proximity of the carboxylate groups in phthalate which is complementary to the distance between the two iodotriazole anion binding sites of **3.4**. However, in the [3]rotaxane, the two anion binding sites are further apart due to the presence of the two macrocycles. Consequently, [3]rotaxane displays a progressive increase in association constant values with increasing distance between the carboxylate groups: phthalate< isophthalate < terephthalate. The [2]rotaxane **3.9** showed enhanced binding of isophthalate over terephthalate in an analogous fashion to the acyclic receptor **3.4**. Following a similar trend, the acyclic host **3.4**, selectively binds maleate over its geometric isomer fumarate, while the [3]rotaxane **3.8** and the [2]rotaxane **3.9** exhibited stronger binding to fumarate.

Succinate, glutarate and adipate are structurally homologous dicarboxylates containing a flexible methylene spacer group. The [3]rotaxane **3.8** showed a notable increase in association constant magnitudes with increasing length of the methylene spacer from succinate to glutarate and a marginal increase from glutarate to adipate, while the acyclic receptor only showed a measurable increase in emission response for succinate and glutarate with a smaller binding constant for the latter. The [2]rotaxane displayed the largest binding constant for adipate followed by succinate and glutarate.

Importantly, among the Ir(III) complexed receptors, the [3]rotaxane displayed the highest increase in luminescence intensity (>100%, in 500 eq. of anion) in the presence of dicarboxylate anions, at a receptor concentration as low as 10^{-6} M. This enhancement in luminescence can be attributed to the rigidification of interlocked components proximal to the photo-active Ir(III) centre, reducing non-radiative decay processes.[295]

Table 3.3: Binding constants (K_a) and percentage increase in emission intensity (upon addition of 500 eq. of anion) of **3.4**, **3.8** and **3.9** hosts with different dicarboxylate anions.[a]

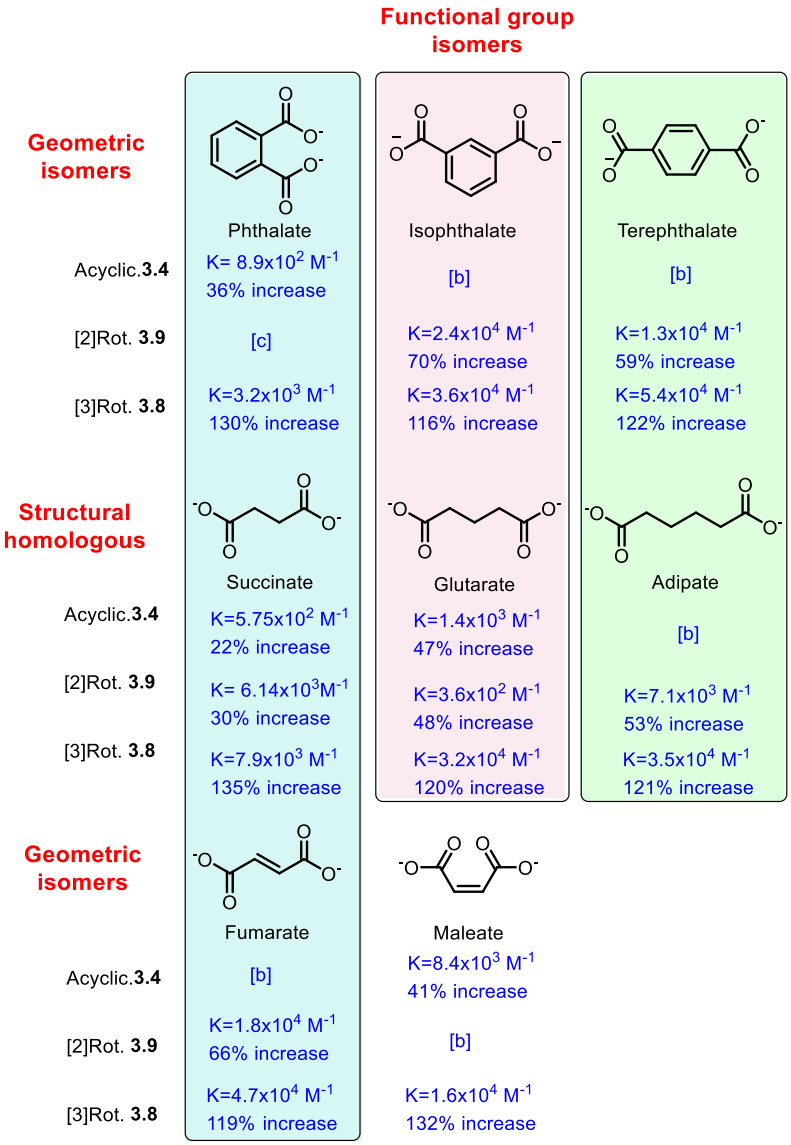

[a] Dicarboxylate anions are added as TBA salts. Titrations were performed in dry degassed CH_3CN. Errors are less than 10%. [b] Change in emission intensity was too small (<15%) to accurately determine K_a, [c] Complex equilibria.

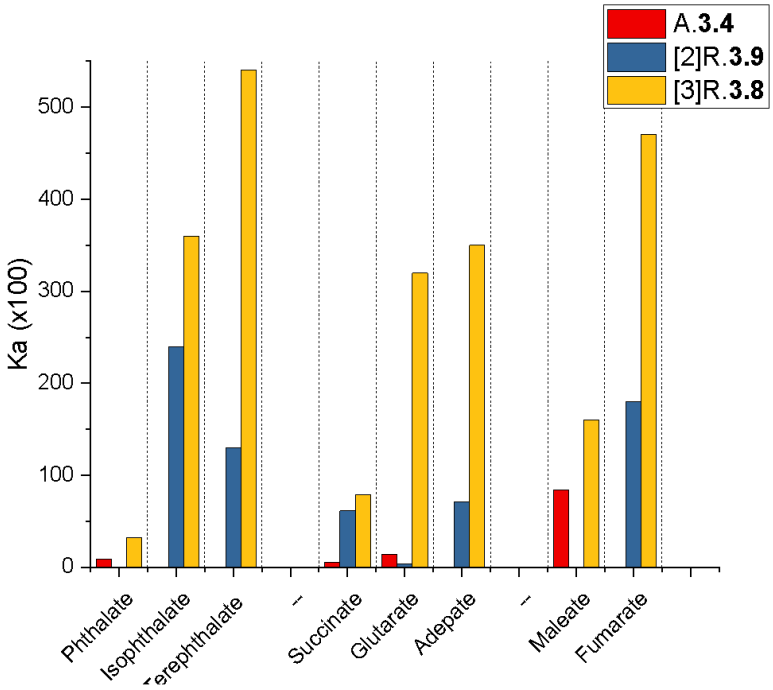

Figure 3.12: Bar chart showing the variations in K_a/M^{-1} values pictorially between different dicarboxylate anions

Attention then turned to investigating binding properties of monodentate inorganic anions with Ir(III) receptors **3.4**, **3.8** and **3.9**. To this end, luminescence titrations were conducted in CH_3CN using a similar procedure used to investigate the binding properties of dicarboxylate anions. Representative emission spectra of receptor **3.4**, **3.8** and **3.9** with the addition of Cl^- and OAc^- are shown in Figure 3.13. The percentage change in intensity upon addition of 500 eq. of anions is shown in Table 3.4. Except for I^- which caused a quenching response, the addition of monodentate anions did not significantly affect the emission intensity of the acyclic host **3.4.** [2]rotaxane **3.9** displayed a noteworthy change in emission intensity only on addition of I^- and AcO^-. However, the emission intensity of [3]rotaxane **3.8** showed a notable increase with the addition of Cl^- and AcO^- and was quenched in the presence of I^-. The observed quenching of MLCT emission intensity upon addition of I^- is likely to be due to the heavy atom effect of the halide.[296]

Bindfit analysis of the luminescence titration data determined host-guest association constants for monodentate anions. A 1:1 host-guest stoichiometric model was found to be the best fit for all anions, with the notable exception of Cl^- where a 1:2 host-guest binding model determined meaningful quantitative data (Table 3.4). The [2]rotaxane **3.9** showed superior binding of AcO^- over I^-. The [3]rotaxane **3.8** displayed the strongest binding for Cl^- and AcO^- over I^-. It is important to note that the [3]rotaxane **3.8** exhibited strong binding and high sensitivity for monodentate anions compared to the analogous [2]rotaxane **3.9** and the acyclic host **3.4**. However, the change in emission intensity upon adding monodentate anions are significantly less (22%-40%) compared with the enhancement percentage magnitudes in emission intensity observed upon addition of dicarboxylate anions (>100%) (Table 3.4, Table 3.3).

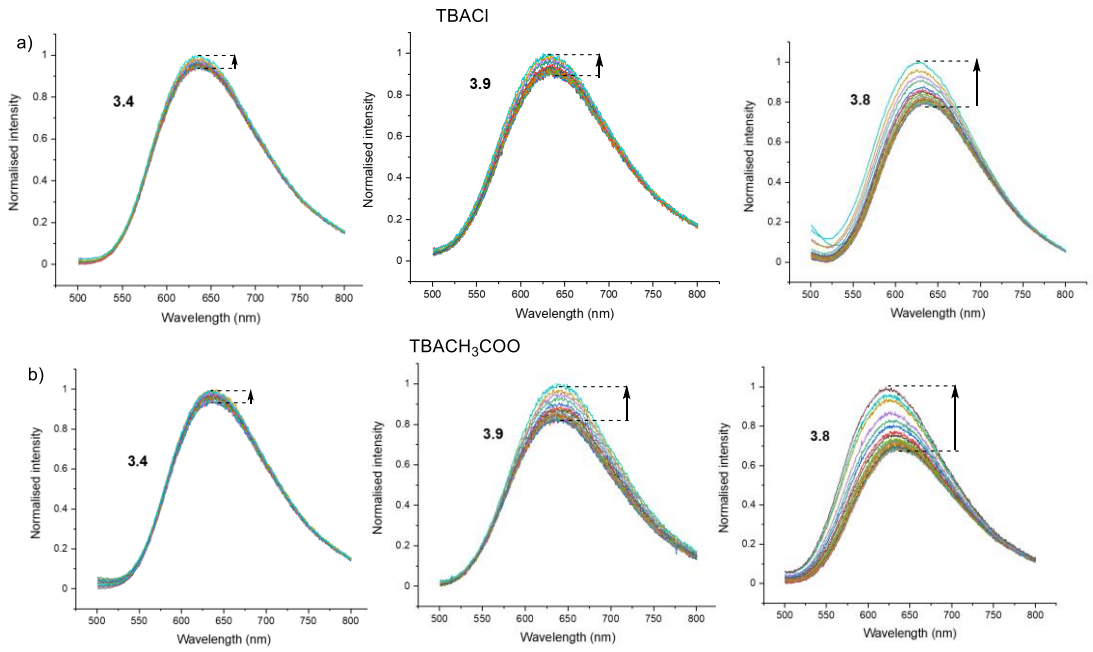

Figure 3.13: Luminescence titration spectra of acyclic receptor **3.4**, [2]rotaxane **3.9** and [3]rotaxane **3.8** upon sequential addition of up to 500 eq. of a) TBACl, b) $TBACH_3COO$. Titrations were performed in CH_3CN, [host]=10^{-6} M.

Table 3.4: Binding constants (K_a) and percentage increase in emission intensity (upon addition of 500 eq. of anion) of **3.4**, **3.8** and **3.9** hosts with different monodentate anions.[a]

	Halides			Oxoanion
	Cl^-	Br^-	I^-	CH_3COO^-
Acyclic.**3.4**	[b]	[b]	$K= 4.18x10^2\ M^{-1}$ 23% decrease	[b]
[2]Rot. **3.9**	[b]	[b]	$K= 7.90x10^2\ M^{-1}$ 20% decrease	$K=5.13x10^3\ M^{-1}$ 23% increase
[3]Rot. **3.8**	$K= 3.19x10^3\ M^{-1}$ 23% increase $K_1= 2.07x10^5\ M^{-1}$ $K_2= 2.50x10^3\ M^{-1}$	[b]	$K= 5.38x10^2\ M^{-1}$ 23% decrease	$K= 3.31x10^3\ M^{-1}$ 42% increase

[a]Anions are added as TBA salts. Titrations were performed in dry degassed CH_3CN. Errors are less than 10%. [b] Change in emission intensity was too small (<15%) to accurately determine K_a.

3.2.5.3. *Preliminary electrochemical anion sensing studies*†††

After confirming the redox reversibility of Ir(III) based receptors **3.4**, **3.8** and **3.9** (Section 3.2.4), qualitative electrochemical anion sensing properties were probed by CV in a electrolyte solution of 0.1M $TBAPF_6$ in CH_3CN. CVs were recorded upon addition of increasing quantities of TBA anion salts and the magnitude of anion-induced cathodic shifts ($\Delta E_{1/2}$) were monitored for all receptors.

Unfortunately, TBA-dicarboxylate anion salts were not soluble at the required concentration of 50 mM in CH_3CN to investigate the redox anion sensing properties of the Ir(III) based receptors by CV. Therefore, attention focused on the electrochemical sensing of monodentate inorganic anions. The stepwise addition of up to 50 mM HSO_4^- induced a cathodic perturbation of the $E_{1/2}$ Ir(III)/Ir(IV) redox couple in all receptors, with a $\Delta E_{1/2}$ of -24 mV, -25 mV and -40 mV observed for the acyclic host **3.4**, [2]rotaxane **3.9** and [3]rotaxane

††† Electrochemical studies were performed by Dr. Robert Hein and Ms. Sophie Patrick

3.8 respectively. However, these anion bound receptor systems suffered from poor reversibility as shown by the representative example of the SWV of HSO_4^- bound [3]rotaxane in Figure 3.14a. Subsequently, the electrochemical sensing of OAc^- by the acyclic host **3.4** was investigated. However, as shown in Figure 3.14b, **3.4** displayed a complex voltammetry whereby a large initial cathodic perturbation was observed followed by anodic shifts.

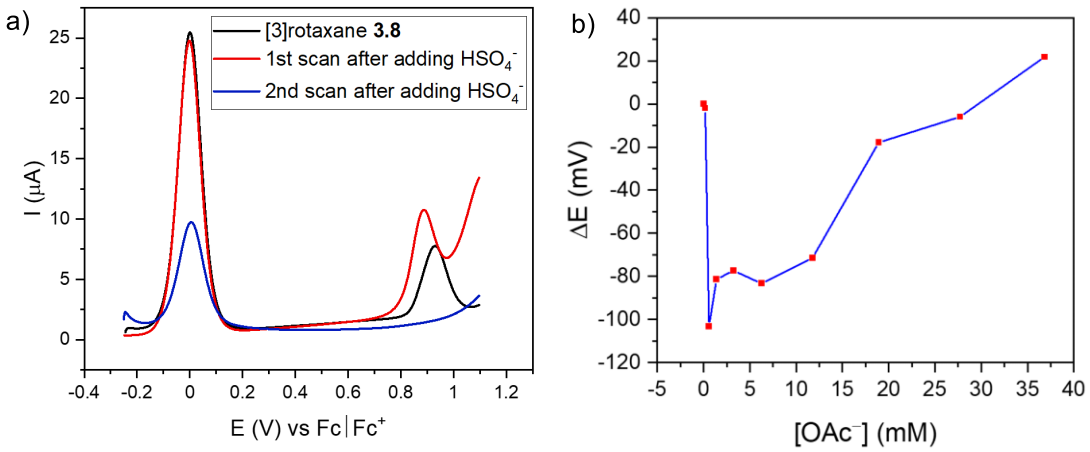

Figure 3.14: a) SWVs of [3]rotaxane **3.8** (0.25 mM) in ACN (100 mM $TBAPF_6$) with $Fc|Fc^+$ couple as an internal standard. (black line-[3]rotaxane in the absence of guest ions, red and blue lines- 1st and 2nd scan of after the addition of HSO_4^-), b) Cathodic perturbations of the half-wave potential ($E_{1/2}$) of acyclic host **3.4** in response to increasing concentrations of OAc^- in ACN (100 mM $TBAPF_6$). A constant ionic strength of 100 mM was maintained throughout.

3.3. Conclusions and Future work

In conclusion, the first example of a luminescent transition metal complexed [3]rotaxane **3.8** for the purpose of anion recognition was synthesised, together with a [2]rotaxane by-product **3.9**, and their dicarboxylate anion recognition and sensing capability are investigated. Compared to acyclic Ir(III) compounds **3.4** and **3.5**, the mechanically interlocked rotaxane hosts displayed significantly higher luminescence quantum yields. Importantly, luminescence anion titration experiments revealed the [3]rotaxane **3.8** to exhibit the largest association constant values towards dicarboxylates over halide anions, compared to the [2]rotaxane **3.9** and acyclic receptor **3.4**. The strong binding of dicarboxylate anions,

mediated by the two axle XB iodo-triazoles flanking the Ir(III) luminophore of the higher order rotaxane, rigidifies the dynamic interlocked components, leading to significant increases in MLCT emission band luminescence intensity. Additionally, the Ir(III) based hosts were able to differentiate geometric isomers of dicarboxylates based on the proximity of the carboxylate groups. For example, the acyclic receptor **3.4** displayed the selectivity trend of phthalate> isophthalate/terephthalate, and maleate > fumarate. By contrast, the [3]rotaxane **3.8** showed selectivity for dicarboxylates with carboxylate groups further apart; terephthalate > isophthalate > phthalate; fumarate > maleate, and adipate > glutarate > succinate. Importantly, these results demonstrate the potential of using transition metal based mechanically interlocked [3]rotaxanes for selective and efficient sensing of dicarboxylate anions.

Future work will focus on synthesising and investigating the anion sensing properties of a series of all XB mechanically interlocked [3]rotaxanes containing photo- and redox-active second and third-row transition metals such as Os(II) and Ru(II) and Ir(III) (Figure 3.15). As discussed in Chapter 2 (Part II), it is envisaged that the [3]rotaxane design would facilitate the binding of bidentate dicarboxylate anions through exodentate XB receptor···anion interactions. Additionally, the axle iodotriazole donor group separation of **3.8** could be fine-tuned to construct receptors with high selectivity for specific dicarboxylate anions.

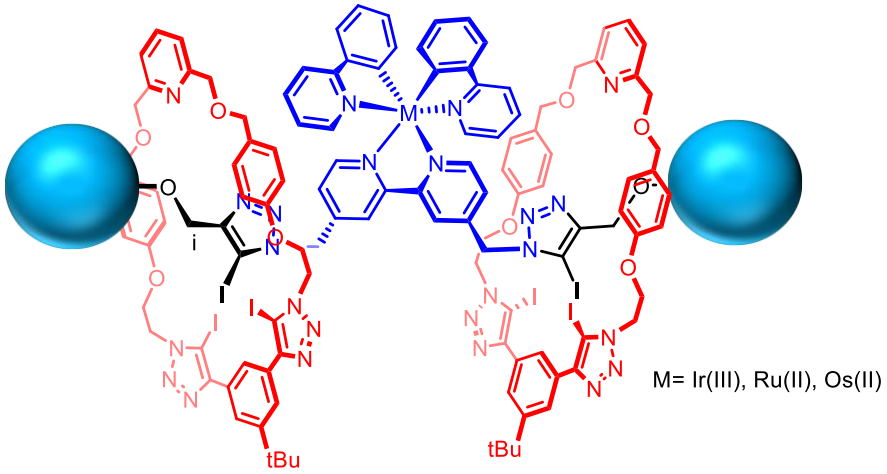

Figure 3.15: Proposed optically active all XB [3]rotaxane hosts with Ir(III), Ru(II) and Os(II) metal centres

Chapter 4

Halogen bonding rhenium(I) complexed tweezer type receptors for anion recognition

Chapter 4: Halogen bonding rhenium(I) complexed tweezer type receptors for anion recognition

4.1. Introduction

4.1.1. Tweezer receptors

Molecular tweezers are synthetic receptors made of two arms containing guest binding sites connected through a spacer group.[297] As shown in Figure 4.1, the spacer group holds the two binding sites in spatial proximity, facilitating strong guest binding through the formation of concerted interactions. The binding sites of the tweezers can consist of various supramolecular interactions, including HB,[298] XB,[299] electrostatic,[300] or π-π interactions.[301] The selectivity of tweezer receptors can be fine-tuned by modifying the spacer group and supramolecular interactions in the binding site.[297,302,303]

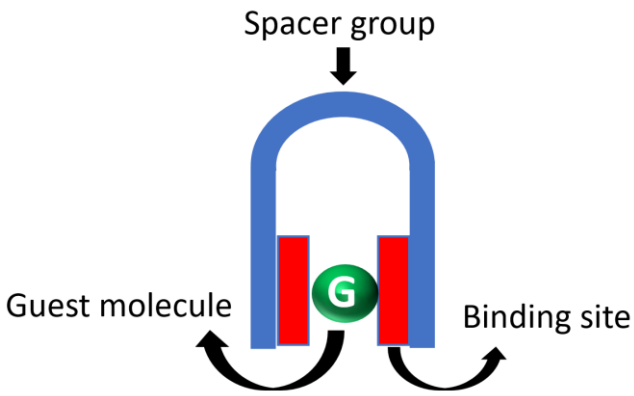

Figure 4.1: Cartoon representation of a molecular tweezer.

The molecular tweezer design has often been employed for the selective recognition of anions. In one example, Ghosh and co-workers synthesised a tweezer receptor (Figure 4.2a) for the selective recognition of dicarboxylate guest species.[298] The receptor binds pimelate ($^{-}$OOC-$(CH_2)_n$-COO^{-}, n=5) more strongly than a range of dicarboxylates with shorter (n=1-4) and

longer (n=6) distances between the carboxylate groups in DMSO. This selectivity for pimelate was attributed to the complementary size of the dianion to the distance between the benzamido pyridinium arms of the tweezer.

Molina and co-workers synthesised a series of XB pyrene-based bromo- and iodo-triazolium containing tweezer-type fluorescent chemosensors depicted in Figure 4.2b.[299] Upon addition of $HP_2O_7^{3-}$ in acetone, all receptors, including mixed XB/HB and all HB proto-triazolium analogues, displayed a fluorescence enhancement due to the formation of the pyrene excimer complex. Interestingly, both ^1H NMR and fluorescence spectroscopy studies revealed the XB halotriazolium tweezers to bind $HP_2O_7^{3-}$ much more strongly than the HB and mixed XB/HB tweezers, indicating superior anion binding properties of XB donors.

Incorporating two or more zinc(II)-dipicolylamine (ZnDPA) motifs into an anion receptor structural framework is an efficient strategy to use for the selective recognition of phosphate-derived substrates.[304] Figure 4.2c depicts a tweezer-type receptor with two ZnDPA anion binding sites bridged via a diketopiperazine spacer group.[300] The receptor displayed a notable selectivity for di- and tri-phosphate anions (PPi, ADP, ATP, GDP) over a range of monophosphate anions including hydrogen phosphate, AMP, cAMP, in aqueous solutions buffered at pH 7.4.

As discussed in Chapter 1, Section 1.4.3.3, transition metal complexation proximal to XB/HB donors can enhance anion binding by second sphere charge-assisted interactions. For example, when a transition metal is complexed proximal to a XB donor, it can polarise the XB donor, which leads to an increase in the size and the potency of the σ-hole, enhancing anion···XB interactions. Additionally, as shown in Chapter 3, transition metals possess well-defined geometries that can preorganise the anion binding site and influence the anion selectivity of the receptor. Despite these advantages, transition metal-based XB tweezer-type receptors are rare.

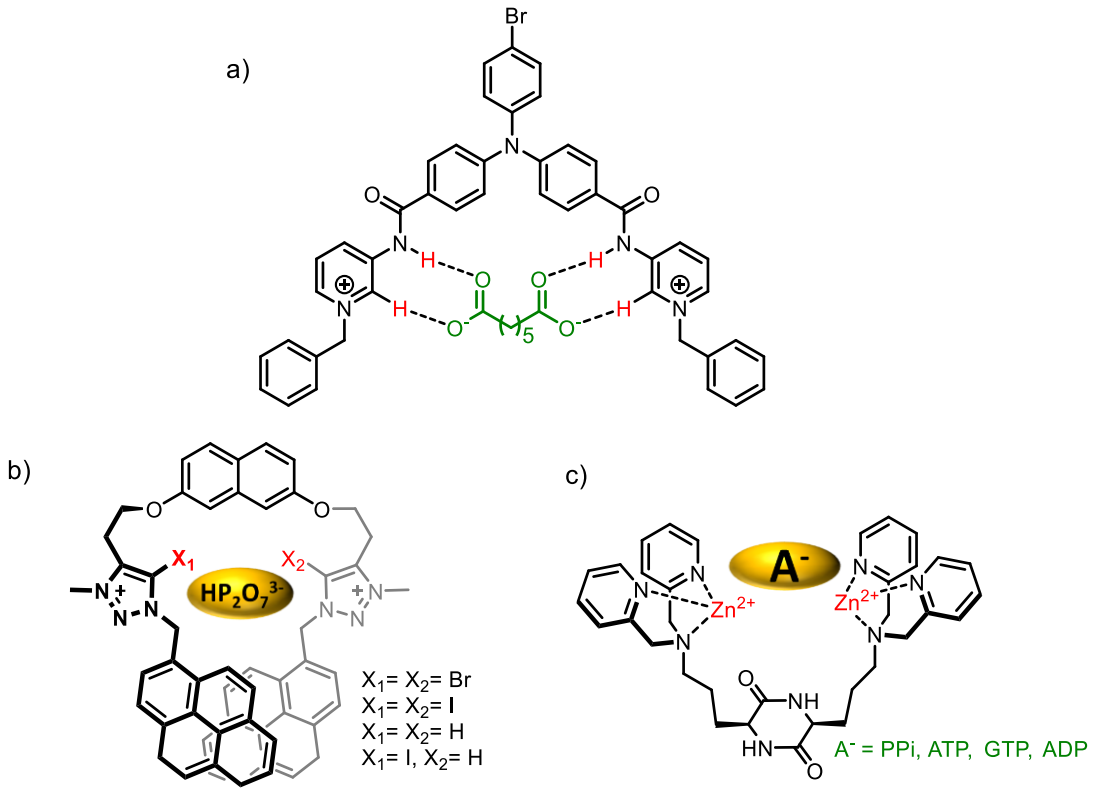

Figure 4.2: Anion tweezer receptors: a) Ghosh's receptor capable of selective dicarboxylate anion recognition,[305] b) Molina's photo-active $HP2O_7^{3-}$ receptor,[306] c) Joliffe's Zn(DPA) receptor.[307]

4.2. Chapter aims‡‡‡

This project aims to investigate how the anion binding properties of XB tweezer receptors can be improved by incorporating transition metals proximal to XB donor groups. To this end, a series of XB/HB monocationic and dicationic rhenium(I) tweezer type receptors are synthesised. Their anion binding properties are analysed in solution via ^{1}H NMR titration studies, and in the solid-state using single crystal X-ray structural analysis.

‡‡‡ This project was conducted in collaboration with Dr. Xiaxiong Li

4.3 Design and synthesis of Re(I) complexed XB/HB receptors

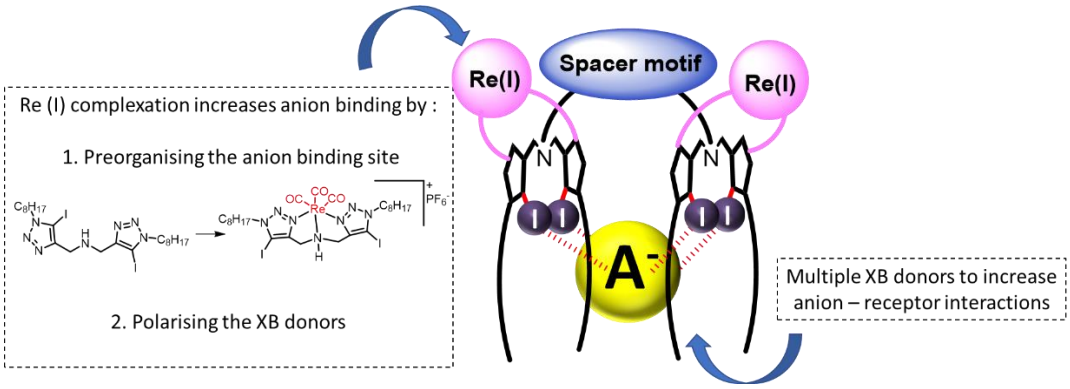

Figure 4.3: Schematic representation of the XB, Re(I) complexed tweezer-type anion receptor

Transition metals are commonly incorporated into anion receptor structural frameworks to preorganise the receptor and increase anion binding through favourable electrostatic interactions.[269] To this end, an anion receptor containing two monocationic $[Re(CO)_3]^+$ motifs covalently linked through a spacer group was designed (Figure 4.3). The receptor contains a tetradentate XB anion binding site which can bind anions in a tweezer-type manner. Complexation of Re(I) preorganises the anion binding site by directing the XB donors towards the anion binding cavity. Additionally, the positively charged Re(I) metal centre was expected to polarise the proximal XB donors, increasing anion···XB interactions.

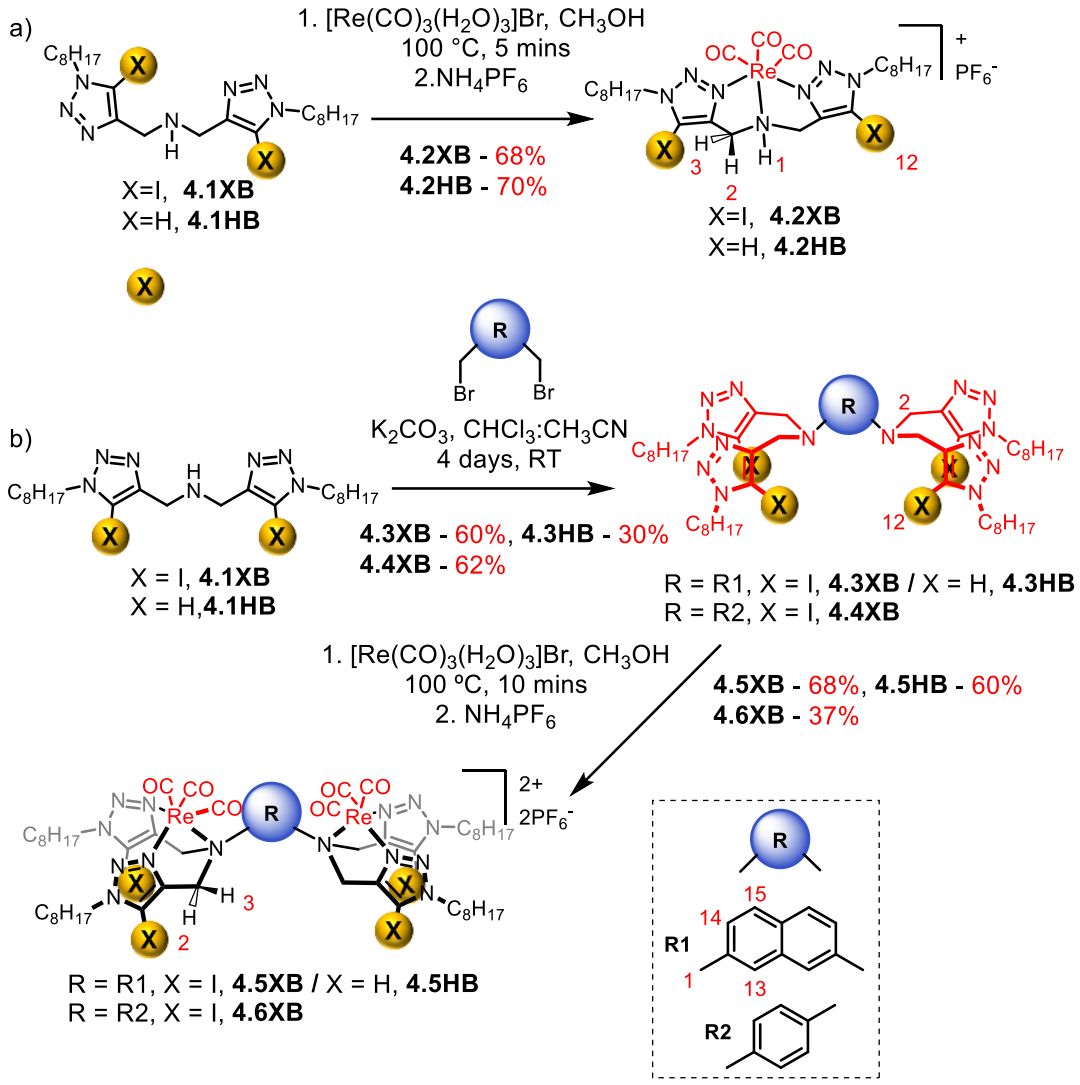

Scheme 4.1: Synthesis of XB/HB; a) monocationic Re(I) receptors **4.1** and **4,2** and b) dicationic Re(I) tweezer type receptors **4.3**-**4.6**

Initial attempts focused on synthesising Re(I) complexed XB/HB monocationic receptors **4.2XB/HB**. As depicted in Scheme 4.1a, the bis-triazole amine **4.1**[308] and $[Re(CO)_3(H_2O)_3]Br$[309,310] were suspended in CH_3OH, and the reaction mixture was heated at 100 °C for 5 mins under microwave reaction conditions. The resultant crude product was anion exchanged with NH_4PF_6 and purified by precipitation to obtain target XB and HB monocationic Re(I) receptors **4.2XB** and **4.2HB** in 68% and 70% yields respectively.

The dicationic Re(I) complexed receptors **4.3**-**4.6** were prepared according to Scheme 4.1b. The bis-triazole amine **4.1**[308] was reacted with 2,7-bis-bromomethyl naphthalene and 1,4-bis-bromomethyl benzene respectively in the presence of K_2CO_3 in a 1:1 CH_3CN:CH_3OH solvent mixture to form the XB/HB tweezer ligands **4.3** and **4.4**. Subsequently, **4.3** and **4.4** were reacted with $[Re(CO)_3(H_2O)_3]Br$ in CH_3OH at 100 ^oC for 10 mins under microwave reaction conditions to form bimetallic Re(I) complexed tweezer receptors. These reaction mixtures were then purified by preparative TLC and anion exchanged with NH_4PF_6 to afford the target dicationic tweezer receptors **4.5XB**, **4.5HB**, and **4.6XB**, in 68%, 60%, and 37% yields respectively. All the novel compounds were characterised by ^1H NMR, ^{13}C NMR, high-resolution ESI mass spectrometry. Single crystal X-ray diffraction structural analysis was performed for the Br^- and PF_6^- bound monocationic Re(I) **4.2XB** receptor and I^- bound dicationic Re(I) **4.6XB** receptor (Section 4.3.1).

^1H and ^{13}C NMR, FTIR and solid state characterisation confirmed the facial complexation mode of the synthesised cationic Re(I) compounds.[311,312] As shown in Figure 4.4a, ^{13}C NMR spectra of all Re(I) complexed hosts showed only two Re-CO peaks in the 190-200 ppm region which is characteristic for the facial complexation of $Re(CO)_3$. Rhenium(I) complexation was further confirmed by ^1H NMR spectroscopy, where a characteristic splitting of $H_{2/3}$ proton signals into two doublets was observed (Figure 4.4b/c). In accordance with the literature, the splitting of the proton signal followed a second order AB spin coupling pattern with a germinal coupling of $^2J \approx 16$ Hz.[312,313] This loss of symmetry can be attributed to the rigidification of $H_{2/3}$ methylene protons upon metal complexation, making them magnetically non-equivalent. FTIR spectra of Re(I) complexed **4.2XB** (Figure 4.5) shows two sharp metal-carbonyl absorption bands at 1917 cm^{-1} and 2035 cm^{-1} characteristic for the symmetry of facial complexation of $Re(CO)_3$.[311–313] Conclusive evidence for the facial complexation of $\{Re(CO)_3\}^+$ was obtained by solid-state structure analysis (Section 4.3.1).

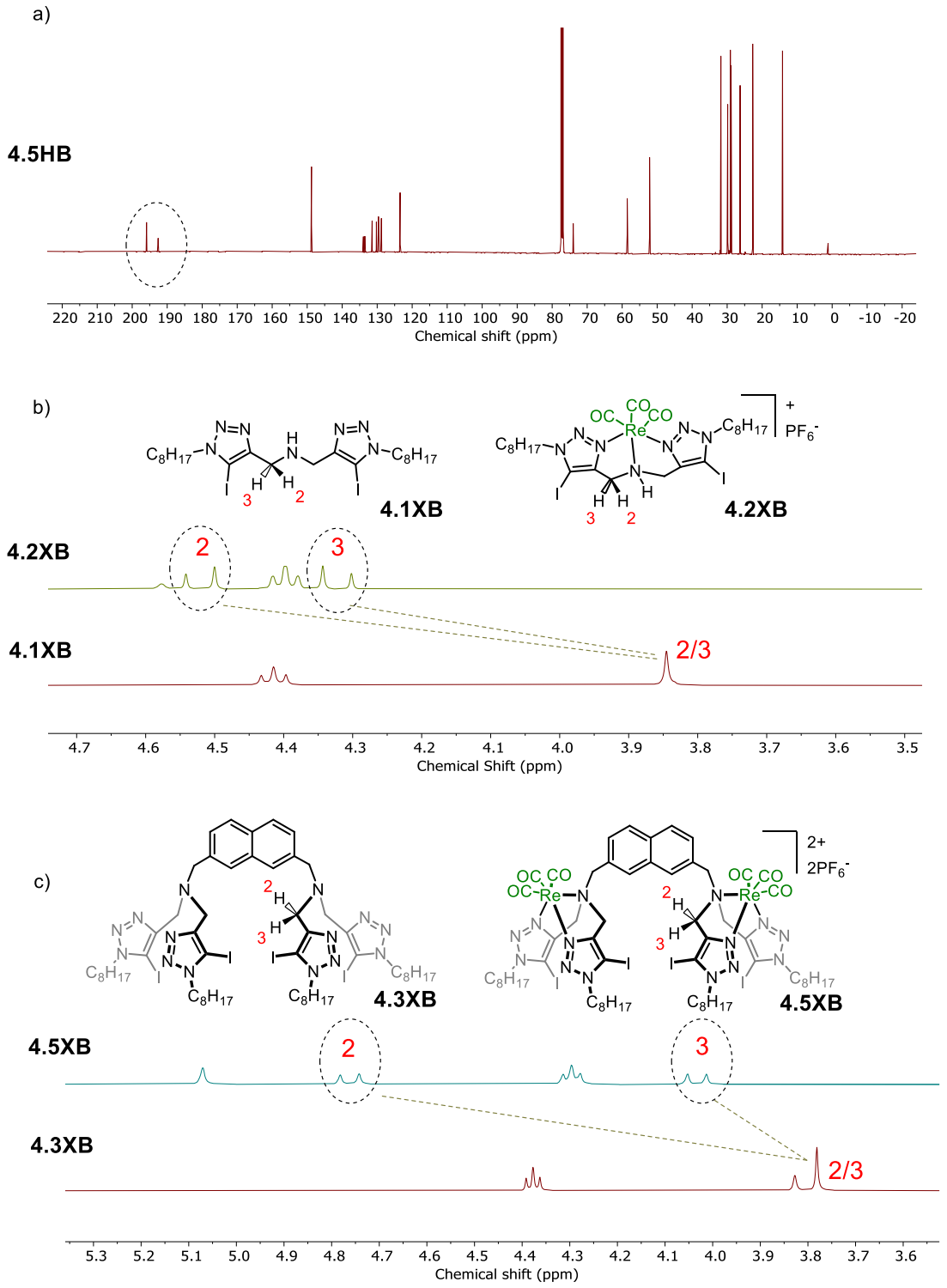

Figure 4.4: NMR spectra of receptors at 298 K; a) ^{13}C NMR spectra of **4.5HB** in $CDCl_3$, 128 MHz b) $^{1}HNMR$ spectra of **4.1XB** and **4.2XB** in CD_3OD, 400MHz, c) $^{1}HNMR$ spectra of **4.3XB** and **4.5XB** in CD_3CN, 400 MHz.

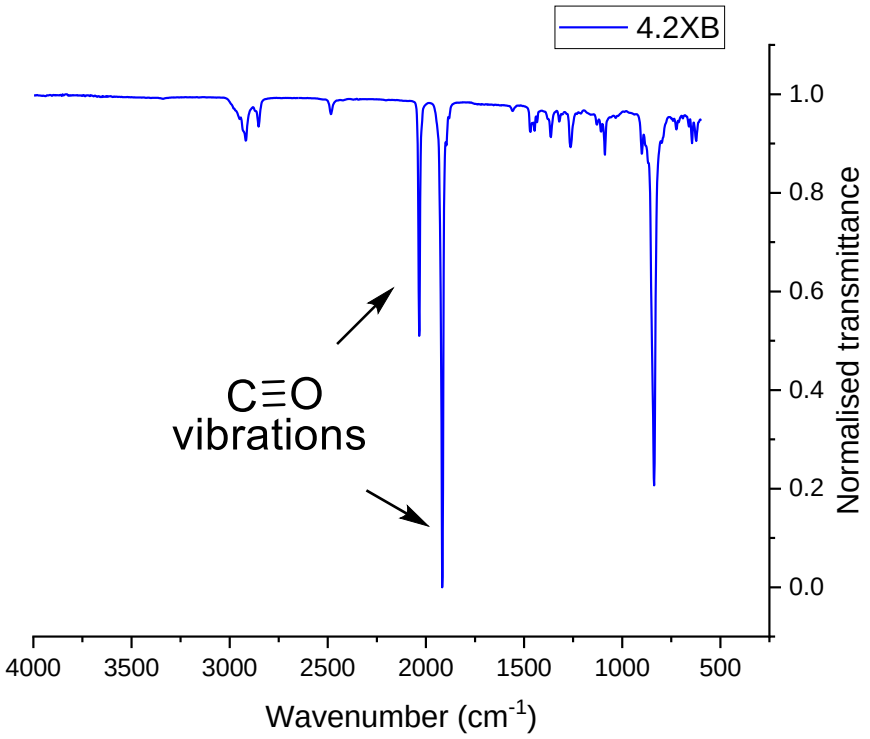

Figure 4.5: FTIR spectra of **4.2XB** indicative of Characteristic sharp metal carbonyl vibration bands

4.3. Anion binding studies

The anion binding properties of the monocationic and dicationic Re(I) receptors were investigated in solution by ^{1}H NMR titration studies, and in the solid state by single crystal X-ray diffraction structural analysis of anion bound receptors.

4.3.1. Solid state structure analysis of anion-bound receptors.[§§§]

Single crystals suitable for X-ray structural analysis of the Br^- and PF_6^- bound monocationic receptor **4.2XB** were obtained by slow evaporation of the respective salt in CH_3OH. As depicted in Figure 4.6, both solid state structures show Re(I) complexation to the parent

[§§§] X-ray crystallography data was collected and the solid state structures determined by Zongyao Zhang and Heike Kuhn

ligand **4.1XB** via two nitrogen donor atoms of adjacent iodotriazoles, and the nitrogen of the secondary amine. The three CO ligands are bound to Re(I) metal centre in a facial arrangement.

Further insight into anion binding modes were obtained by solid state structural analysis of the anion bound **4.2XB** receptor. In the facial Re(I) complexation mode, the two XB donors of the receptor are oriented away from each other, such that the two XB donors of the same molecule cannot form concerted interactions with a single anion. Consequently, a single Br^- /PF_6^- anion forms concerted interactions with triazole XB donors from neighbouring **4.2XB** molecules and an amine proton of a third molecule. **4.2XB**.Br showed near linear C-I···Br^-, XB interactions (174°) with a significant contraction of I···Br^- bond distances (85%) compared to the sum of van der Waals radii (r_{VdW}) of I and Br.[314] The less basic PF_6^- anion showed slightly weaker interactions in the solid state with a 170° average bond angle between C-I···PF_6^- and a reduction in I···PF_6^- bond distances (86%) compared to the sum of r_{VdW} of I and F.[315]

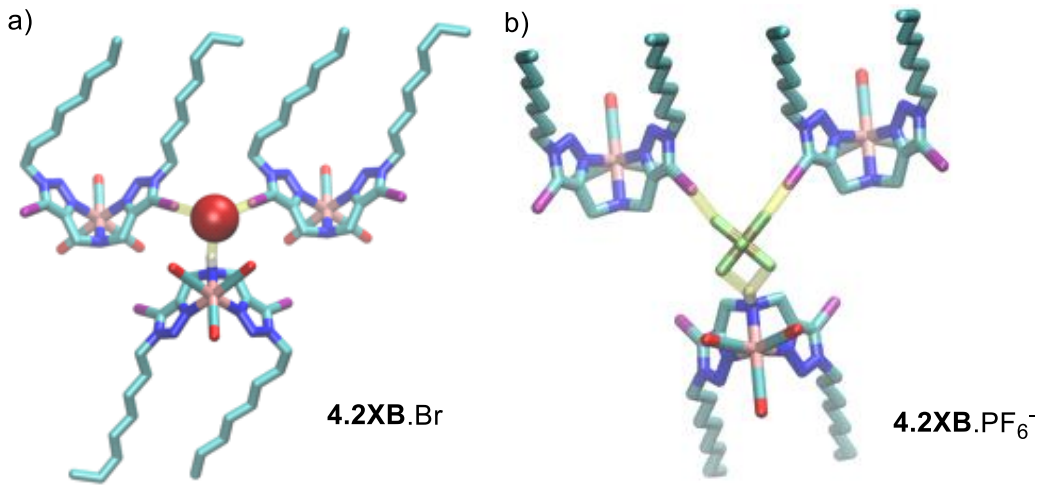

Figure 4.6: Solid state structures of a) Br^- complexed monocationic receptor **4.2XB** b) PF_6^- complexed monocationic receptor **4.2XB.** Colour code of atoms: rhenium-orange, oxygen-red, nitrogen-blue, iodine-purple, bromide- dark red, phosphorous-grey, fluorine- lime green, carbons-green. Host-guest interactions are shown in yellow.

Evidence for the postulated tweezer type anion binding mode of dicationic **4.6XB** host was obtained by single crystal X-ray diffraction analysis of I^- bound **4.6XB**. Crystals were grown by slow evaporation of a CH_3CN:H_2O solvent mixture of the **4.6XB** receptor in the presence of 10.0 eq. of TBAI. As shown in Figure 4.7, the two Re(I) complexed secondary amines act as arms of the tweezer while the benzene spacer motif provides the required spatial separation between the secondary amines for I^- binding. Complexation of Re(I) has preorganised the XB-triazole donors to direct towards the anion binding cavity. Consequently, each I^- anion interacts with a XB donor motif from both tweezer arms, forming an average C-I···I^- angle of 173°, and a I···I^- bond length of 78% of the sum of the respective r_{VdW}.[315] Interestingly, two I^- anions appear to be bound to the same binding cavity despite their mutual electrostatic repulsion, revealing the impressive strength of XB interactions in the dicationic tweezer.

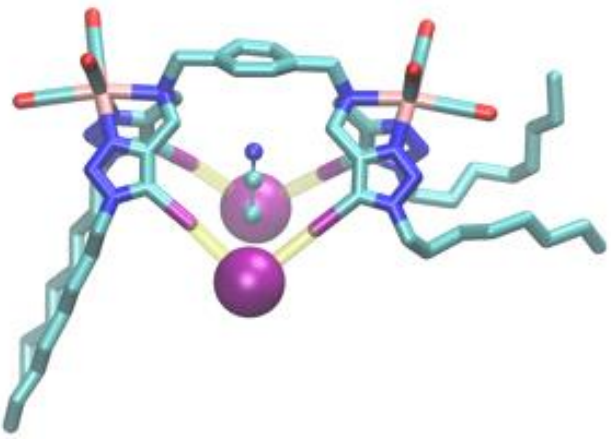

Figure 4.7: Solid-state structure of two iodide anions complexed by dicationic receptor **4.6XB.** Colour code of atoms: rhenium-orange, oxygen-red, nitrogen-blue, iodine-purple, carbons-green. Host-guest interactions are shown in yellow

4.3.2. Solution state ^{1}H NMR anion binding studies

The anion binding properties of all receptors were investigated via ^{1}H NMR titration experiments. Initial titration experiments were conducted with the metal free **4.1HB/XB** and

corresponding monocationic Re(I) **4.2XB/HB** receptors in CD_3CN. The ^1H NMR spectra of **4.2HB** upon addition of TBABr are shown in Figure 4.8. The amine proton H_1 of both **4.2XB/HB** receptors shifted downfield while the triazole proton H_{12} of **4.2HB** exhibited negligible perturbations, indicating that anion binding occurs primarily via the secondary amine proton. This could be due to the facial Re(I) coordination geometry of **4.2HB** preventing co-operative triazole and amine proton HB interactions with potential guest anions.

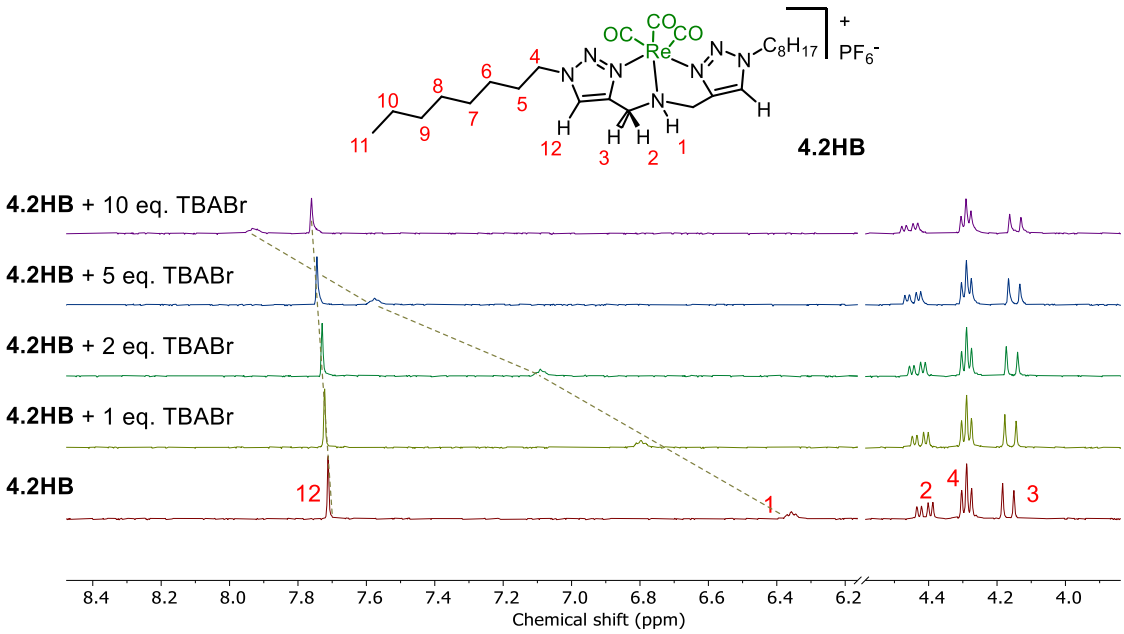

Figure 4.8: Superimposed ^1H NMR spectra of monocationic **4.2HB** receptor in the presence of increasing quantities of TBABr ([**4.2HB**]=1 mM, CD_3CN, T = 298 K)

Quantitative anion association constant values (K_a) were determined by Bindfit analysis[228,229] using a 1:1 host-guest binding model by monitoring the chemical shifts of the respective receptor's H_1 amine proton (Table 4.1). Halide binding constants of both **4.2XB/HB** receptors follow anion basicity ($Cl^- > Br^- > I^-$). Stronger I^- binding was observed by **4.2XB** over **4.2HB**, whereas Br^- is bound with comparable strength to both XB and HB **4.2** receptors. According to the hydrogen bond acceptor (HBA, β) parameters calculated by Hunter and co-workers, HSO_4^- is a better HBA than I^- ($\beta(HSO_4^-) = 10.4$, $\beta(I^-) = 8.9$, $\beta(Br^-) = 10.6$, $\beta(Cl^-) = 12.1$).[316] Despite

this, both **4.2XB/HB** receptors exhibited stronger binding for the heavy halide. Importantly, neither of the metal-free **4.1XB/HB** hosts displayed any proton perturbations upon the addition of anions in CD_3CN, emphasising the importance of Re(I) complexation for anion binding.

Table 4.1: Association constants, K_a (M^{-1}) for monocationic Re(I)-containing receptors **4.2XB** and **4.2HB** with various anions[a]

Receptor	Cl^-	Br^-	I^-	HSO_4^-
4.2XB	b	302(12)	193(2)	22(<1)
4.2HB	699(7)	307(3)	114(1)	93(3)

[a] Anions added as their TBA salts, T = 298 K, solvent = CD_3CN. Absolute errors are in brackets. b. Complex equilibria

The anion binding properties of the metal-free 'tweezers' **4.3XB/HB** were investigated by ^1H NMR titrations in d_6-acetone. As depicted in Figure 4.9a, the sequential addition of Cl^- anion to **4.3HB** resulted in notable downfield shifts of naphthyl H_{13} and triazole H_{12} proton signals, characteristic of anion binding. Similar proton perturbations were observed in the presence of Br^-, I^-, SO_4^{2-}, and N_3^-, while the receptor precipitated after the addition of AcO^-. Likewise, adding TBACl to a d_6-acetone solution of **4.3XB**, resulted in the perturbation of proton signals H_{13}, H_2, H_1 and H_4 which are proximal to the XB donors, suggesting anion association at the receptor's anion binding site (Figure 4.9b). Similar observations were made upon the addition of SO_4^{2-}, Br^-, I^-, N_3^- and AcO^-.

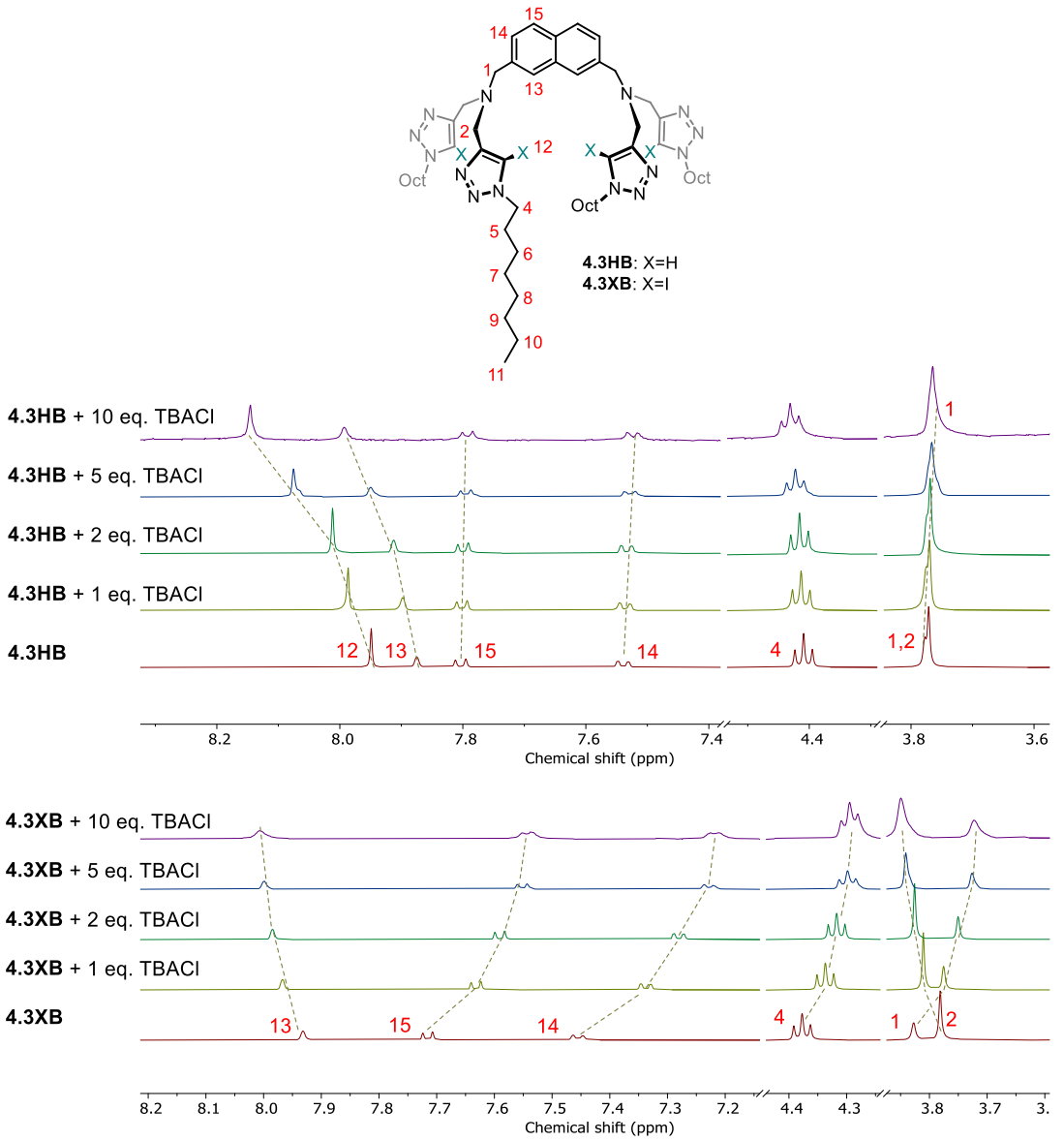

Figure 4.9: ^{1}H NMR spectra of metal-free receptors a) **4.3HB** and b) **4.3XB** in the presence of increasing quantities of TBACl ([**4.3**]=1 mM, d_6-acetone, T = 298 K)

Anion association constants were determined using the Bindfit programme,[228,229] by analysing binding isotherms generated by monitoring the chemical shifts of triazole protons H_{12} of **4.3HB** and naphthyl proton H_{13} of **4.3XB** (Figure 4.10 and Table 4.2). Notably, the **4.3XB** receptor displayed significantly larger anion association constant values in comparison to **4.3HB** which emphasises again the superiority of XB over HB interactions in anion recognition. Both receptors displayed stronger binding of Cl^-, followed by Br^-, and I^-, a trend

determined by halide charge density/basicity. Sulfate is bound the strongest by both receptors, presumably due to the oxoanion's higher charge and size complementarity. Importantly, no anion binding was observed for with the metal-free receptor **4.1XB** in d_6-acetone under identical conditions, which demonstrates the tweezer design significantly enhances anion binding.

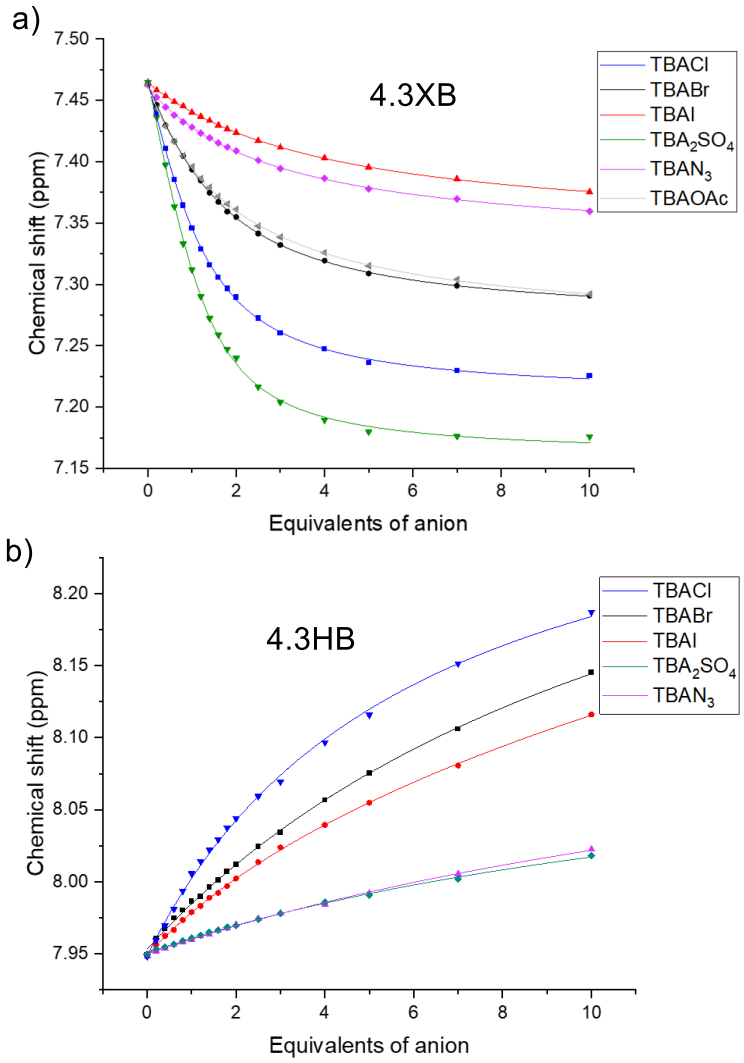

Figure 4.10: Binding isotherms showing changes in chemical shifts of triazole protons H_{12} of **4.3HB** and naphthyl proton H_{13} of **4.3XB** hosts

Table 4.2: Anion association constants, K_a (M^{-1}) for metal-free tweezer-type receptors.[a]

	Cl^-	Br^-	I^-	SO_4^{2-}	OAc^-	N_3^-
4.3XB	1534(61)	868(8)	288(3)	1907(133)	772(15)	492(15)
4.3HB	84(2)	78(2)	42(1)	211(6)	c	57(1)

[a] Anions added as their TBA salts, T = 298 K, solvent = d_6-acetone. Absolute errors are in brackets, c. Precipitate

As expected the association constant magnitudes of the corresponding dicationic bimetallic Re(I) complexed receptors **4.5XB/HB** were significantly higher than the metal-free receptors **4.3XB/HB**, so much so that the ^{1}HNMR titrations were undertaken in the competitive aqueous 1:9 D_2O/CD_3CN solvent mixture, in which the metal-free receptor **4.3XB** did not show anion binding.

As depicted in Figure 4.11, upon addition of the TBA oxalate salt to tweezer receptor **4.5HB**, the triazole proton H_{12} undergoes significant downfield shifts, suggesting the formation of anion-HB interactions. Also, methylene protons proximal to the anion binding site, H_1 and H_2, exhibited progressive upfield and downfield perturbations respectively, indicative of oxalate anion binding in the receptor's anion binding site. Similar ^{1}H NMR perturbations were observed with the addition of TBA salts of $HP_2O_7^{3-}$, phthalate, isophthalate, and SO_4^{2-}. ^{1}H NMR chemical shift perturbations of **4.5XB** receptor upon sequential addition oxalate is shown in Figure 4.11b. In contrast to the analogous HB receptor **4.5HB**, H_1 and H_3 protons of **4.5XB** shifted downfield while H_2 proton did not show any significant perturbation, suggesting two different anion binding modes **4.5XB** and **4.5HB**.

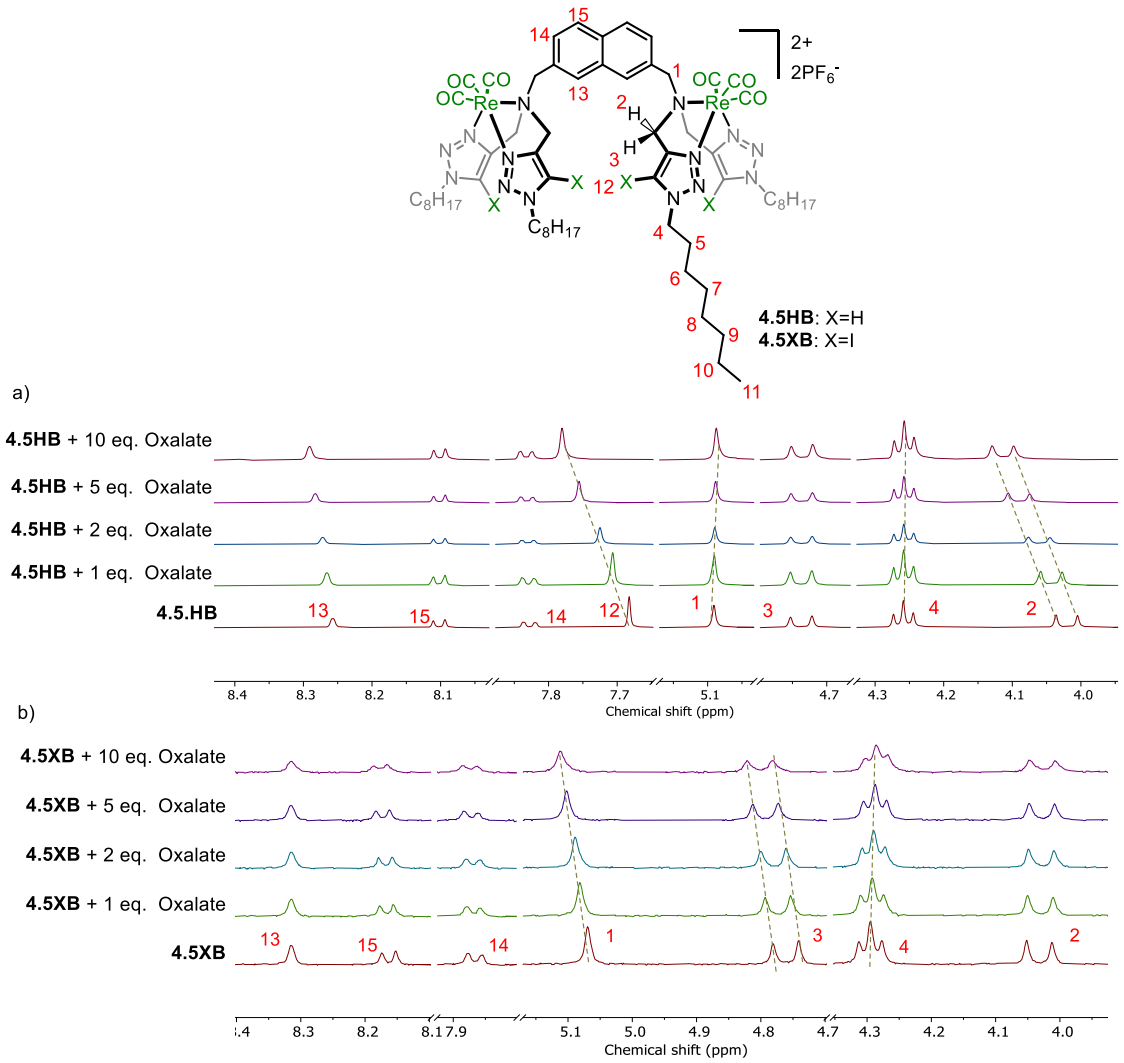

Figure 4.11: ^{1}H NMR spectra of dicationic receptors a) **4.5HB** and b) **4.5XB** in the presence of increasing quantities of TBA-oxalate ([**4.5**]=1 mM, 1:9 D_2O/CD_3CN, T = 298 K)

Anion association constants were calculated by Bindfit software[228,229] by monitoring chemical shift perturbations of the proto triazole H_{12} of **4.5HB** and methylene protons H_1 in **4.5XB** as a function of anion concentration. As shown by solid state structure analysis, while complexation of Re(I) orients the triazole XB donors towards the anion binding cavity, it also reduces the conformational flexibility of the XB donors. Therefore, anions can potentially bind in both 1:1 and 1:2 stoichiometric host-guest binding modes. Hence, as explained by Thordarson and co-workers, a more detailed study was conducted to elucidate the host-guest binding mode of the Re(I) complexed molecular tweezers.[228,229] To this end, a simple

1:1 host-guest binding mode and four variants of 1:2 host-guest binding modes were considered to analyse the titration data. As depicted in Table 4.3, the four variants of the 1:2 binding mode is categorised based on the relationship between the step-wise binding constants (K_1 and K_2) and the chemical shifts resulting from the formation of 1:1 and 1:2 host-guest complexes (δ_1 and δ_2 respectively).

Table 4.3: Different 1:2 host-guest binding modes and their relationships between K_1 & K_2 and δ_1 & δ_2 [a]

Binding modes (Host-Guest)	Relationship between K_1 & K_2	Relationship between δ_1 & δ_2
1:1	Not applicable	Not applicable
1:2 (Full)	$K_1 \neq 4K_2$	$\delta_1 \neq 2\delta_2$
1:2 (Non-cooperative)	$K_1 = 4K_2$	$\delta_1 \neq 2\delta_2$
1:2 (additive)	$K_1 \neq 4K_2$	$\delta_1 = 2\delta_2$
1:2 (statistical)	$K_1 = 4K_2$	$\delta_1 = 2\delta_2$

[a] Stepwise binding constants are represented by K_1 & K_2. Chemical shifts induced by the formation of 1:1 and 1:2 host-guest complexes are shown by δ_1 & δ_2 respectively.

The binding mode that best describes each titration was investigated by fitting the titration isotherms to each binding mode and comparing the resulting covariance of the fit (cov_{fit}). The cov_{fit} is defined as the variance of the residual plot divided by the variance of the raw data which quantifies the randomness of scattering in the residual plot relative to the scattering of the original data. Binding modes that have a lower cov_{fit} value are more likely to fit well with the titration data. However, complex binding modes with more fitted parameters (e.g. 1:2 (Full) model) generally fit better than simpler models (e.g. 1:1 model). Hence it is recommended to select a more complex model only when the cov_{fit} is at least 3-5 times lower than that of the simpler model.[228]

Table 4.4, summarises the calculated association constant values for the oxalate anion and the respective cov_{fit} values calculated by the Bindfit software. The cov_{fit} ratio is calculated by

dividing the cov_{fit} of the 1:1 binding model by the respective cov_{fit} of the 1:2 binding mode. When considering the titration data of **4.5XB** host, the cov_{fit} values of 1:2 (full) binding mode are four times lower than the 1:1 binding mode. Therefore, the 1:2 binding model is a better fit for the **4.5XB** receptor binding oxalate. However, the cov_{fit} values of receptor **4.5HB** are very similar to each other in both 1:1 and 1:2 binding modes (i.e. as mentioned above, not at least 3-5 times lower than that of the simpler model). Hence, the **4.5HB** host most likely displays the 1:1 host-guest binding mode for oxalate.

The solid-state structure of I^- bound **4.5XB** shows the strict linearity of XB interactions that can favour the 1:2 host-guest binding mode in the XB receptor. However, HB donors have a less stringent requirement to form linear anion interactions which makes it possible for all four triazole HB donors of **4.5HB** tweezer to form concerted interactions with the anion guest species, enabling the formation of 1:1 host-guest complexes (See appendix D for further details).

Table 4.4: Stepwise anion association constants (K_1/K_2, M^{-1}) and cov_{fit} values of binding isotherms generated with the addition of oxalate to receptor **4.5XB** and **4.5HB**.[a]

Receptor	Anion	Host-guest binding model	K_1	K_2	cov_{fit} ($x10^{-3}$)	cov_{fit} ratio
4.5XB	Oxalate	1:1	314	-	1.02	1
		1:2 (Full)	16352	165	0.270	4
		1:2 (non-cooperative)	509	127	1.51	1
		1:2 (additive)	587	47	0.457	2
		1:2 (statistical)	940	235	2.36	0.4
4.5HB	Oxalate	1:1	237	-	2.09	1
		1:2 (Full)	34604	186	1.63	1
		1:2 (non-cooperative)	432	108	2.26	1
		1:2 (additive)	376	30	1.87	1
		1:2 (statistical)	666	167	2.44	1

[a] Anions added as their TBA salts, T = 298 K, solvent = 1:9 D_2O/CD_3CN. Errors are less than 10% (except for, 4.5XB[1:2(full)]=22% and 2% (for K_1 and K_2) and 4.5HB[1:2(additive)]=131% and 5% (for K_1 and K_2)). Binding modes best fit for the titration isotherms are highlighted in yellow.

Anion association constants for the bimetallic receptors **4.5XB** and **4.5HB** calculated based on the best fit host-guest binding model selected through the covariance analysis are presented in Table 4.5. Interestingly, in stark contrast to **4.5HB** which binds all the oxoanions tested with similar binding affinities, the bimetallic **4.5XB** receptor is highly selective for oxalate. Indeed, the XB tweezer did not bind the larger spaced dicarboxylates or sulfate in this aqueous solvent mixture. This may be attributed to the steric hindrance caused by the large iodotriazole XB donors reducing the binding cavity size of the XB-tweezer. Interestingly, receptor **4.5XB** binds Cl^- whereas **4.5HB** does not, which reflects the superior ability of the hydrophobic XB donor binding cavity to recognise halide anions in aqueous solvent media.[317,41] Unfortunately, quantitative anion association constant data for receptor **4.6XB** could not be determined due to problematic precipitation issues occurring throughout the ^{1}H NMR titration experiments.

Table 4.5: Anion association constants, K_a (M^{-1}) for Re(I) complexed tweezer-type receptors.[a]

	Cl^-	Oxalate	Phthalate	Isophthalate	SO_4^{2-}
4.5XB	K_1=941 (47) K_2=65 (2)	$K_1 > 10^4$ K_2=165(3)	NB	NB	NB
4.5HB	NB	237 (7)	321 (3)	474 (14)	338 (7)

[a] Anions added as their TBA salts, T = 298 K, solvent = 1:9 D_2O/CD_3CN. Absolute errors are in brackets. NB. No binding

4.4. Conclusions and Future work

A series of XB/HB Re(I) complexed monocationic (**4.2**), and dicationic tweezer (**4.5**) receptors were synthesised and their anion binding properties analysed in the solid state by single crystal XRD analysis and in solution via ^{1}H NMR titration investigations.

^{1}H NMR titration studies revealed the combination of both Re(I) complexation and tweezer design to significantly enhance anion recognition in comparison to the metal-free and non-

tweezer host systems. Consequently, the bimetallic Re(I) complexed tweezer (**4.5**) is the most potent anion receptor from the family. Rhenium(I) complexation enables charge assisted polarisation and preorganisation of the XB/HB donors, while the tweezer cavity design facilitates multiple concerted XB/HB interactions with potential anion guest species. Quantitative binding data of the metal-free XB tweezer **4.3XB** consistently showed enhanced anion recognition compared to the analogous metal-free HB tweezer **4.3HB**. Upon Re(I) complexation, the dicationic Re(I) **4.5HB** receptor was capable of binding all the oxoanions tested with similar affinity, whereas in stark contrast the dicationic Re(I) **4.5XB** is highly selective for oxalate. This may be attributed to the steric hindrance caused by large XB donors reducing the binding cavity size of the XB tweezer. Importantly, all XB tweezer receptors (**4.3XB**, **4.5XB)** consistently showed higher halide binding affinities compared to the analogous HB receptors (**4.3H, 4.5HB**). The solid-state structure of the dicationic Re(I) receptor **4.6XB** complexed with iodide demonstrates the tweezer type anion binding mode in which a tetradentate XB anion binding cavity is formed to bind two I^- anions. This work highlights how anion binding strength and selectivity of XB tweezer receptors can be enhanced by incorporating transition metals proximal to XB donor groups.

Future work on this project includes the synthesis of water soluble XB bimetallic Re(I) receptor systems by integrating polyethylene glycol (PEG) groups into the tweezer host design (Figure 4.12). Additionally, the incorporation of photo- and redox-active reporter spacer groups in between the tweezer arms would imbue anion sensing capability.

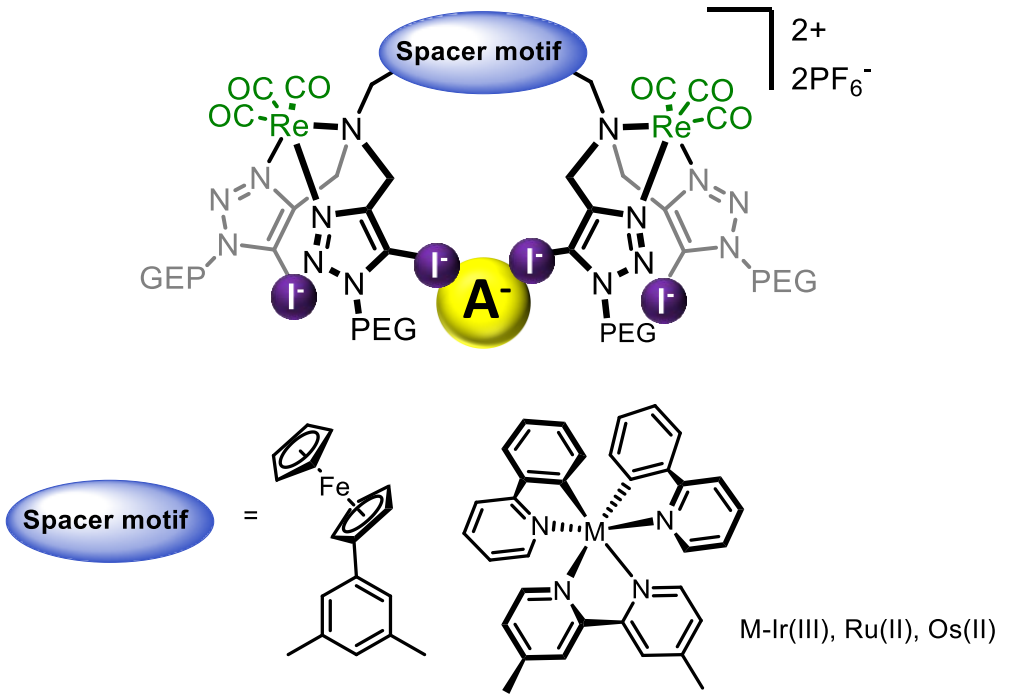

Figure 4.12: Proposed structure of the potential water-soluble molecular tweezer capable of anion recognition and sensing.

Chapter 5

Conclusions

Chapter 5: Conclusions

The work described in this thesis focuses on the anion and ion-pair recognition properties of mechanically interlocked rotaxane and transition metal-based host architectures incorporated with multiple convergent XB donors in their binding cavity.

Chapter 2 highlights the superior ion-pair binding properties of mechanically interlocked XB heteroditopic [2]rotaxane host systems compared to their analogous HB rotaxanes and non-interlocked macrocycles. A series of heteroditopic XB/HB [2]rotaxanes were prepared and their selective lithium halide ion-pair binding properties were investigated by X-ray crystallography, ^{1}H NMR titrations, and theoretical modelling studies. Saliently, the rotaxane binding of Li^{+} was found to 'switch on' cooperative anion recognition by polarising the axle XB iodine donor atom and enhancing the degree of preorganisation of the anion binding site. The strength of lithium halide binding was shown to increase greatly with the number of halogen bond donors integrated into the binding domain. This initial work was further extended to prepare a dynamic two-station [2]rotaxane, followed by the unprecedented use of ion-pair binding as a stimulus to control the translational motion of the rotaxane's macrocycle component. The dynamic behaviour of the macrocycle was akin to the 'AND' Boolean logic gate, where the shuttling of the macrocycle along the rotaxane's axle component from one station to another is increased in the presence of both Li^{+} AND Br^{-}, while either charged guest species alone results in attenuated (Li^{+}) or no (Br^{-}) shuttling.

Chapter 3 and **Chapter 4** explore how coordinated transition metals proximal to XB donors enhance the potency of XB interactions and enable optical sensing of anions. Chapter 3 reports the first examples of Ir(III) complexed XB mechanically interlocked host systems for the purpose of anion recognition and sensing. An Ir(III) complexed XB axle containing [3]rotaxane was synthesised and its selective dicarboxylate anion recognition and optical luminescence sensing properties were investigated. The [3]rotaxane host displayed the

highest luminescence quantum yield and significantly superior dicarboxylate binding with high sensitivity compared to a [2]rotaxane analogue and acyclic host. Additionally, the Ir(III) based hosts were able to differentiate geometric isomers of dicarboxylates. Whereas the acyclic receptor **3.4** exhibited selectivity for dicarboxylates with proximal carboxylate groups (i.e. phthalate> isophthalate/terephthalate, and maleate > fumarate) while the [3]rotaxane **3.8** preferentially bound dicarboxylates with carboxylate groups further apart (i.e. terephthalate > isophthalate > phthalate; fumarate > maleate, and adipate > glutarate > succinate). These results demonstrate the potential of using transition metal based mechanically interlocked [3]rotaxanes for selective and efficient sensing of dicarboxylate anions.

Chapter 4 discusses the design and synthesis of Re(I) complexed dicationic molecular tweezers that contain a tetradentate XB anion binding cavity. Anion binding properties of the dicationic Re(I) tweezer receptors were investigated in the solid state by single crystal XRD analysis, and in solution via ^{1}H NMR titration studies. The combination of both Re(I) complexation and tweezer design was observed to significantly enhance anion binding properties of the receptor compared to the corresponding metal-free receptors and non-tweezer hosts. This is attributed to the charge-assisted polarisation and preorganisation of the anion binding site by Re(I) complexation and the tweezer cavity design that facilitates multiple concerted interactions with the potential anion guest species. The metal-free XB tweezer **4.3XB** displayed stronger anion binding for a range of anions (i.e. Cl^-, Br^-, I^-, SO_4^{2-}, N_3^-) compared to the analogous HB receptor **4.3HB.** Upon Re(I) complexation, the XB dicationic Re(I) **4.5XB** receptor exhibited notable selectivity for smaller anions (i.e. oxalate, Cl^-) compared to the analogous HB receptor **4.5HB**, which was capable of binding a range of oxoanions with similar affinities (i.e. oxalate, isophthalate, phthalate and SO_4^{2-}). This was attributed to the steric hindrance caused by the relatively large metal-coordinated iodotriazole XB donors of **4.5XB** reducing the binding cavity size of the XB tweezer.

In summary, these results serve to highlight how multidentate XB sigma-hole interactions incorporated into mechanically interlocked rotaxane and transition-metal complexed host structural frameworks augment effective anion and ion-pair recognition and sensing. The application of such a strategic host design promises to pave the way for developing the next generation of anion sensory materials with improved sensing capabilities.

Chapter 6

Experimental Section

Chapter 6: Experimental section

6.1. General Remarks

6.1.1. Chemicals and solvents

All reagents and solvents used in this thesis were purchased from commercial suppliers unless otherwise stated. Dry organic solvents were degassed by purging with nitrogen and dehydrated by passing through an MBraun MPSP-800 column. Water was deionised and micro-filtered using a Milli-Q® Millipore machine. TBA salts and $[Cu(CH_3CN)_4]PF_6$ were stored in P_2O_5 powder containing vacuum desiccators. TBTA was synthesised according to a literature procedure[318] and stored at room temperature. Et_3N was distilled from KOH and stored over the same base prior to use. Brine refers to a saturated aqueous solution of NaCl, and basic $EDTA_{(aq.)}$ refers to an aqueous solution of 0.02 M EDTA with 1% NH_3 (28–30%) solution. Chromatography separations were carried out using Merck silica gel (particle size 40-60 μm) under a positive pressure of nitrogen, and preparative TLC (20 × 20 cm, 1 mm silica thickness). Microwave-assisted reactions were performed in a Biotage Initiator 2.0 reactor using sealed standard Biotage pyrex-glass microwave vials. Ratios of solvent mixtures are reported by volume.

6.1.2. Instrumentation

NMR spectra for the nuclei ^{1}H, $^{13}C\{^{1}H\}$, $^{19}F\{^{1}H\}$, $^{31}P\{^{1}H\}$ were recorded on Bruker Avance III 400 HD nanobay NMR spectrometers (Hg400 and Venus400) each equipped with a 9.4 T magnet, or Bruker Avance III 500 HD NMR machine (AVD500) equipped with a 11.75 T magnet, or Bruker Avance NMR machine (AVC500) equipped with a 11.75 T magnet and a ^{13}C detect cryoprobe, or Bruker NEO 600 with broadband helium cryoprobe. High-resolution ESI mass spectra were recorded on a Bruker microTOF spectrometer. UV–visible absorption

and luminescence spectra were recorded on a HORIBA Duetta™ spectrometer using quartz cuvettes (pathlength 10 mm).

6.1.3. ^{1}H NMR titration protocol

In general, all ^{1}H NMR titrations were conducted in Bruker Avance III NMR 500 MHz spectrometer (AVD500) at 298 K. Preliminary ^{1}H NMR studies performed in Chapter 3 were conducted in a Bruker Avance III 700 MHz spectrometer (AV700) with an inverse TCI ^{1}H cryoprobe at 298K. All deuterated solvents were purchased from chemical suppliers. Where available, required tetrabutylammonium (TBA) salts of anions and cation salts were purchased from suppliers and if necessary stored in vacuum desiccators with P_2O_5 desiccant. TBA salts of dicarboxylate derivatives discussed in Chapter 3 were prepared following a reported procedure.[319]

In a typical ^{1}H NMR titration experiment, aliquots from a 50 mM solution of guest ion of interest was sequentially added to a 0.5 mL of a 1.0 mM host solution. Samples were mixed well prior to recording the NMR spectra. At least 17 ^{1}H NMR spectra were recorded with the addition of increasing equivalents of guest ion. Chemical shifts of the NMR peaks of interest were monitored upon addition of the guest ion and the binding constants were determined using Bindfit software.[228,229] Binding of guest ions with all hosts were fast in the NMR time scale.

6.1.4. Optical measurements

UV–visible absorption and luminescence measurements were both performed on a HORIBA Duretta absorbance and emission spectrophotometer at 298 K using 1.0 mL quartz cuvettes of pathlength 1 cm. For luminescence titrations, the charged guest was dissolved in the host solution to maintain the same host concentration throughout the course of titration. In a typical experiment, aliquots of a charged guest stock solution of appropriate concentration were added to a 1.0 mL host solution. The samples were thoroughly mixed before recording

the UV–visible absorption or emission spectra. Stability constants were determined by global fitting using Bindfit software,[228,229] employing a 1:1 host-guest stoichiometric binding model unless otherwise specified.

Quantum yields were measured using the same spectrophotometer at 298 K in aerated CH_3CN. Quantum yields of all Ir(III) compounds in Chapter 3 were calculated relative to a solution of $[Ru(bpy)_3]Cl_2$ (Φ_{PL}=1.80%, in aerated conditions).[290] Absorption/emission spectra of the sample and the reference were measured using identical experiment parameters. All absorption measurements were kept low in the range of 0.02-0.03 to avoid inner filter effect. Solvent spectra of CH_3CN used for sample preparation were subtracted from the fluorescence spectra of the sample/reference to avoid Raman scattering effects. Quantum yields were then calculated according to the following equation where the subscripts *S* and *R* denote the sample and reference respectively. ϕ_R is the known quantum yield of the reference standard, *I* is the integrated photoluminescence spectrum intensity, *A* is the absorbance of the solution at the excitation wavelength.

$$\Phi_S = \frac{I_S}{I_R}\frac{A_R}{A_S}\Phi_R$$

6.1.5. Electrochemical experiments

All electrochemical studies were conducted on an Autolab potentiostat (Metrohm) using a three-electrode set-up. A 3 mm diameter glassy carbon electrode (BASi) was used as the working electrode, which was polished mechanically with alumina slurry (0.05 µm, Buehler) followed by sonication in $EtOH/H_2O$. A Pt wire was used as the counter electrode, while a non-aqueous $Ag|AgNO_3$ was used as a reference electrode. All potentials are reported with respect to Fc/Fc^+ as an internal standard.

Unless stated otherwise, all CV and SWV electrochemical experiments were performed at a scan rate of 0.1 V s^{-1} and a step potential of 2 mV, and a frequency of 25 Hz (SWV). Eight incremental scan rates were applied for experiments with CVs at varying scan rates: 0.025, 0.05, 0.075, 0.1, 0.2, 0.4, 0.6 and 0.8 V s^{-1}. In all cases 100 mM $TBAPF_6$ was used as supporting electrolyte. Concentration of host is 0.25 mM for all characterisation measurements and 0.1 mM for any anion titrations.

6.2. Synthetic procedures and characterisation of compounds

Compounds **2.1**,[226] **2.7**,[165] **2.8a/b**,[165,227] **2.12**,[265] **2.13**,[240] **3.1**,[287] **4.1XB/HB**,[308] $[Re(CO)_3(H_2O)_3]Br$[309,310] and $Ir_2(ppy)_4Cl_2$[288] were synthesised according to literature procedures.

Macrocycle precursor 2.3

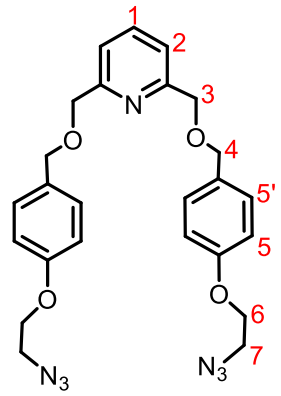

2.3

The alcohol precursor **2.1** (1.50g,7.76 mmol) was dissolved in 50 mL of dry THF. NaH (0.295 g of a 60% dispersion in mineral oil, 7.37 mmol) was added to the reaction mixture and was stirred at room temperature under N_2 for 20 minutes. Subsequently, the bis bromo pyridine precursor **2.2** was added and was stirred for a further 60 mins and then was heated at 50 °C for 48 hours. Solvent was then removed *in vacuo*. The residue was redissolved in DCM (50 mL), washed with brine (50 mL x 2), dried over $MgSO_4$ and solvent was removed *in vacuo*. The crude product was purified by silica gel column chromatography (0-2% MeOH in DCM) to afford the macrocycle precursor **2.3** as a white solid (1.14 g, 70%).

^{1}H NMR (500 MHz, $CDCl_3$) δ 7.58 (t, *J* = 7.7 Hz, 1H, H_1), 7.27 (d, *J* = 7.7 Hz, 2H, H_2), 7.20 (d, *J* = 8.5 Hz, 4H, H_4), 6.78 (d, *J* = 8.5 Hz, 4H, H_3), 4.53 (s, 4H, H_5), 4.46 (s, 4H, $H_{5'}$), 3.99 (t, *J* = 5.0 Hz, 4H, H_6), 3.43 (t, *J* = 5.0 Hz, 4H, H_7)

^{13}C NMR (126 MHz, $CDCl_3$) δ 157.87, 137.15, 130.79, 129.43, 119.91, 114.46, 72.79, 72.39, 66.91, 50.02.

HRMS (ESI +ve) m/z: 490.2197 ($[M+H]^+$, $C_{25}H_{28}N_7O_4$ calc. 490.2197)

Macrocycle precursor 2.4

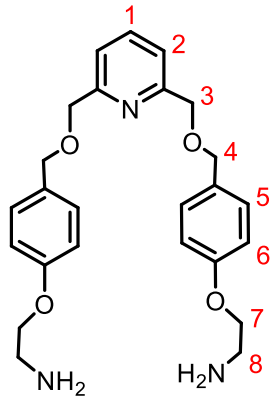

2.4

To a bis-azide precursor **2.3** (2.23 g, 4.55 mmol) in methanol, 10% Pd/C (0.25 g) and hydrazine monohydrate (2.21 mL, 2.28 g, 45.5 mol) were added and the reaction mixture was refluxed under N_2 for 18 hours. Reaction mixture was cooled to room temperature and was filtered through a plug of Celite. Filtrate was collected and solvent evaporated *in vacuo* to afford the bis-amine precursor **2.4** as a white solid (1.79 g, 90%).

^{1}H NMR (400 MHz, $CDCl_3$) δ 7.69 (t, *J* = 7.7 Hz, 1H, H_1), 7.37 (d, *J* = 7.7 Hz, 2H, H_2), 7.29 (d, *J* = 8.5 Hz, 4H, H_6), 6.82 (d, *J* = 8.5 Hz, 4H, H_5), 4.63 (s, 4H, H_3), 4.56 (s, 4H, H_4), 3.98 (t, *J* = 5.2 Hz, 4H, H_8), 3.07 (t, *J* = 5.2 Hz, 4H, H_7)

^{13}C NMR (101 MHz, $CDCl_3$) δ 158.75, 158.10, 137.34, 130.38, 129.62, 120.08, 114.57, 72.92, 72.69, 70.32, 41.69

HRMS (ESI +ve): 438.2386 $[M+H]^+$ ($[C_{25}H_{32}N_3O_4]^+$ calc. 438.2387)

Macrocycle 2.6

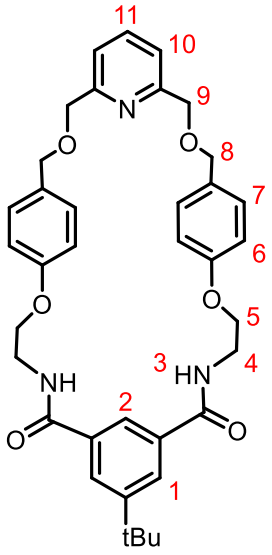

2.6

5-tert-Butylisophthalic acid was suspended in dry DCM (15 mL). Oxalyl chloride (0.34 mL, 0.51 g, 4.02 mmol) and DMF (2 drops) were added and the reaction mixture and was stirred under N_2 at room temperature until a homogenous solution was observed. Solvent was evaporated *in vacuo.* The resultant solid was redissolved in dry DCM (15 mL) and was added dropwise to a solution of the macrocyclic precursor **2.5** (0.438 g, 1.0 mmol) and Et_3N (0.7 mL, 5 mmol) in dry DCM. Reaction mixture was stirred overnight at room temperature under N_2 atmosphere. The resultant mixture was washed with 10% $HCl_{(aq)}$, sat. $NaHCO_3$ and brine and dried over $MgSO_4$ and solvent evaporated *in vacuo* to afford macrocycle **2.6** as a white solid (0.212 g, 34%).

^{1}H NMR (500 MHz, Chloroform-*d*) δ 7.97 (s, 2H, H_1), 7.92 (s, 1H, H_2), 7.68 (t, *J* = 7.7 Hz, 1H, H_{11}), 7.32 (d, *J* = 7.7 Hz, 2H, H_{10}), 7.21 (d, J= 7.7, 4H, H_6), 6.85 (t, *J* = 5.9 Hz, 2H, H_3), 6.79 (d, *J* = 7.7, 4H, H_7), 4.56 (s, 4H, H_9), 4.40 (s, 4H, H_8), 4.11 (t, *J* = 4.9 Hz, 4H, H_4), 3.90-3.84 (m, 4H, H_5), 1.26 (s, 9H, tBu).

^{13}C NMR (126 MHz, $CDCl_3$) δ 167.52, 158.27, 157.79, 152.82, 137.27, 134.53, 130.35, 130.21, 127.91, 121.85, 120.33, 114.44, 72.11, 71.40, 66.91, 39.75, 35.16, 31.25, 29.85.

HRMS (ESI +ve): 624.3062 $[M+H]^+$ ($[C_{37}H_{42}N_3O_6]^+$ calc. 624.3068)

[2]Rotaxane 2.9

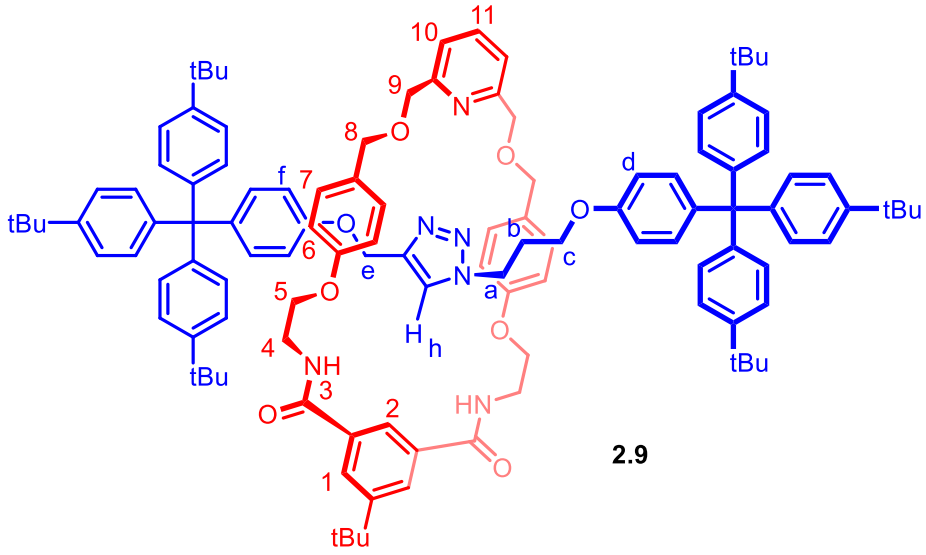

2.9

General procedure (1) for CuAAC-AMT synthesis of [2]rotaxane

Macrocycle **2.6** (8.0 mg, 0.012 mmol) and $[CuPF_6(MeCN)_4]$ (4.54 mg, 0.95 mmol) were dissolved in 0.6 mL dry degassed DCM and was stirred for 30 minutes. A solution of stopper azide **2.7** (30.1 mg, 0.05 mmol) and stopper alkyne **2.8** (27.8 mg, 0.05 mmol) in dry degassed DCM (0.6 mL) was added to the Cu-complexed macrocycle solution. The reaction mixture was sealed and the homogenous solution was stirred for 48 hours. Subsequently, the reaction mixture was diluted with 10 mL DCM, washed with basic EDTA/$NH_4OH_{(aq)}$ (10 mL x 3) and H_2O (10 mL x 2), dried over $MgSO_4$ and was concentrated in a rotary evaporator. The crude product was purified by preparative thin layer chromatography (SiO_2, 0-3% MeOH in DCM) to yield the desired rotaxane as a white solid (17.4 mg, 77%).

^{1}H NMR (500 MHz, $CDCl_3$) δ 8.29 (s, 1H, H_2), 8.24 (s, 2H, H_1), 7.50-7.59 (m, 3H, H_3,H_9), 7.24-7.30 (m, 15H, H_h, H_{10}, $H_{stopper\ ArH}$), 7.14 – 7.07 (m, 16H, $H_{stopper\ ArH}$), 7.03 (d, *J* = 8.1 Hz, 4H,H_7), 6.67 (d, *J* = 8.8 Hz, 2H, H_f), 6.61 (d, *J* = 8.8 Hz, 2H, H_d), 6.47 (d, *J* = 8.1 Hz, 4H, H_6), 4.77 (s, 2H,H_e), 4.45-4.55 (m, 4H, H_8), 4.41 – 4.33 (m, 4H, H_9), 3.86-3.97 (m, 4H, H_5), 3.62-3.79 (m, 6H, H_a,H_4), 3.51 (t, *J* = 5.7 Hz, 2H, H_c), 1.69 – 1.63 (m, 2H, H_b), 1.38-1.34 (m, 63H, $H_{t\text{-}Bu}$).

^{13}C NMR (126 MHz, $CDCl_3$) δ 167.80, 157.94, 157.50, 156.23, 155.92, 152.55, 148.48, 144.22, 144.12, 140.61, 140.21, 137.42, 134.04, 132.48, 132.35, 129.97, 128.99, 124.23, 121.31, 120.97, 114.35, 113.09, 113.02, 72.41, 71.82, 66.30, 63.96, 63.19, 61.19, 47.14, 39.71, 35.20, 34.43, 31.51, 31.36, 29.12.
HRMS: (ESI +ve) m/z: 1755.0437 ($[M+H]^+$, $C_{117}H_{137}N_6O_8$ requires 1755.0525)

[2]Rotaxane 2.10

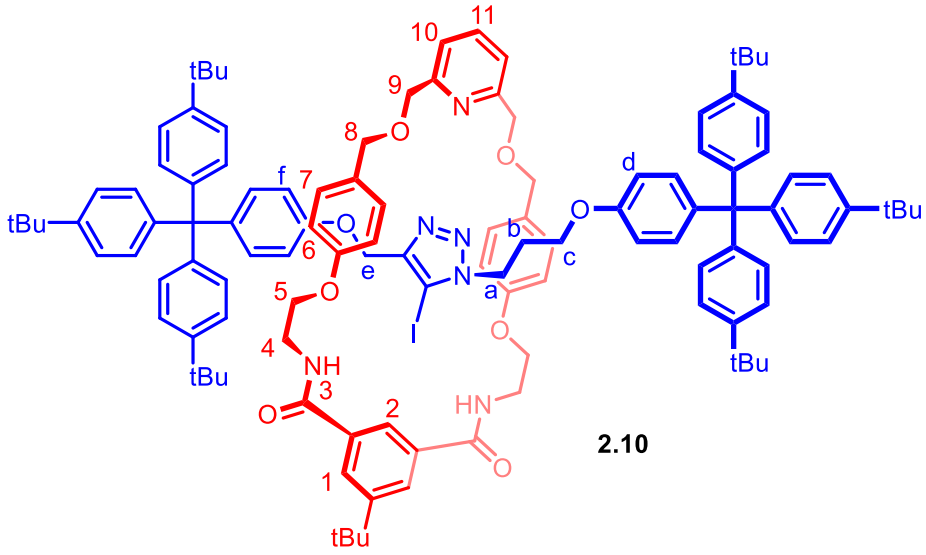

2.10

Rotaxane **2.10** was synthesized following the general procedure (1) for CuAAC-AMT synthesis of [2]rotaxane, using the macrocycle **2.6** (10.0 mg, 0.016 mmol), $[CuPF_6(MeCN)_4]$ (5.66 mg, 0.0095 mmol), stopper azide **2.7** (49.9 mg , 0.08 mmol), stopper alkyne **2.8** (53.5 mg, 0.08 mmol) in dry degassed DCM (1.6 mL total volume). The crude mixture was purified by preparative thin layer chromatography (SiO_2, 0-3% MeOH in DCM) to yield the desired rotaxane as a white solid (22.2 mg, 74%).

^{1}H NMR (500 MHz, $CDCl_3$) δ 8.58 (s, 1H, H_2), 8.23 (s, 2H,H_1), 7.63 (t, *J* = 7.7 Hz, 1H, H_{11}), 7.50 (t, *J* = 5.0 Hz, 2H, H_3), 7.32 (d, *J* = 7.8 Hz, 2H, H_{10}), 7.19-7.24 (m, 12H, $H_{stopper\ ArH}$), 7.04-7.12 (m, 20H, H_7,$H_{stopper\ ArH}$), 6.72 (d, *J* = 8.3 Hz, 2H, H_f), 6.65 (d, *J* = 8.4 Hz, 2H, H_d), 6.40 (d, *J* = 8.0 Hz, 4H, H_6), 4.78 (s, 2H, H_e), 4.56 – 4.46 (m, 4H, H_8), 4.46 – 4.34 (m, 4H, H_9), 3.95 (t, *J* = 7.6 Hz, 2H,H_a), 3.75 (t, *J* = 5.7 Hz, 2H, H_c), 3.49-3.58 (m, *J* = 5.0 Hz, 4H,H_4), 3.60 – 3.48 (m, 4H,H_5), 2.02 – 1.91 (m, 2H, H_b), 1.31 (d, *J* = 15.1 Hz, 63H, $H_{t\text{-}Bu}$).

^{13}C NMR (126 MHz, $CDCl_3$) δ 167.73, 158.38, 157.31, 156.33, 152.54, 148.49, 144.21, 144.11, 140.79, 140.29, 137.72, 133.87, 132.46, 132.43, 130.82, 129.98, 129.07, 124.25, 122.00, 121.61, 114.32, 113.34, 113.07, 72.79, 71.85, 66.41, 64.10, 63.20, 61.47, 48.06, 40.28, 35.21, 34.43, 31.52, 31.38, 29.03.

HRMS: (ESI +ve) m/z: 940.9778 ($[M+2H]^{2+}$, $C_{117}H_{137}N_6O_8$ calc. 940.9783)

Two station [2]rotaxane 2.14

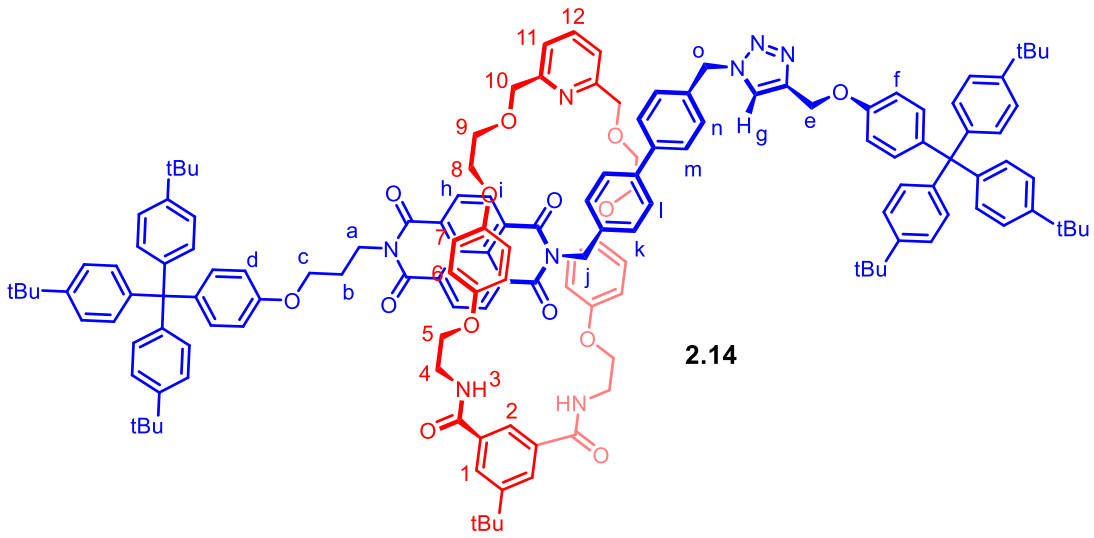

Rotaxane **2.14** was synthesized following the general procedure (1) for CuAAC-AMT synthesis of [2]rotaxane, using the macrocycle **2.12** (10.0 mg, 0.016 mmol), $[CuPF_6(MeCN)_4]$ (5.66 mg, 0.0095 mmol), NDI stopper azide **2.13** (60.0 mg, 0.073 mmol), stopper alkyne **2.8** (31.8 mg, 0.073 mmol) in dry degassed DCM (2 mL total volume). The crude mixture was purified by preparative thin layer chromatography (SiO_2, 0-2% MeOH in DCM) to yield the desired rotaxane as a red powder (21.0 mg, 64%).

^{1}H NMR (600 MHz, $CDCl_3$) δ 8.58 (s, 1H, H_2), 8.46-8.43 (m, 4H, $H_{h,i}$), 8.32 (d, *J* = 1.5 Hz, 2H, H_1), 7.81 (t, *J* = 7.7 Hz, 1H, H_{12}), 7.57 (d, *J* = 8.4 Hz, 2H, H_k), 7.53 (d, *J* = 8.4 Hz, 2H, H_m), 7.52 – 7.48 (m, 3H, $H_{g,l}$), 7.44 (d, *J* = 7.8 Hz, 2H, H_{11}), 7.31 (d, *J* = 8.4 Hz, 2H, H_n), 7.28 (d, *J* = 5.3 Hz, 2H, H_3), 7.21 (dd, *J* = 8.7, 2.6 Hz, 12H, $H_{stopper\ ArH}$), 7.07 (td, *J* = 8.8, 3.2 Hz, 16H, $H_{stopper\ ArH}$), 6.80 (d, *J* = 9.0 Hz, 2H, H_f), 6.73 (d, *J* = 8.9 Hz, 2H, H_d), 5.76 (d, *J* = 9.2 Hz, 4H, $H_{6/7}$), 5.72 (d, *J* = 9.2 Hz, 4H, $H_{6/7}$), 5.50 (s, 2H, H_o), 5.26 (s, 2H, H_j), 5.10 (s, 2H, H_e), 4.82 (s, 4H, H_{10}), 4.27 (t, *J* = 7.3 Hz, 2H, H_a), 4.00 (t, *J* = 6.2 Hz, 2H, H_c), 3.81 (d, *J* = 2.6 Hz, 4H, H_9), 3.70 – 3.61 (m, 8H, $H_{4,8}$), 3.59 – 3.54 (m, 2H, H_5), 3.53 – 3.49 (m, 2H, H_5), 2.22-2.17 (m, 2H, H_b), 1.40 (s, 9H, MC-tBu), 1.29 (s, 54H, stp-tBu).

^{13}C NMR (151 MHz, $CDCl_3$) δ (ppm) 167.65, 163.43, 163.11, 157.83, 156.77, 156.22, 153.08, 152.38, 151.85, 148.49, 148.46, 144.96, 144.23, 144.18, 141.17, 140.38, 140.13, 140.06, 137.59, 136.07, 134.10, 133.81, 132.47, 132.41, 132.29, 132.22, 132.08, 131.05, 130.85, 130.29, 129.35, 128.86, 128.68, 128.60, 127.87, 127.31, 126.22, 126.21, 125.93, 125.06, 124.19, 123.98, 122.76, 121.93, 120.84, 114.68, 114.27, 113.32, 113.26, 74.64, 69.28, 67.62, 67.48, 65.99, 63.20, 62.10, 54.02, 43.97, 40.47, 38.65, 35.35, 34.94, 34.54, 34.43, 34.31, 32.07, 31.77, 31.52, 31.40, 29.84, 29.51, 28.25, 22.84, 14.26, 1.17.

HRMS (ESI +ve) m/z: 2558.1790 ($[M+H]^+$, $C_{147}H_{157}O_{14}N_8$ calc. 2258.1814).

[2]Rotaxane 2.15

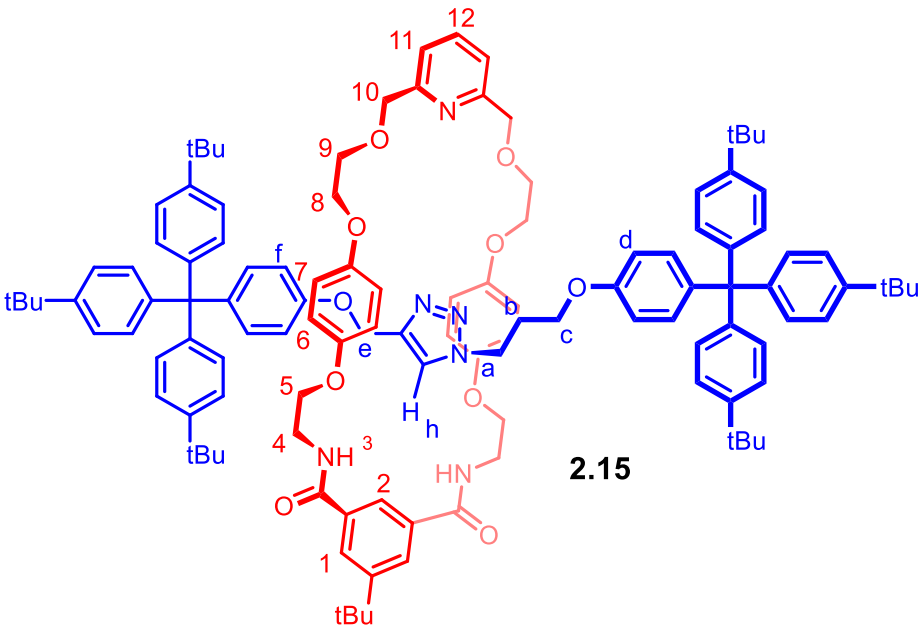

Rotaxane **2.15** was synthesized following the general procedure (1) for CuAAC-AMT synthesis of [2]rotaxane, using macrocycle **2.12** (10.0 mg, 0.0146 mmol), [$CuPF_6(MeCN)_4$] (5.17 mg, 0.0139 mmol), stopper azide **2.7** (42.97 mg , 0.0731 mmol), stopper alkyne **2.8** (39.69 mg, 0.0731 mmol) in dry degassed DCM (1.6 mL total volume). The crude mixture was purified by preparative thin layer chromatography (SiO_2, 0-3% MeOH in DCM) to yield the desired rotaxane as a white solid (21.81 mg, 82%).

^{1}H NMR (500 MHz, $CDCl_3$) δ 8.17 (t, *J* = 1.6 Hz, 1H,H_2), 8.15 (d, *J* = 1.5 Hz, 2H,H_1), 7.49 (t, *J* = 5.3 Hz, 2H, H_3), 7.44 (t, *J* = 7.7 Hz, 1H, H_{12}), 7.25 – 7.19 (m, 14H, H_{11},$H_{stopper\ ArH}$), 7.11 – 7.04 (m, 16H, $H_{stopper\ ArH}$), 6.98 (s, 1H,H_h), 6.67 – 6.60 (m, 4H, $H_{d/f}$), 6.60 – 6.55 (m, 4H, H_7), 6.42 – 6.36 (m, 4H, H_6), 4.72 (s, 2H, H_e), 4.66 – 4.57 (m, 4H, H_{10}), 4.02 – 3.95 (m, 4H, H_8), 3.89 (t, *J* = 7.5 Hz, 2H, H_a), 3.84 – 3.72 (m, 8H, H_9, H_5), 3.66 (q, *J* = 5.2 Hz, 4H, H_4), 3.62 (t, *J* = 5.6 Hz, 2H, H_c).

^{13}C NMR (126 MHz, $CDCl_3$) δ 167.70, 157.57, 156.11, 155.75, 152.85, 152.49, 152.38, 148.36, 144.10, 143.50, 140.61, 140.13, 137.17, 134.01, 132.29, 130.68, 128.69, 124.11, 123.38, 121.42, 120.69, 115.42, 112.92, 74.04, 69.57, 68.00, 66.85, 63.83, 63.07, 61.14, 47.15, 39.84, 35.07, 34.31, 31.94, 31.40, 31.23, 29.71

HRMS: (ESI +ve) m/z: 908.0401 ($[M+2H]^{2+}$, $C_{119}H_{142}N_6O_{10}$ calc. 908.0405)

Proto-triazole macrocycle 2.29

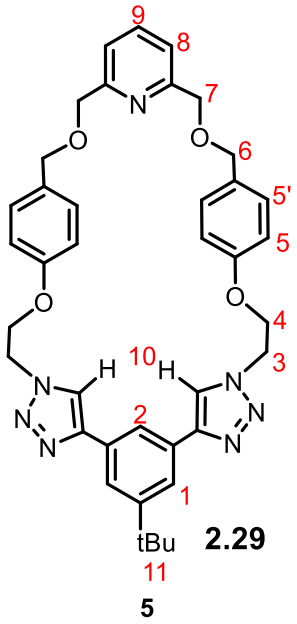

Bis azide precursor **2.3** (250 mg, 0.51 mmol), $[CuPF_6(MeCN)_4]$ (190 mg, 0.51 mmol) and TBTA (271 mg, 0.51 mmol) were dissolved in dry DCM (200 mL) and stirred vigorously for 10 minutes. Bisprotoalkyne **2.28** (93 mg, 0.51 mmol) and DIPEA (0.36 mL, 2.04 mmol) were added sequentially, the flask wrapped in foil and stirred at room temperature for 48 h. The solvent volume was halved *in vacuo*, and washed with basic EDTA/$NH_4OH_{(aq)}$ (30 mL x 3) and H_2O (20 mL), dried over $MgSO_4$ and solvent evaporated *in vacuo*. The crude product was purified by silica gel column chromatography (10-50% EtOAc in DCM) to yield XB macrocycle as a gold foam (92.5 mg, 27%).

^{1}H NMR (400 MHz, $CDCl_3$) δ 8.00 (s, 2H, H_{10}), 7.95 (d, *J* = 1.6 Hz, 2H, H_1), 7.83 (t, *J* = 1.6 Hz, 1H, H_2), 7.68 (broad s, 1H, H_9), 7.33 (d, *J* = 8.0 Hz, 2H, H_8), 7.23 (d, *J* = 8.0 Hz, 4H, H_5), 6.80 (d, *J* = 8.0 Hz, 4H, $H_{5'}$), 4.81 (m, 4H, H_4), 4.57 (s, 4H, H_6), 4.43 (s, 4H, H_7), 4.36 (m, 4H, H_3), 1.41 (s, 9H, H_{11}).

^{13}C NMR (126 MHz, $CDCl_3$) δ 157,67, 157.75, 152.73, 148.21, 137.25, 131.15, 130.10, 122.98, 121.21, 120.79, 120.38, 114.70, 71.38, 72.12, 66.93, 50.13, 35.13, 31.49.

HRMS (ESI +ve) m/z: 672.3276 ($[M+H]^+$, $C_{39}H_{42}N_7O_4$ calc. 672.3293)

Iodo-triazole macrocycle 2.30

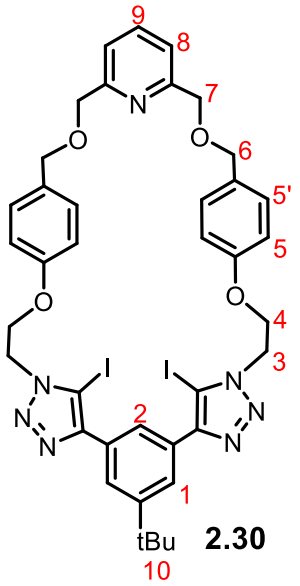

The XB macrocycle **2.30** was synthesized following a similar procedure used to synthesize macrocycle **2.29**, using bis azide precursor **2.3** (128 mg, 0.26 mmol), $[CuPF_6(MeCN)_4]$ (97.5 mg, 0.26 mmol) and TBTA (139 mg, 0.26 mmol), bis iodo alkyne precursor **2.28** (114 mg, 0.26 mmol), DIPEA (0.18 mL, 1.04 mmol) in dry degassed DCM (100 mL). Crude mixture was purified by preparative thin layer chromatography (SiO_2, 0-2% MeOH in DCM) to yield the desired rotaxane as a gold form (65.2 mg, 27%).

^{1}H NMR (500 MHz, $(CD_3)_2CO$) δ 8.32 (t, *J* = 1.6 Hz, 1H, H_2), 8.03 (d, *J* = 1.6 Hz, 2H, H_1), 7.73 (t, *J* = 7.8 Hz, 1H, H_9), 7.34 (d, *J* = 7.7 Hz, 2H, H_8), 7.24 (d, *J* = 10.0 Hz, 4H, H_5), 6.87 (d, *J* = 10.0 Hz, 4H, $H_{5'}$), 4.97 (m, 4H, H_4), 4.58 – 4.53 (m, 8H, H_3 & H_6), 4.34 (s, 4H, H_7), 1.44 (s, 9H, H_{10}).

^{13}C NMR (126 MHz, $(CD_3)_2CO$) δ 157.98, 157.93, 151.55, 149.43, 136.88, 131.05, 130.82, 129.58, 124.50, 123.72, 119.80, 114.35, 71.48, 71.31, 66.83, 49.88, 34.82, 30.78.

HRMS (ESI +ve) m/z: 924.1212 ($[M+H]^+$, $C_{39}H_{40}N_7O_4I_2$ calc. 924.1226)

All HB [2]rotaxane 2.21

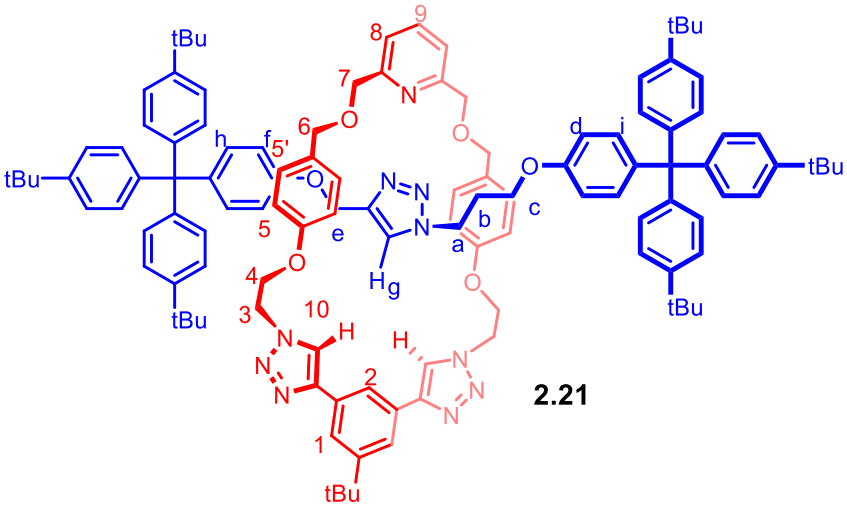

2.21

General procedure (2) for CuAAC-AMT synthesis of [2]rotaxane

Macrocycle **2.29** (10 mg, 0.015 mmol) and $[CuPF_6(MeCN)_4]$ (5.27 mg, 0.0142 mmol) were dissolved in 0.75 mL dry degassed DCM and was stirred for 30 minutes. A solution of stopper azide **2.7** (44.0 mg, 0.075 mmol) and stopper alkyne **2.8** (40.4 mg, 0.075 mmol) in dry degassed DCM (0.75 mL) was added to the Cu-complexed macrocycle solution, followed by 4-5 drops of DIPEA. The reaction mixture was sealed and the homogenous solution was stirred for 48 hours. Subsequently, the reaction mixture was diluted with 10 mL DCM, washed with basic EDTA/$NH_4OH_{(aq)}$ (10 mL x 3) and H_2O (10 mL x 2), dried over $MgSO_4$ and was concentrated in a rotary evaporator. The crude product was purified by preparative thin layer chromatography (SiO_2, 0-2% MeOH in DCM) to yield the desired rotaxane as a white solid (9.1 mg, 34%).

^{1}H NMR (500 MHz, $(CD_3)_2CO$) δ 8.36 (s, 2H, H_{10}), 8.02 (d, *J* = 1.5 Hz, 2H, H_1), 7.98 (t, *J* = 1.5 Hz, 1H, H_2), 7.59 (t, *J* = 7.7 Hz, 1H, H_9), 7.48 (s, 1H, H_g), 7.31 – 7.27 (m, 16H, H_8 & $H_{stopper\ Ar}$***H***), 7.11 – 7.07 (m, 14H, $H_{stopper\ Ar}$***H***), 7.00 (m, 6H, H_5&H_h), 6.92 (d, *J* = 10 Hz, 2H, H_i), 6.73 (d, *J* = 10 Hz, 2H, H_f), 6.59 (d, *J* = 10 Hz, 4H, $H_{5'}$), 6.34 (d, *J* = 10 Hz, 2H, H_d), 4.84 (s, 2H, H_e), 4.78 (m, 4H, H_3), 4.44 (s, 4H, H_6), 4.33 (m, 4H, H_4), 4.28 (s, 4H, H_7), 3.84 (t, *J* = 7.1 Hz, 2H, H_a), 3.32 (t, *J* = 5.9 Hz, 2H, H_c), 1.63 (m, 2H, H_b), 1.30 (m, 63H, $H_{t\text{-}Bu}$).

^{13}C NMR (126 MHz, $(CD_3)_2CO$) δ 158.77, 157.23, 152.93, 149.09, 149.05, 148.17, 145.35, 145.26, 144.02, 140.47, 140.18, 137.87, 132.73, 132.53, 131.49, 131.40, 130.50, 125.10, 124.81, 122.79, 122.27, 121.32, 120.89, 115.34, 114.27, 113.95, 72.43, 72.23, 67.42, 64.66, 63.88, 61.94, 54.97, 50.43, 47.26, 35.51, 34.87, 32.64, 31.73, 31.68, 23.33, 14.36.

HRMS: (ESI +ve) m/z: 1803.0628 ($[M+H]^+$, $C_{119}H_{137}N_{10}O_6$ requires 1803.0749)

Mix XB/HB [2]rotaxane 2.22

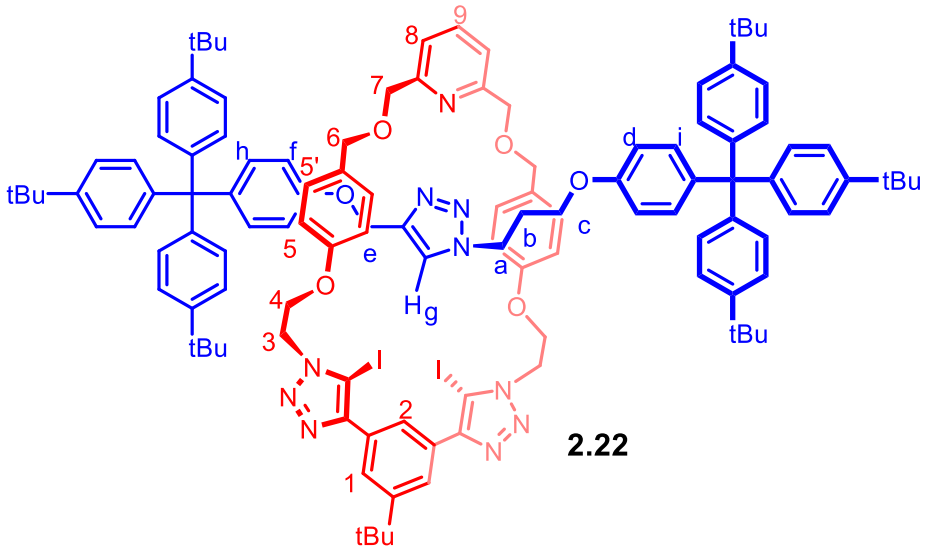

Rotaxane **2.22** was synthesized following the general procedure (2) for CuAAC-AMT synthesis of [2]rotaxane, using the XB macrocycle **2.30** (10 mg, 0.01 mmol), $[CuPF_6(MeCN)_4]$ (3.97 mg, 0.0095 mmol), stopper azide **2.7** (31.8 mg , 0.05 mmol), stopper alkyne **2.8** (29.4 mg, 0.05 mmol) in dry degassed DCM (1.1 mL total volume). The crude mixture was purified by preparative thin layer chromatography (SiO_2, 0-2% MeOH in DCM) to yield the desired rotaxane as a white solid (7.78 mg, 35%).

^{1}H NMR (400 MHz, $CDCl_3$) δ 8.23 (t, *J* = 1.6 Hz, 1H, H_2), 7.99 (d, *J* = 1.6 Hz, 2H, H_1), 7.43 (t, *J* = 7.7 Hz, 1H, H_9), 7.23 – 7.17 (m, 17H, $H_{stopper\ ArH}$,H_g ,H_8), 7.09 – 7.02 (m, 16H, H_h , $H_{stopper\ ArH}$), 6.97 – 6.89 (m, 6H, H_5 & H_i), 6.65 (d, *J* = 7.7 Hz, 2H, H_f), 6.52 (d, *J* = 7.7 Hz, 4H, $H_{5'}$), 6.24 (d, *J* = 7.7 Hz, 2H, H_d), 4.80-4.71 (m, 6H, H_e,H_3), 4.42 (s, 4H, H_6), 4.34 – 4.18 (m, 8H, H_4, H_7), 3.73 (t, *J* = 7.4 Hz, 2H, H_a), 3.23 (t, *J* = 5.7 Hz, 2H, H_c), 1.29 (s, 63H, $H_{t\text{-}Bu}$).

^{13}C NMR (126 MHz, $(CD_3)_2CO$) δ 158.76, 158.65, 157.30, 157.14, 152.41, 150.25, 149.17, 148.99, 145.39, 145.32, 143.90, 140.28, 139.97, 137.76, 132.69, 132.54, 131.84, 131.45, 131.35, 130.40, 125.29, 125.14, 124.62, 124.52, 120.65, 115.23, 114.29, 113.93, 80.49, 72.49, 72.20, 67.61, 64.69, 63.90, 62.06, 50.79, 47.33, 35.71, 34.87, 32.63, 31.73, 31.68, 23.32, 14.35.

HRMS: (ESI +ve) m/z: 2054.8544 ($[M+H]^+$, $C_{119}H_{136}N_{10}O_6I_2$ requires 2054.8682)

All XB [2]rotaxane 2.23

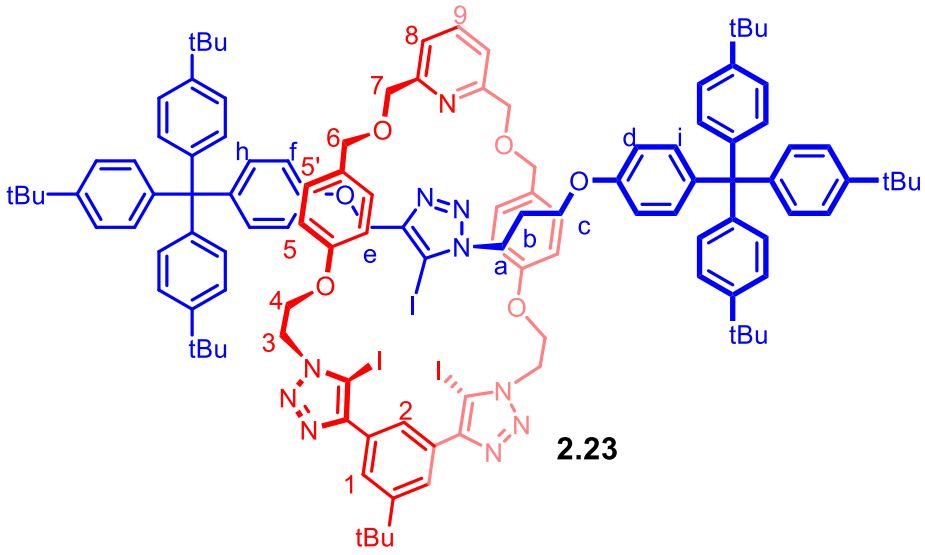

Macrocycle **2.30** (10 mg, 0.01 mmol) and $[CuPF_6(MeCN)_4]$ (3.97 mg, 0.0095 mmol) were dissolved in 0.55 mL dry degassed DCM and was stirred for 30 minutes. A solution of stopper azide **2.7** (31.8 mg , 0.05 mmol), stopper alkyne **2.8** (29.4 mg, 0.05 mmol) in dry degassed DCM (0.55 mL) was added to the Cu-complexed macrocycle solution. Reaction mixture was sealed and heated to 30 °C. Subsequently, $[CuPF_6(MeCN)_4]$ (11.91 mg, 0.0285 mmol) was added portion wise after 48 hours, 72 hours and 96 hours. After 5 days, the reaction mixture was diluted with 10 mL DCM, washed with basic EDTA/$NH_4OH_{(aq)}$ (10 mL x 3) and H_2O (10 mL x 2), dried over $MgSO_4$ and was concentrated in a rotary evaporator. The crude product was purified by preparative thin layer chromatography (SiO_2, 0-2% MeOH in DCM) to yield the desired rotaxane as a white solid (2.00 mg, 8.5%)

^{1}H NMR (500 MHz, $(CD_3)_2CO$) δ 8.17 (t, *J* = 1.7 Hz, 1H, H_2), 8.02 (d, *J* = 1.7 Hz, 2H, H_1), 7.51 (t, *J* = 7.8 Hz, 1H, H_9), 7.34 – 7.26 (m, 14H, $H_{stopper\ ArH}$), 7.23 (d, *J* =8.0 Hz, 2H, H_8), 7.18 – 7.08 (m, 14H, $H_{stopper\ ArH}$), 7.06 (d, *J* =8.8 Hz, 2H, H_h), 7.00 (d, *J* = 8.6 Hz, 4H, H_5), 6.89 (d, *J* = 8.8 Hz, 2H, H_i), 6.77 (d, *J* = 8.8 Hz, 2H, H_f), 6.60 (d, *J* = 8.8 Hz, 4H, $H_{5'}$), 6.21 (d, *J* = 8.8 Hz, 2H, H_d), 4.92 (t, *J* = 4.7 Hz, 4H, H_3), 4.74 (s, 2H, H_e), 4.46 (d, *J* = 2.5 Hz, 4H, H_6), 4.37 (dt, *J* = 13.1, 4.9 Hz, 4H, H_4), 4.23 (s, 4H, H_7), 3.87 (t, *J* = 7.1 Hz, 2H, H_a), 3.22 (t, *J* = 5.7 Hz, 2H, H_c), 1.59 (d, *J* = 6.7 Hz, 2H, H_b), 1.30 (m, 63H, $H_{t\text{-}Bu}$).

^{13}C NMR (126 MHz, $(CD_3)_2CO$) δ 157.95, 157.80, 156.53, 156.28, 151.37, 149.35, 148.22, 148.13, 146.64, 144.56, 144.46, 139.64, 138.98, 136.75, 131.78, 131.65, 130.96, 130.62, 130.57, 129.59, 124.35, 124.30, 124.21, 123.90, 119.31, 114.31, 113.58, 113.09, 81.83, 71.63, 71.15, 66.77, 63.56, 63.06, 61.37, 50.00, 46.90, 34.85, 33.99, 31.74, 30.79, 22.43, 13.45.

HRMS (ESI +ve) m/z: 2180.7568 ($[M+H]^+$, $C_{119}H_{134}N_{10}O_6I_3$ requires 2180.7649)

XB bipyridine receptor 3.3

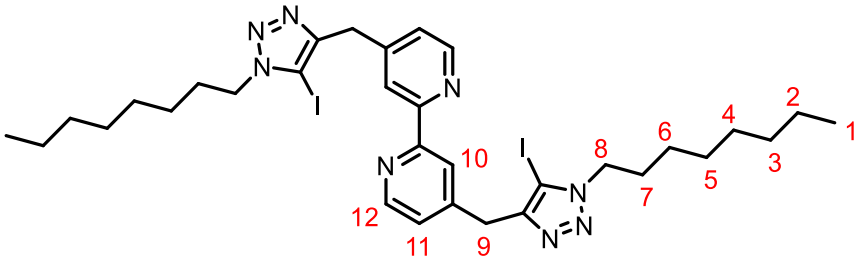

3.3

The bipyridine bis azide precursor **3.1** (100 mg, 0.375 mg) was dissolved in 2 mL of dry degassed THF. NaI (494.64 mg, 3.30 mmol) and $Cu(ClO_4)_2.6H_2O$ (611.391 mg, 1.65 mmol) was added to the reaction mixture and stirred for 5 minutes in dark. TBTA (44.12 mg, 0.08 mmol), DBU (125.60 mg, 0.825 mmol) dissolved in 1 mL of dry degassed THF and 1-decyne **3.2** (0.15 mL, 114.10 mg, 0.826 mmol) were added to the reaction mixture portion wise sequentially. Solution mixture was stirred overnight and the resulting crude was diluted with 100 mL of $CHCl_3$ and was washed successively with basic EDTA (3x25 mL), brine (2x25 mL) and was dried by $MgSO_4$. Crude mixture was concentrated by rotary evaporator. The obtained solid residue was suspended in 20 mL of CH_3CN and was heated at reflux for 1 hour. Solution was cooled to room tempreture. The precipitate formed was filtered off and washed sequentially with CH_3CN (25 mL), Et_2O (25 mL) and dried in the high vacuum to obtain the desired product as a white solid (238.25 mg, 80 %).

^{1}H NMR (400 MHz, $CDCl_3$) δ 8.61 (d, *J* = 5.0 Hz, 2H, H_{12}), 8.36 (s, 2H, H_{10}), 6.94 (d, *J* = 5.1 Hz, 2H, H_{11}), 5.65 (s, 4H, H_9), 2.66 (t, J = 7.7 Hz, 4H, H_8), 1.77-1.63 (m, 4H, H_7), 1.42 – 1.23 (m, 20H, $H_{2\text{-}6}$), 0.86 (t, *J* = 7.03 Hz, 6H, H_1).

^{13}C NMR (126 MHz, $CDCl_3$) δ 156.16, 152.99, 150.04, 144.66, 122.18, 119.84, 78.75, 53.13, 31.92, 29.34, 29.26, 29.23, 28.96, 26.22, 22.73, 14.20.

HRMS (ESI): 795.1843 $[M+H]^+$ ($[C_{32}H_{45}I_2N_8]^+$ calc. 795.1851)

Ir(III) based XB bipyridine receptor 3.4

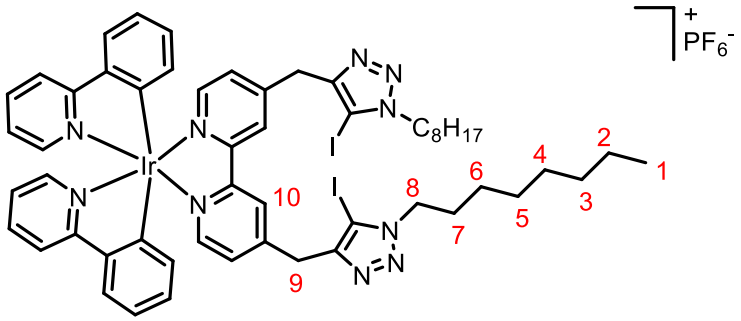

3.4

Bipyridine precursor **3.3** (15 mg, 0.019 mmol) and $[Ir_2(ppy)_4Cl_2]$ (13.94 mg, 0.013 mmol) was dissolved in DCM:MeOH (1:1, 5 mL) solution and was stirred at 55 °C for 16 hours. Solution was concentrated by rotary evaporator and purified by preparative TLC (silica, 4-8% MeOH in DCM eluent). Product was taken up to DCM (20 mL) and washed with 0.1 M NH_4PF_6(aq) solution (8x 10 mL) and H_2O (2x 10 mL). The organics were dried over $MgSO_4$ and concentrated by rotary evaporator to afford the desired product as a yellow solid (22.24 mg, 82 %)

^{1}H NMR (400 MHz, $CDCl_3$) δ 9.85 (s, 2H, H_{10}), 7.88 (d, *J* = 8.2 Hz, 2H, ArH), 7.83 – 7.70 (m, 4H, ArH), 7.63 (d, *J* = 7.8 Hz, 2H, ArH), 7.44 (d, *J* = 5.8 Hz, 2H, ArH), 7.03 (t, *J* = 7.4 Hz, 2H, ArH), 6.98 (t, *J* = 7.4 Hz, 2H, ArH), 6.86 (t, *J* = 7.4 Hz, 2H, ArH), 6.80 (d, *J* = 5.7 Hz, 2H, ArH), 6.22 (d, *J* = 7.6 Hz, 2H, ArH), 6.12 – 5.89 (m, 4H, H_9), 2.59 (t, *J* = 7.8 Hz, 4H, H_8), 1.63 (p, *J* = 7.3 Hz, 4H, H_7), 1.41 – 1.08 (m, 20H, $H_{2\text{-}6}$), 0.85 (t, *J* = 6.7 Hz, 6H, H_1).[****]

^{13}C NMR (126 MHz, $CDCl_3$) δ 167.91, 156.03, 152.88, 150.63, 149.77, 148.96, 148.54, 143.45, 138.35, 131.71, 130.99, 126.05, 125.95, 124.95, 123.57, 122.93, 119.87, 83.04, 52.46, 31.94, 29.81, 29.40, 29.30, 29.13, 26.39, 22.77, 14.24.

HRMS (ESI): 1295.2688 $[M]^+$ ($[C_{54}H_{60}I_2IrN_{10}]^+$ calc. 1295.2719)

[****] Phenylpyridine and bipyridine protons are designated as ArH, unless otherwise stated.

Ir(III) based bis azide axle precursor 3.5

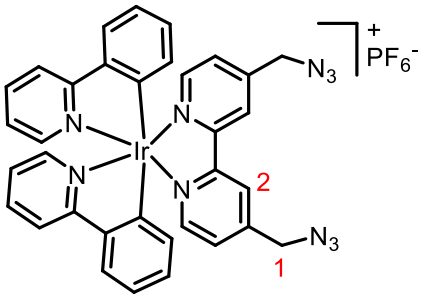

3.5

Bipyridine bis-azide precursor **3.1** (7 mg, 0.026 mmol) and $[Ir_2(ppy)_4Cl_2]$ (16.92 mg, 0.016 mmol) was dissolved in DCM:MeOH (1:1, 5 mL) solution and was stirred at 55 °C for 16 hours. Solution was concentrated by rotary evaporator and purified by preparative TLC (silica, 8-10% MeOH in DCM eluent). Product was taken up to DCM (20 mL) and washed with 0.1 M NH_4PF_6(aq.) solution (8x 10 mL) and H_2O (2x 10 mL). The organics were dried over $MgSO_4$ and concentrated by rotary evaporator to afford the desired product as a yellow solid (16.84 mg, 71 %)

^{1}H NMR (400 MHz, $CDCl_3$) δ 9.84 (s, 2H, H_2), 7.91 (d, *J* = 8.2 Hz, 2H, ArH), 7.85 (d, *J* = 5.6 Hz, 2H, ArH), 7.76 (t, *J* = 7.8 Hz, 2H, ArH), 7.68 (d, *J* = 7.9 Hz, 2H, ArH), 7.45 (t, *J* = 7.8 Hz, 4H, ArH), 7.04 (t, *J* = 7.4, 4H, ArH), 6.99 (t, *J* = 7.4, 4H, ArH), 6.91 (t, *J* = 7.4, 2H, ArH), 6.29 (d, *J* = 7.7 Hz, 2H, ArH), 5.08 – 4.86 (m, 4H, H_1).[††††]

^{13}C NMR (126 MHz, $CDCl_3$) δ 168.06, 156.05, 150.38, 150.34, 150.08, 148.54, 143.53, 138.20, 131.86, 131.00, 126.32, 126.30, 125.94, 124.96, 123.34, 122.82, 119.78, 52.65, 1.14.

HRMS (ESI): 767.1959 $[M]^+$ ($[C_{34}H_{26}IrN_{10}]^+$ calc. 767.1967)

[††††] Phenylpyridine and bipyridine protons are designated as ArH, unless otherwise stated.

Ir(III) complexed [3]rotaxane 3.8 and [2]rotaxane 3.9

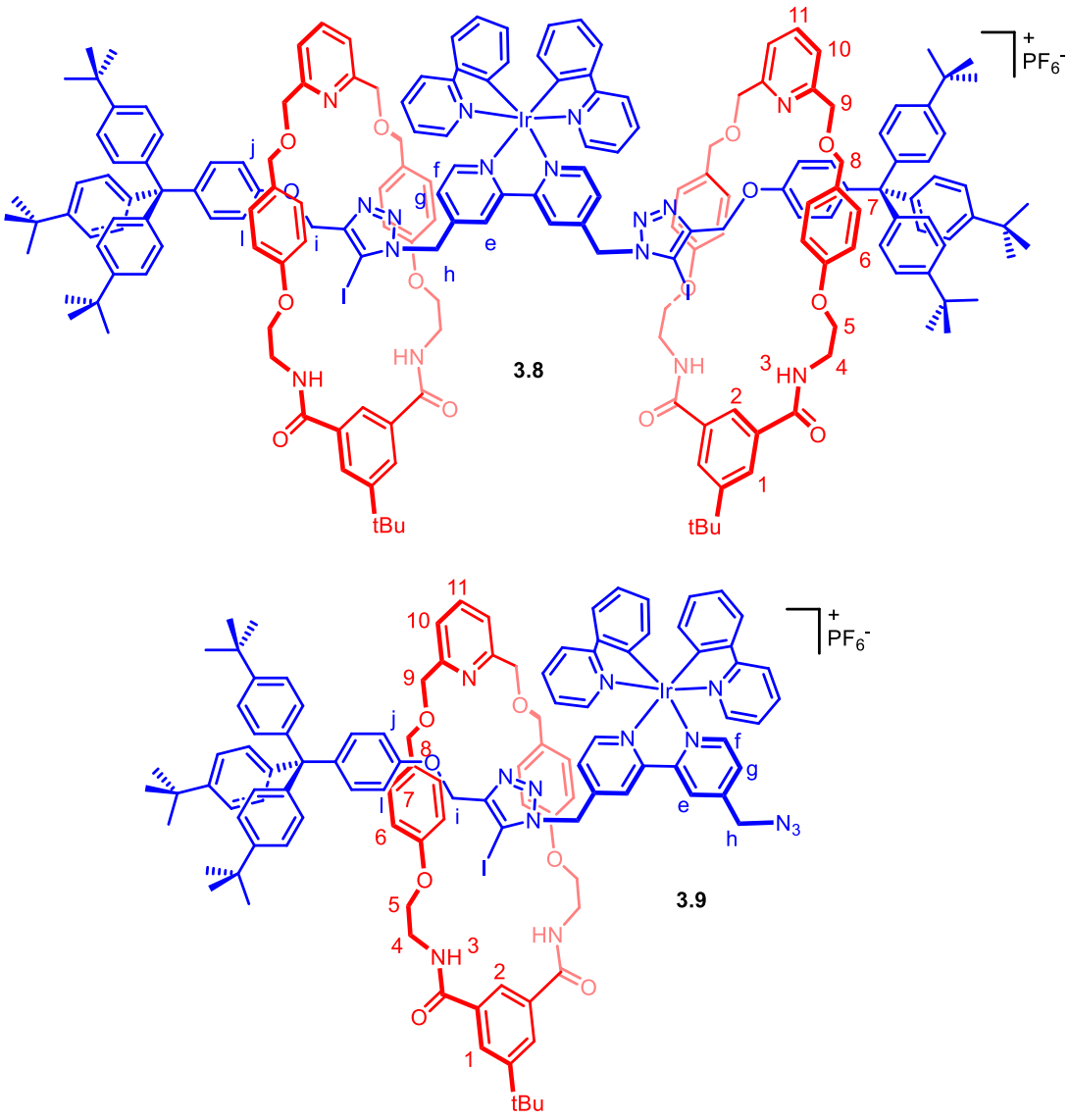

Method 01:

Macrocycle **2.6** (13.7 mg, 0.022 mmol) and [$CuPF_6(MeCN)_4$] (8.03 mg, 0.021 mmol) were dissolved in 0.08 mL dry degassed DCM and was stirred for 30 minutes. A solution of Ir(III) complexed bis-azide **3.5** (30.0 mg , 0.033 mmol), stopper iodo alkyne **2.8** (44.1 mg, 0.066 mmol) in dry degassed DCM (0.5 mL) was added to the Cu-complexed macrocycle solution. Reaction mixture was covered in foil and stirred at room temperature for 9 days. On the 9th day, macrocycle **2.6** (623.7 mg, 0.011 mmol), [$CuPF_6(MeCN)_4$] (4.01 mg, 0.010 mmol) and stopper iodo alkyne **2.8** (7.35 mg, 0.011 mmol) were dissolved in 0.4 mL of dry degassed DCM

separately and was added to the reaction mixture. The final reactant ratio of the reaction mixture was 3:7:3 (**2.6/2.8/3.5).** After 14 days, the reaction mixture was diluted with 10 mL DCM, washed with basic EDTA/$NH_4OH_{(aq)}$ (10 mL x 3) and H_2O (10 mL x 2), dried over $MgSO_4$ and was concentrated in a rotary evaporator. The crude product was purified by preparative thin layer chromatography (SiO_2, 80%-EtOAc in Hexane and 4% MeOH in DCM). Seperated products were taken up to DCM (20 mL) and washed with 0.1 M NH_4PF_6(aq.) solution (8x 10 mL) and H_2O (2x 10 mL). The organics were dried over $MgSO_4$ and concentrated by rotary evaporator to afford the desired [3]rotaxane **3.8** as an orange solid (7.84 mg, 7.3%). [2]rotaxane **3.9** was isolated as by product in (4.0 mg, 5.5%) yield as an orange solid.

Method 2: Following similar steps stated in Method 1, macrocycle **2.6** (13.7 mg, 0.022 mmol), $[CuPF_6(MeCN)_4]$ (7.78 mg, 0.021 mmol), Ir(III) complexed bis-azide **3.5** (10.0 mg , 0.011 mmol), stopper alkyne **2.8** (14.7 mg, 0.022 mmol) in dry degassed DCM (1.5 mL total volume). After 9 days, macrocycle **2.6** (6.87 mg, 0.011 mmol), $[CuPF_6(MeCN)_4]$ (3.89 mg, 0.010 mmol), stopper alkyne **2.8** (7.4 mg, 0.011 mmol) in dry degassed DCM (0.5 mL total volume) was added to the reaction mixture. The final reactant ratio of the reaction mixture was 3:3:1 (**2.6/2.8/3.5).** The crude mixture was purified by preparative thin layer chromatography (SiO_2, 80%-EtOAc in Hexane and 4% MeOH in DCM) to yield the desired [3]rotaxane **3.8** as an orange solid (7.02 mg, 20%). (Preparative thin layer chromatography afforded <1 mg of the [2]rotaxane **3.9** and hence the [2]rotaxane was not exchanged to the PF_6^- anion).

Characterisation of [3]rotaxane **3.8:**

^{1}H NMR (400 MHz, $CDCl_3$) δ 8.40 (s, 2H, H_2), 8.36 (s, 2H, H_e), 8.04 (d, *J* = 13.4 Hz, 4H, H_1), 7.86 (d, *J* = 8.2 Hz, 2H, H_g), 7.76 – 7.63 (m, 6H, H_g, H_{Ar-H}), 7.46 – 7.35 (m, 6H, H_{11}, H_3, H_{Ar-H}), 7.19 – 6.87 (m, 48H, $H_{stopper\ ArH}$, H_{Ar-H}, H_{10}, $H_{6'}$, $H_{3'}$), 6.58 (d, *J* = 8.5 Hz, 4H, H_7), 6.28 (m, 6H, H_6,H_j), 6.20 (d, *J* = 8.2 Hz, 4H, $H_{7'}$), 5.99 (d, *J* = 5.8 Hz, 2H, H_l), 5.34 – 5.15 (m, 4H, H_i), 4.75 – 4.64 (m, 4H, H_h), 4.50 – 4.22 (m, 16H, H_8,H_9), 3.64 – 2.94 (m, 16H, H_4,H_5), 1.22 (m, 54H, $H_{t\text{-}Bu}$).[‡‡‡‡]

^{13}C NMR (126 MHz, $CDCl_3$) δ 167.75, 158.03, 155.80, 152.19, 148.37, 143.98, 143.53, 140.75, 138.47, 133.74, 132.34, 131.71, 130.67, 128.63, 124.93, 124.13, 122.91, 119.78, 114.11, 113.16, 72.73, 66.28, 63.07, 39.27, 35.03, 34.32, 31.95, 29.72, 22.71, 14.14, 1.04.

^{19}F NMR (377 MHz, $CDCl_3$) δ -71.445 (d, $J_{F\text{-}P}$ = 714 Hz)

^{31}P NMR (162 MHz, $CDCl_3$) δ -144.14 (sep, $J_{F\text{-}P}$ = 714 Hz)

HRMS (ESI +ve) m/z: 1676.1542 ($[M+H]^{2+}$, $C_{188}H_{199}N_{16}O_{14}I_2Ir_1$ calc. 1676.1552)

Characterisation of [2]rotaxane **3.9:**

^{1}H NMR (400 MHz, $CDCl_3$) δ 8.59 (s, 1H, H_2), 8.48 (s, 2H, H_e), 8.15 (d, *J* = 11.4 Hz, 2H, H_1), 7.93 – 7.87 (m, 3H, H_f,H_{Ar-H}), 7.81 – 7.64 (m, 6H, H_g,H_{Ar-H}), 7.62 – 7.34 (m, 6H, H_3, H_{11}, H_{Ar-H}), 7.23 – 6.97 (m, 26H, $H_{stopper\ ArH}$, H_{Ar-H}, H_{10}, $H_{6'}$), 6.92 (t, *J* = 7.4 Hz, 1H, H_{Ar-H}), 6.67 (d, *J* = 8.8 Hz, 2H, H_7), 6.35 – 6.22 (m, 7H, H_7,H_6,H_j,H_l), 5.29 (s, 2H,H_i), 4.82 – 4.67 (m, 4H,H_h), 4.58 – 4.32 (m, 8H, $H_{8,9}$), 3.72 – 3.13 (m, 8H,$H_{4,5}$), 1.29 (s, 27H, $H_{t\text{-}Bu}$).

^{13}C NMR (151 MHz, $CDCl_3$) δ 167.73, 155.81, 155.36, 150.59, 150.05, 149.77, 148.55, 144.09, 143.72, 143.56, 138.40, 134.04, 132.51, 131.79, 131.15, 130.80, 129.05, 128.86, 126.50, 125.00, 124.28, 123.75, 123.06, 119.72, 114.18, 63.22, 52.69, 35.20, 34.45, 33.46, 32.07, 31.53, 31.37, 29.85, 24.91, 22.84, 14.26, 1.16.

^{31}P NMR (162 MHz, $CDCl_3$) δ -144.43 (d, $J_{F\text{-}P}$ = 714 Hz)

^{19}F NMR (377 MHz, $CDCl_3$) δ -72.19 (sep, $J_{F\text{-}P}$ = 714 Hz)

HRMS: (ESI +ve) m/z: 2059.7453 ($[M+H]^+$, $C_{111}H_{112}N_{13}O_{14}I_1Ir_1$ calc. 2058.7488)

[‡‡‡‡] Phenylpyridine and bipyridine protons are designated as ArH, unless otherwise stated.

Monocationic XB receptor 4.2XB

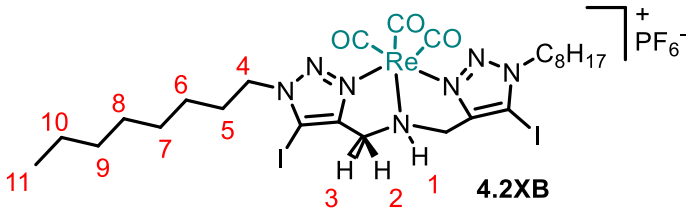

4.2XB

Bis-iodotriazole-amine **4.1XB** (36 mg, 0.054 mmol) and $Re[(CO)_3(H_2O)_3]Br$ (22 mg, 0.054 mmol) were suspended in 0.5 mL of CH_3OH in a microwave vial and then the reaction mixture was heated at 100 °C for 5 min under microwave reaction conditions. The reaction mixture was diluted using 1 mL of CH_3OH and stirred with NH_4PF_6 powder (8.8 mg, 0.054 mmol) at 0 °C for 30 min. Subsequently, 10 mL of saturated NH_4PF_6 aqueous solution was added in one portion. The resulting white precipitate was collected by filtration, washed with H_2O (2 x 5 mL) and then dried with high vacuum to afford the product **4.2XB** as a white solid (40 mg, 68%).

^{1}H NMR (400 MHz, CD_3OD) δ (ppm): 4.54 (2H, d, ^2J = 16.6 Hz, H_2), 4.40 (4H, t, ^3J = 6.8 Hz, H_4), 4.34 (2H, d, ^2J = 16.6 Hz, H_3), 1.86 (4H, quin, ^3J = 7.2 Hz, H_5), 1.34–1.22 (20H, m, H_6-H_{10}), 0.91 (6H, t, ^3J = 7.1 Hz, H_{11})

^{13}C NMR (126 MHz, CD_3OD) δ 204.80, 203.96, 163.62, 92.09, 61.97, 60.83, 58.09, 40.60, 38.25, 37.95, 37.51, 34.74, 31.55, 23.44.

^{19}F NMR (376 MHz, CD_3OD) δ (ppm): -74.0 (d, $^1J_{F\text{-}P}$ = 752 Hz)

^{31}P NMR (162 MHz, CD_3OD) δ (ppm): -144.6 (sep., $^1J_{F\text{-}P}$ = 752 Hz)

HRMS (ESI +ve) m/z = 926.07493 ($[M - PF_6]^+$, $C_{25}H_{39}O_3N_7I_2Re$, calc. 926.07558).

Monocationic HB receptor 4.2HB

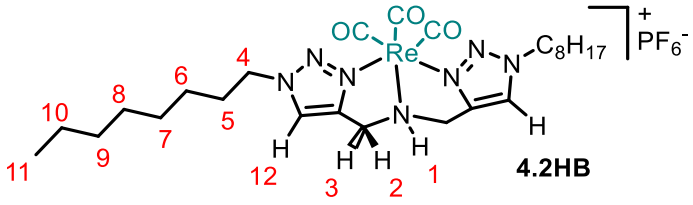

Bis-triazole-amine **4.1HB** (20 mg, 0.0496 mmol) and $Re[(CO)_3(H_2O)_3]Br$ (20 mg, 0.0495 mmol) were suspended in 0.5 mL of CH_3OH in a microwave vial and then the reaction mixture was heated at 100 °C for 5 min under microwave reaction conditions. The reaction was diluted using 1 mL of CH_3OH and stirred with NH_4PF_6 powder (8.1 mg, 0.0496 mmol) at 0 °C for 30 min. Subsequently, 10 mL of saturated NH_4PF_6 aqueous solution was added in one portion. The resulting white precipitate was collected by filtration, washed with H_2O (2 x 5 mL) and then dried with high vacuum to afford the product **4.2HB** as a white solid (28 mg, 70%).

^{1}H NMR (400 MHz, CD_3CN) δ (ppm): 7.82 (2H, s, H_{12}), 6.47 (1H, s, H_1), 4.52 (2H, dd, J = 16.4, 6.7 Hz, H_2), 4.40 (4H, t, J = 7.2 Hz,H_4), 4.26 (2H, d, J = 16.4, H_3), 1.91 – 1.85 (4H, m, H_5), 1.37–1.28 (20H, m, H_6–H_{10}), 1.00 (6H, t, ^3J = 7.0 Hz, H_{11})

^{13}C NMR (500 MHz, $CDCl_3$) δ 194.71, 193.14, 148.10, 122.83, 53.31, 52.25, 31.84, 29.83, 29.15, 28.92, 26.38, 22.81, 14.23, 1.19.

^{19}F NMR (376 MHz, $CDCl_3$) δ -71.4 (d, $^1J_{F\text{-}P}$ = 757 Hz);

^{31}P NMR (162 MHz, $CDCl_3$) δ -144.3 (sep., $^1J_{F\text{-}P}$ = 757 Hz);

HRMS (ESI +ve) m/z = 674.28189 ($[M - PF_6]^+$, $C_{25}H_{41}O_3N_7Re$, calc. 674.28229).

Neutral XB tweezer receptor 4.3XB

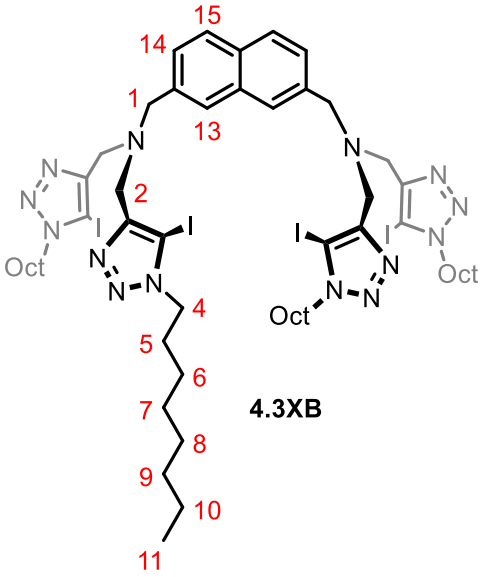

Bis-iodotriazole-amine **4.1XB** (30 mg, 0.046 mmol) and 2,7-Bis(bromomethyl)naphthalene (7 mg, 0.023 mmol) were dissolved in 1 mL of $CHCl_3$ before N,N-Diisopropylethylamine (12 mg, 0.092 mmol) was added. The reaction mixture was stirred at room temperature for 48 hrs and then diluted using 10 mL of $CHCl_3$. The organic phase was washed with H_2O (10 mL x 5) and dried with $MgSO_4$. The solvent was removed by vacuum and purification of the compound was achieved by preparative TLC chromatography (98:2 CH_2Cl_2/CH_3OH) to give the product **4.3XB** as an off-white solid (20.2 mg, 60% yield).

^{1}H NMR (400 MHz, d_6-acetone) δ (ppm): 7.83 (2H, s, H_{13}), 7.60 (2H, d, ^3J = 8.4 Hz, H_{15}), 7.37 (2H, d, ^3J = 8.4 Hz, H_{14}), 4.28 (8H, t, ^3J = 7.2 Hz, H_4), 3.73 (4H, s, H_1), 3.68 (8H, s, H_2), 1.75 (8H, quin, ^3J = 7.0 Hz, H_5), 1.21-1.14 (40H, m, $H_6 – H_{10}$), 0.74 (12H, t, ^3J = 7.1 Hz, H_{11})

^{13}C NMR (126 MHz, d_6-acetone) δ 148.19, 136.69, 133.21, 132.13, 127.56, 127.14, 127.07, 81.36, 57.10, 50.21, 48.90, 31.58, 29.70, 26.14, 22.38, 13.47.

HRMS (ESI +ve) m/z = 1463.33509, ($[M+H]^+$, $C_{56}H_{87}N_{14}I_2$, calc. 1463.34114).

Neutral HB tweezer receptor 4.3HB

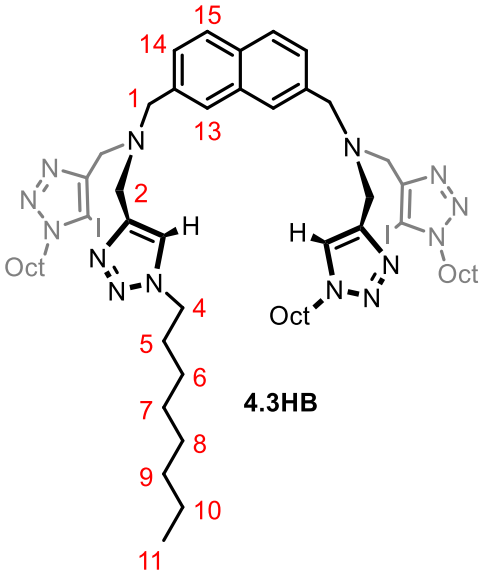

Bis-iodotriazole-amine **4.1HB** (100 mg, 0.248 mmol) and 2,7-Bis(bromomethyl)naphthalene (37.1 mg, 0.118 mmol) were dissolved in 2 mL of 1:1 $CHCl_3$/CH_3CN before K_2CO_3 (163 mg, 1.18 mmol) was added. The reaction mixture was stirred at room temperature for 5 days and then diluted using 10 mL of $CHCl_3$. The organic phase was washed with H_2O (10 mL x 5) and dried with $MgSO_4$. The solvent was removed by vacuum and purification of the compound was achieved by preparative TLC chromatography (98:2 CH_2Cl_2/CH_3OH) to give the product **4.3XB** as an off-white solid (34 mg, 30% yield).

^{1}H NMR (400 MHz, $CDCl_3$) δ (ppm): 7.80 (s, 2H, H_{13}), 7.76 (d, *J* = 8.4 Hz, 2H, H_{15}), 7.60 (s, 4H, H_{12}), 7.50 (d, *J* = 8.3 Hz, 2H, H_{14}), 4.32 (t, *J* = 7.3 Hz, 8H, H_4), 3.81 (s, 4H, H_1), 3.78 (s, 8H, H_2), 1.81-1.93 (m, 8H, H_5), 1.40 – 1.13 (m, 40H, $H_{6\text{-}10}$), 0.84 (t, *J* = 6.7 Hz, 12H, H_{11}).

^{13}C NMR (126 MHz, $CDCl_3$) δ 144.39, 136.82, 133.42, 132.20, 127.75, 127.56, 127.08, 123.17, 58.16, 50.40, 47.50, 31.77, 30.41, 29.13, 29.04, 26.60, 22.66, 14.13.

HRMS (ESI): 959.7546 $[M+H]^+$ ($[C_{56}H_{91}N_{14}]^+$ calc.959.7542)

Neutral XB tweezer receptor 4.4XB

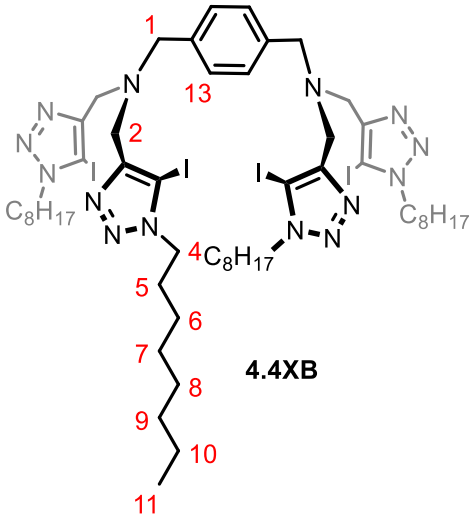

4.4XB

Bis-iodotriazole-amine **4.1XB** (90 mg, 0.137 mmol) and 1,4-bis(bromomethyl)benzene (15.1 mg, 0.057 mmol) were dissolved in 2 mL of 1:1 $CHCl_3/CH_3CN$ before K_2CO_3 (79 mg, 0.57 mmol) was added. The reaction mixture was stirred at room temperature for 2 days and then diluted using 10 mL of $CHCl_3$. The organic phase was washed with H_2O (10 mL x 5) and dried with $MgSO_4$. The solvent was removed by vacuum and purification of the compound was achieved by preparative TLC chromatography (8:2 $CH_2Cl_2/C_4H_8O_2$) to give the product **4.4XB** as an off-white solid (50 mg, 62% yield).

^{1}H NMR (500 MHz, $CDCl_3$) δ (ppm): 0.85 (t, *J* = 6.6, 6.6 Hz, 12H, H_{11}), 1.16-1.35 (m, 40H, $H_{6\text{-}10}$), 1.79-1.89 (m, 8H, H_5), 3.60 (s, 4H, H_1), 3.70 (s, 8H, H_2), 4.31 (t, *J* = 7.4, 7.4 Hz, 8H, H_4), 7.32 (s, 4H, H_{13}).

^{13}C NMR (126 MHz, $CDCl_3$) δ 13.07, 21.59, 25.38, 27.95, 28.05, 28.96, 30.69, 47.38, 49.67, 56.30, 79.66, 128.45, 136.35, 147.44.

HRMS (ESI): 1413.31909 $[M+H]^+$ ($[C_{52}H_{85}N_{14}{}^{127}I_4]^+$ calc. 1413.32549)

Dicationic XB tweezer receptor 4.5XB

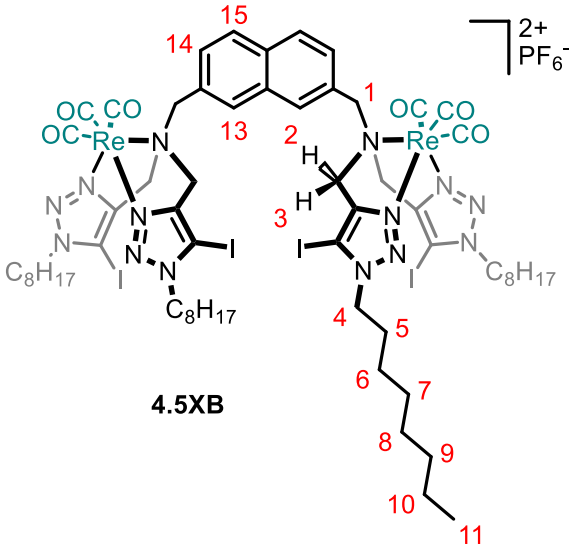

4.5XB

Compound **4.3.XB** (30 mg, 0.021 mmol) and $Re[(CO)_3(H_2O)_3]Br$ (17 mg, 0.042 mmol) were suspended in 1 mL of CH_3OH in a microwave vial and then the reaction mixture was heated at 100 °C for 5 min. under microwave reaction conditions. The reaction mixture was diluted using 1 mL of CH_3OH and stirred with NH_4PF_6 powder (17.6 mg, 0.108 mmol) at 0 °C for 30 min. Subsequently, 10 mL of saturated NH_4PF_6 aqueous solution was added in one portion. The resulting white precipitate was collected by filtration, washed with H_2O (2 x 5 mL) and then dried with high vacuum to afford the product **4.5XB** as a white solid (29 mg, 58%).

^{1}H NMR (500 MHz, $CDCl_3$) δ(ppm): 8.46 (2H, s, H_{13}), 8.12 (2H, d, ^3J = 8.4 Hz, H_{15}), 7.72 (2H, d, ^3J = 8.4 Hz, H_{14}), 5.09 (4H, s, H_1), 4.74 (4H, d, ^2J = 15.9 Hz, H_2), 4.32 (8H, m, H_4), 4.74 (4H, d, ^2J = 15.9 Hz, H_3), 1.88 (8H, quin, ^3J = 7.0 Hz, H_5), 1.34-1.28 (40H, m, $H_6 - H_{10}$), 0.91 (12H, t, ^3J = 7.4 Hz, H_{11})

^{13}C NMR (126 MHz, $CDCl_3$) δ 194.79, 192.14, 153.28, 133.98, 133.72, 133.52, 129.91, 129.19, 129.03, 71.59, 57.46, 52.67, 31.81, 29.85, 29.50, 29.14, 28.89, 26.35, 22.74, 14.22.

^{19}F NMR (376 MHz, $CDCl_3$) δ -70.1 (d, $^1J_{F-P}$ = 752 Hz)

^{31}P NMR (162 MHz, $CDCl_3$) δ -144.6 (sep., $^1J_{F-P}$ = 752 Hz)

HRMS (ESI +ve) m/z = 1002.10524 ($[M - 2PF_6]^{2+}$, $C_{62}H_{86}O_6N_{14}I_4Re_2$, calc. 1001.10548)

Dicationic HB tweezer receptor 4.5HB

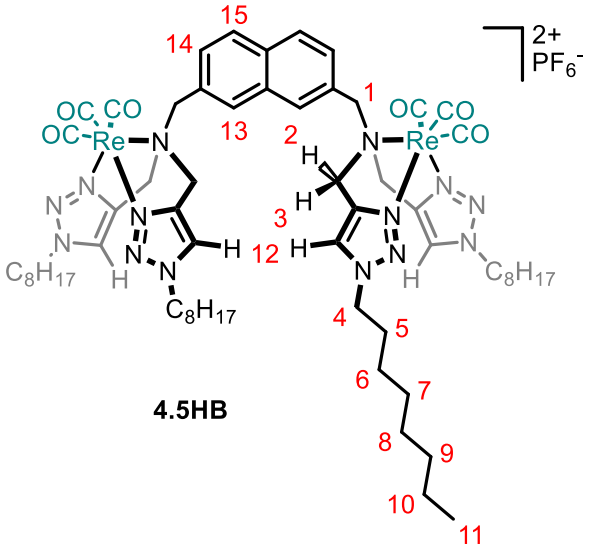

4.5HB

Compound **4.3.HB** (20 mg, 0.021 mmol) and $Re[(CO)_3(H_2O)_3]Br$ (17.4 mg, 0.043 mmol) were suspended in 1 mL of CH_3OH in a microwave vial and then the reaction mixture was heated at 100 °C for 5 min under microwave reaction conditions. The reaction mixture was diluted using 1 mL of CH_3OH and stirred with NH_4PF_6 powder (17.6 mg, 0.108 mmol) at 0 °C for 30 min. Subsequently, 10 mL of saturated NH_4PF_6 aqueous solution was added in one portion. The resulting white precipitate was collected by filtration, washed with H_2O (2 x 5 mL) and then dried with high vacuum to afford the product **4.5.HB** as a white solid (23 mg, 60%).

^{1}H NMR (500 MHz, $CDCl_3$) δ (ppm): 8.45 (s, 2H, H_{13}), 8.00 (d, *J* = 8.4 Hz, 2H, H_{15}), 7.66 (s, 4H, H_{12}), 7.56 (dd, *J* = 8.3, 1.6 Hz, 2H, H_{14}), 5.13 (s, 4H,H_1), 4.56 (d, *J* = 15.9 Hz, 4H, H_3), 4.13-4.27 (m, 8H, H_4), 4.07 (d, *J* = 15.9 Hz, 4H, H_2), 1.85-1.74 (m, 8H, H_5), 1.31-1.20 (m, 40H, $H_{6\text{-}11}$), 0.87 (t, *J* = 6.9 Hz, 12H, H_{11}).

^{13}C NMR (101 MHz, $CDCl_3$) δ 195.77, 192.47, 148.64, 133.82, 133.41, 131.32, 130.10, 129.50, 128.67, 73.86, 58.43, 52.04, 31.67, 29.71, 28.96, 28.75, 26.17, 22.57, 14.06.

^{19}F NMR (377 MHz, $CDCl_3$) δ -72.1 (d, $^1J_{F\text{-}P}$ = 712.7 Hz)

^{31}P NMR (162 MHz, $CDCl_3$) δ -144.6 (sep., $^1J_{F\text{-}P}$ = 712.8 Hz)

HRMS (ESI +ve) m/z = 750.3140 ($[M - 2PF_6]^{2+}$, $C_{62}H_{90}O_6N_{14}Re_2$, calc. 750.3130).

Dicationic XB tweezer receptor 4.6XB

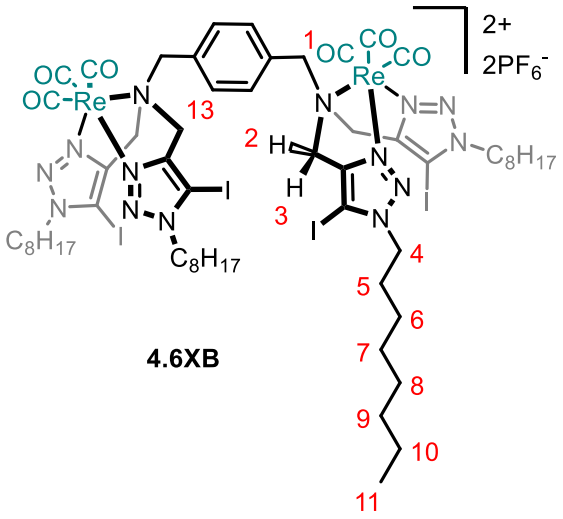

4.6XB

Compound **4.4XB** (15 mg, 0.0106 mmol) and $Re[(CO)_3(H_2O)_3]Br$ (8.56 mg, 0.021 mmol) were suspended in 1 mL of CH_3OH in a microwave vial and then the reaction mixture was heated at 100 °C for 5 min under microwave reaction conditions. The resultant mixture was washed with 0.1 M NH_4PF_6(aq) (10x10 mL) and then deionized water (2x20 mL) and dried with $MgSO_4$. The solvent was removed by vacuum and purification of the compound was achieved by preparative TLC chromatography (3:97 CH_2Cl_2/CH_3OH) to give the product **4.6XB** as an off-white solid (8.8 mg, 37% yield).

^{1}H NMR (500 MHz, $(CD_3)_2CO$) δ (ppm): 0.87 (t, *J* = 7.1, 7.1 Hz, 12H, H_{11}), 1.14 – 1.41 (m, 40H, $H_{6\text{-}10}$), 1.79-1.90 (m, 8H, H_5), 4.49-4.40 (m, 4H, H_2 ,H_4), 4.34 – 4.48 (t, *J* = 7.4, 7.4 Hz, 8H, H_4), 5.26 (d, *J = 16 Hz,* 4H, H_3), 5.31 (s, 4H, H_1), 8.24 (s, 4H, H_{13}).

^{13}C NMR (500 MHz, $(CD_3)_2CO$) δ 13.50, 22.41, 25.80, 28.36, 28.55, 28.75, 28.94, 29.13, 29.32, 29.52, 31.61, 51.66, 59.12, 71.70, 91.35, 132.70, 133.33, 152.37, 193.27, 195.64, 205.24.

^{19}F NMR (376 MHz, $CDCl_3$) δ (ppm): -72.3 (d, $^1J_{F\text{-}P}$ = 706.9 Hz)

^{31}P NMR (162 MHz, $CDCl_3$) δ (ppm): -144.3 (sep., $^1J_{F\text{-}P}$ = 709.6 Hz)

HRMS (ESI): 976.0976 $[M]^{2+}$ ($[C_{58}H_{84}I_4N_{14}O_6Re_2]^{2+}$ calc.976.0987)

Appendices

Appendix A: Titration data of heteroditopic [2]rotaxanes

Calculation of the percentage of lithium precomplexed rotaxane **2.9** and **2.22** upon addition of 1 eq. of $LiClO_4$

Assuming that Li^+ can only exist in the form of Li^+ ion and as a complex with the rotaxane (Rot-Li), the following equilibria can be derived.

$$Rot + Li^+ \leftrightharpoons Rot\text{-}Li\ complex$$

Therefore, association constant (K_a) of Li^+ complexing with the rotaxane is shown below:

$$Ka = \frac{[Rot - Li]}{[Rot][\ Li^+]} \quad (1)$$

If, x = [Rot-Li] moles upon addition of 1 eq. $LiClO_4$

V= solvent volume in NMR tube = 0.0005 L

Initial number of moles of rotaxane in NMR tube = $5x10^{-7}$ mol

In the presence of 1 eq. of $LiClO_4$: [*Rot*] = [Li^+] = $(5 * 10^{-7} - x)/_v$

[*Rot-Li*] = $x/_v$

$LiClO_4$ association constants to rotaxane **2.9** = K_a = 312 M^{-1}

By substituting all the above values to equation (1):

$$312 = \frac{x/_v}{\left((5 * 10^{-7} - x)/_v\right)^2}$$

By solving the above equation for x: x'= 1×10^{-7} and x''=2.5×10^{-6}

As x''>5×10^{-7} , which is the initial number of moles of rotaxane

x=x'= 1×10^{-7} mol

Therefore, $[\mathrm{Rot}-\mathrm{Li}]\ \% = \left(\frac{1*10^{-7}}{5*10^{-7}}\right) 100 = 20\%$

According to calculations, ca.20% of rotaxane **2.9** is bound to Li^+ and the rest remains as uncomplexed rotaxane, in the presence of 1 equivalent of $LiClO_4$.

By using the same equation (1), analogous calculations were conducted to quantify the percentage of Li^+ precomplexed rotaxane **2.22** upon addition of 1 equivalent of $LiClO_4$ to rotaxane **2.22.** According to calculations ca.32% of rotaxane **2.22** is bound to Li^+ and the rest remains as uncomplexed rotaxane, in the presence of 1 equivalent of $LiClO_4$.

Estimating percentage station occupancy of two station rotaxane with macrocycle **2.6**

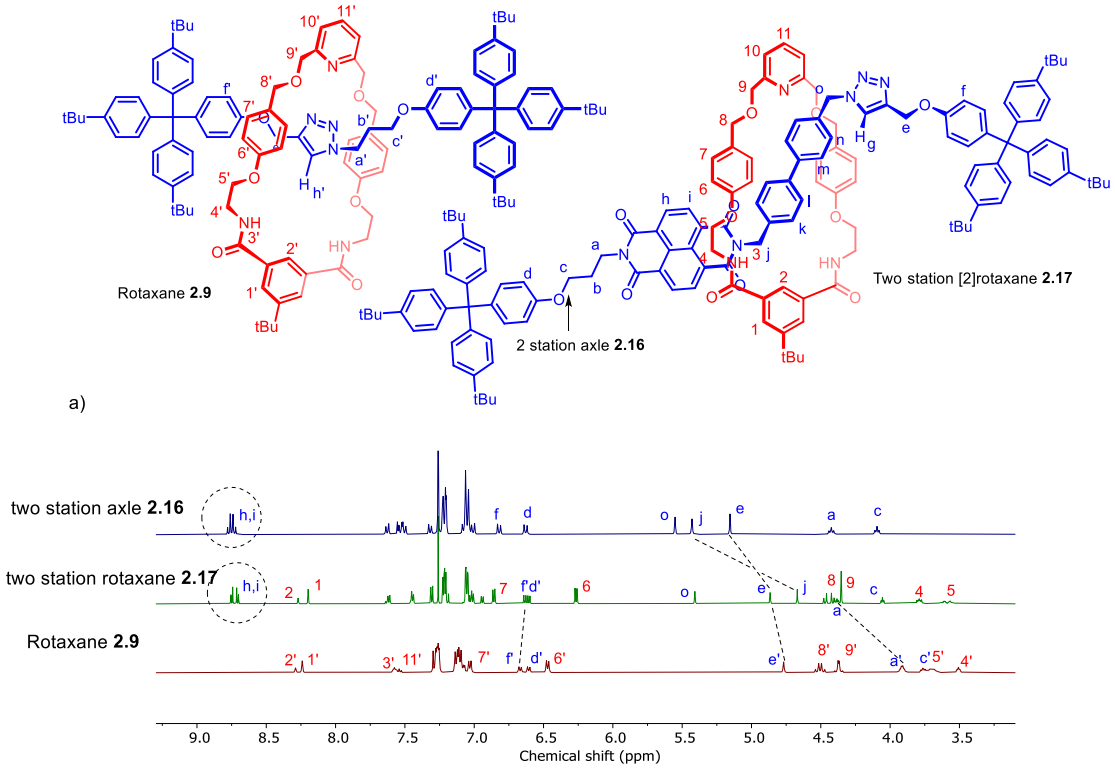

Figure A.1: Superimposed ^{1}H NMR spectra of the two-station axle **2.16**, two-station rotaxane **2.17** and analogous one station rotaxane **2.9** in $CDCl_3$, 298 K, 500 MHz

To estimate the occupancy of the triazole station in **2.17**, comparative ^{1}H NMR studies of rotaxanes **2.17** and one-station rotaxane **2.9**, as well as two-station axle **2.16**, were undertaken. It was assumed that **2.9** represents the environment at the triazole station when it is fully occupied by the macrocycle, while **2.16** corresponds to the triazole station in the absence of the macrocycle.

^{1}H NMR spectra of the two station [2]rotaxane **2.17** displayed notable perturbations in proton signals proximal to both the NDI station and triazole station indicative of the macrocycle occupying both the stations of the rotaxane (Figure A.1).

To quantify the macrocycle occupancy of the two stations in rotaxane **2.17**, **2.9** and **2.16** were treated as models for the two extremes of triazole station occupancy (100% for **2.9**; 0%

for **2.16**). Assuming that the chemical shifts of the protons in the axle of rotaxane **2.17** scale linearly with station occupancy, comparing these peaks to the analogous signals in **2.9** and **2.16** would provide an estimate of the triazole station occupancy.

The percentage occupancy of the triazole station in **2.17** was calculated following the chemical shifts of proton H_e using the equation below:

$$\%occ_{trz} = \frac{|\delta(H_e)_{\mathbf{2.17}} - \delta(H_e)_{\mathbf{2.16}}|}{|\delta(H_e)_{\mathbf{2.9}} - \delta(H_e)_{\mathbf{2.16}}|} \times 100\% \quad (2)$$

Where $\%occ_{trz}$ is the percentage occupancy of the triazole station and $\delta(H_e)_{\boldsymbol{n}}$ are the chemical shift values of H_e in each compound in ppm (n = **2.17, 2.9, 2.16**).

$$\delta(H_e)_{\mathbf{2.17}} = 4.87\ ppm$$

$$\delta(H_e)_{\mathbf{2.9}} = 4.77\ ppm$$

$$\delta(H_e)_{\mathbf{2.16}} = 5.16\ ppm$$

Therefore, the percentage occupancy of the triazole station in the free rotaxane was estimated as follows:

$$\%occ_{trz} = \frac{|4.87 - 5.16|}{|4.77 - 5.16|} \times 100\% = 74\%$$

From the calculations it is evident that the macrocycle primarily resides in the triazole station. This could be attributed to both steric effects of the macrocycle and the inability of the macrocycle aryl groups to act as an efficient electron donor to form π-π donor acceptor interactions with the electron deficient NDI group. Therefore, a larger macrocycle **2.12** which consists of two electron rich hydroquinone motifs was chosen to synthesise the two station rotaxane **2.14** (See section 2.4.1)

Estimating percentage station occupancy of Rotaxane **2.14**

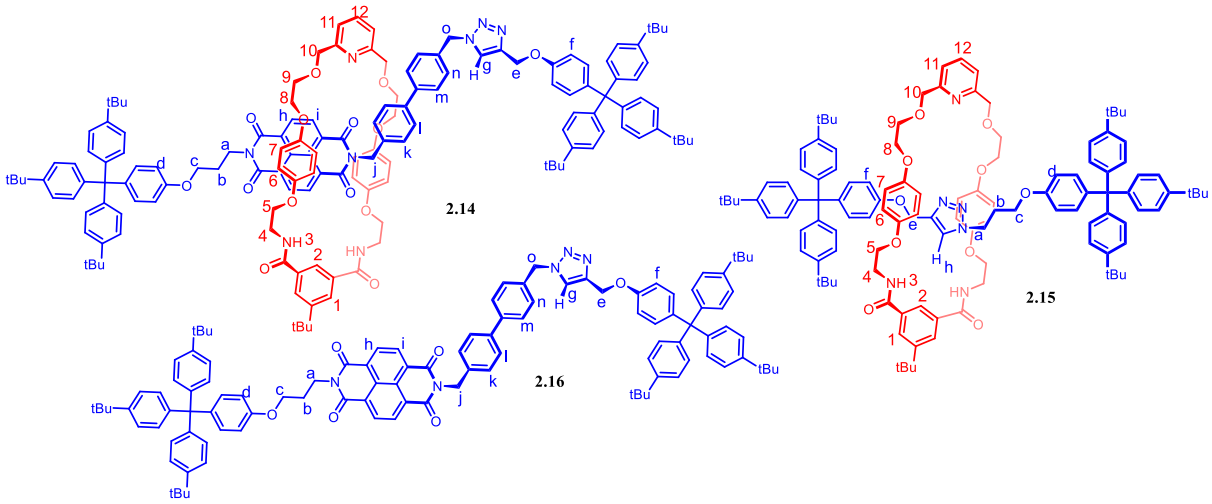

Figure A.2: Chemical structures of rotaxane **2.14**, **2.15** and axle **2.16**

Following a similar procedure as discussed above, the percentage occupancy of the triazole station in **2.14**, was calculated by a comparative ^{1}H NMR study of rotaxanes **2.14** and one-station rotaxane **2.15**, as well as two-station axle **2.16**. Rotaxane **2.15** represents the environment at the triazole station when it is fully occupied by the macrocycle, while **2.16** corresponds to the triazole station in the absence of the macrocycle (triazole station occupancy is 100% for **2.15**; 0% for **2.16**). Hence, the percentage occupancy of the triazole station in **2.14** can be calculated following the chemical shifts of proton H_e using equation (3).

For example, in 30% $CD_3CN/CDCl_3$ without any guest ions:

$$\delta(H_e)_{\mathbf{2.14}} = 4.90\ ppm$$

$$\delta(H_e)_{\mathbf{2.15}} = 4.51\ ppm$$

$$\delta(H_e)_{\mathbf{2.16}} = 4.94\ ppm$$

Therefore, the percentage occupancy of the triazole station in the free rotaxane was estimated as follows:

$$\%occ_{trz} = \frac{|4.91 - 4.94|}{|4.51 - 4.94|} \times 100\% = 7.3\% \quad (3)$$

The calculation was repeated to obtain the triazole station occupancy in the presence of $LiClO_4$ and in the presence of both $LiClO_4$ and TBABr. All relevant data are shown in Table A.1, Table A.2.

Table A.1: Changes in occupancy of triazole station in **2.14** upon addition of $LiClO_4$ in 3:7 $CD_3CN/CDCl_3$ (v/v) [a]

Equivalents of guest ions Li^+	$\delta(H_e)_{2.16}$ (ppm)	$\delta(H_e)_{2.15}$ (ppm)	$\delta(H_e)_{2.14}$ (ppm)	$\%occ_{trz}$ (%)
0	4.94	4.53	4.91	7.3
1.0	4.94	4.50	4.89	11.4
2.0	4.94	4.48	4.88	13.0
2.5	4.94	4.48	4.87	15.2
3.0	4.94	4.47	4.87	14.9
4.0	4.94	4.47	4.87	14.9
5.0	4.94	4.46	4.86	16.7
7.0	4.94	4.46	4.86	16.7
10.0	4.94	4.46	4.85	18.8

[a][Receptor] = 1.0 mM. Li^+ and Br^- added as $LiClO_4$ and TBABr salts respectively.

Table A.2: Changes in occupancy of triazole station in **2.14** upon addition of $LiClO_4$ and TBABr in 3:7 $CD_3CN/CDCl_3$ (v/v) [a]

Equivalents of guest ions		$\delta(H_e)_{2.16}$ (ppm)	$\delta(H_e)_{2.15}$ (ppm)	$\delta(H_e)_{2.14}$ (ppm)	$\%occ_{trz}$ (%)
Li^+	Br^-				
0	0	4.94	4.53	4.91	7.3
1.0	0	4.94	4.52	4.88	14.3
1.0	1.0	4.94	4.52	4.86	19.0
1.0	2.0	4.94	4.52	4.85	21.4
1.0	3.0	4.94	4.52	4.85	21.4
1.0	4.0	4.94	4.52	4.84	23.8
1.0	5.0	4.94	4.52	4.84	23.8
1.0	7.0	4.94	4.53	4.84	24.4
1.0	10.0	4.94	4.53	4.83	26.8

[a][Receptor] = 1.0 mM. Li^+ and Br^- added as $LiClO_4$ and TBABr salts respectively.

Appendix B: Crystallographic Data

Data collection

Single crystals suitable for X-ray analysis were each coated with Paratone-N oil, suspended in a small fiber loop, and placed in a cold gaseous nitrogen stream on an Oxford Diffraction Supernova X-ray diffractometer performing ϕ- and ω-scans at 150(2) K. Diffraction intensities were measured using graphite monochromated Cu $K\alpha$ radiation (λ = 1.54184 Å). Data collection, indexing, initial cell refinements, frame integration, final cell refinements and absorption corrections were accomplished using the program Crysalispro.[320] Scattering factors and anomalous dispersion corrections were taken from the *International Tables for X-ray Crystallography*. All structures were solved by direct methods using SHELXS-97[321] and refined against F^2 on all data by full-matrix least squares with SHELXL[322] following established refinement strategies.

All non-hydrogen atoms were refined anisotropically. All hydrogen atoms binding to carbon were included in the model at geometrically calculated positions and refined using a riding model. The isotropic displacement parameters of all hydrogen atoms were fixed to 1.2 times the U value of the atoms they are linked to (1.5 times for methyl groups). Details of the data quality and a summary of the residual values for the refinements are listed in Table A.3-Table A.7.

Table A.3: Crystal data and structure refinement for macrocycle **2.6**

Identification code	Macrocycle **2.6**	
Empirical formula	C37 H41 N3 O6	
Formula weight	623.73	
Temperature	150(2) K	
Wavelength	1.54184 Å	
Crystal system	Monoclinic	
Space group	$P2_1/c$	
Unit cell dimensions	a = 12.9519(5) Å	α= 90°.
	b = 24.9339(13) Å	β= 111.716(5)°.
	c = 10.7337(6) Å	γ= 90°.
Volume	3220.3(3) $Å^3$	
Z	4	
Density (calculated)	1.286 Mg/m^3	
Absorption coefficient	0.708 mm^{-1}	
F(000)	1328	
Crystal size	0.25 x 0.20 x 0.15 mm^3	
Theta range for data collection	3.545 to 76.531°.	
Index ranges	-16<=h<=11, -31<=k<=31, -13<=l<=13	
Reflections collected	31029	
Independent reflections	6689 [R(int) = 0.0832]	
Completeness to theta = 67.684°	100.0 %	
Absorption correction	Semi-empirical from equivalents	
Max. and min. transmission	1.00000 and 0.93907	
Refinement method	Full-matrix least-squares on F^2	
Data / restraints / parameters	6689 / 0 / 449	
Goodness-of-fit on F^2	1.004	
Final R indices [I>2sigma(I)]	R1 = 0.0534, wR2 = 0.1239	
R indices (all data)	R1 = 0.0996, wR2 = 0.1539	
Largest diff. peak and hole	0.210 and -0.226 e.$Å^{-3}$	

Table A.4: Crystal data and structure refinement for heteroditopic rotaxane **2.10**.HCl

Identification code	Rotaxane **2.10**.HCl	
Empirical formula	C117 H136 Cl I N6 O8	
Formula weight	1916.66	
Temperature	150(2) K	
Wavelength	1.54184 Å	
Crystal system	Triclinic	
Space group	P-1	
Unit cell dimensions	a = 15.1239(2) Å	α=80.7200(10)°
	b = 15.2550(3) Å	β=79.3540(10)°
	c = 29.0440(4) Å	γ=72.2440(10)°
Volume	6232.31(18) $Å^3$	
Z	2	
Density (calculated)	1.021 Mg/m^3	
Absorption coefficient	2.600 mm^{-1}	
F(000)	2028	
Crystal size	0.4 x 0.2 x 0.15 mm^3	
Theta range for data collection	3.588 to 76.634°.	
Index ranges	-19<=h<=18, -19<=k<=16, -36<=l<=35	
Reflections collected	135494	
Independent reflections	25857 [R(int) = 0.0708]	
Completeness to theta = 67.684°	100.0 %	
Absorption correction	Semi-empirical from equivalents	
Max. and min. transmission	1.00000 and 0.18761	
Refinement method	Full-matrix least-squares on F^2	
Data / restraints / parameters	25857 / 0 / 1219	
Goodness-of-fit on F^2	1.045	
Final R indices [I>2sigma(I)]	R1 = 0.0492, wR2 = 0.1375	
R indices (all data)	R1 = 0.0557, wR2 = 0.1441	
Largest diff. peak and hole	1.852 and -1.268 e.$Å^{-3}$	

Table A.5: Crystal data and structure refinement for compound **2.6.**HCl.

Identification code	Macrocycle **2.6.HCl**	
Empirical formula	C40 H43 Cl4 I2 N7 O5	
Formula weight	1097.41	
Temperature	150(2) K	
Wavelength	1.54184 Å	
Crystal system	Triclinic	
Space group	P-1	
Unit cell dimensions	a = 9.3137(4) Å	α= 78.421(3)°.
	b = 14.9357(6) Å	β= 81.256(3)°.
	c = 17.3935(5) Å	γ= 75.301(4)°.
Volume	2279.65(16) $Å^3$	
Z	2	
Density (calculated)	1.599 Mg/m^3	
Absorption coefficient	13.398 mm^{-1}	
F(000)	1092	
Crystal size	0.35 x 0.20 x 0.15 mm^3	
Theta range for data collection	3.701 to 77.138°.	
Index ranges	-11<=h<=11, -14<=k<=18, -21<=l<=21	
Reflections collected	21749	
Independent reflections	9359 [R(int) = 0.0540]	
Completeness to theta = 67.684°	99.8 %	
Absorption correction	Semi-empirical from equivalents	
Max. and min. transmission	0.7541 and 0.5069	
Refinement method	Full-matrix least-squares on F^2	
Data / restraints / parameters	9359 / 2 / 526	
Goodness-of-fit on F^2	1.106	
Final R indices [I>2sigma(I)]	R1 = 0.0853, wR2 = 0.2098	
R indices (all data)	R1 = 0.0990, wR2 = 0.2322	
Largest diff. peak and hole	2.515 and -0.546 e.$Å^{-3}$	

Table A.6: Crystal data and structure refinement for compound **4.2XB.PF_6^-**.

Identification code	4.2XB.PF_6^-	
Empirical formula	C25 H39 F6 I2 N7 O3 P Re	
Formula weight	1070.60	
Temperature	150(2) K	
Wavelength	1.54184 Å	
Crystal system	Triclinic	
Space group	P-1	
Unit cell dimensions	a = 7.49450(10) Å	α= 98.839(2)°.
	b = 11.7359(3) Å	β= 97.641(2)°.
	c = 20.9942(5) Å	γ= 90.131(2)°.
Volume	1807.92(7) $Å^3$	
Z	2	
Density (calculated)	1.967 Mg/m^3	
Absorption coefficient	21.004 mm^{-1}	
F(000)	1024	
Crystal size	0.3 x 0.3 x 0.3 mm^3	
Theta range for data collection	3.813 to 76.348°.	
Index ranges	-9<=h<=7, -14<=k<=14, -26<=l<=26	
Reflections collected	26206	
Independent reflections	7446 [R(int) = 0.1056]	
Completeness to theta = 67.684°	99.8 %	
Absorption correction	Sphere	
Max. and min. transmission	0.04186 and 0.00166	
Refinement method	Full-matrix least-squares on F^2	
Data / restraints / parameters	7446 / 0 / 408	
Goodness-of-fit on F^2	1.264	
Final R indices [I>2sigma(I)]	R1 = 0.1206, wR2 = 0.2879	
R indices (all data)	R1 = 0.1232, wR2 = 0.2948	
Extinction coefficient	n/a	
Largest diff. peak and hole	8.624 and -1.393 e.$Å^{-3}$	

Table A.7: Crystal data and structure refinement for compound **4.2XB.Br$^-$**

Identification code	4.2XB.Br$^-$	
Empirical formula	C25 H39 Br I2 N7 O3 Re	
Formula weight	1005.54	
Temperature	150 K	
Wavelength	1.54180 Å	
Crystal system	Triclinic	
Space group	P -1	
Unit cell dimensions	a = 7.3293(2) Å	α=95.5049(16)°
	b = 12.5111(2) Å	β=93.4650(17)°
	c = 18.6333(4) Å	γ=91.6501(17)°
Volume	1696.61(7) Å^3	
Z	2	
Density (calculated)	1.968 Mg/m^3	
Absorption coefficient	22.963 mm^{-1}	
F(000)	956	
Crystal size	0.05 x 0.17 x 0.25 mm^3	
Theta range for data collection	3.551 to 77.112°.	
Index ranges	-9<=h<=9, -15<=k<=15, -23<=l<=23	
Reflections collected	28454	
Independent reflections	7104 [R(int) = 0.049]	
Completeness to theta = 77.112°	98.9 %	
Absorption correction	Multi-Scan	
Max. and min. transmission	0.32 and 0.03	
Refinement method	Full-matrix least-squares on F^2	
Data / restraints / parameters	7104 / 0 / 352	
Goodness-of-fit on F^2	1.045	
Final R indices [I>2sigma(I)]	R1 = 0.0714, wR2 = 0.1856	
R indices (all data)	R1 = 0.0704, wR2 = 0.1827	
Extinction coefficient	n/a	
Largest diff. peak and hole	5.69 and -1.11 e.Å^{-3}	

Table A.8: Crystal data and structure refinement for compound **4.5XB.2I$^-$**

Identification code	4.5XB.2I$^-$	
Empirical formula	C60 H86 I6 N15 O6 Re2	
Formula weight	2247.23	
Temperature	150(2) K	
Wavelength	1.54184 Å	
Crystal system	Triclinic	
Space group	P-1	
Unit cell dimensions	a = 10.2571(3) Å	α= 100.495(3)°.
	b = 15.9234(6) Å	β= 102.025(3)°.
	c = 24.3013(9) Å	γ= 91.124(3)°.
Volume	3810.2(2) Å^3	
Z	2	
Density (calculated)	1.959 Mg/m^3	
Absorption coefficient	25.640 mm^{-1}	
F(000)	2134	
Crystal size	0.04 x 0.04 x 0.04 mm^3	
Theta range for data collection	3.692 to 61.708°.	
Index ranges	-6<=h<=11, -17<=k<=18, -27<=l<=26	
Reflections collected	24644	
Independent reflections	11583 [R(int) = 0.0593]	
Completeness to theta = 61.708°	97.4 %	
Absorption correction	Sphere	
Max. and min. transmission	0.05473 and 0.00614	
Refinement method	Full-matrix least-squares on F^2	
Data / restraints / parameters	11583 / 31 / 801	
Goodness-of-fit on F^2	1.166	
Final R indices [I>2sigma(I)]	R1 = 0.1178, wR2 = 0.3262	
R indices (all data)	R1 = 0.1340, wR2 = 0.3647	
Extinction coefficient	n/a	
Largest diff. peak and hole	5.946 and -2.767 e.Å^{-3}	

Appendix C: DFT optimised structures

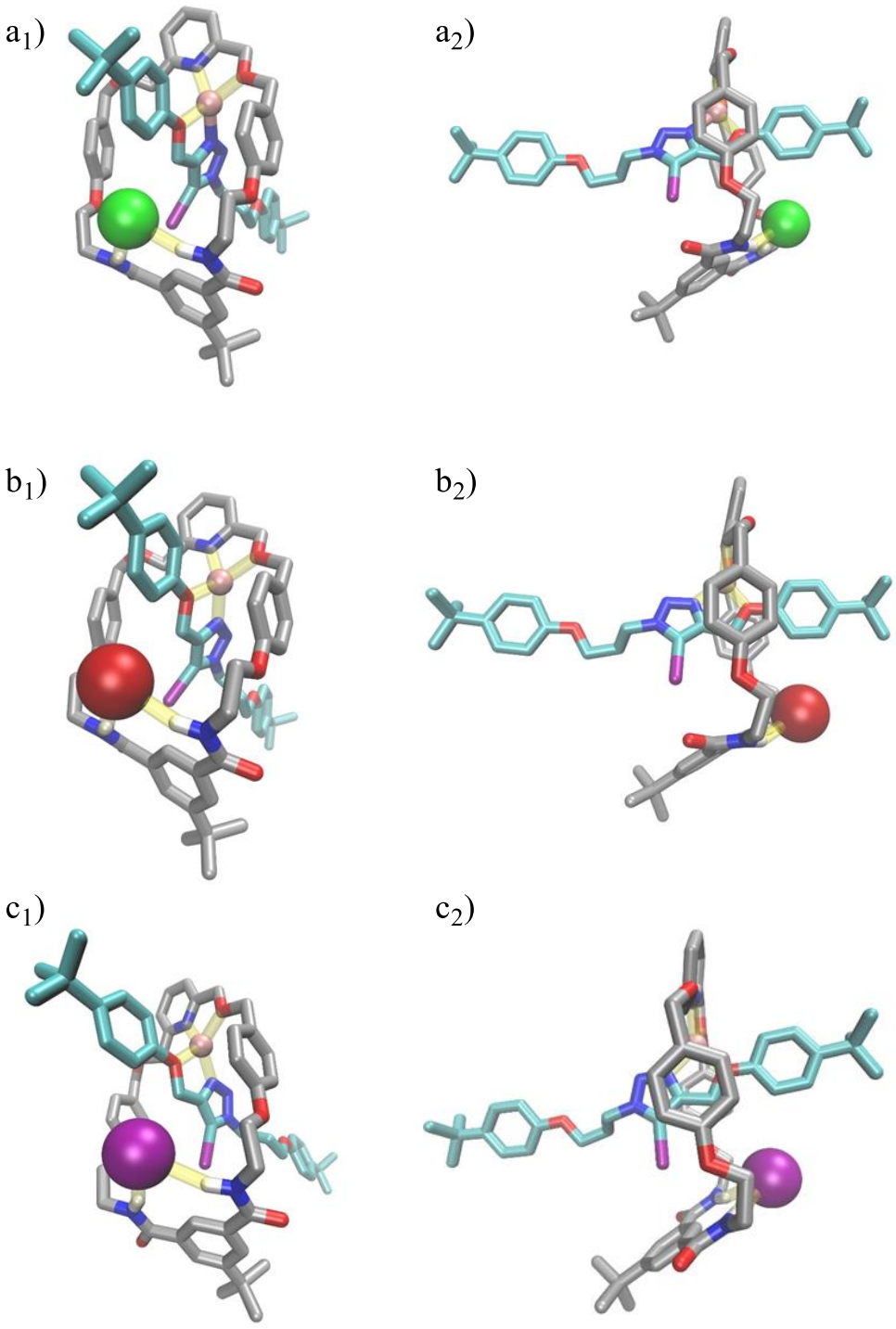

Figure A.3: DFT optimised ion-pair bound rotaxane **2.10**; a) LiCl bound rotaxane **2.10** (front and size view), b) LiBr bound rotaxane **2.10** (front and size view), c) LiI bound rotaxane **2.10** (front and size view), Colour code of atoms: O-red, N-blue, I-purple, Li-pink, Br- brown, Cl-green, $C_{(MC)}$ -gray $C_{(axle)}$-teal. Non-covalent host-guest interactions are shown by yellow

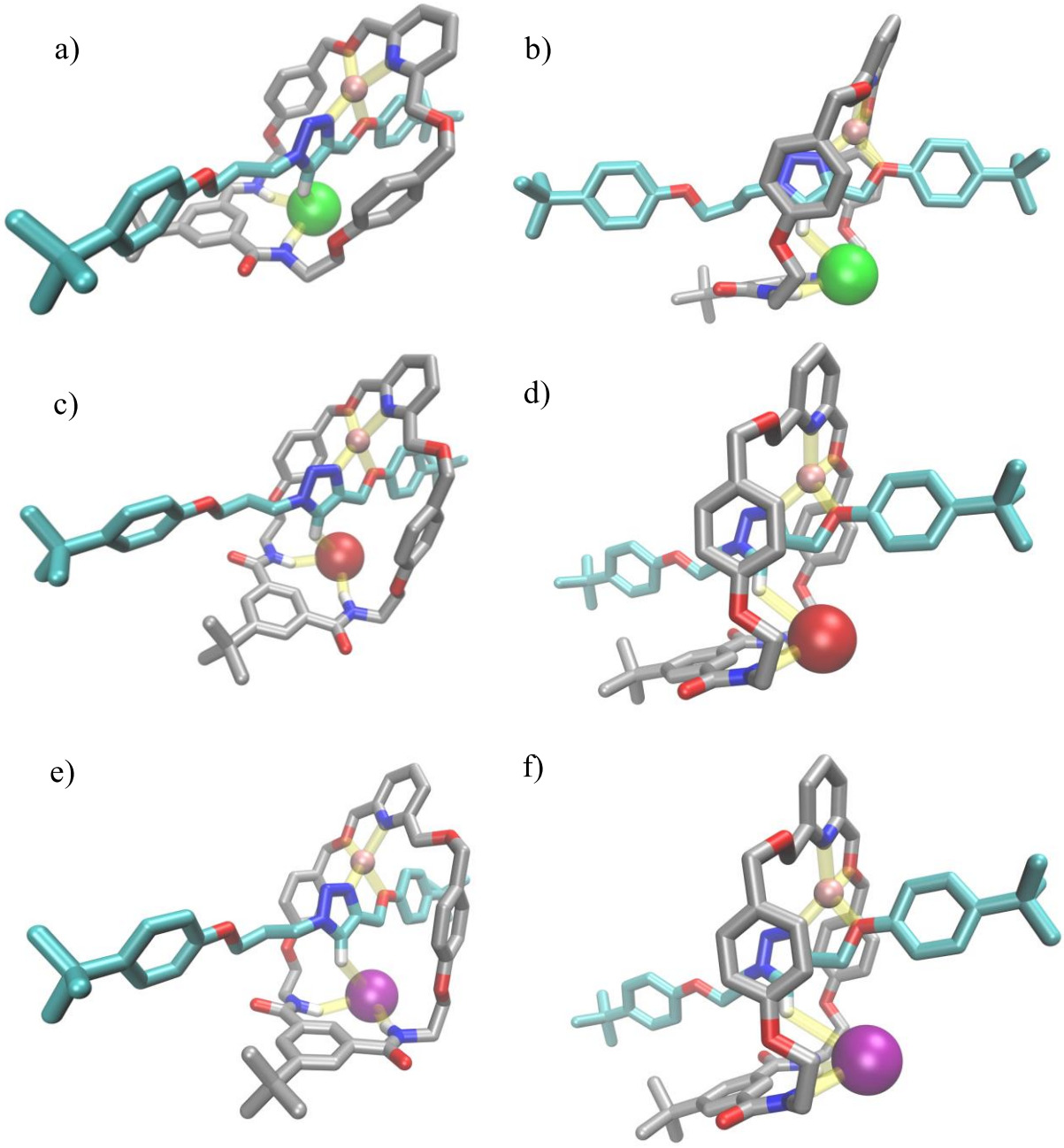

Figure A.4: DFT optimised ion-pair bound rotaxane **2.9**; a) front view of LiCl bound rotaxane **2.9**, b) side view of LiCl bound rotaxane **2.9**, c) front view of LiBr bound rotaxane **2.9**, d) side view of LiBr bound rotaxane **2.9**, e) front view of LiI bound rotaxane **2.9,** f) side view of LiI bound rotaxane **2.9.** Colour code of atoms: O-red, N-blue, I-purple, Li-pink, Br- brown, Cl-green, $C_{(MC)}$ -gray $C_{(axle)}$-teal. Non-covalent host-guest interactions are shown by yellow.

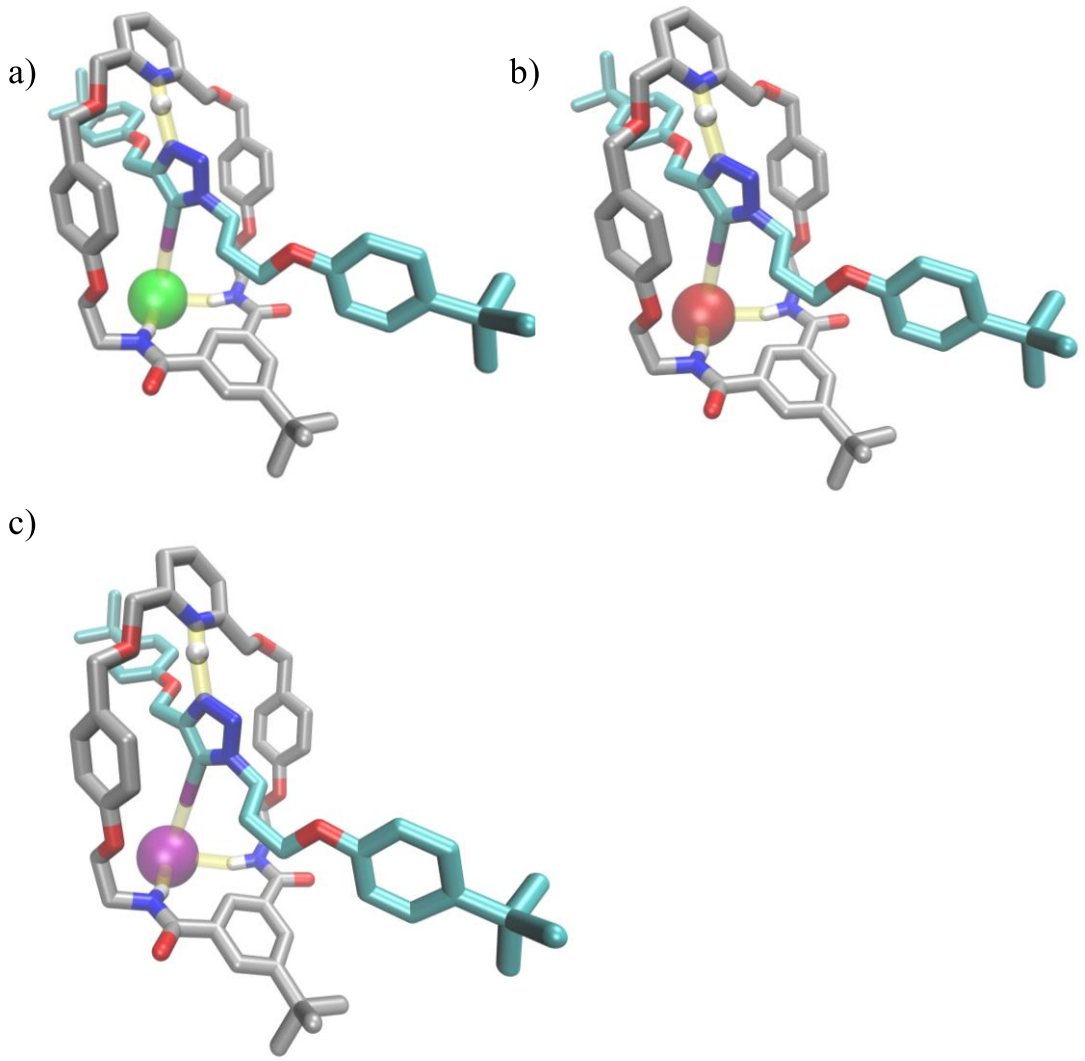

Figure A.5: DFT optimised ion-pair bound rotaxane **2.10**; a) HCl bound rotaxane **2.10**, b) HBr bound rotaxane **2.10**, c) HI bound rotaxane **2.10.** Colour code of atoms: H-white, O-red, N-blue, I-purple, Li-pink, Br- brown, Cl-green, $C_{(MC)}$ -gray $C_{(axle)}$-teal. Non-covalent host-guest interactions are shown by yellow

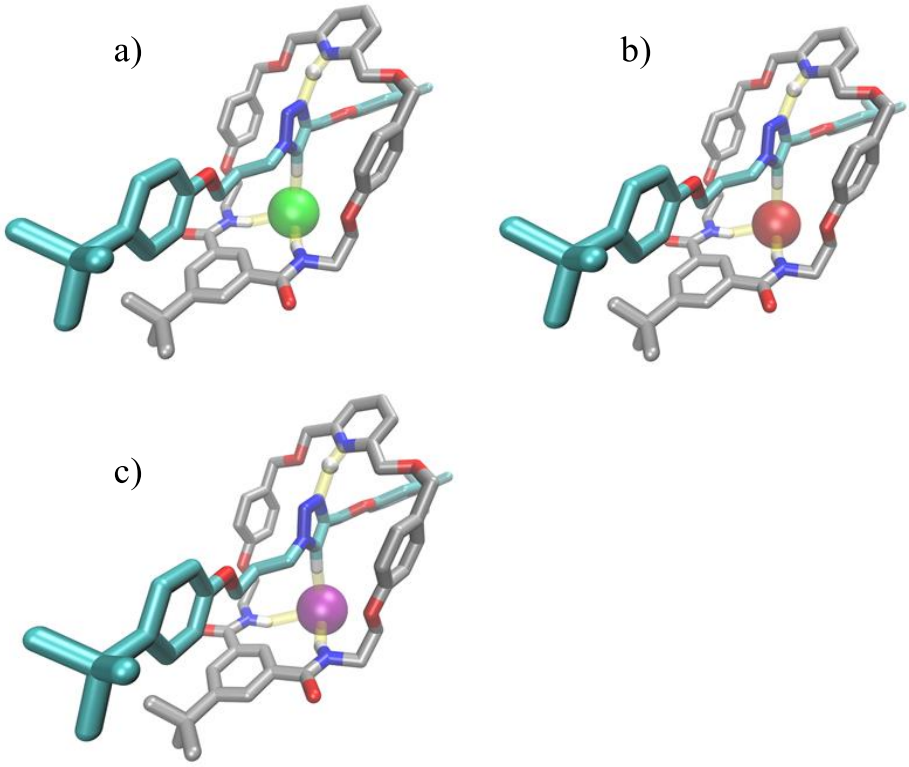

Figure A.6: DFT optimised ion-pair bound rotaxane **2.9**; a) HCl bound rotaxane **2.9**, b) HBr bound rotaxane **2.9**, c) HI bound rotaxane **2.9**, Colour code of atoms: H-white, O-red, N-blue, I-purple, Li-pink, Br- brown, Cl-green, $C_{(MC)}$ -gray $C_{(axle)}$-teal. Non-covalent host-guest interactions are shown by yellow

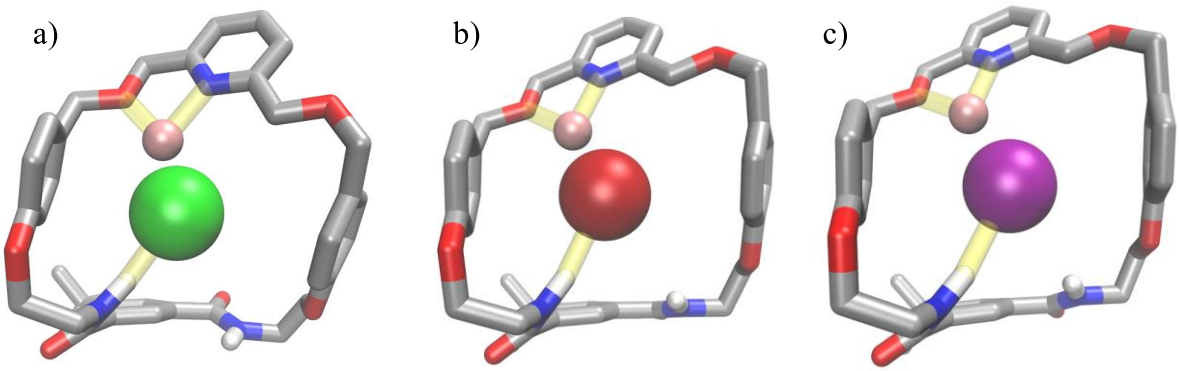

Figure A.7: DFT optimised ion-pair bound macrocycle **2.6**; a) LiCl bound macrocycle **2.6**, b) LiBr bound macrocycle **2.6**, c) LiI bound macrocycle **2.6**, Colour code of atoms: H-white, O-red, N-blue, I-purple, Li-pink, Br- brown, Cl-green, C-gray. Non-covalent host-guest interactions are shown by yellow

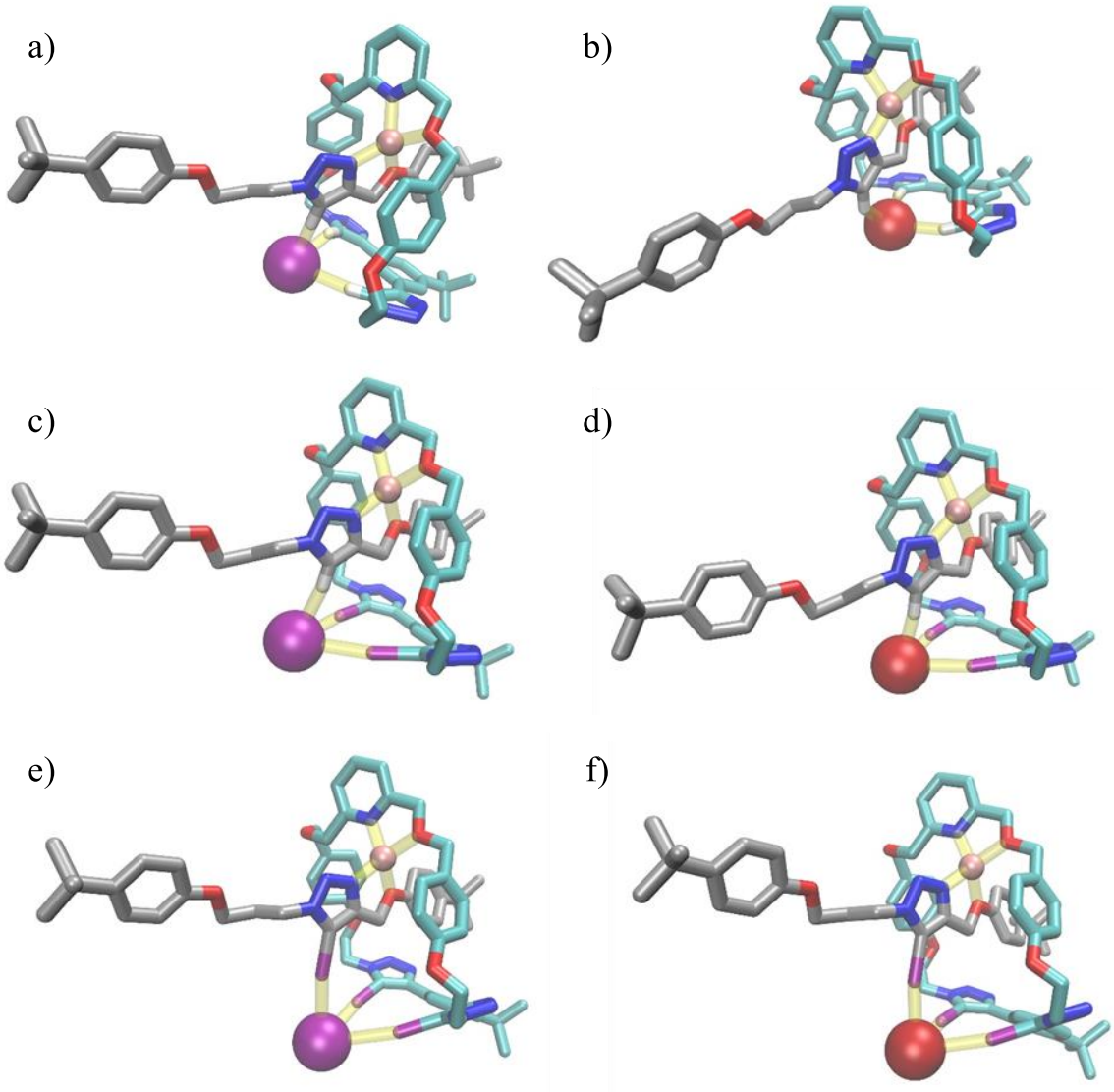

Figure A.8: DFT optimised ion-pair bound rotaxane structures; a) LiI bound rotaxane **2.21**, b) LiBr bound rotaxane **2.21**, c) LiI bound rotaxane **2.22**, d) LiBr bound rotaxane **2.22**, e) LiI bound rotaxane **2.23**, f) LiBr bound rotaxane **2.23**. All noninteracting H atoms are omitted for clarity. Colour code of atoms: O-red, N-blue, I-purple, Li-pink, Br- brown, Cl-green, $C_{(axle)}$ - gray $C_{(MC)}$-teal. Non-covalent host-guest interactions are shown by yellow

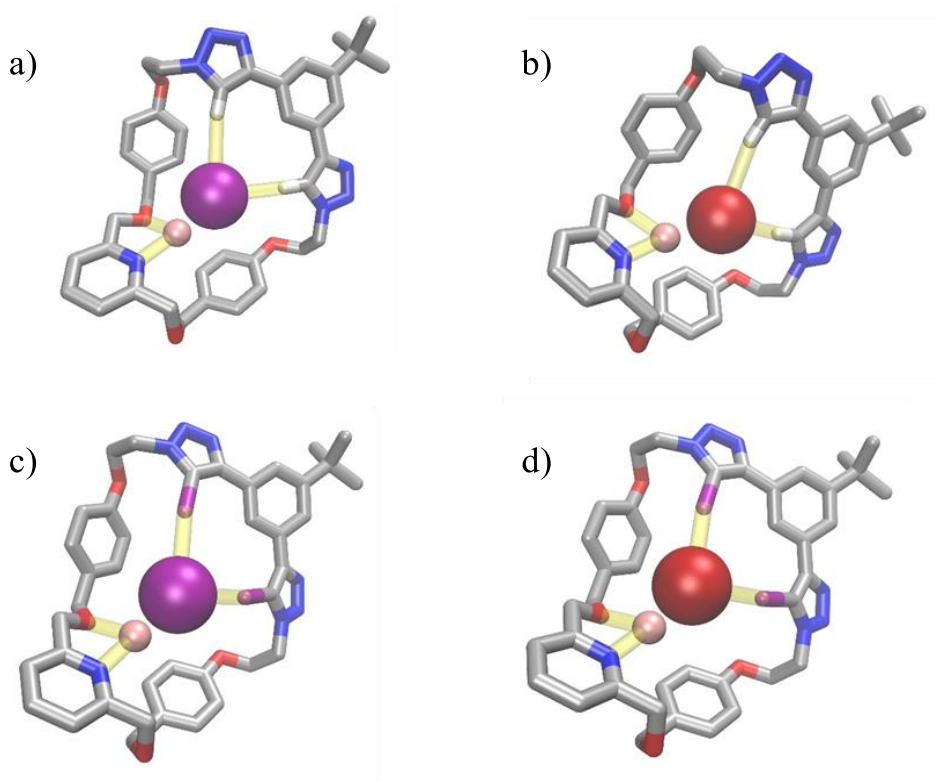

Figure A.9: DFT optimised ion-pair bound macrocycle structures: a) LiI bound macrocycle **2.29**, b) LiBr bound macrocycle **2.29**, c) LiI bound macrocycle **2.30**, d) LiBr bound macrocycle **2.30.** All noninteracting H atoms are omitted for clarity. Colour code of atoms: O-red, N-blue, I-purple, Li-pink, Br- brown, C-gray. Non-covalent host-guest interactions are shown by yellow

Appendix D: Titration data of dicationic Re(I) receptors.

The suitability of 1:1 and 1:2 host-guest binding models were accessed through a comparison of the covariance of fit (cov_{fit}) indicator of the titration isotherms. Binding modes with lower cov_{fit} are more likely to fit with the titration data. However, as Thordarson and co-workers explain, complex binding modes with more parameters (e.g. 1:2 (Full) model) generally fit better than simpler models (e.g. 1:1 model). Hence, to select a more complex model the cov_{fit} should be at least 3-5 times lower than that of the simpler model.[228] Titration data of receptors **4.5XB/HB** are summarised in Table A.9. Binding model that fits best is highlighted in yellow.

Table A.9: Stepwise anion association constants (K_1/K_2, M^{-1}) and cov_{fit} values of binding isotherms generated with the addition of oxalate to receptor **4.5XB** and **4.5HB**.[a]

Host	Anion	Host-guest binding model	K_1	K_2	cov_{fit} ($x10^{-3}$)	cov_{fit} ratio
4.5XB	Cl^-	1:1	199	-	1.77	1
		1:2 (Full)	941	65	0.47	4
		1:2 (non-cooperative)	Fit failed			
		1:2 (additive)	361	31	0.79	2
		1:2 (statistical)	498	125	2.71	1
4.5HB	Phthalate	1:1	321	-	0.28	1
		1:2 (Full)	Fit failed			
		1:2 (non-cooperative)	519	130	0.53	0.5
		1:2 (additive)	779	95	0.18	2
		1:2 (statistical)	976	244	1.08	0.3
4.5HB	Isophthalate	1:1	474		2.34	1
		1:2 (Full)	Fit failed			
		1:2 (non-cooperative)	731	183	3.66	1
		1:2 (additive)	1004	62	0.73	3
		1:2 (statistical)	1608	402	6.46	0.4
4.5HB	SO_4^{2-}	1:1	338		1.30	1
		1:2 (Full)	Fit failed			
		1:2 (non-cooperative)	534	133	1.93	1
		1:2 (additive)	650	51	0.58	2
		1:2 (statistical)	1026	257	3.12	0.4

[a] Anions added as their TBA salts, T = 298 K, solvent = 1:9 D_2O/CD_3CN. Errors are less than 10%. Binding modes best fit for the titration isotherms are highlighted in yellow.

Appendix E: Chemical structures of all receptors

Chapter 2 receptors

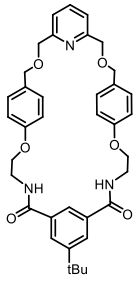

2.6

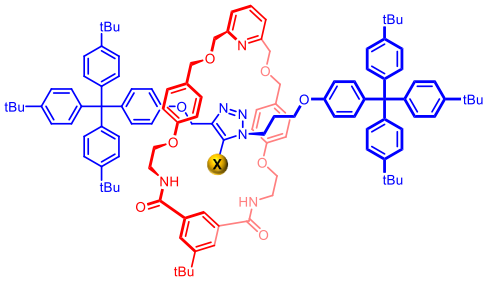

2.9 - X=H
2.10 - X=I

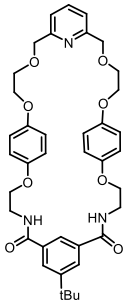

2.12

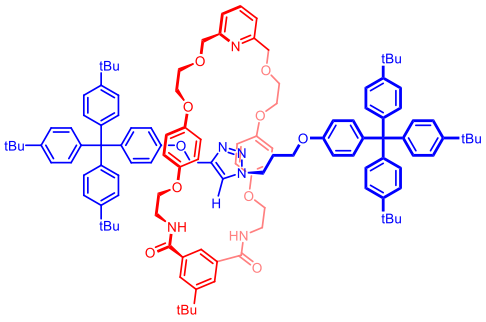

2.15

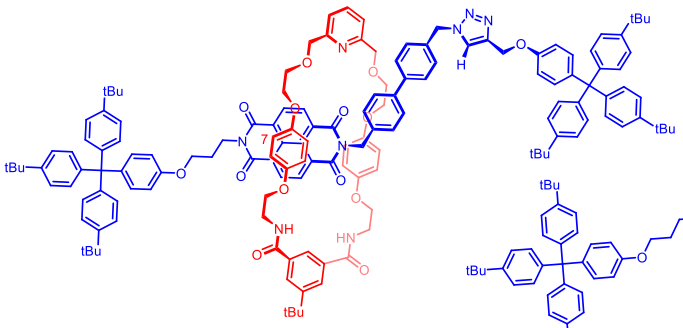

2.14 (rotaxane)
2.16 (axle)

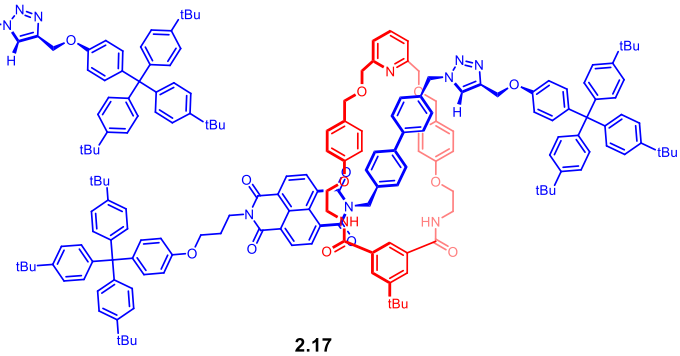

2.17

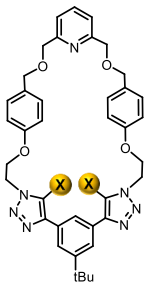

2.29 - X=H
2.30 - X=I

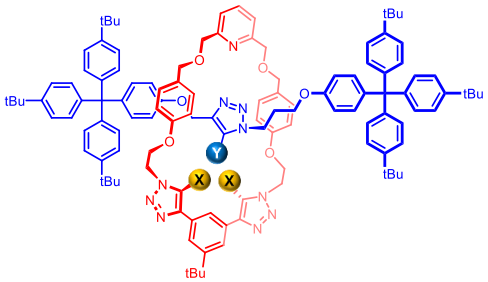

2.21 - X=H, Y=H
2.22 - X=I, Y=H
2.23 - X=I, Y=I

Chapter 3 receptors

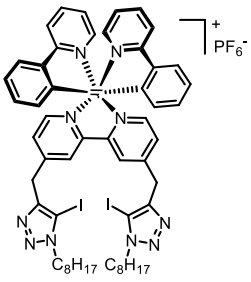

3.4

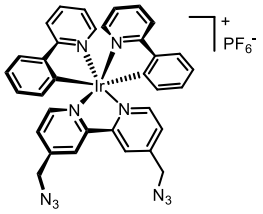

3.5

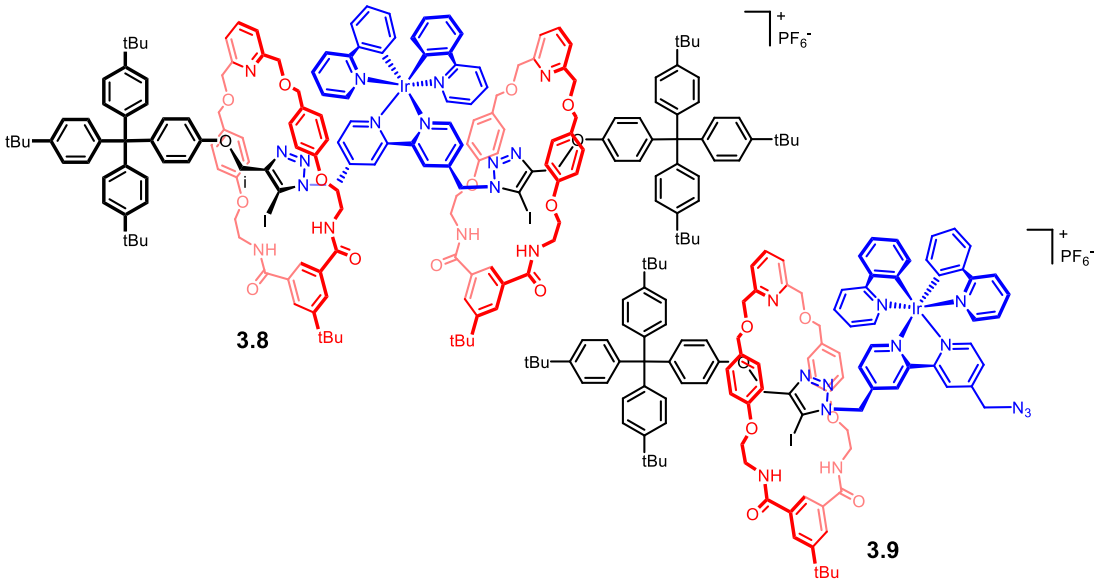

3.8

3.9

Chapter 4 receptors

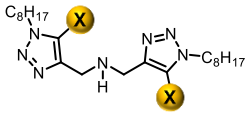

4.1XB- X=I
4.1HB- X=H

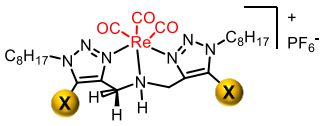

4.2XB- X=I
4.2HB- X=H

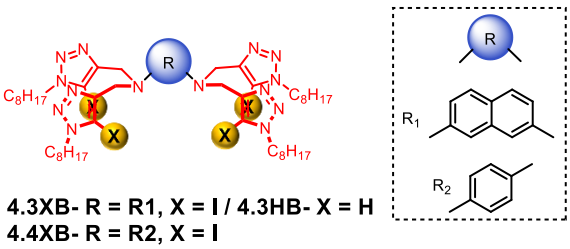

4.3XB- R = R1, X = I / 4.3HB- X = H
4.4XB- R = R2, X = I

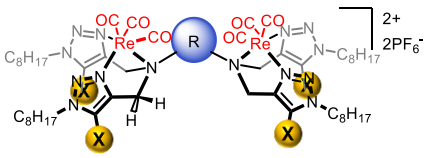

4.5XB- R = R1, X = I / 4.5HB- X = H
4.6XB- R = R2, X = I

References

1. Council, N. R. *Opportunities in Biology*. (The National Academies Press, 1989). doi:10.17226/742.
2. Berg, J. M., Tymoczko, J. L., Gatto, G. J., Jr., & Stryer, L. *Biochemistry*. (New York: W.H. Freeman/McMillan Learning, 2019).
3. Lehn, J.-M. Toward complex matter: Supramolecular chemistry and self-organization. *Proc. Natl. Acad. Sci.* **99**, 4763–4768 (2002).
4. Fischer, E. Einfluss der Configuration auf die Wirkung der Enzyme. *Berichte der Dtsch. Chem. Gesellschaft* **27**, 2985–2993 (1894).
5. Pedersen, C. J. Cyclic polyethers and their complexes with metal salts. *J. Am. Chem. Soc.* **89**, 7017–7036 (1967).
6. Lehn, J. M. Cryptates: The Chemistry of Macropolycyclic Inclusion Complexes. *Acc. Chem. Res.* **11**, 49–57 (1978).
7. Cram, D. J. Preorganization—From Solvents to Spherands. *Angew. Chemie Int. Ed.* **25**, 1039–1057 (1986).
8. Pedersen, C. J. The discovery of crown ethers (Noble Lecture). *Angew. Chemie Int. Ed.* **27**, 1021–1027 (1988).
9. Cram, D. J. The design of molecular hosts, guests, and their complexes (Nobel lecture). *Angew. Chemie Int. Ed.* **27**, 1009–1020 (1988).
10. Lehn, J.-M. Supramolecular Chemistry—Scope and Perspectives Molecules, Supermolecules, and Molecular Devices (Nobel Lecture). *Angew. Chemie Int. Ed.* **27**, 89–112 (1988).
11. Sauvage, J.-P. From Chemical Topology to Molecular Machines (Nobel Lecture). *Angew. Chemie Int. Ed.* **56**, 11080–11093 (2017).
12. Stoddart, J. F. Mechanically Interlocked Molecules (MIMs)—Molecular Shuttles, Switches, and Machines (Nobel Lecture). *Angew. Chemie Int. Ed.* **56**, 11094–11125 (2017).
13. Feringa, B. L. The Art of Building Small: From Molecular Switches to Motors (Nobel Lecture). *Angew. Chemie Int. Ed.* **56**, 11060–11078 (2017).
14. Dietrich-Buchecker, C. O., Sauvage, J. P. & Kintzinger, J. P. Une nouvelle famille de molecules: les metallo-catenanes. *Tetrahedron Lett.* **24**, 5095–5098 (1983).
15. Anelli, P. L., Spencer, N. & Stoddart, J. F. A molecular shuttle. *J. Am. Chem. Soc.* **113**, 5131–5133 (1991).
16. Koumura, N., Zijlstra, R. W., van Delden, R. A., Harada, N. & Feringa, B. L. Light-driven monodirectional molecular rotor. *Nature* **401**, 152–155 (1999).
17. Badjić, J. D., Balzani, V., Credi, A., Silvi, S. & Stoddart, J. F. A Molecular Elevator. *Science.* **303**, 1845–1849 (2004).
18. Liu, Y. *et al.* Linear artificial molecular muscles. *J. Am. Chem. Soc.* **127**, 9745–9759 (2005).
19. Kudernac, T. *et al.* Electrically driven directional motion of a four-wheeled molecule on a metal surface. *Nature* **479**, 208–211 (2011).
20. Amano, S., Borsley, S., Leigh, D. A. & Sun, Z. Chemical engines: driving systems away from equilibrium through catalyst reaction cycles. *Nat. Nanotechnol.* **16**, 1057–1067 (2021).
21. Thomas, D. *et al.* Pumping between phases with a pulsed-fuel molecular ratchet. *Nat. Nanotechnol.* **17**, 701–707 (2022).
22. Borsley, S., Leigh, D. A. & Roberts, B. M. W. A Doubly Kinetically-Gated Information Ratchet Autonomously Driven by Carbodiimide Hydration. *J. Am. Chem. Soc.* **143**,

4414–4420 (2021).
23. The Nobel Prize in Chemistry 2016. *Nobel Prize Chem. 2016. NobelPrize.org. Nobel Prize Outreach AB 2022. Sun. 1 May 2022.<https//www.nobelprize.org/prizes/chemistry/2016/summary/>*.
24. Martell, A. The Chelate Effect. in *Advances in Chemistry* vol. 62 19–272 (American Chemical Society, 1967).
25. Breslow, R., Belvedere, S., Gershell, L. & Leung, D. The chelate effect in binding, catalysis, and chemotherapy. *Pure Appl. Chem.* **72**, 333–342 (2000).
26. Hancock, R. D. & Martell, A. E. The Chelate, Cryptate and Macrocyclic Effects. *Comments Inorg. Chem.* **6**, 237–284 (1988).
27. Hinz, F. P. & Margerum, D. W. Effect of ligand solvation on the stability of metal complexes in solution. Explanation of the macrocyclic effect. *J. Am. Chem. Soc.* **96**, 4993–4994 (1974).
28. Martell, A. E., Hancock, R. D. & Motekaitis, R. J. Factors affecting stabilities of chelate, macrocyclic and macrobicyclic complexes in solution. *Coord. Chem. Rev.* **133**, 39–65 (1994).
29. Lehn, J. M. Cryptates: inclusion complexes of macropolycyclic receptor molecules. in *Chemistry for the Welfare of Mankind* 871–892 (Elsevier, 1979).
30. Steed, J. L. & Atwood, J. W. *Supramolecular Chemistry*. (Wiley, 2013).
31. Schmidtchen, F. P. Inclusion of Anions in Macrotricyclic Quaternary Ammonium Salts. *Angew. Chemie Int. Ed.* **16**, 720–721 (1977).
32. Jeffrey, G. A. Hydrogen-Bonding: An update. *Crystallogr. Rev.* **9**, 135–176 (2003).
33. Steiner, T. & Desiraju, G. R. Distinction between the weak hydrogen bond and the van der Waals interaction. *Chem. Commun.* 891–892 (1998).
34. Howard, J. A. K., Hoy, V. J., O'Hagan, D. & Smith, G. T. How good is fluorine as a hydrogen bond acceptor? *Tetrahedron* **52**, 12613–12622 (1996).
35. Emsley, J. Very strong hydrogen bonding. *Chem. Soc. Rev.* **9**, 91–124 (1980).
36. Molina, P., Zapata, F. & Caballero, A. Anion Recognition Strategies Based on Combined Noncovalent Interactions. *Chem. Rev.* **117**, 9907–9972 (2017).
37. Hassel, O. & Romming, C. Direct structural evidence for weak charge-transfer bonds in solids containing chemically saturated molecules. *Q. Rev. Chem. Soc.* **16**, 1–18 (1962).
38. Desiraju, G. R. *et al.* Definition of the halogen bond (IUPAC Recommendations 2013). *Pure Appl. Chem.* **85**, 1711–1713 (2013).
39. Bickerton, L. E., Sterling, A. J., Beer, P. D., Duarte, F. & Langton, M. J. Transmembrane anion transport mediated by halogen bonding and hydrogen bonding triazole anionophores. *Chem. Sci.* **11**, 4722–4729 (2020).
40. Cavallo, G. *et al.* Halogen bonding: a general route in anion recognition and coordination. *Chem. Soc. Rev.* **39**, 3772–3783 (2010).
41. Pancholi, J. & Beer, P. D. Halogen bonding motifs for anion recognition. *Coord. Chem. Rev.* **416**, 213281 (2020).
42. Kaasik, M. & Kanger, T. Supramolecular Halogen Bonds in Asymmetric Catalysis. *Front. Chem.* **8**, 599064 (2020).
43. Sutar, R. L. & Huber, S. M. Catalysis of Organic Reactions through Halogen Bonding. *ACS Catal.* **9**, 9622–9639 (2019).
44. Mukherjee, A., Tothadi, S. & Desiraju, G. R. Halogen Bonds in Crystal Engineering: Like Hydrogen Bonds yet Different. *Acc. Chem. Res.* **47**, 2514–2524 (2014).
45. Clark, T., Hennemann, M., Murray, J. S. & Politzer, P. Halogen bonding: the sigma-hole. Proceedings of 'Modeling interactions in biomolecules II', Prague, September 5th-9th, 2005. *J. Mol. Model.* **13**, 291–296 (2007).
46. Hassel, O. & Mark, H. Über die Kristallstruktur des Graphits. *Zeitschrift für Phys.* **25**,

317–337 (1924).
47. Budzianowski, A. & Katrusiak, A. Pressure-frozen benzene I revisited. *Acta Crystallogr. Sect. B Struct. Sci.* **62**, 94–101 (2006).
48. Hunter, C. A. & Sanders, J. K. M. The nature of .pi.-.pi. interactions. *J. Am. Chem. Soc.* **112**, 5525–5534 (1990).
49. Thakuria, R., Nath, N. K. & Saha, B. K. The Nature and Applications of π–π Interactions: A Perspective. *Cryst. Growth Des.* **19**, 523–528 (2019).
50. Ma, J. C. & Dougherty, D. A. The Cation−π Interaction. *Chem. Rev.* **97**, 1303–1324 (1997).
51. Li, S., Fa, S. X., Wang, Q. Q., Wang, D. X. & Wang, M. X. Synthesis and structure of oxacalix[2]arene[2]triazines of an expanded π-electron-deficient cavity and their interactions with anions. *J. Org. Chem.* **77**, 1860–1867 (2012).
52. Sokkalingam, P., Shraberg, J., Rick, S. W. & Gibb, B. C. Binding Hydrated Anions with Hydrophobic Pockets. *J. Am. Chem. Soc.* **138**, 48–51 (2016).
53. Langton, M. J., Serpell, C. J. & Beer, P. D. Anion recognition in water: Recent advances from a supramolecular and macromolecular perspective. *Angew. Chemie Int. Ed.* **55**, 1974–1987 (2016).
54. Assaf, K. I. & Nau, W. M. The Chaotropic Effect as an Assembly Motif in Chemistry. *Angew. Chemie Int. Ed.* **57**, 13968–13981 (2018).
55. Sessler, J. L., Gale, P. & Cho, W.-S. *Anion Receptor Chemistry*. (The Royal Society of Chemistry, 2006). doi:10.1039/9781847552471.
56. Puljak, L. & Kilic, G. Emerging roles of chloride channels in human diseases. *Biochimica et Biophysica Acta - Molecular Basis of Disease* vol. 1762 404–413 (2006).
57. Carrasco, N. Iodide transport in the thyroid gland. *Biochim. Biophys. Acta - Rev. Biomembr.* **1154**, 65–82 (1993).
58. Aasenden, R. & Peebles, T. C. Effects of fluoride supplementation from birth on human deciduous and permanent teeth. *Arch. Oral Biol.* **19**, 321–326 (1974).
59. Schindler, D. W. Eutrophication and recovery in experimental lakes: Implications for lake management. *Science.* **184**, 897–899 (1974).
60. Majumdar, D. The Blue Baby Syndrome. *Resonance* **8**, 20–30 (2003).
61. Oliver, D. B. *et al.* Azide-resistant mutants of Escherichia coli alter the SecA protein, an azide-sensitive component of the protein export machinery. *Proc. Natl. Acad. Sci.* **87**, 8227–8231 (1990).
62. Leavesley, H. B., Li, L., Prabhakaran, K., Borowitz, J. L. & Isom, G. E. Interaction of Cyanide and Nitric Oxide with Cytochrome c Oxidase: Implications for Acute Cyanide Toxicity. *Toxicol. Sci.* **101**, 101–111 (2007).
63. Evans, N. H. & Beer, P. D. Advances in anion supramolecular chemistry: From recognition to chemical applications. *Angew. Chemie Int. Ed.* **53**, 11716–11754 (2014).
64. Chen, L., Berry, S. N., Wu, X., Howe, E. N. W. & Gale, P. A. Advances in Anion Receptor Chemistry. *Chem* **6**, 61–141 (2020).
65. Hein, R., Beer, P. D. & Davis, J. J. Electrochemical Anion Sensing: Supramolecular Approaches. *Chem. Rev.* **120**, 1888–1935 (2020).
66. Tay, H. M. & Beer, P. Optical sensing of anions by macrocyclic and interlocked hosts. *Org. Biomol. Chem.* **19**, 4652–4677 (2021).
67. Gloe, K., Stephan, H. & Grotjahn, M. Where is the Anion Extraction Going? *Chem. Eng. \& Technol.* **26**, 1107–1117 (2003).
68. Busschaert, N., Caltagirone, C., Van Rossom, W. & Gale, P. A. Applications of Supramolecular Anion Recognition. *Chem. Rev.* **115**, 8038–8155 (2015).
69. Stern, K. H. Ionic size. *Chem.Rev* **59**, 1–64 (1959).
70. Haynes, W. M., Lide, D. R. & Bruno, T. J. *CRC handbook of chemistry and physics*. (CRC Press, 2016).

71. Beer, P. D. & Gale, P. A. Anion recognition and sensing: The state of the art and future perspectives. *Angew. Chemie Int. Ed.* vol. 40 486–516 (2001).
72. Park, C. H. & Simmons, H. E. Macrobicyclic Amines. III. Encapsulation of Halide Ions by in,in-1,(k + 2)-Diazabicyclo[k.l.m]aIkane-ammonium Ions. *J. Am. Chem. Soc.* **90**, 2431–2432 (1968).
73. Lehn, J. M., Sonveaux, E. & Willard, A. K. Molecular Recognition. Anion Cryptates of a Macrobicyclic Receptor Molecule for Linear Triatomic Species. *J. Am. Chem. Soc.* **100**, 4914–4916 (1978).
74. Dietrich, B., Lehn, J.-M., Guilhem, J. & Pascard, C. Anion receptor molecules : Synthesis of an octaaza-cryptand and structure of its fluoride cryptate. *Tetrahedron Lett.* **30**, 4125–4128 (1989).
75. Dietrich, B., Guilhem, J., Lehn, J.-M., Pascard, C. & Sonveaux, E. Molecular recognition in anion coordination chemistry. Structure, binding constants and receptor-substrate complementarity of a series of anion cryptates of a macrobicyclic receptor molecule. *Helv. Chim. Acta* **67**, 91–104 (1984).
76. Dietrich, B. *et al.* Anion Cryptates: Synthesis, crystal structures, and complexation constants of fluoride and chloride inclusion complexes of polyammonium macrobicyclic ligands. *Helv. Chim. Acta* **79**, 569–587 (1996).
77. Zhou, H. *et al.* Highly Selective Fluorescent Recognition of Sulfate in Water by Two Rigid Tetrakisimidazolium Macrocycles with Peripheral Chains. *J. Am. Chem. Soc.* **135**, 14908–14911 (2013).
78. Kumar, A. & Pandey, P. S. Anion Recognition by 1,2,3-Triazolfile Receptors: Application of Click Chemistry in Anion Recognition. *Org. Lett.* **10**, 165–168 (2008).
79. Cho, J. *et al.* Crown ether-appended calix[2]triazolium[2]arene as a macrocyclic receptor for the recognition of the $H_2PO_4^-$ anion. *Chem. Commun.* **56**, 1038–1041 (2020).
80. Hua, Y. & Flood, A. H. Click chemistry generates privileged CH hydrogen-bonding triazoles: the latest addition to anion supramolecular chemistry. *Chem. Soc. Rev.* **39**, 1262–1271 (2010).
81. Haridas, V., Sahu, S., Praveen Kumar, P. P. & Sapala, A. R. Triazole: a new motif for anion recognition. *RSC Adv.* **2**, 12594–12605 (2012).
82. Pascal, R. A., Spergel, J. & Van Engen, D. Synthesis and X-ray crystallographic characterization of a (1,3,5)cyclophane with three amide N-H groups surrounding a central cavity. A neutral host for anion complexation. *Tetrahedron Lett.* **27**, 4099–4102 (1986).
83. Kavallieratos, K., de Gala, S. R., Austin, D. J. & Crabtree, R. H. A Readily Available Non-preorganized Neutral Acyclic Halide Receptor with an Unusual Nonplanar Binding Conformation. *J. Am. Chem. Soc.* **119**, 2325–2326 (1997).
84. Kavallieratos, K., Bertao, C. M. & Crabtree, R. H. Hydrogen Bonding in Anion Recognition: A Family of Versatile, Nonpreorganized Neutral and Acyclic Receptors. *J. Org. Chem.* **64**, 1675–1683 (1999).
85. Manna, U. & Das, G. An overview of anion coordination by hydroxyl, amine and amide based rigid and symmetric neutral dipodal receptors. *Coord. Chem. Rev.* **427**, 213547 (2021).
86. Billing, B. K. & Verma, M. Anion Recognition Employing -NH Linked Organic Moieties. *ChemistrySelect* **6**, 4273–4284 (2021).
87. Kubik, S., Goddard, R., Kirchner, R., Nolting, D. & Seidel, J. A Cyclic Hexapeptide Containing L-Proline and 6-Aminopicolinic Acid Subunits Binds Anions in Water. *Angew. Chemie Int. Ed.* **40**, 2648–2651 (2001).
88. Kubik, S. & Goddard, R. Conformation and anion binding properties of cyclic hexapeptides containing L-4-hydroxyproline and 6-aminopicolinic acid subunits. *Proc.*

Natl. Acad. Sci. U. S. A. **99**, 5127–5132 (2002).
89. Kubik, S., Kirchner, R., Nolting, D. & Seidel, J. A molecular oyster: A neutral anion receptor containing two cyclopeptide subunits with a remarkable sulfate affinity in aqueous solution. *J. Am. Chem. Soc.* **124**, 12752–12760 (2002).
90. Sommer, F. & Kubik, S. Anion binding of a neutral bis(cyclopeptide) in water–methanol mixtures containing up to 95% water. *Org. Biomol. Chem.* **12**, 8851–8860 (2014).
91. Bartl, J. & Kubik, S. Anion Binding of a Cyclopeptide-Derived Molecular Cage in Aqueous Solvent Mixtures. *Chempluschem* **85**, 963–969 (2020).
92. Kaur, S., Day, V. W. & Bowman-James, K. Urea-Based Macrocycle Selective for Sulfate and Structurally Sensitive to Water. *Cryst. Growth Des.* **20**, 4212–4216 (2020).
93. Wezenberg, S. J. *et al.* Photomodulation of Transmembrane Transport and Potential by Stiff-Stilbene Based Bis(thio)ureas. *J. Am. Chem. Soc.* **144**, 331–338 (2022).
94. Ronchetti, R., Moroni, G., Carotti, A., Gioiello, A. & Camaioni, E. Recent advances in urea- and thiourea-containing compounds: focus on innovative approaches in medicinal chemistry and organic synthesis. *RSC Med. Chem.* **12**, 1046–1064 (2021).
95. Dey, S. K., Basu, A., Chutia, R. & Das, G. Anion coordinated capsules and pseudocapsules of tripodal amide, urea and thiourea scaffolds. *RSC Adv.* **6**, 26568–26589 (2016).
96. Mele, A., Metrangolo, P., Neukirch, H., Pilati, T. & Resnati, G. A Halogen-Bonding-Based Heteroditopic Receptor for Alkali Metal Halides. *J. Am. Chem. Soc.* **127**, 14972–14973 (2005).
97. Sarwar, M. G., Dragisic, B., Sagoo, S. & Taylor, M. S. A tridentate halogen-bonding receptor for tight binding of halide anions. *Angew. Chemie Int. Ed.* **49**, 1674–1677 (2010).
98. Mungalpara, D., Stegmüller, S. & Kubik, S. A neutral halogen bonding macrocyclic anion receptor based on a pseudocyclopeptide with three 5-iodo-1,2,3-triazole subunits. *Chem. Commun.* **53**, 5095–5098 (2017).
99. Borissov, A. *et al.* Anion Recognition in Water by Charge-Neutral Halogen and Chalcogen Bonding Foldamer Receptors. *J. Am. Chem. Soc.* **141**, 4119–4129 (2019).
100. Massena, C. J., Riel, A. M. S., Neuhaus, G. F., Decato, D. A. & Berryman, O. B. Solution and solid-phase halogen and C--H hydrogen bonding to perrhenate. *Chem. Commun.* **51**, 1417–1420 (2015).
101. Massena, C. J. *et al.* A Halogen-Bond-Induced Triple Helicate Encapsulates Iodide. *Angew. Chemie Int. Ed.* **55**, 12398–12402 (2016).
102. Tepper, R. *et al.* Anion Receptors Based on Halogen Bonding with Halo-1,2,3-triazoliums. *J. Org. Chem.* **80**, 3139–3150 (2015).
103. Jungbauer, S. H. & Huber, S. M. Cationic Multidentate Halogen-Bond Donors in Halide Abstraction Organocatalysis: Catalyst Optimization by Preorganization. *J. Am. Chem. Soc.* **137**, 12110–12120 (2015).
104. Bayly, S. R. & Beer, P. D. Metal-Based Anion Receptor Systems. in *Recognition of Anions* 45–94 (Springer Berlin Heidelberg, 2008). doi:10.1007/430_2007_073.
105. Mercer, D. J. & Loeb, S. J. Metal-based anion receptors: An application of second-sphere coordination. *Chem. Soc. Rev.* **39**, 3612–3620 (2010).
106. Aletti, A. B., Gillen, D. M. & Gunnlaugsson, T. Luminescent/colorimetric probes and (chemo-) sensors for detecting anions based on transition and lanthanide ion receptor/binding complexes. *Coord. Chem. Rev.* **354**, 98–120 (2018).
107. Beer, P. D. & Cadman, J. Electrochemical and optical sensing of anions by transition metal based receptors. *Coord. Chem. Rev.* **205**, 131–155 (2000).
108. Liu, Z., He, W. & Guo, Z. Metal coordination in photoluminescent sensing. *Chem. Soc. Rev.* **42**, 1568–1600 (2013).

109. Ma, D. L., Wu, C., Liu, H., Wu, K. J. & Leung, C. H. Luminescence approaches for the rapid detection of disease-related receptor proteins using transition metal-based probes. *J. Mater. Chem. B* **8**, 3249–3260 (2020).
110. Bickerton, L. E., Johnson, T. G., Kerckhoffs, A. & Langton, M. J. Supramolecular chemistry in lipid bilayer membranes. *Chem. Sci.* **12**, 11252–11274 (2021).
111. Steyer, S., Jeunesse, C., Armspach, D., Matt, D. & Harrowfteld, J. Coordination Chemistry and Catalysis. in *Calixarenes 2001* (eds. Asfari, Z., Böhmer, V., Harrowfield, J., Vicens, J. & Saadioui, M.) 513–535 (Springer Netherlands, 2001). doi:10.1007/0-306-47522-7_28.
112. Motekaitis, R. J., Martell, A. E., Dietrich, B. & Lehn, J. M. Anion binding in macrobicyclic metal cryptate complexes: copper (II)-BISTREN. *Inorg. Chem.* **23**, 1588–1591 (1984).
113. Fujita, K. *et al.* Design and Function of Supramolecular Recognition Systems Based on Guest-Targeting Probe-Modified Cyclodextrin Receptors for ATP. *J. Org. Chem.* **82**, 976–981 (2017).
114. Plajer, A. J. *et al.* Conformational Control in Main Group Phosphazane Anion Receptors and Transporters. *J. Am. Chem. Soc.* **142**, 1029–1037 (2020).
115. Comarmond, J. *et al.* Dinuclear copper(II) cryptates of macrocyclic ligands: synthesis, crystal structure, and magnetic properties. Mechanism of the exchange interaction through bridging azido ligands. *J. Am. Chem. Soc.* **104**, 6330–6340 (1982).
116. Chowdhury, B., Sinha, S. & Ghosh, P. Selective Sensing of Phosphates by a New Bis-heteroleptic RuIIComplex through Halogen Bonding: A Superior Sensor over Its Hydrogen-Bonding Analogue. *Chem. - A Eur. J.* **22**, 18051–18059 (2016).
117. Mole, T. K., Arter, W. E., Marques, I., Félix, V. & Beer, P. D. Neutral bimetallic rhenium(I)-containing halogen and hydrogen bonding acyclic receptors for anion recognition. *J. Organomet. Chem.* **792**, 206–210 (2015).
118. Gasa, T. B., Valente, C. & Stoddart, J. F. Solution-phase counterion effects in supramolecular and mechanostereochemical systems. *Chem. Soc. Rev.* **40**, 57–78 (2011).
119. Böhmer, V., Cort, A. D. & Mandolini, L. Counteranion effect on complexation of quats by a neutral calix[5]arene receptor. *J. Org. Chem.* **66**, 1900–1902 (2001).
120. Sessler, J. L. *et al.* Calix [4] pyrrole as a chloride anion receptor: solvent and countercation effects. *J. Am. Chem. Soc.* **128**, 12281–12288 (2006).
121. Akhuli, B. & Ghosh, P. Selective recognition and extraction of KBr via cooperative interactions with a urea functionalized crown ether dual-host. *Chem. Commun.* **51**, 16514–16517 (2015).
122. He, Q. *et al.* Selective Solid–Liquid and Liquid–Liquid Extraction of Lithium Chloride Using Strapped Calix[4]pyrroles. *Angew. Chemie Int. Ed.* **57**, 11924–11928 (2018).
123. He, Q. *et al.* Hemispherand-Strapped Calix[4]pyrrole: An Ion-pair Receptor for the Recognition and Extraction of Lithium Nitrite. *J. Am. Chem. Soc.* **138**, 9779–9782 (2016).
124. Webber, P. R. A. & Beer, P. D. Ion-pair recognition by a ditopic calix[4]semitube receptor. *Dalt. Trans.* 2249–2252 (2003) doi:10.1039/B302141F.
125. Zakrzewski, M., Kwietniewska, N., Walczak, W. & Piątek, P. A non-multimacrocyclic heteroditopic receptor that cooperatively binds and effectively extracts KAcO salt. *Chem. Commun.* **54**, 7018–7021 (2018).
126. Lee, J. H. *et al.* Synthetic K+/Cl–-Selective Symporter across a Phospholipid Membrane. *J. Org. Chem.* **79**, 6403–6409 (2014).
127. Park, I.-W. *et al.* Oligoether-Strapped Calix[4]pyrrole: An Ion-Pair Receptor Displaying Cation-Dependent Chloride Anion Transport. *Chem. – A Eur. J.* **18**, 2514–2523 (2012).
128. He, Q., Vargas-Zúñiga, G. I., Kim, S. H., Kim, S. K. & Sessler, J. L. Macrocycles as Ion Pair Receptors. *Chem. Rev.* **119**, 9753–9835 (2019).

129. Qiao, B. *et al.* Electrostatic and allosteric cooperativity in ion-pair binding: A quantitative and coupled experiment-theory study with aryl-triazole-ether macrocycles. *J. Am. Chem. Soc.* **137**, 9746–9757 (2015).
130. Evans, A. J. & Beer, P. D. Potassium cation cooperative anion recognition by heteroditopic calix[4]arene bis(benzo-15-crown-5) receptor molecules. *J. Chem. Soc. Dalt. Trans.* **3**, 4451–4456 (2003).
131. Deetz, M. J., Shang, M. & Smith, B. D. A macrobicyclic receptor with versatile recognition properties: simultaneous binding of an ion pair and selective complexation of dimethylsulfoxide. *J. Am. Chem. Soc.* **122**, 6201–6207 (2000).
132. Mahoney, J. M., Beatty, A. M. & Smith, B. D. Selective recognition of an alkali halide contact ion-pair. *J. Am. Chem. Soc.* **123**, 5847–5848 (2001).
133. Maity, K., Panda, D. K., Gallup, R. J., Choudhury, C. K. & Saha, S. Cation-Assisted Reversible Folding and Anion Binding by a Naphthalenediimide-Based Ditopic Ion-Pair Receptor. *Org. Lett.* **20**, 962–965 (2018).
134. McConnell, A. J., Docker, A. & Beer, P. D. From Heteroditopic to Multitopic Receptors for Ion-Pair Recognition: Advances in Receptor Design and Applications. *Chempluschem* **85**, 1824–1841 (2020).
135. Carreira-Barral, I. *et al.* Ditopic receptors containing urea groups for solvent extraction of Cu (II) salts. *Dalt. Trans.* **46**, 3192–3206 (2017).
136. DeLeo, P. C., Summers, H., Stanton, K. & Lam, M. W. Environmental risk assessment of polycarboxylate polymers used in cleaning products in the United States. *Chemosphere* **258**, 127242 (2020).
137. Khwaja, H. A. Atmospheric concentrations of carboxylic acids and related compounds at a semiurban site. *Atmos. Environ.* **29**, 127–139 (1995).
138. Zakrzewski, M., Załubiniak, D. & Piątek, P. Development of effective potassium acetate extractant. *RSC Adv.* **11**, 10860–10865 (2021).
139. White, D. J. *et al.* Ditopic ligands for the simultaneous solvent extraction of cations and anions. *Chem. Commun.* 2077–2078 (1999).
140. Grauwels, G., Valkenier, H., Davis, A. P., Jabin, I. & Bartik, K. Repositioning Chloride Transmembrane Transporters: Transport of Organic Ion Pairs. *Angew. Chemie Int. Ed.* **58**, 6921–6925 (2019).
141. Gotor, R., Costero, A. M., Gil, S., Gaviña, P. & Rurack, K. On the Ion-Pair Recognition and Indication Features of a Fluorescent Heteroditopic Host Based on a BODIPY Core. *European J. Org. Chem.* **2014**, 4005–4013 (2014).
142. Molina, P., Tárraga, A. & Alfonso, M. Ferrocene-based multichannel ion-pair recognition receptors. *Dalt. Trans.* **43**, 18–29 (2014).
143. Otón, F. *et al.* Ion Pair Recognition Receptor Based on an Unsymmetrically 1,1'-Disubstituted Ferrocene–Triazole Derivative. *J. Org. Chem.* **77**, 10083–10092 (2012).
144. Bruns, C. J. & Stoddart, J. F. *The Nature of the Mechanical Bond*. (John Wiley \& Sons, 2017).
145. Pentecost, C. D. *et al.* A molecular solomon link. *Angew. Chemie Int. Ed.* **46**, 218–222 (2007).
146. Liu, W., Stern, C. L. & Stoddart, J. F. Suit [4] ane. *J. Am. Chem. Soc.* **142**, 10273–10278 (2020).
147. Rotzler, J. & Mayor, M. Molecular daisy chains. *Chem. Soc. Rev.* **42**, 44–62 (2013).
148. Chichak, K. S. *et al.* Molecular borromean rings. *Science.* **304**, 1308–1312 (2004).
149. Harrison, I. T. & Harrison, S. Synthesis of a stable complex of a macrocycle and a threaded chain. *J. Am. Chem. Soc.* **89**, 5723–5724 (1967).
150. Chiu, C.-W., Lai, C.-C. & Chiu, S.-H. "Threading-followed-by-swelling": a new protocol for rotaxane synthesis. *J. Am. Chem. Soc.* **129**, 3500–3501 (2007).
151. Ko, J.-L. *et al.* Using a Threading-Followed-by-Swelling Approach to Synthesize [2]

Rotaxanes. *Chem. Eur. J.* **16**, 6950–6960 (2010).
152. Huang, X. *et al.* Slipping synthesis of cucurbit [7] uril-based [2] rotaxane in organic environment. *Tetrahedron Lett.* **53**, 6414–6417 (2012).
153. Yin, J., Dasgupta, S. & Wu, J. Synthesis of [n] rotaxanes by template-directed clipping: the role of the dialkylammonium recognition sites. *Org. Lett.* **12**, 1712–1715 (2010).
154. Dietrich-Buchecker, C. O. & Sauvage, J. P. Interlocking of molecular threads: from the statistical approach to the templated synthesis of catenands. *Chem. Rev.* **87**, 795–810 (1987).
155. Fletcher, B. E., Peach, M. J. G. & Evans, N. H. Rapidly accessible "click" rotaxanes utilizing a single amide hydrogen bond templating motif. *Org. Biomol. Chem.* **15**, 2797–2803 (2017).
156. Harrison, I. T. The effect of ring size on threading reactions of macrocycles. *J. Chem. Soc. Chem. Commun.* 231–232 (1972).
157. Wisner, J. A., Beer, P. D., Drew, M. G. B. & Sambrook, M. R. Anion-Templated Rotaxane Formation. *J. Am. Chem. Soc.* **124**, 12469–12476 (2002).
158. Hamann, C., Kern, J.-M. & Sauvage, J.-P. Zinc(II)-Templated Synthesis of a [2]-Catenane Consisting of a 2,2',6',2'-Terpyridine-Incorporating Cycle and a 1,10-Phenanthroline-Containing Ring. *Inorg. Chem.* **42**, 1877–1883 (2003).
159. Goldup, S. M., Leigh, D. A., Lusby, P. J., McBurney, R. T. & Slawin, A. M. Z. Gold(I)-Template Catenane and Rotaxane Synthesis. *Angew. Chemie Int. Ed.* **47**, 6999–7003 (2008).
160. Wasserman, E. Chemical topology. *Sci. Am.* **207**, 94–106 (1962).
161. Schill, G. & Lüttringhaus, A. The preparation of catena compounds by directed synthesis. *Angew. Chemie Int. Ed.* **3**, 546–547 (1964).
162. Blake, A. J., Dietrich-Buchecker, C. O., Hyde, T. I., Sauvage, J.-P. & Schröder, M. C-H activation in a co-ordinated catenand: ortho-metallation of cat30 by palladium (II). *J. Chem. Soc. Chem. Commun.* 1663–1665 (1989).
163. Hamann, C., Kern, J.-M. & Sauvage, J.-P. Palladium (II)-directed formation of pseudo-rotaxanes: the 3+ 1 approach to threaded species using square-planar geometries. *Dalt. Trans.* 3770–3775 (2003).
164. Sauvage, J. P. & Ward, M. A bis (terpyridine) ruthenium (II) catenate. *Inorg. Chem.* **30**, 3869–3874 (1991).
165. Aucagne, V., Hänni, K. D., Leigh, D. A., Lusby, P. J. & Walker, D. B. Catalytic "Click" Rotaxanes: A Substoichiometric Metal-Template Pathway to Mechanically Interlocked Architectures. *J. Am. Chem. Soc.* **128**, 2186–2187 (2006).
166. Lahlali, H., Jobe, K., Watkinson, M. & Goldup, S. M. Macrocycle Size Matters: "Small" Functionalized Rotaxanes in Excellent Yield Using the CuAAC Active Template Approach. *Angew. Chemie Int. Ed.* **50**, 4151–4155 (2011).
167. Movsisyan, L. D. *et al.* Polyyne rotaxanes: stabilization by encapsulation. *J. Am. Chem. Soc.* **138**, 1366–1376 (2016).
168. Alcântara, A. F. P. *et al.* Olefin cyclopropanation by radical carbene transfer reactions promoted by cobalt (II)/porphyrinates: active-metal-template synthesis of [2] rotaxanes. *Angew. Chemie Int. Ed.* **130**, 9117–9121 (2018).
169. Goldup, S. M., Leigh, D. A., Lusby, P. J., McBurney, R. T. & Slawin, A. M. Z. Active Template Synthesis of Rotaxanes and Molecular Shuttles with Switchable Dynamics by Four-Component Pd (II)-Promoted Michael Additions. *Angew. Chemie Int. Ed.* **120**, 3429–3432 (2008).
170. Tung, S.-T., Lai, C.-C., Liu, Y.-H., Peng, S.-M. & Chiu, S.-H. Synthesis of a [2]Catenane from the Sodium Ion Templated Orthogonal Arrangement of Two Diethylene Glycol Chains. *Angew. Chemie Int. Ed.* **52**, 13269–13272 (2013).
171. Kaiser, G. *et al.* Lithium-Templated Synthesis of a Donor--Acceptor Pseudorotaxane

and Catenane. *Angew. Chemie Int. Ed.* **43**, 1959–1962 (2004).
172. Mitra, R., Thiele, M., Octa-Smolin, F., Letzel, M. C. & Niemeyer, J. A bifunctional chiral [2] catenane based on 1, 1'-binaphthyl-phosphates. *Chem. Commun.* **52**, 5977–5980 (2016).
173. Hancock, L. M. & Beer, P. D. Sodium and barium cation-templated synthesis and cation-induced molecular pirouetting of a pyridine N-oxide containing [2]rotaxane. *Chem. Commun.* **47**, 6012–6014 (2011).
174. Zhang, G. *et al.* Lanthanide template synthesis of trefoil knots of single handedness. *J. Am. Chem. Soc.* **137**, 10437–10442 (2015).
175. Lincheneau, C., Jean-Denis, B. & Gunnlaugsson, T. Self-assembly formation of mechanically interlocked [2]-and [3] catenanes using lanthanide ion [Eu (III)] templation and ring closing metathesis reactions. *Chem. Commun.* **50**, 2857–2860 (2014).
176. Tokunaga, Y. *et al.* Base–acid-induced translational isomerism in a branched [4]rotaxane. *Tetrahedron Lett.* **57**, 1120–1123 (2016).
177. Rao, S.-J., Zhang, Q., Ye, X.-H., Gao, C. & Qu, D.-H. Integrative Self-Sorting: One-Pot Synthesis of a Hetero[4]rotaxane from a Daisy-Chain-Containing Hetero[4]pseudorotaxane. *Chem. – An Asian J.* **13**, 815–821 (2018).
178. Ashton, P. R. *et al.* A [2] Catenane Made to Order. *Angew. Chemie Int. Ed.* **28**, 1396–1399 (1989).
179. Hübner, G. M., Gläser, J., Seel, C. & Vögtle, F. High-Yielding Rotaxane Synthesis with an Anion Template. *Angew. Chemie Int. Ed.* **38**, 383–386 (1999).
180. Qiao, B., Liu, Y., Lee, S., Pink, M. & Flood, A. H. A high-yield synthesis and acid--base response of phosphate-templated [3] rotaxanes. *Chem. Commun.* **52**, 13675–13678 (2016).
181. Sambrook, M. R., Beer, P. D., Wisner, J. A., Paul, R. L. & Cowley, A. R. Anion-templated assembly of a [2] catenane. *J. Am. Chem. Soc.* **126**, 15364–15365 (2004).
182. Bunchuay, T., Docker, A., Martinez-Martinez, A. J. & Beer, P. D. A Potent Halogen-Bonding Donor Motif for Anion Recognition and Anion Template Mechanical Bond Synthesis. *Angew. Chemie Int. Ed.* **131**, 13961–13965 (2019).
183. Cirulli, M. *et al.* Rotaxane-Based Transition Metal Complexes: Effect of the Mechanical Bond on Structure and Electronic Properties. *J. Am. Chem. Soc.* **141**, 879–889 (2019).
184. Langton, M. J. & Beer, P. D. Nitrate anion templated synthesis of a [2]catenane for nitrate recognition in organic–aqueous solvent media. *Chem. Commun.* **50**, 8124–8127 (2014).
185. Collins, C. G., Peck, E. M., Kramer, P. J. & Smith, B. D. Squaraine rotaxane shuttle as a ratiometric deep-red optical chloride sensor. *Chem. Sci.* **4**, 2557–2563 (2013).
186. Langton, M. J., Robinson, S. W., Marques, I., Félix, V. & Beer, P. D. Halogen bonding in water results in enhanced anion recognition in acyclic and rotaxane hosts. *Nat. Chem.* **6**, 1039–1043 (2014).
187. Brown, A. & Beer, P. D. Halogen bonding anion recognition. *Chem. Commun.* **52**, 8645–8658 (2016).
188. Beer, P., Barendt, T., Lim, J. & others. *Supramolecular Chemistry: Fundamentals and Applications*. (Oxford university press, 2022).
189. Browne, W. R. & Feringa, B. L. Making molecular machines work. *Nat. Nanotechnol.* **1**, 25–35 (2006).
190. Iijima, T. *et al.* Controllable Donor–Acceptor Neutral [2]Rotaxanes. *Chem. – A Eur. J.* **10**, 6375–6392 (2004).
191. Meng, Z., Xiang, J.-F. & Chen, C.-F. Tristable [n]rotaxanes: from molecular shuttle to molecular cable car. *Chem. Sci.* **5**, 1520–1525 (2014).
192. Witus, L. S. *et al.* Relative contractile motion of the rings in a switchable palindromic

[3]rotaxane in aqueous solution driven by radical-pairing interactions. *Org. Biomol. Chem.* **12**, 6089–6093 (2014).
193. Zhang, Z.-J., Han, M., Zhang, H.-Y. & Liu, Y. A double-leg donor--acceptor molecular elevator: new insight into controlling the distance of two platforms. *Org. Lett.* **15**, 1698–1701 (2013).
194. Chatterjee, M. N., Kay, E. R. & Leigh, D. A. Beyond Switches: Ratcheting a Particle Energetically Uphill with a Compartmentalized Molecular Machine. *J. Am. Chem. Soc.* **128**, 4058–4073 (2006).
195. Echavarren, J. *et al.* Sequence-Selective Decapeptide Synthesis by the Parallel Operation of Two Artificial Molecular Machines. *J. Am. Chem. Soc.* **143**, 5158–5165 (2021).
196. Amano, S., Fielden, S. D. P. & Leigh, D. A. A catalysis-driven artificial molecular pump. *Nature* **594**, 529–534 (2021).
197. Cheng, C. *et al.* An artificial molecular pump. *Nat. Nanotechnol.* **10**, 547–553 (2015).
198. Kassem, S. *et al.* Site-to-site peptide transport on a molecular platform using a small-molecule robotic arm. *Chem. Sci.* **12**, 2065–2070 (2021).
199. Brown, A., Mennie, K. M., Mason, O., White, N. G. & Beer, P. D. Copper(II)-directed synthesis of neutral heteroditopic [2]rotaxane ion-pair host systems incorporating hydrogen and halogen bonding anion binding cavities. *Dalt. Trans.* **46**, 13376–13385 (2017).
200. Kim, S. K. & Sessler, J. L. Ion pair receptors. *Chem. Soc. Rev.* **39**, 3784–3809 (2010).
201. Denis, M., Pancholi, J., Jobe, K., Watkinson, M. & Goldup, S. M. Chelating Rotaxane Ligands as Fluorescent Sensors for Metal Ions. *Angew. Chemie Int. Ed.* **57**, 5310–5314 (2018).
202. Nandi, M., Bej, S., Ghosh, T. K. & Ghosh, P. A multifunctional catenated host for the efficient binding of Eu3+ and Gd3+. *Chem. Commun.* **55**, 3085–3088 (2019).
203. Baggi, G. & Loeb, S. J. Rotationally Active Ligands: Dialing-Up Multiple Interlocked Co-Conformations for Silver(I) Coordination. *Chem. – A Eur. J.* **23**, 14163–14166 (2017).
204. Bąk, K. M., Porfyrakis, K., Davis, J. J. & Beer, P. D. Exploiting the mechanical bond for molecular recognition and sensing of charged species. *Mater. Chem. Front.* **4**, 1052–1073 (2020).
205. Zhang, L. *et al.* Coordination Chemistry of a Molecular Pentafoil Knot. *J. Am. Chem. Soc.* **141**, 3952–3958 (2019).
206. Langton, M. J., Marques, I., Robinson, S. W., Félix, V. & Beer, P. D. Iodide Recognition and Sensing in Water by a Halogen-Bonding Ruthenium(II)-Based Rotaxane. *Chem. – A Eur. J.* **22**, 185–192 (2016).
207. Lim, J. Y. C., Marques, I., Félix, V. & Beer, P. D. A Chiral Halogen-Bonding [3]Rotaxane for the Recognition and Sensing of Biologically Relevant Dicarboxylate Anions. *Angew. Chemie Int. Ed.* **57**, 584–588 (2018).
208. Byrne, J. P., Blasco, S., Aletti, A. B., Hessman, G. & Gunnlaugsson, T. Formation of Self-Templated 2,6-Bis(1,2,3-triazol-4-yl)pyridine [2]Catenanes by Triazolyl Hydrogen Bonding: Selective Anion Hosts for Phosphate. *Angew. Chemie Int. Ed.* **55**, 8938–8943 (2016).
209. Spence, G. T. & Beer, P. D. Expanding the Scope of the Anion Templated Synthesis of Interlocked Structures. *Acc. Chem. Res.* **46**, 571–586 (2013).
210. Knighton, R. C. & Beer, P. D. Axle component separated ion-pair recognition by a neutral heteroditopic [2]rotaxane. *Chem. Commun.* **50**, 1540–1542 (2014).
211. Denis, M., Qin, L., Turner, P., Jolliffe, K. A. & Goldup, S. M. A Fluorescent Ditopic Rotaxane Ion-Pair Host. *Angew. Chemie Int. Ed.* **57**, 5315–5319 (2018).
212. Molina-Muriel, R., Romero, J. R., Li, Y., Aragay, G. & Ballester, P. The effect of solvent on the binding of anions and ion-pairs with a neutral [2]rotaxane. *Org. Biomol. Chem.*

19, 9986–9995 (2021).
213. Knighton, R. C. & Beer, P. D. Sodium cation-templated synthesis of an ion-pair binding heteroditopic [2]catenane. *Org. Chem. Front.* **8**, 2468–2472 (2021).
214. Martin, G., Rentsch, L., Höck, M. & Bertau, M. Lithium market research – global supply, future demand and price development. *Energy Storage Mater.* **6**, 171–179 (2017).
215. Flexer, V., Baspineiro, C. F. & Galli, C. I. Lithium recovery from brines: A vital raw material for green energies with a potential environmental impact in its mining and processing. *Sci. Total Environ.* **639**, 1188–1204 (2018).
216. Sverdrup, H. U. Modelling global extraction, supply, price and depletion of the extractable geological resources with the LITHIUM model. *Resour. Conserv. Recycl.* **114**, 112–129 (2016).
217. Zhang, Y., Hu, Y., Wang, L. & Sun, W. Systematic review of lithium extraction from salt-lake brines via precipitation approaches. *Miner. Eng.* **139**, 105868 (2019).
218. Zavahir, S. *et al.* A review on lithium recovery using electrochemical capturing systems. *Desalination* **500**, 114883 (2021).
219. Newman, P. K. & Saunders, M. Lithium neurotoxicity. *Postgrad. Med. J.* **55**, 701–703 (1979).
220. Niethammer, M. & Ford, B. Permanent lithium-induced cerebellar toxicity: Three cases and review of literature. *Mov. Disord.* **22**, 570–573 (2007).
221. Choi, H.-B., Ryu, J.-S., Shin, W.-J. & Vigier, N. The impact of anthropogenic inputs on lithium content in river and tap water. *Nat. Commun.* **10**, 5371 (2019).
222. He, Q. *et al.* Hemispherand-Strapped Calix[4]pyrrole: An Ion-pair Receptor for the Recognition and Extraction of Lithium Nitrite. *J. Am. Chem. Soc.* **138**, 9779–9782 (2016).
223. He, Q. *et al.* Selective Solid–Liquid and Liquid–Liquid Extraction of Lithium Chloride Using Strapped Calix[4]pyrroles. *Angew. Chemie Int. Ed.* **57**, 11924–11928 (2018).
224. Tse, Y. C., Docker, A., Zhang, Z. & Beer, P. D. Lithium halide ion-pair recognition with halogen bonding and chalcogen bonding heteroditopic macrocycles. *Chem. Commun.* **57**, 4950–4953 (2021).
225. Mahoney, J. M., Beatty, A. M. & Smith, B. D. Selective solid-liquid extraction of lithium halide salts using a ditopic macrobicyclic receptor. *Inorg. Chem.* **43**, 7617–7621 (2004).
226. Tian, Y. *et al.* A sub-milligram-synthesis protocol for in vitro screening of HDAC11 inhibitors. *Bioorg. Med. Chem. Lett.* **26**, 2434–2437 (2016).
227. Kilah, N. L. *et al.* Enhancement of Anion Recognition Exhibited by a Halogen-Bonding Rotaxane Host System. *J. Am. Chem. Soc.* **132**, 11893–11895 (2010).
228. Brynn Hibbert, D. & Thordarson, P. The death of the Job plot, transparency, open science and online tools, uncertainty estimation methods and other developments in supramolecular chemistry data analysis. *Chem. Commun.* **52**, 12792–12805 (2016).
229. Thordarson, P. Determining association constants from titration experiments in supramolecular chemistry. *Chem. Soc. Rev.* **40**, 1305–1323 (2011).
230. Frisch, M. J. *et al.* Gaussian-16 Rev. C.01. Gaussian Inc. Wallingford CT (2016).
231. Lee, C., Yang, W. & Parr, R. G. Development of the Colle-Salvetti correlation-energy formula into a functional of the electron density. *Phys. Rev. B* **37**, 785–789 (1988).
232. Becke, A. D. Density-functional thermochemistry. I. The effect of the exchange-only gradient correction. *J. Chem. Phys.* **96**, 2155–2160 (1992).
233. Woon, D. E. & Dunning, T. H. Gaussian basis sets for use in correlated molecular calculations. III. The atoms aluminum through argon. *J. Chem. Phys.* **98**, 1358–1371 (1993).
234. Peterson, K. A., Shepler, B. C., Figgen, D. & Stoll, H. On the spectroscopic and

thermochemical properties of ClO, BrO, IO, and their anions. *J. Phys. Chem. A* **110**, 13877–13883 (2006).
235. Peterson, K. A., Figgen, D., Goll, E., Stoll, H. & Dolg, M. Systematically convergent basis sets with relativistic pseudopotentials. II. Small-core pseudopotentials and correlation consistent basis sets for the post-d group 16–18 elements. *J. Chem. Phys.* **119**, 11113–11123 (2003).
236. Boys, S. F. & Bernardi, F. The calculation of small molecular interactions by the differences of separate total energies. Some procedures with reduced errors. *Mol. Phys.* **19**, 553–566 (1970).
237. van Duijneveldt, F. B., van Duijneveldt-van de Rijdt, J. G. C. M. & van Lenthe, J. H. State of the Art in Counterpoise Theory. *Chem. Rev.* **94**, 1873–1885 (1994).
238. Barendt, T. A. *et al.* Anion-mediated photophysical behavior in a C60Fullerene [3]Rotaxane Shuttle. *J. Am. Chem. Soc.* **140**, 1924–1936 (2018).
239. Barendt, T. A., Ferreira, L., Marques, I., Félix, V. & Beer, P. D. Anion- and Solvent-Induced Rotary Dynamics and Sensing in a Perylene Diimide [3]Catenane. *J. Am. Chem. Soc.* **139**, 9026–9037 (2017).
240. Barendt, T. A., Robinson, S. W. & Beer, P. D. Superior anion induced shuttling behaviour exhibited by a halogen bonding two station rotaxane. *Chem. Sci.* **7**, 5171–5180 (2016).
241. Cao, Z.-Q. *et al.* A fluorescent bistable [2]rotaxane molecular switch on SiO2 nanoparticles. *Chem. Commun.* **51**, 4973–4976 (2015).
242. Thordarson, P., Bijsterveld, E. J. A., Rowan, A. E. & Nolte, R. J. M. Epoxidation of polybutadiene by a topologically linked catalyst. *Nature* **424**, 915–918 (2003).
243. Hidalgo Ramos, P. *et al.* Processive Rotaxane Systems. Studies on the Mechanism and Control of the Threading Process. *J. Am. Chem. Soc.* **129**, 5699–5702 (2007).
244. Blanco, V., Carlone, A., Hänni, K. D., Leigh, D. A. & Lewandowski, B. A Rotaxane-Based Switchable Organocatalyst. *Angew. Chemie Int. Ed.* **51**, 5166–5169 (2012).
245. Kench, T., Summers, P. A., Kuimova, M. K., Lewis, J. E. M. & Vilar, R. Rotaxanes as Cages to Control DNA Binding, Cytotoxicity, and Cellular Uptake of a Small Molecule. *Angew. Chemie Int. Ed.* **60**, 10928–10934 (2021).
246. Barat, R. *et al.* A mechanically interlocked molecular system programmed for the delivery of an anticancer drug. *Chem. Sci.* **6**, 2608–2613 (2015).
247. Cotí, K. K. *et al.* Mechanised nanoparticles for drug delivery. *Nanoscale* **1**, 16–39 (2009).
248. Hou, X. *et al.* Tunable solid-state fluorescent materials for supramolecular encryption. *Nat. Commun.* **6**, 6884 (2015).
249. Suhan, N. D., Loeb, S. J. & Eichhorn, S. H. Mesomorphic [2]Rotaxanes: Sheltering Ionic Cores with Interlocking Components. *J. Am. Chem. Soc.* **135**, 400–408 (2013).
250. Aprahamian, I. *et al.* A Liquid-Crystalline Bistable [2]Rotaxane. *Angew. Chemie Int. Ed.* **46**, 4675–4679 (2007).
251. Du, G., Moulin, E., Jouault, N., Buhler, E. & Giuseppone, N. Muscle-like Supramolecular Polymers: Integrated Motion from Thousands of Molecular Machines. *Angew. Chemie Int. Ed.* **51**, 12504–12508 (2012).
252. Oku, T., Furusho, Y. & Takata, T. A Concept for Recyclable Cross-Linked Polymers: Topologically Networked Polyrotaxane Capable of Undergoing Reversible Assembly and Disassembly. *Angew. Chemie Int. Ed.* **43**, 966–969 (2004).
253. Green, J. E. *et al.* A 160-kilobit molecular electronic memory patterned at 1011 bits per square centimetre. *Nature* **445**, 414–417 (2007).
254. Yao, B., Sun, H., Yang, L., Wang, S. & Liu, X. Recent Progress in Light-Driven Molecular Shuttles. *Front. Chem.* **9**, 832735 (2021).
255. Andersen, S. S. *et al.* Mechanistic Evaluation of Motion in Redox-Driven Rotaxanes

Reveals Longer Linkers Hasten Forward Escapes and Hinder Backward Translations. *J. Am. Chem. Soc.* **136**, 6373–6384 (2014).
256. Saha, S. *et al.* A Redox-Driven Multicomponent Molecular Shuttle. *J. Am. Chem. Soc.* **129**, 12159–12171 (2007).
257. Raiteri, P. *et al.* Unravelling the Shuttling Mechanism in a Photoswitchable Multicomponent Bistable Rotaxane. *Angew. Chemie Int. Ed.* **47**, 3536–3539 (2008).
258. Brouwer, A. M. *et al.* Photoinduction of Fast, Reversible Translational Motion in a Hydrogen-Bonded Molecular Shuttle. *Science.* **291**, 2124–2128 (2001).
259. Marlin, D. S., González Cabrera, D., Leigh, D. A. & Slawin, A. M. Z. Complexation-Induced Translational Isomerism: Shuttling through Stepwise Competitive Binding. *Angew. Chemie Int. Ed.* **45**, 77–83 (2006).
260. Berná, J., Alajarín, M. & Orenes, R.-A. Azodicarboxamides as Template Binding Motifs for the Building of Hydrogen-Bonded Molecular Shuttles. *J. Am. Chem. Soc.* **132**, 10741–10747 (2010).
261. Caballero, A., Swan, L., Zapata, F. & Beer, P. D. Iodide-Induced Shuttling of a Halogen- and Hydrogen-Bonding Two-Station Rotaxane. *Angew. Chemie Int. Ed.* **53**, 11854–11858 (2014).
262. Kassem, S. *et al.* Artificial molecular motors. *Chem. Soc. Rev.* **46**, 2592–2621 (2017).
263. Collin, J.-P., Dietrich-Buchecker, C., Gaviña, P., Jimenez-Molero, M. C. & Sauvage, J.-P. Shuttles and Muscles: Linear Molecular Machines Based on Transition Metals. *Acc. Chem. Res.* **34**, 477–487 (2001).
264. Kay, E. R., Leigh, D. A. & Zerbetto, F. Synthetic Molecular Motors and Mechanical Machines. *Angew. Chemie Int. Ed.* **46**, 72–191 (2007).
265. Brown, A., Lang, T., Mullen, K. M. & Beer, P. D. Active metal template synthesis of a neutral indolocarbazole-containing [2]rotaxane host system for selective oxoanion recognition. *Org. Biomol. Chem.* **15**, 4587–4594 (2017).
266. Vignon, S. A. *et al.* Switchable Neutral Bistable Rotaxanes. *J. Am. Chem. Soc.* **126**, 9884–9885 (2004).
267. Tepper, R. *et al.* Halogen-bond-based cooperative ion-pair recognition by a crown-ether-embedded 5-iodo-1,2,3-triazole. *Chem. Commun.* **53**, 2260–2263 (2017).
268. Miyazaki, Y. *et al.* CuAAC in a Distal Pocket: Metal Active-Template Synthesis of Strapped-Porphyrin [2]Rotaxanes. *Chem. – A Eur. J.* **23**, 13579–13582 (2017).
269. Langton, M. J., Xiong, Y. & Beer, P. D. Active-Metal Template Synthesis of a Halogen-Bonding Rotaxane for Anion Recognition. *Chem. - A Eur. J.* **21**, 18910–18914 (2015).
270. Mullaney, B. R., Thompson, A. L. & Beer, P. D. An All-Halogen Bonding Rotaxane for Selective Sensing of Halides in Aqueous Media. *Angew. Chemie Int. Ed.* **53**, 11458–11462 (2014).
271. Yu, M. *et al.* Cationic iridium(iii) complexes for phosphorescence staining in the cytoplasm of living cells. *Chem. Commun.* 2115–2117 (2008) doi:10.1039/B800939B.
272. Jiang, W. *et al.* Zwitterionic Iridium Complexes: Synthesis, Luminescent Properties, and Their Application in Cell Imaging. *Inorg. Chem.* **49**, 3252–3260 (2010).
273. Lu, G.-Z. *et al.* A series of red iridium(iii) complexes using flexible dithiocarbamate derivatives as ancillary ligands for highly efficient phosphorescent OLEDs. *Mater. Chem. Front.* **3**, 860–866 (2019).
274. Mills, I. N., Porras, J. A. & Bernhard, S. Judicious Design of Cationic, Cyclometalated Ir(III) Complexes for Photochemical Energy Conversion and Optoelectronics. *Acc. Chem. Res.* **51**, 352–364 (2018).
275. Lee, S. & Han, W.-S. Cyclometalated Ir(iii) complexes towards blue-emissive dopant for organic light-emitting diodes: fundamentals of photophysics and designing strategies. *Inorg. Chem. Front.* **7**, 2396–2422 (2020).
276. Ma, D.-L. *et al.* Iridium(III)-based chemosensors for the detection of metal ions.

Methods **168**, 3–17 (2019).
277. Ma, D. L., Lin, S., Wang, W., Yang, C. & Leung, C. H. Luminescent chemosensors by using cyclometalated iridium(iii) complexes and their applications. *Chem. Sci.* **8**, 878–889 (2017).
278. Reddy, M. L. P. & Bejoymohandas, K. S. Evolution of 2, 3′-bipyridine class of cyclometalating ligands as efficient phosphorescent iridium(III) emitters for applications in organic light emitting diodes. *J. Photochem. Photobiol. C Photochem. Rev.* **29**, 29–47 (2016).
279. Bian, Z. *Molecular organometallic materials for optics*. vol. 28 (Springer Science & Business Media, 2009).
280. Kim, J.-H. *et al.* A Detailed Evaluation for the Nonradiative Processes in Highly Phosphorescent Iridium(III) Complexes. *J. Phys. Chem. C* **122**, 4029–4036 (2018).
281. Zanoni, K. P. S., Coppo, R. L., Amaral, R. C. & Murakami Iha, N. Y. Ir(III) complexes designed for light-emitting devices: beyond the luminescence color array. *Dalt. Trans.* **44**, 14559–14573 (2015).
282. Zanoni, K. P. S., Coppo, R. L., Amaral, R. C. & Murakami Iha, N. Y. Ir(III) complexes designed for light-emitting devices: Beyond the luminescence color array. *Dalt. Trans.* **44**, 14559–14573 (2015).
283. Hu, Y. *et al.* Iridium complex bearing urea groups as a phosphorescent chemosensor for chiral anion recognition. *Sensors Actuators B Chem.* **241**, 224–229 (2017).
284. Kampes, R. *et al.* Facile and Reliable Emission-Based Nanomolar Anion Sensing by Luminescent Iridium Receptors Featuring Chelating Halogen-Bonding Sites. *Chem. - A Eur. J.* **26**, 14679–14687 (2020).
285. Lim, J. Y. C., Marques, I., Félix, V. & Beer, P. D. A Chiral Halogen-Bonding [3]Rotaxane for the Recognition and Sensing of Biologically Relevant Dicarboxylate Anions. *Angew. Chemie Int. Ed.* **57**, 584–588 (2018).
286. Bunchuay, T. Sigma-Hole Donor Host Systems for Anion and Ion-Pair Recognition. (University of Oxford, 2018).
287. Kroll, A., Monczak, K., Sorsche, D. & Rau, S. A Luminescent Ruthenium Azide Complex as a Substrate for Copper-Catalyzed Click Reactions. *Eur. J. Inorg. Chem.* **2014**, 3462–3466 (2014).
288. Hasan, K. *et al.* Tuning the Emission of Cationic Iridium (III) Complexes Towards the Red Through Methoxy Substitution of the Cyclometalating Ligand. *Sci. Rep.* **5**, 12325 (2015).
289. Chen, Y., Liu, C. & Wang, L. Effects of fluorine substituent on properties of cyclometalated iridium(III) complexes with a 2,2′-bipyridine ancillary ligand. *Tetrahedron* **75**, 130686 (2019).
290. Suzuki, K. *et al.* Reevaluation of absolute luminescence quantum yields of standard solutions using a spectrometer with an integrating sphere and a back-thinned CCD detector. *Phys. Chem. Chem. Phys.* **11**, 9850–9860 (2009).
291. Würth, C., Grabolle, M., Pauli, J., Spieles, M. & Resch-Genger, U. Relative and absolute determination of fluorescence quantum yields of transparent samples. *Nat. Protoc.* **8**, 1535–1550 (2013).
292. Ladouceur, S., Fortin, D. & Zysman-Colman, E. Role of substitution on the photophysical properties of 5,5′-diaryl-2,2′-bipyridine (bpy*) in [Ir(ppy) 2(bpy*)]PF6 complexes: A combined experimental and theoretical study. *Inorg. Chem.* **49**, 5625–5641 (2010).
293. Ilic, S., Cairnie, D. R., Bridgewater, C. M. & Morris, A. J. Investigation into dual emission of a cyclometalated iridium complex: The role of ion-pairing. *J. Photochem. Photobiol.* **8**, 100084 (2021).
294. Ilic, S., Cairnie, D. R., Bridgewater, C. M. & Morris, A. J. Investigation into dual emission

of a cyclometalated iridium complex: The role of ion-pairing. *J. Photochem. Photobiol.* **8**, 100084 (2021).

295. Beer, P. D. *et al.* Anion selective recognition and sensing by novel macrocyclic transition metal receptor systems. ^{1}H NMR, electrochemical, and photophysical investigations. *J. Am. Chem. Soc.* **119**, 11864–11875 (1997).
296. Sharma, A. & Schulman, S. G. *Introduction to fluorescence spectroscopy*. vol. 13 (Wiley New York, 1999).
297. Leblond, J. & Petitjean, A. Molecular tweezers: concepts and applications. *ChemPhysChem* **12**, 1043–1051 (2011).
298. Ghosh, K., Masanta, G. & Chattopadhyay, A. P. Triphenylamine-Based Pyridine N-Oxide and Pyridinium Salts for Size-Selective Recognition of Dicarboxylates. *Eur. J. Org. Chem.* **2009**, 4515–4524 (2009).
299. Zapata, F., Caballero, A., Molina, P., Alkorta, I. & Elguero, J. Open Bis(triazolium) Structural Motifs as a Benchmark To Study Combined Hydrogen- and Halogen-Bonding Interactions in Oxoanion Recognition Processes. *J. Org. Chem.* **79**, 6959–6969 (2014).
300. Veliscek Carolan, J., Butler, S. J. & Jolliffe, K. A. Selective Anion Binding in Water with Use of a Zinc(II) Dipicolylamino Functionalized Diketopiperazine Scaffold. *J. Org. Chem.* **74**, 2992–2996 (2009).
301. Klärner, F.-G., Burkert, U., Kamieth, M., Boese, R. & Benet-Buchholz, J. Molecular Tweezers as Synthetic Receptors: Molecular Recognition of Electron-Deficient Aromatic and Aliphatic Substrates. *Chem. Eur. J.* **5**, 1700–1707 (1999).
302. Hardouin–Lerouge, M., Hudhomme, P. & Sallé, M. Molecular clips and tweezers hosting neutral guests. *Chem. Soc. Rev.* **40**, 30–43 (2011).
303. Valderrey, V., Aragay, G. & Ballester, P. Porphyrin tweezer receptors: Binding studies, conformational properties and applications. *Coord. Chem. Rev.* **258**–**259**, 137–156 (2014).
304. Ngo, H. T., Liu, X. & Jolliffe, K. A. Anion recognition and sensing with Zn(ii)–dipicolylamine complexes. *Chem. Soc. Rev.* **41**, 4928–4965 (2012).
305. Ghosh, K., Masanta, G. & Chattopadhyay, A. P. Triphenylamine-Based Pyridine N-Oxide and Pyridinium Salts for Size-Selective Recognition of Dicarboxylates. (2009).
306. Zapata, F., Caballero, A., Molina, P., Alkorta, I. & Elguero, J. Open Bis(triazolium) Structural Motifs as a Benchmark To Study Combined Hydrogen- and Halogen-Bonding Interactions in Oxoanion Recognition Processes. *J. Org. Chem.* **79**, 6959–6969 (2014).
307. Veliscek Carolan, J., Butler, S. J. & Jolliffe, K. A. Selective Anion Binding in Water with Use of a Zinc(II) Dipicolylamino Functionalized Diketopiperazine Scaffold. *J. Org. Chem.* **74**, 2992–2996 (2009).
308. Li, X., Lim, J. Y. C. & Beer, P. D. Acid-Regulated Switching of Metal Cation and Anion Guest Binding in Halogen-Bonding Rotaxanes. *Chem. – A Eur. J.* **24**, 17788–17795 (2018).
309. Harada, N. *et al.* Effective synthesis of 99mTc tricarbonyl complexes by microwave heating. *J. Organomet. Chem.* **696**, 3745–3749 (2011).
310. Lazarova, N., James, S., Babich, J. & Zubieta, J. A convenient synthesis, chemical characterization and reactivity of $[Re(CO)_3(H_2O)_3]Br$: the crystal and molecular structure of [Re(CO)3(CH3CN)2Br]. *Inorg. Chem. Commun.* **7**, 1023–1026 (2004).
311. Mindt, T. L. *et al.* A Click Approach to Structurally Diverse Conjugates Containing a Central Di-1,2,3-triazole Metal Chelate. *ChemMedChem* **4**, 529–539 (2009).
312. Banerjee, S. R. *et al.* Bifunctional single amino acid chelates for labeling of biomolecules with the $\{Tc(CO)_3\}^+$ and $\{Re(CO)_3\}^+$ cores. Crystal and molecular structures of $[ReBr(CO)_3(H_2NCH_2\ C_5H_4N)]$, $[Re(CO)_3\{(C_5H_4\ NCH_2)_2NH\}]Br$,. *Inorg. Chem.*

41, 6417–6425 (2002).
313. Eychenne, R. *et al.* Rhenium complexes based on an N_2O tridentate click scaffold: from synthesis, structural and theoretical characterization to a radiolabelling study. *Eur. J. Inorg. Chem.* **2017**, 69–81 (2017).
314. Alvarez, S. A cartography of the van der Waals territories. *Dalt. Trans.* **42**, 8617–8636 (2013).
315. Alvarez, S. A cartography of the van der Waals territories. *Dalt. Trans.* **42**, 8617–8636 (2013).
316. Pike, S. J., Hutchinson, J. J. & Hunter, C. A. H-Bond Acceptor Parameters for Anions. *J. Am. Chem. Soc.* **139**, 6700–6706 (2017).
317. Pancholi, J. & Beer, P. D. Halogen bonding motifs for anion recognition. *Coord. Chem. Rev.* **416**, 213281 (2020).
318. Lee, B.-Y., Park, S. R., Jeon, H. B. & Kim, K. S. A new solvent system for efficient synthesis of 1,2,3-triazoles. *Tetrahedron Lett.* **47**, 5105–5109 (2006).
319. Lim, J. Y. C., Marques, I., Félix, V. & Beer, P. D. Chiral halogen and chalcogen bonding receptors for discrimination of stereo- and geometric dicarboxylate isomers in aqueous media. *Chem. Commun.* **54**, 10851–10854 (2018).
320. CrysAlisPRO. CrysAlisPRO. *Oxford Diffr. /Agilent Technol. UK Ltd, Yarnton, Engl.*
321. Thorn, A. & Sheldrick, G. M. P03. 02.12. *Acta Cryst* **64**, C221--222 (2008).
322. Sheldrick, G. M. Crystal structure refinement with SHELXL. *Acta Crystallogr. Sect. C Struct. Chem.* **71**, 3–8 (2015).